Polarization resolved nonlinear multimodal microscopy in lipids: from model membranes to myelin in tissues.

Paulina Gasecka

To cite this version:

Paulina Gasecka. Polarization resolved nonlinear multimodal microscopy in lipids: from model membranes to myelin in tissues.. Nonlinear Sciences [physics]. Université Aix-Marseille, 2015. English. NNT : . tel-01272893

HAL Id: tel-01272893
https://theses.hal.science/tel-01272893

Submitted on 11 Feb 2016

Université Aix-Marseille

THÈSE

pour obtenir le grade de **Docteur en Sciences**
de l'Université Aix-Marseille

École Doctorale : Physique & Sciences de la Matière

Discipline : Optique photonique et traitement d'image

Polarization resolved nonlinear multimodal microscopy in lipids: from model membranes to myelin in tissues.

Microscopie multimodale non-linéaire résolue en polarisation pour l'étude des lipides: modèles membranes à la myéline dans les tissus.

soutenue publiquement le **11 Decembre 2015** par

Paulina Gąsecka

Rapporteurs :	Prof. Andreas Zumbusch
	Dr. Laurent Bourdieu
Examinateurs :	Dr. Olivier Piot
	Dr. Franck Debarbieux
	Dr. Hervé Rigneault
Directeurs de thèse :	Dr. Sophie Brasselet

Institut Fresnel — CNRS UMR 6133 — Équipe MOSAIC

Acknowledgements

It is a pleasure to express my appreciation and deepest gratitude for the help of many people who in one way or another have contributed in making this study possible.

Firstly, I would like to offer my sincerest gratitude to **Sophie Brasselet** for her excellent supervision, advice and care. Throughout my PhD thesis she supported me with her enthusiasm and knowledge as well as open-mindedness to diverse laboratory trials allowing me at the same time to work in my own way. Her never-ending ideas, remarkable intuition and passion in science, which exceptionally inspired, encouraged me to follow my instinct and scientific ambitions to become a student and a scientist I want to be. One could not have imagined a better supervisor having such extraordinary human qualities, who gave her care and shelter in doing this research and finally giving endless help and infinite patience to finish this manuscript.

I would like give my special thanks to **Hervé Rigneault** for giving me the opportunity to do my PhD thesis at Institut Fresnel, his very warm welcome upon my arrival at MOSAIC group and his faith in my skills irrespective of my scientific background. His unusual inventiveness to find a solution to any kind of situation particularly encouraged me and gave me a feeling of the oasis of calm during the initial months of my doctoral studies.

I would like to thank to the members of the jury: **Prof. Andreas Zumbusch**, **Dr. Laurent Bourdieu** and **Dr. Olivier Piot** for their time, interest in the subject of this thesis, careful reading of the manuscript and insightful questions.

I highly appreciate the collaboration with **Franck Debarbieux** for his advice, his patience, his constant willingness to help and answer the simplest questions as well as fruitful discussions on the immunology of the central nervous system. I would like to specially thank **Alexandre Jaouen**, excellently prepared samples of spinal cord which made it possible to achieve the fascinating results.

My external gratitude goes to three special persons, my colleagues and friends: **Xueqin (Christine) Chen**, **Fatma-Zohra (Zola) Bioud** and **Naveen Balla**. During the past three and a half years I had a great pleasure to spend a huge amount of time in the lab with them working on different scientific projects. I thank them for their infinite patience, open-mindedness and constant willingness to help and answer my interminable questions on CARS/SRS microscopy (Christine); on math, theoretical model and programming (Zola); on technical and theoretical optics and also programming (Naveen). They provided

excellent company and pleasurable working atmosphere which made me feel safe and made me think that there is no unsolvable problem. I am also truly thankful for the moments of leisure shared together that helped me to overcome some difficult moments.

My sincere gratitude also belong to **Hilton Barbosa de Aguiar**. I was continually impressed by his open-mindedness, fathomless well of new ideas and his inspiring curiosity in science. He patiently answered all my questions, tracked down book and papers and generally went above and beyond in helping find any resources which might have been helpful to me. As a friend, he has encouraged me and gave me a strength and motivation in difficult moments when I doubted myself.

I greatly appreciate and wish to thank a few people who in different ways contributed and helped me to perform this studies: **Patric Ferrand** for the help with the Labview program, **Julien Savatier** for his ever readiness to help with the equipment in the chem lab, and **Julien Duboisset** for the help with the Matlab program.

I would like to express my deepest appreciation to the technical staff at Institut Fresnel for their great assistance which made all informatics and administrative hurdles appear simple. Special thanks to **Nelly Bardet** without whose support I would not be able to go through the complexity of the French bureaucracy. Particular thanks to **Frédéric Forestier**, not only for his informatics skills, but especially for the extraordinary introduction to the sailing adventures.

There are many people I would like to thank, friends, colleagues and members of the MOSAIC group who I have met during almost four years of stay in Marseille. People, who made Marseille a very special place, who shared with me the good as well as bad moments, but unforgettable: **Pascal**, **Hilton**, **Magali**, **Irène**, **Maud**, **Tassos**, **Soizic**, **Ilanit**, **Madeleine**, **Juan**, **Alberto**, **Thomas**, **Sidiky**, **Carolina**, **Yoann**, **Rebecca**, **Zola**, **Naveen**, **Susmita**, **Suzanne** and many many others. I am grateful for the time spent with them, for the memorable apéros on Cours Julien, trips to the Calanques, climbing sessions, games, movies and brewery sessions. I truly thank them to re-open my mind and inspired me in music and photography, and also for their huge amount of patience during the last months of writing this manuscript.

And last but not least I would like to thank my sister and my parents for always supporting me. My sister in particular for being a pole star in my pursuit of my life path. And my parents for giving me a conviction that everything is possible.

Abstract

Polarization resolved nonlinear microscopy is a powerful tool to image structural information in biomolecular assemblies. Nonlinear interaction between light and matter lead to complex processes where coherent combinations of optical fields couple to assemblies of molecular transition dipoles. Controlling polarized optical fields and monitoring nonlinear induced signals in a medium can nevertheless bring rich information on molecular orientational organization within the focal spot of a microscope objective. In this PhD thesis we apply this polarization sensitivity to different label-free optical coherent techniques (coherent anti-Stokes Raman scattering (CARS), stimulated Raman scattering (SRS)) and to two-photon fluorescence (2PEF) to retrieve quantitative information on the static molecular distribution shape and orientation of lipids in model membranes and biological membranes such as myelin sheaths in spinal cord tissues. With this technique, we address fundamental questions about lipid packing behavior in membranes, and how it can be affected by other molecules such as cholesterol and the insertion of fluorescent lipid probes. We demonstrate that polarization resolved CARS give access to fine details on lipids arrangement in myelin sheaths, at a sub-diffraction scale. In the context of experimental autoimmune encephalomyelitis disease (EAE) we show, that even at the stage of disruption of the myelin envelope during the demyelination process, lipids multilayers reveal strong capability to preserve their macroscopic self-assembly into highly organized structures, with a degree of disorganization occurring only at the molecular scale. At last, we show that such technique can be combined with a larger scope of studies in bioimaging; we use multimodal microscopy (combined CARS and 2PEF) to image axonal degeneration and immune cell recruitment associated to demyelination process in order to address biological questions related to the immune response and axon damage during progression of the neurodegenerative disease.

Keywords : nonlinear microscopy, polarization, multimodal microscopy, molecular organization, lipid membranes, myelin, neurodegenerative disease.

Résumé

La microscopie non-linéaire résolue en polarisation est un outil puissant pour accéder à des informations structurelles dans les assemblages biomoléculaires. Les interactions non-linéaire entre matière et lumière induisent des processus complexes où des champs électromagnétiques cohérents interagissent avec les dipôles de transitions moléculaires. Le contrôle de la polarisation des champs électromagnétiques excitateurs et l'étude des réponses non-linéaires induites procurent de riches informations sur la distribution angulaire des molécules présentes dans le volume focal de l'objectif du microscope. Dans cette thèse, nous appliquons cette sensibilité à la polarisation à plusieurs modalités de microscopie cohérentes sans marquage (diffusion cohérente Raman anti-Stokes (CARS), diffusion Cohérente stimulée (SRS)) et à la fluorescence à deux photons (2PEF) afin d'obtenir des informations quantitatives sur la forme de la distribution moléculaire et l'orientation des lipides dans les membranes artificielles, ainsi que dans les membranes biologiques telles que la myéline des tissues de la moelle épinière. Avec cette technique, nous adressons une question fondamentale sur le comportement des ensembles lipidiques dans les membranes et sur l'effet d'autres molécules telles que le cholestérol et les marqueurs fluorescents. Nous démontrons que le CARS résolu en polarisation permet d'accéder à de fines informations sur l'organisation des lipides dans les membranes de la myéline, en deçà de la limite de diffraction. Dans le contexte de l'encéphalomyélite allergique expérimentale (EAE), nous démontrons que même au stade de la perturbation de la couche de myéline lors du processus de démyélinisation, les multicouches de lipides présentent une forte capacité de préserver leur auto-assemblage macroscopique en présentant une structure hautement organisée avec un niveau de désorganisation qui ne se retrouve qu'à l'échelle moléculaire. Finalement, nous démontrons qu'une telle technique peut être combinée à d'autres pour un plus grand éventail d'études en bio-imagerie; nous utilisons la microscopie multimodale (combinaison de CARS et de 2PEF) pour imager la dégénération des axones et le recrutement de cellules immunitaires associé au processus de démyélinisation afin d'adresser des questions biologiques reliées à la réponse immunitaire et les dommages des axones durant la progression des maladies neurodégénératives.

Keywords : microscopie non-linéaire, polarisation, microscopie multimodale, l'organisation moléculaire, membranes lipidiques, myéline, maladies neurodégénératives.

Contents

Introduction

Microscopy imaging has notably developed this last decade in order to answer more and more complex questions addressed by biologists. The information that can be brought by microscopy imaging essentially revolutionized the way that molecular and cell biologists, as well as biomedical researchers, perform their research. It has given a possibility to observe specific biomolecules in a cell or in a tissue, *in vitro* or *in vivo*, following their interaction with neighbor molecules and their environment on spatial scales down to nanometers, and most importantly, to relate this observation to their biological function.

Benefiting from the bioengineering which provided molecular and inorganic nanoprobes able to stain biological components, fluorescence microscopy has become an essential tool in most laboratories. These probes attached to proteins, biomolecular clusters or lipid assemblies offer a great flexibility in terms of chemical specificity, variable excitation and emission wavelengths and sensitivity to various physical and chemical properties of their local environment such as pH or cell membrane potential (1). Apart from these synthesized probes, fluorescent proteins encoded on a specific site of DNA can be directly expressed in cells to avoid difficulties of *in situ* chemical staining and in the same time reducing the toxicity. They give a great possibility for long term *in vivo* imaging of dynamic behavior of different cell species and their interaction with each other on a sub-cellular level (2).

While one-photon fluorescence microscopy is a standard tool for bio-imaging, the development of nonlinear contrasts brought new opportunities to the study of biological tissues. The basics of the nonlinear optical effect has been recognized in the early 60's by the group of Nicolaas Bloembergen (3, 4), Akhmanov and Khokhlov (5) who studied and formalized the responses of a medium to several electromagnetic fields applied simultaneously. Although the first nonlinear microscope generating second harmonic generation (SHG) has been developed over 35 years ago (6), only in the past $10-15$ years has it begun to emerge as a viable microscope imaging contrasts mechanism for visualization of cells and tissues' structure and function.

The generation of nonlinear effects has this advantage over the "one-photon" or linear one that it uses near infra-red excitation wavelengths which are less affected by scattering in tissues and therefore allow a deeper optical penetration, which is crucial for tissue imaging (7, 8). Moreover, the nonlinear nature of the excitation light reduces the longitudinal length of excitation leading to a spatial resolution of ≈ 300 nm x 600 nm and as a result to the reduction of out-of-plane photobleaching and phototoxic effects (9). With these advantages two-photon microscopy (2PEF) has been largely applied to the biological samples since 1990 (9). 2PEF microscopy has had a great impact in neuroscience. *In vivo* functional imaging has been dedicated to the architecture of the nervous system tissues (2, 10, 11), their physiology (12–14) and dynamics (15–17) as well as their pathological state in neurological and neurodegenerative diseases (14, 18).

Fluorescence microscopy, however, even if has been proven for its high specificity to a single molecule level, still has a few drawbacks: a fluorescent molecule need to be inserted into the system or produced by the gene expression in order to be "visible" for imaging which makes the whole process not fully effective, the photobleaching and phototoxicity are also an issue. For these reasons the nonlinear label-free imaging tools propose an interesting alternative and are more and more employed.

Versatile and high resolution- both time and frequency- spectroscopic/microscopic techniques based on four-wave-mixing processes such as coherent anti-Stokes Raman scattering (CARS), stimulated Raman Scattering (SRS), pump-probe and multiphoton microscopes (THG) were developed in the due course of time which generated wealth of new insights into the biology, chemistry, medicine and material science. The CARS process, a chemically specific contrast targeting Raman vibrational resonances of molecules, was used in microscopy for the first time in 1982 (19). The improved version in 1999 (20) has introduced the collinear configuration of excitation beam which facilitated experimental implementation and provided superior image quality with high sensitivity and spatial resolution as compared to the non-collinear beam geometry (19). The improved sensitivity and spatial resolution of this technique allowed to visualize different molecular assemblies such as lipids, proteins, DNA and water by their Raman vibrational modes in living cells and in tissues (21, 22). Meanwhile, CARS has proved to be a powerful imaging modality for studying tissues *in vivo*. Benefiting from the fact that the signal from lipid assemblies is so high that allows for visualizing a single phospholipid bilayer (23), the CARS technique found a great interest in neuroimaging. The myelin sheath (multilamellar lipid membrane surrounding neurons) which consist largely of lipids and a small addition of proteins has been successfully imaged in the context of the demyelination process associated to neurodegenerative diseases (24, 25). One of the important drawback of this process is that it contains not only response from the Raman vibrational mode but also from the electronic vibration of the medium, named four-wave mixing process (FWM). Many approaches has been developed to remove this non-resonant contribution (26, 27) and other proposed to use it as the non-linear contrast, although nonspecific (28–30). Another non-linear Raman based process, named SRS (stimulated Raman Scattering) overcomes limitations of CARS. It is not sensitive to the electronic vibration of the medium and therefore does not contain the non-resonant background. Benefiting from this intrinsic feature, SRS process as a label-free and background-free technique is an attractive alternative to probe the functionality, dynamics and morphology of biological systems (31, 32) on a submicrometric scale in a case when a resonant CARS signal, especially in "crowded" fingerprint region is hidden behind its non-resonant contribution. It has been shown for instance that SRS enables to differentiate the distribution of unsaturated from saturated lipids in living cells, based on their C=C molecular vibrations (33).

One can see, that the combination of all techniques is a powerful tool enabling in vivo imaging of whole biological systems. Information on tissue morphology, cell behavior or diseases states is often obtained by combining different contrasts for instance multiphoton fluorescence with coherent label-free microscopes: SHG (7, 34), third harmonic generation (THG) (35, 36) or CARS (37, 38) or using the four-wave mixing (FWM) together with THG microscopy (29).

While bio-imaging is able today to bring information on biomolecular assemblies, understanding how such molecules organize in complex structures can enrich the knowledge of the functionality and dynamics of biological molecular systems. The use of light polarization give a possibility of such investigation, because of the vectorial nature of light-matter interaction. In general, the highest optical signals collected from the response of the matter occur when the incident optical polarized field is oriented in parallel with the oscillation of electrons, or to vibration modes directions, in atoms and molecules. Under nonlinear optical selection of induced molecular dipoles this gives a way to monitor, by polarization tuning, the way molecules are oriented in complex assemblies. Together with polarization the nonlinear contrasts give a new perspective on studying the biological samples. Such method has been firstly developed for SHG (39–42) by studying orientations of collagen fibers in tendons, muscles and cornea (39, 40). Polarization resolved Coherent anti-Stokes Raman Scattering (PR-CARS) has been mostly applied to probe the organization of lipids by their CH stretching vibrations in model membranes (23, 43–45) and biological membranes, the myelin sheath (46, 47) but also to biopolymers, such as cellulose (48). Recently, the third order process, polarization-resolved THG has been also used to probe the orientational order of lipid barriers in tissues (49). Numerous studies on cell membrane organization have been performed by 2PEF which targeting fluorescent probes have shown a high sensitivity to the lipids' and proteins' orientational order within the membrane (50, 51). Such studies have also been done on model lipid membranes (52).

These demonstrations showed the full potential and interest in exploiting the nonlinear contrast combined with polarization in order to access structural information in molecular media, e.g. orientational organization, also named ”molecular order”. Based on these seminal works, this thesis is focused on probing the molecular organization of complex lipid assemblies, such as model membranes and myelin sheath, which are accessible by polarization resolved nonlinear contrasts, but also shows the potential of these techniques to study the molecular order and architecture or biological samples as a future diagnostics tool for the lipid related diseases.

Chapter 1 of this thesis recalls the principles of the nonlinear processes, especially CARS/FWM/SRS and 2PEF. The theoretical formalisms which allow for monitoring the molecular order by the polarization-resolved (PR) nonlinear processes are introduced.

Chapter 2 presents optical microscopes developed and used in this thesis work to perform PR multimodal measurements. We discuss how the linearly polarized light can suffer from variety of distortions introduced either by the instrumentation factors or by the sample itself and how to provide relevant and accurate data.

In this introduction we have mentioned the biological context of nonlinear microscopy imaging. In Chapter 3 we discuss in detail the importance of probing molecular lipids packing in a biological as well as in a model membranes. The model lipid system used in this study will be introduced.

Finally, in Chapter 4 the practical application of PR nonlinear microscopy is presented, especially in the model lipid membranes. The capacity of each nonlinear process (SRS, CARS, FWM and 2PEF) to probe the lipid molecular order will be discussed. We address fundamental questions about lipid packing behavior in membranes, and how the insertion of other molecules, such as cholesterol and fluorescent lipid probes can affect the organization of lipid assemblies.

In Chapter 5 we introduce the myelin sheath as the biological lipid membrane naturally occurring in the central nervous system. Its detailed structure, its pathological state and related changes in the nervous tissue will be presented in the context of neurodegenerative disorders. The imaging techniques used to probe such a complex biological system will be also discussed.

Chapter 6 is devoted to the structural and molecular investigation of lipid membranes in the myelin sheath using PR-CARS. We show the first evidence that even at the stage of disruption of the myelin envelope during the demyelination process, lipids reveal strong capability to preserve their macroscopic self-assembly into highly organized structures, even though modifications can be detected at a molecular scale.

To complete this studies, in Chapter 7 we show the potential of combined nonlinear processes, CARS and 2PEF in bioimaging of the central nervous system. The use of multimodal imaging is extended to the structural tissue degradation, e.g. axon degeneration and immune cell recruitment in the progression of neurodegenerative disease.

Chapter 1

Polarization-resolved nonlinear microscopy: probing the molecular order of lipids

In this Chapter we describe the methodology that leads to the possibility to read-out molecular orientational order thanks to polarized microscopy. We will first describe the optical contrast mechanisms which are exploited in the imaging techniques used in this work, emphasizing their differences in terms of sensitivity to light polarization. We will then define how these optical signals can allow retrieval of information on orientational distributions of molecules. A model for these distributions will be introduced that permits to measure information without *a priori* knowledge on their shape or orientation.

1.1 Polarized light-matter interaction, the source of light

In order to show how it is possible to probe molecular orientational order in a sample, first, we need to understand what is the origin of the nonlinear contrast that produces the polarization response.

1.1.1 Two Photon Excited Fluorescence (2PEF)

Probably one of the most powerful and commonly employed techniques for obtaining insight into molecular organization and interactions in biological tissues is two-photon fluorescence (2PEF). It requires however the use of fluorescent dyes or fluorescent proteins to visualize bio-molecular assemblies. Although it can be highly specific to a single protein, lipids cannot be labeled with fluorescent dyes and therefore their visualization needs to be perform indirectly by embedding fluorophores within the lipid membrane. As can be seen on the molecular energy-level diagram in Fig. 1.1a, 2PEF is the result of two successive processes, the absorption of incident photons at frequency ω and the emission of fluorescence photons of lower frequency (1). The absorption of incident photons by the molecule results in its transition to higher electronic excited levels ($|S_1\rangle$ in Fig. 1.1a or even higher levels). The efficiency of this process is driven by the absorption transition dipole μ_{abs} on the molecule. Within the following 10^{-12} s, the molecule relaxes to the lowest vibrational level of $|S_1\rangle$, due to internal conversion with release of energy to the molecular environment. After a certain time ($|S_1\rangle$ level lifetime), the molecule has a given probability to return to its ground state $|S_0\rangle$, emitting a fluorescence photon driven by the emission transition dipole μ_{em}. Such a time delay has important consequences. First,

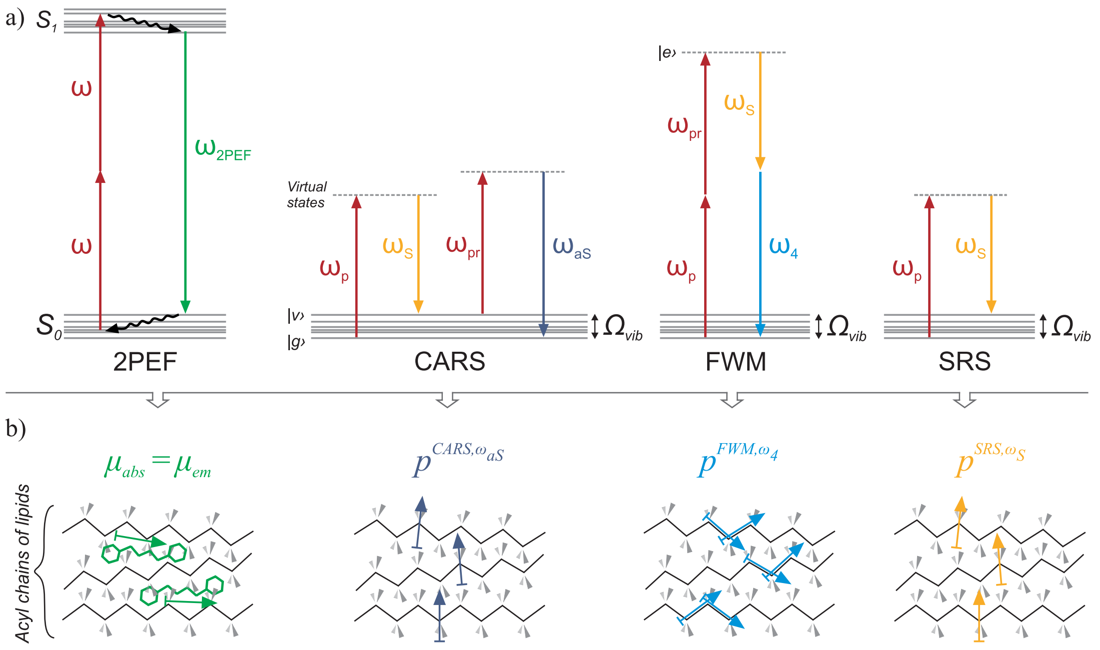

Figure 1.1: (***a***) Energy diagram schemes of the different contrasts used in these studies. (***b***) The radiation from a molecule either originates from the emission transition dipoles μ_{em} (2PEF) or the third order nonlinear dipoles $p^{SRS,CARS,FWM}$ (SRS, CARS, FWM) induced by the excitation fields involved in the contrast used. The colored arrows exhibit the directions of the induced dipoles involved in the nonlinear processes, which define the probed molecular organization directions.

this process is incoherent (different molecules emit fluorescence radiation with no phase correlation between them) and second, the fluorescence efficiency is proportional to the product of two un-correlated probabilities: the absorption between the ground state and the excited state and the emission from the fluorescent state to the ground state. At last, the efficiency of the fluorescence emission can be lowered by the existence of non-radiative relaxation processes. The energy of the relaxation to the ground state is in this case dissipated without the emission of a photon. This is the reason why the fluorescence quantum yield is generally below 1 (the quantum yield is defined by the ratio between the radiative decay rate and total decay rate present in the system). This limitation is additionally raised by the fact that concentration of fluorescent molecules cannot be very high in order to not perturb the biological system.

The fluorescence intensity overall depends on the excitation polarization because it is governed by a coupling mechanism between fields and transition dipoles. For a single molecule excited by a field $\vec{E}$, the fluorescence intensity measured along a polarization direction $\vec{i}$ is (52, 53):

$$I_{molec,i}^{2PEF} \propto |\vec{\mu_{abs}} \cdot \vec{E}|^4 \, |\vec{\mu_{em}} \cdot \vec{i}|^2$$

where the absorption probability $|\vec{\mu_{abs}} \cdot \vec{E}|^4$ depends on the fourth power of the field due to its two-photon nonlinear nature (53). The $\propto$ signs contains universal constants and radiation emission/collection factors. The fluorescence by a collection of molecules which form an angular distribution $f(\Omega)$, when averaged over time in a stationary measurement, is the incoherent sum of the intensity over all molecules:

$$I_i^{2PEF} \propto \int |\vec{\mu_{abs}}(\Omega) \cdot \vec{E}|^4 \, |\vec{\mu_{em}}(\Omega) \cdot \vec{i}|^2 f(\Omega) d\Omega$$

where $f(\Omega)$ is the probability of a molecule to lie at an orientation $\Omega = (\theta, \varphi)$ in the macroscopic frame. In this expression we supposed that the molecules do not rotate in time between the absorption and emission events, and that both absorption and emission transition dipoles lie along the same directions. Refinement of these assumptions can be accounted for in this equation if needed.

Alternatively, when an un-polarized detection is used, the two-photon fluorescence process simplifies into the read-out of a two-photon absorption process, which can be described as a third order tensorial process (53):

$$I^{2PEF} \propto \int T^{2PEF}(\Omega) \bullet \vec{E}\vec{E}\vec{E}^{*}\vec{E}^{*} f(\Omega) d\Omega$$

where $T^{2PEF} = \vec{\mu_{abs}}\vec{\mu_{abs}}\vec{\mu_{abs}}^{*}\vec{\mu_{abs}}^{*}$ is the third order tensor describing two-photon absorption, and $\bullet$ denotes the scalar tensorial product.

Finally it is visible that in the two-photon fluorescence process, tuning the optical field direction of $\vec{E}$ can provide information on the distribution $f(\Omega)$. The detail of this procedure will be described below.

1.1.2 Coherent Anti Stokes Raman Scattering (CARS) and Four Wave Mixing (FWM)

Coherent Anti Stokes Raman Scattering (CARS) microscopy exhibits the strong advantage of being a label-free technique, sensitive to molecular vibrations (20, 21) and to the way they are oriented if light polarization is controlled (21, 54). In this third order nonlinear process (Fig. 1.1 a) three frequencies called pump ω_p, Stokes ω_S and probe ω_{pr} (where usually $\omega_p = \omega_{pr}$), interact coherently with molecules. The interaction of these three fields induces a third order polarization $\vec{P}^{CARS}$ in the medium, which gives rise to the radiation of the fourth field at the anti-Stokes frequency $\omega_{aS} = 2\omega_p - \omega_S$. The strength of this nonlinear polarization depends on the intrinsic property of the medium defined as the nonlinear susceptibility $\chi^{(3)}$. When the frequency difference between ω_p and ω_S coincide with the frequency of a molecular bond vibration Ω_{vib}, such that $\Omega_{vib} = \omega_p - \omega_S$, the system is under resonance conditions for this vibration(55). As a result the amplitude of the scattered light is largely enhanced and the coherent signal emitted at the frequency ω_{aS}. In contrast with fluorescence, the direction of the emission is driven by phase-matching conditions, since this process is coherent (56).

The resonant CARS signal, however, is superposed with another signal that is intrinsically generated in the sample, which makes the resonance read-out more delicate. A non-resonant contribution to the overall signal indeed needs to be considered, issued from a four-wave mixing (FWM) process generated by the third order nonlinear response from electronic oscillations in the medium (Fig. 1.1a), at the frequency $2\omega_p - \omega_S$, independently of the existence of a vibrational resonance. FWM is defined by the third order nonlinear susceptibility $\chi^{(3)}_{NR}$ (54, 57, 58). Therefore, under vibrational resonant conditions, the CARS process results in the superposition of two fields, a non-resonant (FWM) field due to pure electronic response, and a resonant field (CARS) due to the presence of vibrational Raman modes. The CARS intensity signal is then written accounting of these two processes, with a total susceptibility $\chi^{(3)} = \chi^{(3)}_R + \chi^{(3)}_{NR}$. The induced CARS polarization $\vec{P}^{CARS}$ is thus written:

$$\begin{aligned}\vec{P}^{CARS} &\propto (\chi_R^{(3)} + \chi_{NR}^{(3)}) : \vec{E}_S^* \vec{E}_p \vec{E}_p \\ I^{CARS} &\propto \left|\vec{P}^{CARS}\right|^2\end{aligned} \tag{1.1}$$

where the $\propto$ signs contains universal constants and radiation emission/collection factors. This expression is written in a planar wave approximation, valid for low apertures (59).

If the system is not under vibrational resonance, the induced polarization is a pure FWM response $\vec{P}^{FWM}$ with :

$$\begin{aligned}\vec{P}^{FWM} &\propto \chi_{NR}^{(3)} : \vec{E}_S^* \vec{E}_p \vec{E}_p \\ I^{FWM} &\propto \left|P^{F\vec{W}M}\right|^2\end{aligned} \tag{1.2}$$

In both cases, since the optical process is coherent, the macroscopic response comes from the coherent addition of nonlinear responses from individual molecules, with nonlinear third order susceptibilities γ_{NR} and γ_R:

$$\chi_{R,NR}^{(3)} = \int \gamma_{R,NR}(\Omega) f(\Omega) d\Omega \tag{1.3}$$

here $\gamma_{R,NR}^{(3)}(\Omega)$ depends on the molecular orientation Ω since it is expressed as a molecular response projected in the laboratory frame (53).

The high sensitivity of CARS/FWM to molecular organization can be seen in these equations. If molecules / molecular bonds are highly organized, it will lead to a specific $\chi_{R,NR}^{(3)}$ third order tensor shape that will reflect in the polarization response of the optical process. CARS and FWM are more specifically dependent on the symmetry of the considered bond/molecules at the microscopic scale ($\gamma_{R,NR}$ tensors), as well as on their macroscopic orientational organization ($f(\Omega)$). For instance the organization of a lipid assembly arises from the nature of the molecules themselves, as well as from interactions between them. At the microscopic scale, the lipidic acyl chain direction consists in CC repetitive units along which the electronic response is dominant (49), which will reflect in the most favorable optical coupling direction for the FWM response. Addressing now the CH_2 symmetric stretching vibration, the resonant CARS response is expected to be mostly directional along the highly organized repetitive units of CH_2, and thus perpendicularly to the CC bonds (Fig. 1.2 and Fig. 1.1b) (45, 60). Overall the CARS process is expected to also contain the polarization response described for FWM, to a level that depends on the strength of the resonant contribution.

1.1.3 Stimulated Raman Scattering (SRS)

Stimulated Raman Scattering (SRS) (Fig. 1.1a) comes from the fact that coherent simultaneous interaction of the pump ω_p and Stokes ω_S frequencies leads to the transfer of energy from the pump to the Stokes beams, in case they match with a molecular vibration in the sample ($\omega_p - \omega_S = \Omega_{vib}$) (33, 61). This effect is the result of the generation of a nonlinear polarization oscillating at the Stokes frequency ω_S, involving the resonant third order tensor $\chi_R^{(3)}$. The SRS signal can be then detected in two ways: amplification of the Stokes beam, called stimulated Raman gain (SRG), or attenuation of the pump beam called stimulated Raman loss (SRL). SRS exhibits a major advantage over CARS: it is free of the non-resonant FWM background, because the nonlinear response occurs only if $\omega_p - \omega_S$ matches a vibrational resonance. Therefore in this case the intensity will be only dependent on the strength of the resonant $\chi_R^{(3)}$ susceptibility (33, 61):

$$I^{SRS} = \chi_R^{(3)}(\Omega) \bullet \vec{E}_p^* \vec{E}_S \vec{E}_p \vec{E}_S^* \tag{1.4}$$

Similarly as in CARS/FWM, the consequence of the vectorial nature of the light-matter interaction in the SRS process gives access to a way to probe the orientational organization of molecular bonds in a medium (Fig. 1.1b) by monitoring the polarization of the incident light.

1.2 Description of the measured molecular angular distribution

In this section we describe how to describe the orientation distribution function $f(\Omega)$ that appears in the different optical contrasts described above. $f(\Omega)$ represents the orientation distribution taken by all molecules present in the volume of the focal spot of the objective, integrated over a time which is generally much longer than molecular rotational fluctuation times. It therefore represents a stationary picture of orientations, that reflects the degree of organization at a given position in the sample. Various theoretical models and analysis based on polarization-resolved (PR) measurements has been developed in order to probe molecular order. Molecular order can vary between complete disorder (isotropic medium) to complete order (such an in crystalline medium). The intermediate situations require models of such a distribution function $f(\Omega)$. In most cases to describe molecular order, a specific

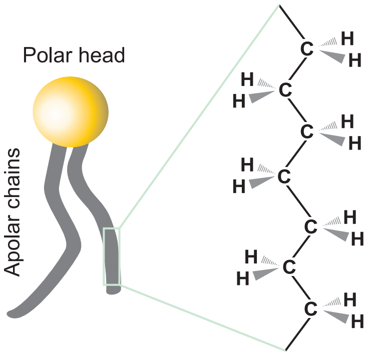

Figure 1.2: Schematic representation of a lipid and its lipidic acyl chain, showing repetitive units of CH_2.

shape of the distribution function $f(\Omega)$ is assumed as the physical picture of probability distribution of molecules to be present at a given angular orientation Ω. In lipid membranes for instance, functions resembling a Gaussian distribution (49) or a cone (51, 62, 63) have been frequently chosen. Lipid molecules have indeed a special structure (Fig. 1.2) which allows them to self-assemble in organized and stable structures (see Chapter 3). The illustration of lipids in membranes in Fig. 1.3 shows different possible reasons for local organization: disorder can in particular occur due to lipid conformational changes, lipid-lipid interactions, or mesoscopic changes of the membrane morphology at scales much below the diffraction limit. In all cases, the obtained organization within a focal volume can be intuitively pictured by a Gaussian distribution function with an increasing disorder σ (Gaussian width).

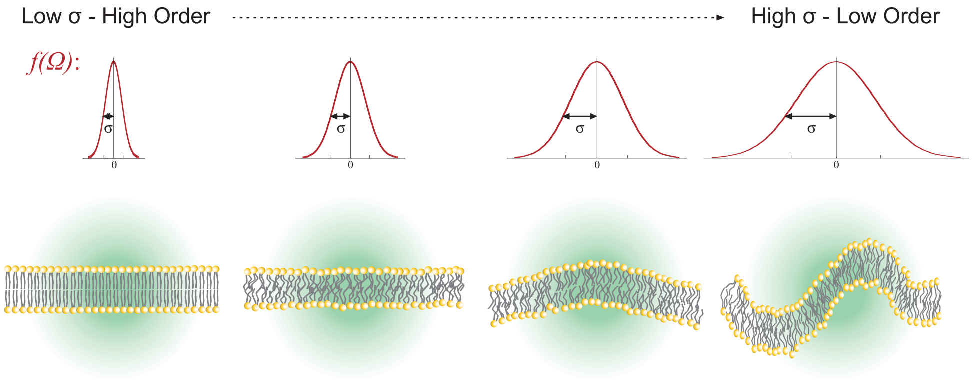

Figure 1.3: The organization of lipid membrane in the focal volume. Small angular aperture σ of the distribution function (Gaussian function) corresponds to highly organized lipids within a membrane. The increase of the aperture σ indicates the either highly disorganized lipids within a membrane, or the folding of the membrane, or both situations.

If such *a priori* model for the molecular distribution is implemented, the main exploited information is the width of this already predefined function that quantifies the level of orientational angular constraint of probed molecules. The biggest inconvenient of this approach is that it requires the knowledge of the complete molecular scale response, and thus the knowledge of the tensorial structure of $\gamma_{R,NR}$ for CARS, FWM and SRS processes, which is needed to compute $\chi^{(3)}_{R,NR}$. This is possible in case of simple model lipid assemblies (49), but not for complex mixtures of unknown lipids for instance. The other inconvenient is that the supposed model might be far from reality.

Here, we introduce a different way to describe molecular organization. In our method, angular distributions are defined without *a priori* knowledge of their shape and without a pre-required knowledge on the molecular microscopic response. We will decompose molecular responses into individual directions (made of molecular bonds or electronic induced nonlinear dipoles), that form a macroscopic "effective" distribution, which is decomposed onto symmetry orders, similarly as in the Fourier decomposition of any angular function (53). These symmetry orders are the read-out parameters in polarized microscopy, and can be finally related to a distribution *a posteriori*, which is particularly useful for interpretations.

1.3 From an assembly of nonlinear dipoles to the symmetry orders of the effective distribution function

Probing the molecular orientation of lipids by polarization excitation implies the coupling between nonlinear-induced/excitation dipoles which fluctuate in time and space and a tunable incident polarization. The result of the PR measurement is thus a steady-like averaged observation, since the individual orientations and positions of molecules cannot be resolved. In this part, we introduce the methodology that allows to go from individual induced/excitation dipoles to a macroscopic distribution function $f(\Omega)$.

1.3.1 Macroscopic nonlinear induced dipoles

CARS/FWM/SRS processes. As has been described in the previous section, the coupling between the excitation field and the medium results in the induction of nonlinear dipoles related directly to electronic nonlinear induced dipoles or indirectly to molecular bonds' directions (CH_2 stretching bonds in the case of CARS in lipids) (Fig. 1.4a). Each of the nonlinear induced dipoles have their own amplitude and orientation (θ', φ') in the molecular frame. Their individual unit vector direction will be denoted $\mathbf{e}$. Their coherent sum creates the full molecular response, characterized by the third order nonlinear susceptibility $\gamma_{R,NR}$ tensor (Fig. 1.4a,b) (64). The assembly of vectors $\mathbf{e}$ is therefore compatible with the symmetry of the molecular structures involved in the CARS, SRS and

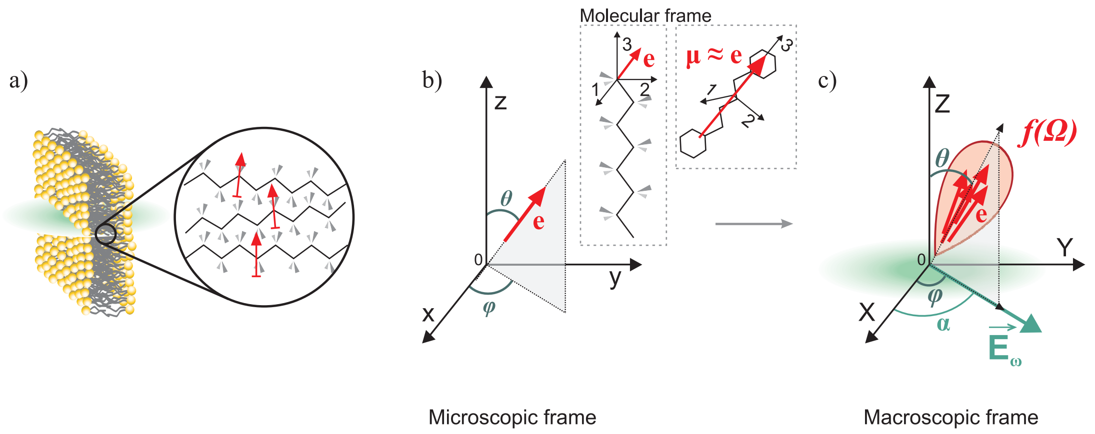

Figure 1.4: (***a***) Assemblies of lipids in the focal volume, pointing an individual CH bond direction. (***b***) Nonlinear induced dipoles: individual bond/electronic dipoles directions (SRS, CARS and FWM) or μ_{abs} (2PEF), represented as **e** and its orientation angles $\Omega' = (\theta', \varphi')$ in the molecular frame $(1, 2, 3)$. The molecular orientation in the macroscopic frame is defined by $\Omega" = (\theta", \varphi", \psi")$ (not depicted). (***c***) Collection of dipoles **e** with orientation $\Omega = (\theta, \varphi)$ present in the $f(\Omega)$ function in the macroscopic (X, Y, Z) frame.

FWM processes. In the macroscopic (laboratory) frame (denoted X, Y, Z) the probability to find individual bond dipoles **e** induced by a given nonlinear process is described by a function $f(\Omega)$ with an orientation $\Omega = (\theta, \varphi)$ (Fig. 1.4c). Note that Ω in this case does not define anymore the molecular orientation, but rather the dipoles' orientation (65). The collection of these bond dipoles **e** in the laboratory frame produces a nonlinear third order susceptibility:

$$\chi^{(3)}_{IJKL} = N\gamma \int_{\Omega} (\mathbf{I} \cdot \mathbf{e})(\mathbf{J} \cdot \mathbf{e})(\mathbf{K} \cdot \mathbf{e})(\mathbf{L} \cdot \mathbf{e}) f(\Omega) d\Omega \tag{1.5}$$

where $(I, J, K, L) \in (X, Y, Z)$ are macroscopic frame axes, N is the molecular dipoles density, γ represents the norm of the molecular susceptibility tensor and $(\mathbf{I} \cdot \mathbf{e})$ is the scalar projection of dipoles's directions over macroscopic directions (similar to the expression of the transformation matrix between the molecular and macroscopic frames).

Note that the Ω directions can be related to the dipoles' orientations in the molecular frame by a transformation relating the molecule's orientation in the macroscopic frame:

$$\int_{\Omega} f(\Omega) d\Omega = \int_{\Omega''} \int_{\Omega'} g(\Omega') h(\Omega'') d\Omega' d\Omega'' \tag{1.6}$$

where $h(\Omega'')$ is the angular distribution function of molecules in the macroscopic frame, and $g(\Omega')$ the angular distribution of dipoles in the molecular frame (see Fig. 1.4) (65).

2PEF process. In the 2PEF process, the μ_{abs} dipoles are pointing along the orientation Ω in the macroscopic frame (Fig. 1.4b). An absorption dipole can be related to the molecular structure of a molecule, therefore Ω is tightly related to the molecule orientation. In this work we probe the absorption probability and not the emission one, since no specific analysis direction is set in the experiment (53, 66). To follow the same methodology as described for CARS/FWM/SRS, the direction of the transition dipole μ_{abs} is defined as lying along the generic unit vector direction **e**. The macroscopic tensorial form of the susceptibilities involved in the 2PEF process is then defined as:

$$T^{2PEF}_{IJKL}(\Omega) = N\gamma \int_{\Omega} (\mathbf{I}\cdot\mathbf{e})(\mathbf{J}\cdot\mathbf{e})(\mathbf{K}\cdot\mathbf{e})(\mathbf{L}\cdot\mathbf{e}) f(\Omega) d\Omega \tag{1.7}$$

with γ the norm of the molecular third order tensor involved in the two-photon absorption process, $(I, J, K) \in (X, Y, Z)$ the macroscopic frame axes, and N the molecular density.

In the case of 2PEF, the measured distribution function $f(\Omega)$ will thus be directly related to the direction of the molecular structure in the macroscopic frame.

1.3.2 Description of the distribution function $f(\Omega)$ of an assembly of dipoles

In the most general case, the distribution function $f(\Omega)$ is unknown. A typical distribution function is schematically shown in the Fig. 1.5a, for what would be expected from CH bonds orientations in a lipid membrane (see Fig. 1.4a). Any given function can however be decomposed on a basis that is invariant upon rotation: the spherical harmonics $Y^l_m(\Omega)$ functions (67). $f(\Omega)$ can be then expressed by :

$$f(\Omega) = \sum_{m,l} f_{m,l} Y^l_m(\Omega) \tag{1.8}$$

where the $f_{m,l}$ coefficients are the weights of the unknown function on the $Y^l_m(\Omega)$ basis functions, that finally determine the shape of the distribution function $f(\Omega)$. The l coefficients are called "orders of symmetry" of the spherical function with $-l \leqslant m \leqslant l$. The real spherical function is defined as:

$$\begin{aligned} Y^l_m(\theta,\varphi) &= N_{(m,l)} P^l_m(\cos\theta)\cos(m\varphi) \text{ for } m > 0 \\ &= N_{(|m|,l)} P^l_{|m|}(\cos\theta)\sin(|m|\varphi) \text{ for } m < 0 \\ &= Y^l_0(\theta,\varphi) \text{ for } m = 0 \end{aligned} \tag{1.9}$$

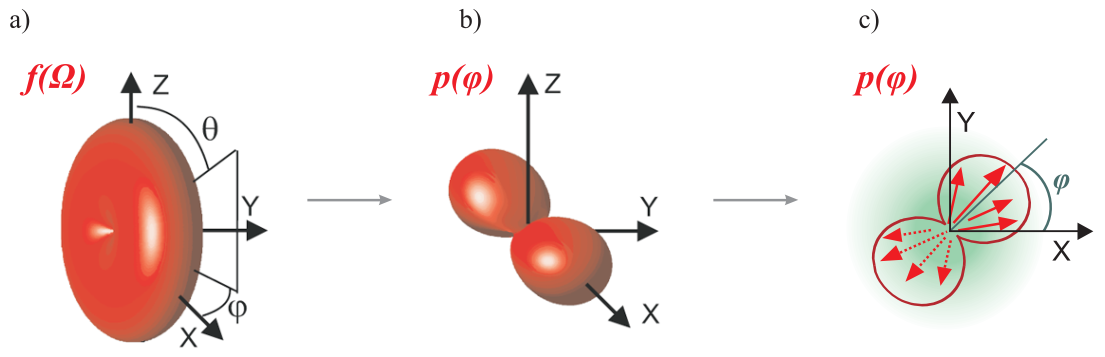

Figure 1.5: (***a***) 3D nonlinear dipoles distribution defined into the focal volume $f(\theta, \varphi)$. This specific example is related to CH bonds in a lipid membrane, see Fig. 1.4a. (***b***) 3D nonlinear dipoles distribution which contributes to the signal. (***c***) 2D distribution function $p(\varphi)$.

with $P_m^l(\cos\theta)$ the associated Legendre polynomials and $N_{(m,l)} = \sqrt{\frac{(2l+1)(l-m)!}{\pi(l+m)!}}$.

This expression is therefore only dependent on the symmetry orders $f_{m,l}$, which define the way individual nonlinear dipoles are angularly distributed. Using such coefficients, the unknown parameters are therefore not anymore the aperture and the orientation of an *a priori* defined $f(\theta, \phi)$ shape, but its symmetry decomposition. This un-supervised analysis is particularly interesting when measuring structural behaviors in complex membrane systems, such as unknown lipid / protein compositions and unknown membrane nanoscale morphologies.

1.3.3 From the 3D $f(\Omega)$ function to the distribution function $p(\varphi)$ in the sample plane

We consider the case where the excitation fields $\vec{E}$ involved in the nonlinear coupling lie in the transverse (X, Y) sample plane; we can then reduce the previous expression where only in-plane coupling angles between dipoles and fields occur. Note that we implicitly assume here that there is no Z component ($E_Z = 0$) in the tensorial coupling with the fields, even though it is known that focused fields contain such contribution. However, the E_Z component does not surpass 40% in amplitude comparing to in-plane components in the case of strong focusing conditions (68), which is far from the cases studied in this work (here, NA $<$ 1.2). We will thus neglect this contribution, which contributes only under numerical apertures above 1.2 and strongly tilted molecular angular distributions (69, 70).

It means in particular that the nonlinear radiation equations, written above in the context of planar wave, are still considered as valid.

Let us consider the nonlinear tensorial expressions of the susceptibilities probed by the SRS ($\chi_R^{(3)}$), CARS ($\chi_{R,NR}^{(3)}$), FWM ($\chi_{NR}^{(3)}$) or 2PEF ($T^{(2PEF)}$). Considering only in-plane tensor-fields coupling, each remaining in-plane tensorial components from the previous expressions (Eqs. 1.7 and 1.5) can be written more specifically as for instance (here we use χ as a generic notation for all third order tensors invoked in the studied optical processes):

$$\chi_{XXXX} = N\gamma \int_\theta \int_\varphi \sin^5\theta \cos^4\varphi f(\theta,\varphi) d\varphi d\theta \tag{1.10}$$

and similarly for the other components (67, 71). Defining an in-plane effective distribution function $p(\varphi)$ as:

$$p(\varphi) = \int_\theta \sin^5\theta f(\theta,\varphi) d\theta \tag{1.11}$$

permits to only account for in-plane orientation dependencies, the out-of plane orientation θ being averaged-out. Therefore the Ω 3D orientation of these dipoles can be reduced to the in-plane orientation φ. Using the spherical expression of the function $f(\theta,\varphi)$ (Eq. 1.8) it is possible to integrate this expression over the θ parameter and separate it from φ, which introduces a further simplification of the tensorial expression:

$$\begin{aligned}
p \quad (\varphi) &= \sum_{m,l} \int_\theta \sin^5\theta f_{m,l} Y_m^l(\theta,\varphi) d\theta \\
&= \left[\sum_l \int_\theta \sin^5\theta f_{0,l} Y_0^l(\theta) d\theta\right] \\
&+ \sum_{m>0} \cos(m\varphi) \left[\sum_l \int_\theta \sin^5\theta f_{m,l} N_{(m,l)} P_m^l(\cos\theta) d\theta\right] \\
&+ \sum_{m<0} \sin(|m|\varphi) \left[\sum_l \int_\theta \sin^5\theta f_{|m|,l} N_{(|m|,l)} P_{|m|}^l(\cos\theta) d\theta\right] \\
&= p_0 + \sum_n p_n \cos(n\varphi) + q_n \sin(n\varphi)
\end{aligned} \tag{1.12}$$

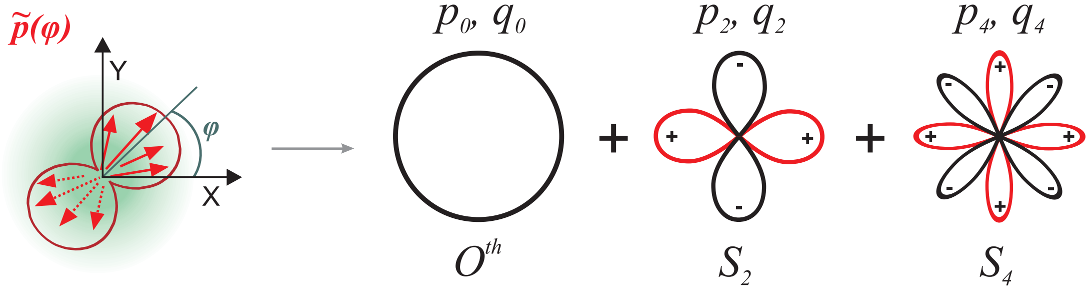

Figure 1.6: Spherical decomposition of the $\tilde{p}$ distribution function. The (+, -) signs indicate the positive and the negative part of the function, respectively.

with n a positive integer. The macroscopic tensor components become therefore:

$$\begin{aligned}
\chi_{XXXX} &= N\gamma \int_0^{2\pi} \cos^4 \varphi p(\varphi) d\varphi \\
\chi_{XXXY} &= N\gamma \int_0^{2\pi} \cos^3 \varphi \sin \phi p(\varphi) d\varphi \\
\chi_{XYXY} &= N\gamma \int_0^{2\pi} \cos^2 \varphi \sin^2 \varphi p(\varphi) d\varphi \\
\chi_{XYYY} &= N\gamma \int_0^{2\pi} \sin^3 \varphi \cos \varphi p(\varphi) d\varphi \\
\chi_{YYYY} &= N\gamma \int_0^{2\pi} \sin^4 \varphi p(\varphi) d\varphi \qquad (1.13)
\end{aligned}$$

The nonlinear response finally depends only on a function $p(\varphi)$ characterizing the orientation of the nonlinear dipoles. The order parameters (p_n, q_n) can be interpreted in a similar way as the order parameters $\langle P_n(\cos(\theta))\rangle$ derived from Legendre polynomials, used in structural analyzes (72, 73). The $p(\varphi)$ effective distribution permits thus to characterize molecular order in the medium by its order parameters (p_n, q_n), which correspond to orders of symmetry of the distribution. As shown in Figs. 1.5a and b, the distribution $f(\Omega)$ will be reduced to the final distribution $p(\varphi)$. $p(\varphi)$ is not a 2D section nor a geometric 2D projection of the nonlinear dipoles distributed in 3D $f(\Omega)$ function, it is rather an effective 2D function that embeds 3D information within an average, weighted over $\sin^5 \theta$.

1.3.4 The reduced effective distribution function $\tilde{p}(\varphi)$

One can notice that the macroscopic tensors involved in SRS, CARS, FWM but also 2PEF, only involve a φ dependence of even orders, up to the fourth order n=4 (eq 1.13) (53, 66). Therefore only even orders $n = 0, 2, 4$ of $p(\varphi)$ will be involved in the light-matter coupling (Fig. 1.6). The retrieved distribution can be thus limited to a reduced effective distribution function $\widetilde{p}(\varphi)$:

$$\widetilde{p}(\varphi) = p_0 + p_2\cos(2\varphi) + q_2\sin(2\varphi) + p_4\cos(4\varphi) + q_4\sin(4\varphi) \tag{1.14}$$

Using Eqs. 1.13 and 1.14, the macroscopic nonlinear susceptibility components in the X, Y plane can be written based on the symmetry orders of this reduced function:

$$\begin{aligned}
\chi_{XXXX} &= N\gamma\frac{\pi(6p_0 + 4p_2 + p_4)}{8} \\
\chi_{XXXY} &= N\gamma\frac{\pi(2q_2 + q_4)}{8} \\
\chi_{XYXY} &= N\gamma\frac{\pi(2p_0 - p_4)}{8} \\
\chi_{XYYY} &= N\gamma\frac{\pi(2q_2 - q_4)}{8} \\
\chi_{YYYY} &= N\gamma\frac{\pi(6p_0 - 4p_2 + p_4)}{8}
\end{aligned} \tag{1.15}$$

PR nonlinear signals, which depend on these coefficients, should therefore allow the access to the order parameters (p_n, q_n) of second and fourth symmetry, and therefore to structural information in the investigated sample. We will show how to retrieve these parameters from PR measurements (section 1.5) but first, we will demonstrate what kind of information they represent.

1.4 Interpretation of order parameters of lipids and fluorophores assemblies

The measured order parameters (p_n, q_n) allow to quantify structural information in a general way based on the nonlinear dipoles' disorder contributing to the nonlinear coupling in the focal volume.

1.4.1 The symmetry orders S_2 and S_4

Although the read-out of the $\tilde{p}(\varphi)$ function by the optical processes studied here gives only access to its second and fourth order parameters, rich information on the orientational organization of measured dipoles can be obtained. To illustrate this gain of information, first, we introduce four parameters in order to quantify the symmetry order magnitude and the main orientation of the distribution function. The global amplitudes of second and fourth order symmetry contributions will be quantified by "orders" S_2 and S_4, which

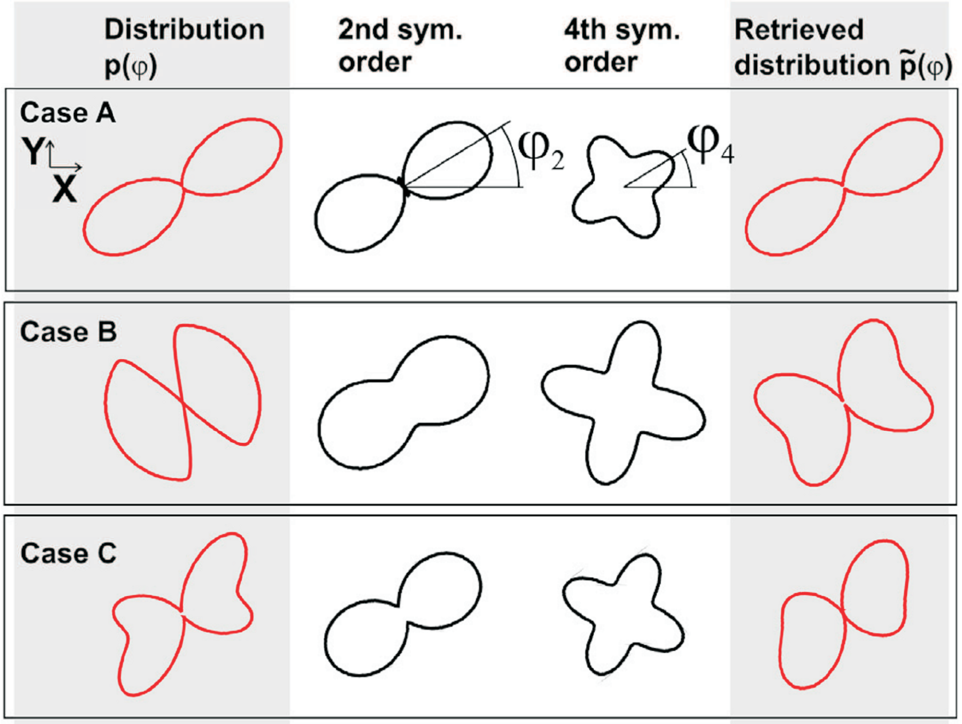

Figure 1.7: Examples of $p(\varphi)$ distributions visualized by their 2nd and 4th symmetry order parameters together with filtered-out angular distribution $\widetilde{p}(\varphi)$ (Adapted from (74)).

do not depend on the orientation of the observed angular distribution but rather on their shape:

$$\begin{aligned} S_2 &= \tfrac{1}{p_0}\sqrt{(p_2^2+q_2^2)} \\ S_4 &= \tfrac{1}{p_0}\sqrt{p_4^2+q_4^2}. \end{aligned} \tag{1.16}$$

where the $(p_2, q_2,\ p_4, q_4)$ coefficients are normalized to p_0 which we set equal to $p_0 = 1$. Moreover, we introduce the angles φ_2 and φ_4 to describe respectively the orientation of the symmetry contributions of the distribution function in the sample plane:

$$\varphi_2 = \begin{cases} \frac{1}{2}\operatorname{arc\,tg}(q_2/p_2), & \text{if } p_2 > 0 \\ \frac{1}{2}\operatorname{arc\,tg}(q_2/p_2) + \frac{\pi}{2}, & \text{else} \end{cases} \tag{1.17}$$

$$\varphi_4 = \begin{cases} \frac{1}{4}\operatorname{arc\,tg}(q_4/p_4), & \text{if } p_4 > 0 \\ \frac{1}{4}\operatorname{arc\,tg}(q_4/p_4) + \frac{\pi}{4}, & \text{else} \end{cases}. \tag{1.18}$$

These four independent parameters play distinct roles in the description of the distribution function as shown in Fig. 1.7. The angle φ_2 reports the main orientation of the distribution and S_2 reports the degree of anisotropy of the distribution regardless its orientation (see Fig. 1.7). S_4 is attributed to higher angular frequencies and thus to more complex details in the shape of the distribution. A smooth Gaussian-like distribution (see Fig. 1.7 case A) will contain less fourth order symmetry than a distribution with sharper edges (see Fig. 1.7 case B) or than a distribution made of lobes (see Fig. 1.7 case C). The order 4 orientation φ_4 plays also a role in the shape distribution: if φ_4 is along φ_2, the distribution is of cylindrical symmetry (see Fig. 1.7 cases A,B). If not, the distribution becomes asymetric (see Fig. 1.7 case C). It is thus convenient to separate this degree of symmetry into two new coefficients for S_4, one symmetric ($S_4^{(s)}$) and one antisymmetric ($S_4^{(a)}$) (74):

$$S_4^{(s)} = S_4\cos(4(\varphi_4 - \varphi_2)) \tag{1.19}$$

$$S_4^{(a)} = S_4\sin(4(\varphi_4 - \varphi_2)). \tag{1.20}$$

$S_4^{(a)}$ is nonvanishing only for asymmetric distributions. In the case of symmetric distributions, $(\varphi_4 - \varphi_2)$ is either 0 or 45°, leading to $S_4^{(a)} = 0$.

Finally, the parameters S_2 and S_4 holds therefore not only information on the disorder of the angular distribution (its angular aperture), but also on its shape, making more obvious the apparition of sharper features and of asymmetry.

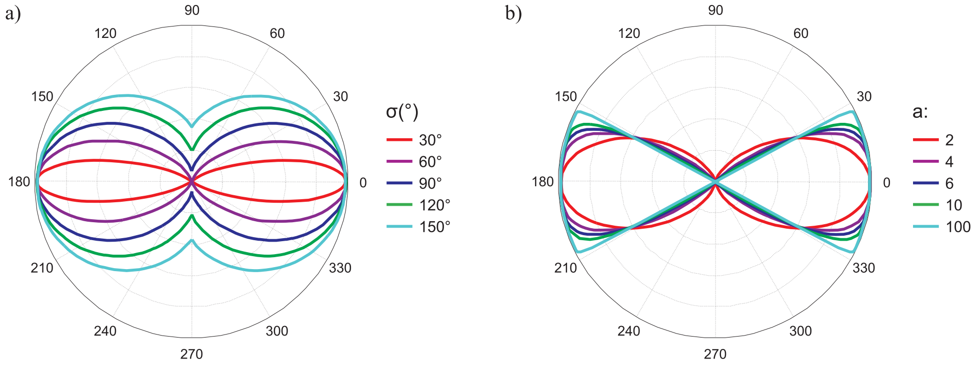

Figure 1.8: (***a***) Gaussian distribution function (polar representation) for different widths σ. (***b***) Super-Gaussian function with increasing steepness a.

1.4.2 From symmetry orders to real distribution functions

Every distribution function read-out by a PR-nonlinear process used in this study will be represented by its symmetry spectrum (S_2, S_4), which is a reduced view of the complete picture, as mentioned above. The next step is to interpret these coefficients in the frame of a physical picture of what could be the real distribution function related to these orders. In this section we illustrate the symmetry decomposition of a few model distribution functions, inspired from possible lipid organization as illustrated in Fig. 1.2. The CARS susceptibility of the lipids in resonance with their symmetric CH_2-stretching vibration mode is for instance governed by the orientation of these modes perpendicularly to the lipid alkyl chain (Fig. 1.1b and Fig. 1.4a). The resulting distribution $p(\varphi)$ could in this case resemble a Gaussian function, as introduced earlier (45). In order to provide a larger symmetry spectrum for this distribution, we introduce a super-Gaussian function centered on φ_0 and of width σ and the steepness a of the angular constraint:

$$p(\varphi) \propto e^{-(|\varphi-\varphi_0|/2\sigma)^a} \tag{1.21}$$

Fig. 1.8 illustrates such functions. Their width decreases with σ (Fig. 1.8a) and their shape gets sharper with a, from a Gaussian (a=2) to a sharp cone (a=100 and above). The parameter a of this distribution function thus represents higher angular constraints imposed to the molecules defining the shape of the distribution.

Once such function is defined, we can deduced its S_2 and S_4 symmetry orders, follow-

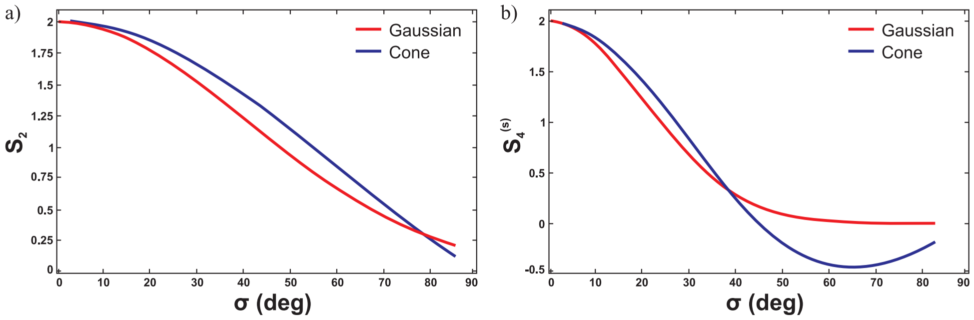

Figure 1.9: Symmetry orders of Gaussian (a =2) (***a***) and Cone (a =100) (***b***) distribution functions as a function of their width σ.

ing:

$$\begin{aligned} p_0 &= \int p(\varphi)d\varphi \\ q_0 &= 0 \\ p_{n>0} &= 2\int p(\varphi)\,\cos(n\varphi)d\varphi \\ q_{n>0} &= 2\int p(\varphi)\,\sin(n\varphi)d\varphi \end{aligned} \tag{1.22}$$

The values of S_2 and S_4 symmetry orders can directly be deduced from these expressions. They are represented in Fig. 1.9 as a function of σ for the distributions considered here.

Visibly, Gaussian and cone functions can be well differentiated by their (S_2,S_4) coefficients at $2\sigma > 90°$. For smaller apertures, the difference between Gaussian and cone shapes is less obvious and would require higher symmetry orders to be read-out. In the examples studied in this work the distributions are nevertheless found to be often sufficiently large to be able to interpret such shape variations. Note that such a study cannot be performed if supposing *a priori* known distribution functions: here the symmetry orders are specifically used to discriminate between different possible distribution functions.

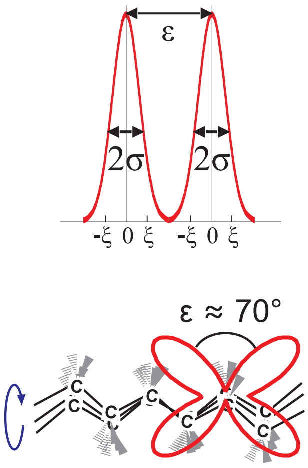

Figure 1.10: The scheme of a bi-Gaussian function picturing the lipid acyl chain.

Another interesting example is the existence of lobes in the distribution function. In FWM for instance in highly ordered lipids, the signal originates from a third order tensor dominated by a *trans* alkyl chain symmetry (49), which could be pictured

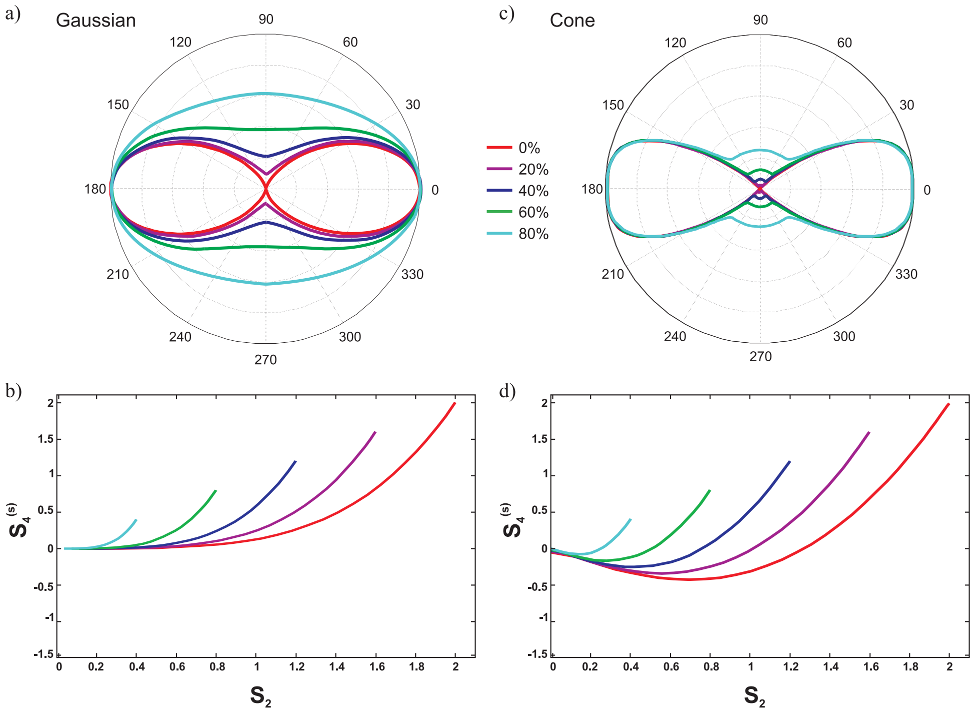

Figure 1.11: Representation of variations of a Gaussian function in ***a*** and a cone function in ***b***, respectively, with an increasing isotropic contribution ($0\%, 20\%, 40\%, 60\%, 80\%$ of the total population) to these functions. Theoretical distribution functions (above) and their (S_2, S_4) symmetry spectrum (below).

by two main directions of the CC bonds with an inter-angle of about 70° (Fig. 1.1b) (see Chapter 4). Assuming that the angular disorder experienced by the lipids is modeled by a Gaussian function (45, 49) centered on φ_0 and of width σ, this disorder will cause the associated nonlinear bond dipoles to lie within a bi-Gaussian function:

$$p(\varphi) \propto e^{-(\varphi-\varphi_0-\varepsilon/2)^2/2\sigma^2} + e^{-(\varphi-\varphi_0+\varepsilon/2)^2/2\sigma^2} \tag{1.23}$$

made of two Gaussian functions distant by about $\varepsilon \sim 70°$ (Fig. 1.10). This function has been shown to exhibit much higher S_4 values ($S_4 > 0.5$ for $S_2 \approx 0.5$), as can be expected from its four lobes shape (65) (see Chapter 4).

At last, a case possibly met in samples is the presence of an isotropic population in the focal spot of an objective (coming for instance from internalized fluorescent molecules close to a membrane or from vesicles close to the membrane with diameter much below the diffraction limit), that gets superposed with an ordered population. The resulting distribution we can modeled by new orders that are lowered by the presence of the isotropic contribution. If this contribution is of $\eta\%$ (of the total molecular population), then the new measured order parameters will be ηS_2 and ηS_4 as demonstrated in (74). Fig. 1.11 shows different Gaussian and cone functions altered by the presence of an isotropic population in their distribution, together with the behavior of their (S_2, S_4) symmetry spectrum. Interestingly this situation also contributes to raise the effective S_4 coefficient to higher and positive values (for a given S_2 value). This situation is clearly distinct from the case of distributions free from isotropic population leakage.

1.5 Deduction of the order parameters (p_n, q_n) from the PR nonlinear signals

Since the different optical contrasts described above exhibit a different relation between the nonlinear susceptibility tensors and the nonlinear intensity signal observed, we will discuss the retrieval of the order parameters separately for each contrast.

1.5.1 Deduction of (p_n, q_n) from PR-SRS

As has been discussed at the beginning of this chapter, the stimulated Raman gain (SRG) process is based on the interference between the electric field induced by the nonlinear dipole at ω_S and the incoming field at ω_S (33, 75). Due to this heterodyne behavior, the gain on the Stokes beam at resonance is linear with the susceptibility, and reads (76):

$$I^{SRG} \propto \sum_{IJKL} \chi^R_{IJKL} E^*_{p,I} E_{S,J} E_{p,K} E^*_{S,L} \tag{1.24}$$

where $(I, J, K, L) \in (X, Y, Z)$. The vectors $\vec{E}_{p,S}$ are the incident electrical fields for the pump and Stokes frequencies ω_p and ω_s. Both fields are linearly polarized along the same direction, defined by an angle α with respect to the X axis (see inset in the Fig. 2.1, Chapter 2). Thus: $\vec{E}_{p,S} = (E_X = E_{p,S}\cos\alpha, E_Y = E_{p,S}\sin\alpha, E_Z = 0)$ with $E_{p,S}$ is the field amplitude of the pump/Stokes beam. The intensity (Eq. 1.24) is then expressed as function of α:

$$\begin{aligned} I^{SRG}(\alpha) \propto\; & \chi^R_{XXXX}\cos^4\alpha + 4\chi^R_{XXXY}\cos^3\alpha\sin\alpha \\ & +6\chi^R_{XXYY}\cos^2\alpha\sin^2\alpha \\ & +4\chi^R_{XYYY}\cos\alpha\sin^3\alpha + \chi^R_{YYYY}\sin^4\alpha. \end{aligned} \tag{1.25}$$

and can be rearranged to exhibit its Fourier coefficients a_n and b_n, for $n = 0, 2, 4$:

$$\begin{aligned} I^{SRG}(\alpha) \propto a_0 \; & +a_2\cos(2\alpha) + b_2\sin(2\alpha) \\ & +a_4\cos(4\alpha) + b_4\sin(4\alpha) \end{aligned} \tag{1.26}$$

which are linked to the distribution order parameters by (77):

$$\begin{array}{lll} a_0 = \frac{3\pi}{4}p_0 & a_2 = \frac{\pi}{2}p_2 & a_4 = \frac{\pi}{8}p_4 \\ b_2 = \frac{\pi}{2}q_2 & b_4 = \frac{\pi}{8}q_4 & \end{array} \tag{1.27}$$

The polar-resolved SRS intensity is then described by a Fourier series where the Fourier coefficients are linearly related to the distribution function parameters. These coefficients are easily calculated by projection of $I^{SRS}(\alpha)$ on the $(cos(n\alpha), sin(n\alpha))$ function. This way, the polar-resolved SRS signal shows directly how the molecular bonds are oriented and distributed into the focal volume.

1.5.2 Deduction of $(p_n,\, q_n)$ from PR-CARS

Deduction of the order parameters from the CARS-FWM intensity is not as straightforward as from the SRS signal since the relation between the nonlinear susceptibility and the electric field is not linear. The induced macroscopic dipole is proportional to:

$$P_I(\omega_{as}) \;=\; \sum_{JKL} \chi_{IJKL} E^*_{S,J} E_{p,K} E_{p,L} \tag{1.28}$$

with the CARS induced dipole oriented along the direction I (X or Y). The intensity oriented along X is thus proportional to the square modulus of the CARS dipoles which leads to:

$$I_X^{CARS} \;\propto\; \sum_{\substack{JKL\\MNO}} \chi_{XJKL}\chi^*_{XMNO} E^*_J E_K E_L E_M E^*_N E^*_O \tag{1.29}$$

and the total intensity is the summation of the intensity along X plus the intensity along Y: $I^{CARS} = I_X^{CARS} + I_Y^{CARS}$.

Due to the fact that I^{CARS} Fourier series coefficients a_n and b_n are going up to the sixth order ($n = 0, 2, 4, 6$) (71, 78) (see Appendix A), the retrieval of the distribution function is complex and requires iterative algorithm to find the right set of order parameters that fit with a given PR intensity response (71) (see section 2.3.2, Chapter 2). We will thus use an approximate calculation of the order parameters, to simplify and decrease the time of analysis (77).

As the CARS intensity is quadratically dependent on the susceptibility (Eq. 1.29), it can be written as the square of a truncated Fourier series:

$$\begin{aligned} \widetilde{I}^{CARS}(\alpha) \;\propto\; & [a'_0 + a'_2\cos(2\alpha) + b'_2\sin(2\alpha) \\ & +a'_4\cos(4\alpha) + b'_4\sin(4\alpha)]^2 . \end{aligned} \tag{1.30}$$

Consequently, $\sqrt{I^{CARS}(\alpha)}$ is used in the calculations and decomposed as

$$\begin{aligned}\sqrt{I^{CARS}(\alpha)} = a_0 \qquad & +a_2\cos(2\alpha) + b_2\sin(2\alpha)\\ +a_4\cos(4\alpha) + b_4\sin(4\alpha) & \\ +a_6\cos(6\alpha) + b_6\sin(6\alpha), &\end{aligned} \tag{1.31}$$

The parameters (a_0, a_2, a_4, b_2 and b_4) can be directly deduced by projection on the $(cos(n\alpha), sin(n\alpha))$ basis function and are expressed as a function of a'_0, a'_2, a'_4, b'_2 and b'_4,

$$\begin{aligned} a_0 &= a_0^{'2} + a_2^{'2}/2 + b_2^{'2}/2 + a_4^{'2} + b_4^{'2}\\ a_2 &= 2a'_0a'_2 + a'_2a'_4 + b'_2b'_4\\ a_4 &= a_2^{'2}/2 - b_2^{'2}/2 + 2a'_0a'_4\\ a_6 &= a'_2a'_4 - b'_2b'_4\\ b_2 &= 2a'_0b'_2 + a'_2b'_4 - a'_4b'_2\\ b_4 &= 2a'_0b'_4 + a'_2b'_2\\ b_6 &= a'_2b'_4 + a'_4b'_2. \end{aligned} \tag{1.32}$$

Therefore an approximate relationship can be found between the Fourier parameters (a'_n, b'_n) and the order parameters (p_n, q_n):

$$\begin{aligned} a'_0 \approx \tfrac{3\pi}{4}p_0 \qquad a'_2 &\approx \tfrac{\pi}{2}p_2 \qquad a'_4 \approx \tfrac{\pi}{8}p_4\\ b'_2 &\approx \tfrac{\pi}{2}q_2 \qquad b'_4 \approx \tfrac{\pi}{8}q_4. \end{aligned} \tag{1.33}$$

A numerical comparison has been done between the exact and the approximate calculation of the CARS signal which showed that both outcomes were identical with 1% whatever the set of a_n, b_n parameters considered (77). The negligible difference comes from the eighth frequency presents in $\widetilde{I}^{CARS}$, whereas I^{CARS} contained only six orientational frequencies.

1.5.3 Deduction of (p_n, q_n) from PR-2PEF

The polarization dependence of the collected 2PEF intensity from the in-plane components of the $\vec{\mu}_{abs}$ vector in a steady state regime can be written (52):

$$\begin{aligned} I^{2PEF}(\alpha) &\propto \int_0^{2\pi} |\vec{\mu}^{2D}_{abs}(\varphi)\cdot\vec{E}(\alpha)|^4\, p(\varphi)\,\mathrm{d}\varphi\\ &\propto \int_0^{2\pi} \cos^4(\varphi-\alpha)\,p(\varphi)\,\mathrm{d}\varphi, \end{aligned} \tag{1.34}$$

with $\vec{\mu}^{2D}_{abs}(\varphi) = \mu_{abs}\,(\cos\varphi, \sin\varphi, 0)$ and

$$p(\varphi) = \int_0^{\pi} \sin^5\theta f(\theta,\varphi)J(\theta,\varphi)\,\mathrm{d}\theta. \tag{1.35}$$

where the $\vec{\mu}_{abs}$ is the absorption dipole vector of the fluorophores contributing to the signal, $\vec{E}$ assumed to be linearly polarized in the sample plane and the factor $J(\theta, \varphi)$ is the detection probability of fluorescence (51, 52). The 2PEF intensity can also be rearranged to exhibit the Fourier coefficients a_n and b_n, for $n = 0, 2, 4$:

$$\begin{aligned} I^{2PEF}(\alpha) \quad \propto a_0 \quad &+a_2 \cos(2\alpha) + b_2 \sin(2\alpha) \\ &+a_4 \cos(4\alpha) + b_4 \sin(4\alpha), \end{aligned} \tag{1.36}$$

which are linked linearly, in the same way as SRS, to the distribution order parameters by:

$$\begin{aligned} a_0 = \tfrac{3\pi}{4} p_0 \qquad a_2 &= \tfrac{\pi}{2} p_2 \qquad a_4 = \tfrac{\pi}{8} p_4 \\ b_2 &= \tfrac{\pi}{2} q_2 \qquad b_4 = \tfrac{\pi}{8} q_4. \end{aligned} \tag{1.37}$$

This way, the PR-2PEF signal shows directly how the fluorophores are oriented and distributed into the focal volume.

1.6 Conclusion

In this chapter, we demonstrated an analytical model to read out the angular organization of biomolecular assemblies. This fully tensorial approach permits revealing a high level of details on the orientational disorder and depends only on the nonlinear contrast used to target not only fluorescent probes (2PEF) but also unlabeled molecules by their vibrational resonances (CARS, SRS) or electronic responses (FWM). We show finally that a simple Fourier decomposition of the PR-responses measured for all these optical contrasts gives access to symmetry order parameters of the observed molecular distribution function. This considerably simplifies and speeds-up data processing, allowing large images to be analyzed. In the following chapters we will demonstrate the application of this model to target the organization of lipid assemblies in model (MLV) and biological (myelin) membranes as well as of fluorophores embedded in membranes as probes for lipids' orientational order.

Chapter 2

Polarization resolved multimodal microscopy and data processing

In this chapter we will present the experimental set-ups that were used to perform PR and multimodal imaging. Two optical systems using different laser sources were used in this work to perform the experiments according specific tasks. A picosecond system was used to perform PR-CRS measurements on the model membranes that required spectral vibrational selectivity, especially in the Raman bond region different from the "lipids region", benefiting from its high spectral resolution. However, when higher intensities were needed and not necessarily a high spectral resolution, we used a femtosecond optical set-up. We employed this system to perform PR measurements using different contrasts such as CARS, SRS and 2PEF as well as multimodal imaging of complex biological samples. Both laser sources operating in a wide spectral range are based on two Optical Parametric Oscillators (OPO's) that deliver two optical frequencies known as the pump and the Stokes frequencies which together generate simultaneously various nonlinear processes at the focal spot of the microscope objective. These systems are described in the first part of this chapter.

The linearly polarized light, which is the main player in the PR measurement, needs to be well controlled in order to retrieve a valuable information about molecular order. Therefore, in the second part of this chapter, we will discuss how the linearly polarized light can suffer from a variety of distortions introduced either by instrumental factors or by the sample itself, and how to overcome these problems.

The last part of the chapter is focused on finding the best solutions for data acquisition and retrieval of the order parameters discussed in Chapter 1. The image processing before any polarimetric analysis is also addressed since it is sometimes necessary to evaluate the high accuracy of the method depending on signal to noise conditions.

2.1 Experimental set-up

In this section we present in detail the two optical set-ups used in this work. Configurations of the wavelengths as well as optical filters and dichroic mirrors used in the individual experiments are sketched in the Appendix B.

2.1.1 The picosecond system

The excitation source in the picosecond system shown in Fig. 2.1 is a mode-locked frequency doubled Nd:YVO laser (picotrain HighQ laser) operating at $\lambda = 532$ nm with an output average power of 8 W. It delivers picosecond pulses to two independent OPOs (Emerald, APE, Berlin, Germany). Each of them then generates the ≈ 5 ps (repetition

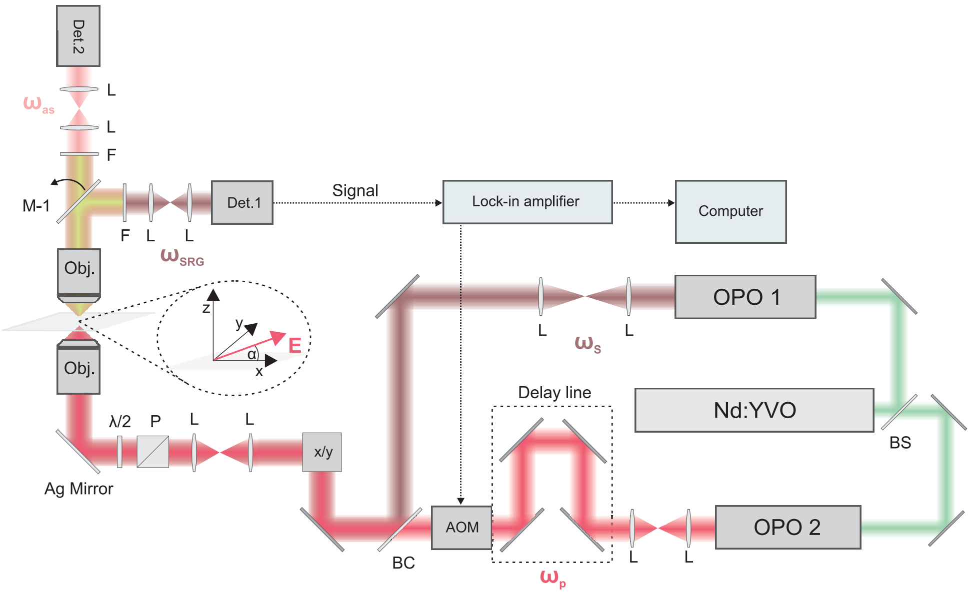

Figure 2.1: The experimental picosecond set-up. Key: Nd:YVO: mode-locked frequency doubled picosecond laser; OPO: tunable optical parametric oscillator ($730 - 960$ nm); AOM: acousto-optic modulator; BS: beam splitter; L: lens; P: polarizing beamsplitter cube; $\lambda/2$: tunable achromatic half-wave plate; Obj.: high numerical aperture; BC: beam combiner; M-1: flip mirror; F: filter; Det.1: PD: photodiode, SRS detection; Det.2: PMT: photomultiplier tube, CARS detection. Inset: Enlarged window of the polarized excitation in the (X, Y) sample plane.

rate 76 MHz) pulses within a maximal wavelength range of $\lambda = 730 - 960$ nm. In our experiment the pump beam is usually fixed at $\lambda = 735$ nm and the Stokes beam is tuned to perform CARS and SRS spectra or to target a specific Raman resonance. These two beams, the pump (ω_p) and the Stokes (ω_S), are temporally synchronized and spatially overlapped on a beam combiner (BC, see Fig. 2.1) and sent into a custom-made scanning microscope (79). The imaging system uses a pair of galvonometric mirrors (6200 H, Cambridge Technology) which scan the sample and is controlled through a home built software (Labview, National Instruments) (80). The data is acquired by a data acquisition board (NI USB 6353, National Instruments Corp). After reflection on the silver mirror in the inverted microscope (Eclipse Ti, Nikon Instruments Inc.) the two beams are focused by a high numerical aperture objective (see Appendix B) and the emitted signal is collected in the forward direction. In the CARS operation mode the anti-Stokes (ω_{as}) signal is filtered and detected with a photomultiplier tube (PMT, Hamamatsu R9110, spectral response: 185 to 900 nm) coupled with a preamplifier (C7950, Hamamatsu) or channel photomultiplier tube (CPM, Perkin Elmer Optoelectronics C972, spectral response: 115 to 900 nm). In the SRS operation mode, the pump beam is modulated in amplitude at a frequency of 20 MHz thanks to an acousto-optic modulator (AOM - AAOptoelectronic MT200 A0,2 − 800). The stimulated Raman gain (ω_{SRG}) induced on the Stokes beam is filtered and detected with a high spead photodiode (PD, Thorlabs DET100A, spectral response: 350 to 1100 nm) and a fast lock-in amplifier manufactured by APE.

We used the picosecond system to perform PR -CARS, -FWM and -SRS measurements on the model lipid membranes (multilamellar vesicles) in order to better understand the spectral specificities of the polarization response from the sample and also to investigate the intrinsic properties of the PR nonlinear contrast.

2.1.2 The femtosecond system

In the femtosecond system the light source is a tunable mode-locked Ti:Sapphire laser (Chameleon Ultra II, Coherent Inc.) operating in the range from 690 to 1080 nm which delivers 150 fs pulses (repetition rate 80 MHz) to an optical parametric oscillator (Compact OPO-Vis, Coherent Inc.) with an output average power of 5 W. The OPO system has several simultaneous outputs operating at different spectral range shown in Fig 2.2. The pump (ω_p) and the Stokes (ω_S) beams can be individually tuned according to a certain OPO output giving access to a large spectrum of possible wavelength combinations. In our experiment we use two output configurations which for clarity are presented in separate

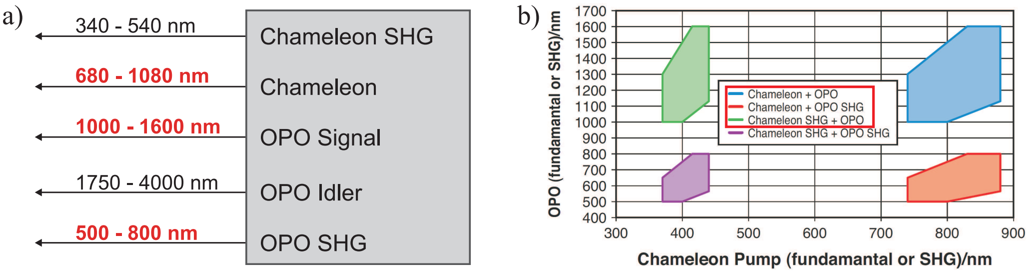

Figure 2.2: Specifications of the femtosecond system. (***a***) Independent wavelength tuning of laser+OPO with multiple outputs operating at different spectral range. Outputs used in our studies are marked in red. (***b***) Possible wavelength combinations.

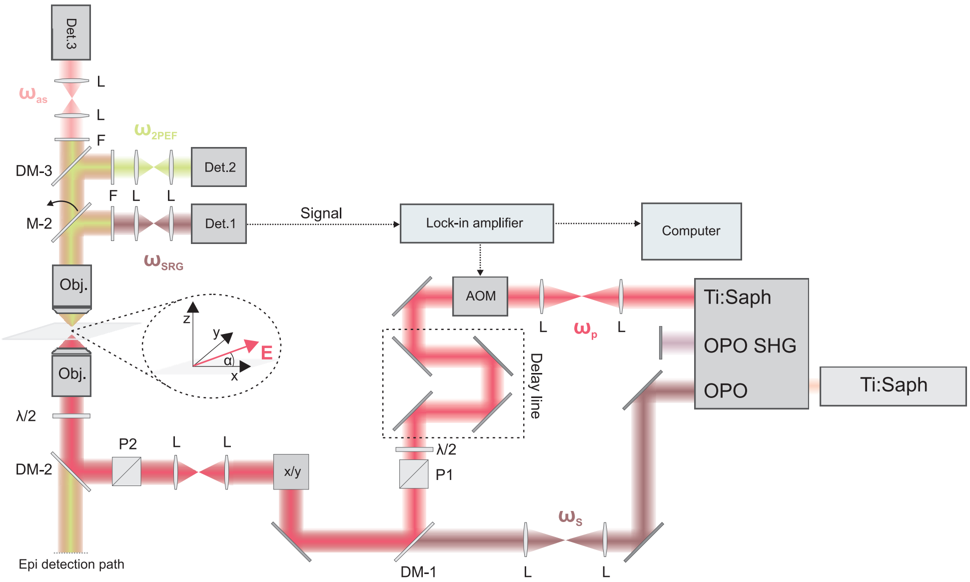

Figure 2.3: The main configuration in experimental femtosecond set-up. Key: Ti:Saph: tunable Ti:Sapphire femtosecond laser (690 − 1080 nm); OPO: tunable optical parametric oscillator (1000 − 1600 nm); AOM: acousto-optic modulator; L: lens; DM-1, -2, -3: dichroic mirrors; P-1, -2: polarizing beamsplitter cubes; $\lambda/2$: tunable achromatic half-wave plate; Obj.: high numerical objective; M-1, -2: flip mirrors; F: filter. Forward detection: Det.1: photodiode detector; Det.2, Det.3: photomultiplier tube detectors. Inset: Enlarged window of the polarized excitation in the (X, Y) sample plane.

set-ups (Fig. 2.3/Fig. 2.4 and Fig. 2.5) called the "Main configuration" and the "Alternative configuration", respectively. We use the "Main configuration" largely in most of experiments. The "Alternative configuration" is used to perform experiments in the case when, for instance, a detector efficiency to collect a signal operates at different spectral range or we want to target resonances below 1000 cm^{-1} wavenumbers (Main configuration targets wavenumbers in the range from 2100 cm^{-1} to 3030 cm^{-1}). We have chosen this configuration due to the efficiency of detector (operating at lower spectral range) to perform one set of PR measurements as discussed in Section 4.2.

The layout of the optical path is similar for both configurations. However, the "Main configuration" uses the Ti:Saph and the OPO output for the pump and the Stokes beams, respectively (Fig. 2.3) while the "Alternative configuration" uses the Ti:Saph and the OPO-SHG output for the Stokes and the pump beam, respectively (Fig. 2.5). The combination of half-wave plate and polarizing cube (P-1) placed before the dichroic mirror (DM-1) on the invariant Ti:Saph-output path allows us to switch easily between two configurations. Both beams, the pump and the Stokes are overlapped in time and space on a dichroic mirror (DM-1) and sent to an inverted microscope (Eclipse Ti, Nikon Instruments Inc.) using a pair of galvonometric scan mirrors (6215H, Cambridge Technology Inc.). The excitation light is focused on the sample by a high numerical aperture objective

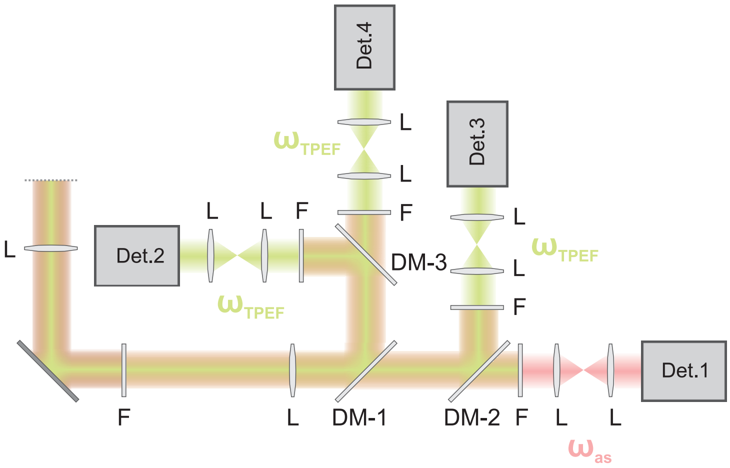

Figure 2.4: The configuration of the epi detection used in the multimodal imaging. A nonlinear signals were spectrally separated by the combination of filters (F) and dichroic mirrors (DM-1, DM-2 or DM-3) and sent simultaneously to identical 4 detectors - PMTs. Detected signal is usually in the range of 350 to 700 nm.

(see Appendix B) and the filtered nonlinear signal is recorded either in the forward- or in the epi-direction. The choice of forward- versus epi detection is governed by the type of measured sample (epi-direction being for instance more appropriate for thick samples such as tissues). We use invariably photomultiplier tubes (PMTs, Hamamatsu R9110, spectral response: 185 to 900 nm) to collect the fluorescence (ω_{2PEF}) or the anti-Stokes (ω_{as}) signal in the CARS operation mode while photodiodes (PD, Thorlabs DET36A, spectral response: 350 to 1100 nm) and a fast lock-in amplifier (APE) while collecting the SRS signal. Scanning and data acquisition is performed using an in-house LabVIEW (National Instruments Corp.) program (80). The data is acquired by a data acquisition board (NI USB 6353, National Instruments Corp). At this point we should specify the detection path for the two different configurations.

Main configuration

In this configuration (Fig. 2.3) the pump beam is tuned in frequency and modulated in amplitude in the SRS operation mode which results in the emission of the stimulated Raman gain (ω_{SRG}) signal induced on the Stokes beam which is detected by a photodiode. The transmitted anti-Stokes and reflected fluorescence signals by a dichroic mirror (DM-3) are detected simultaneously on the PMT detectors. For the specification of wavelengths, filters and dichroic mirrors see Appendix B (Section B.2).

The PR-measurements are performed using the forward detection scheme (Fig. 2.3). On the other hand, multimodal imaging (Chapter 7) is performed using the epi-detection path. A nonlinear signal collected by the excitation high numerical aperture objective and transmitted by a dichroic mirror (DM-2) is spectrally separated and filtered as shown in Fig. 2.4 (see Appendix B.4 for setting wavelengths). In all cases fluorescence and the anti-Stokes signals are recorded simultaneously using identical PMT detectors.

Alternative configuration

For the alternative configuration which uses the OPO-SHG source, we perform PR-measurements using either the forward or the epi-detection paths (Fig. 2.5, Fig. 2.4). We record the SRL signal in the forward direction while the anti-Stokes and fluorescence signals are collected in the epi- direction. Note that in comparison to the ”Main configuration”, here the modulation of the amplitude and frequency is done on the Stokes beam which generates the emission of the stimulated Raman loss (ω_{SRL}) signal on the pump beam. The experimental settings are detailed in Appendix B (Section B.3).

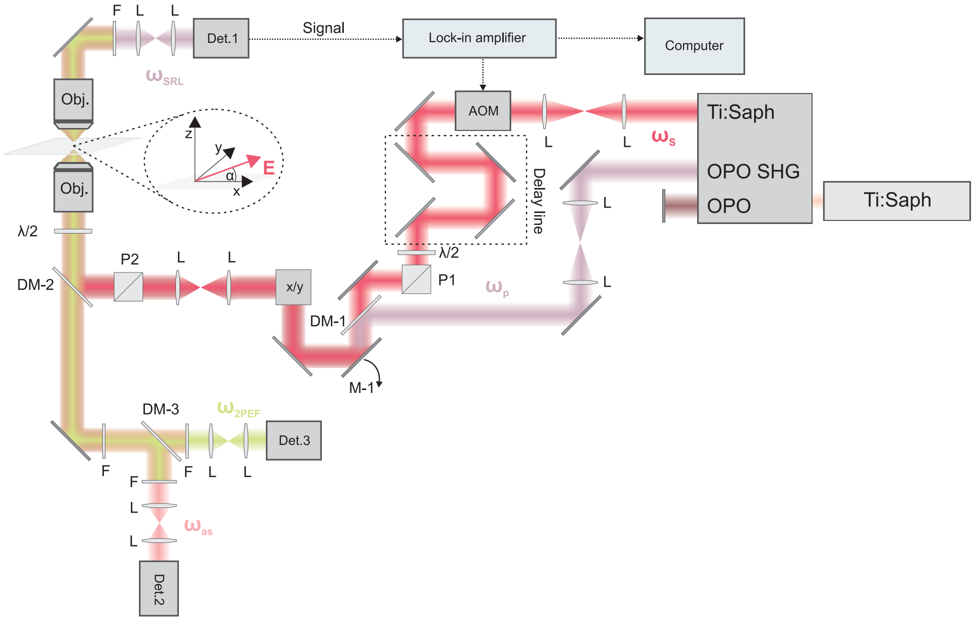

Figure 2.5: The alternative configuration in the experimental femtosecond set-up. Key: Ti:Saph: tunable Ti:Sapphire femtosecond laser ($690 - 1080$ nm); OPO SHG: tunable optical parametric oscillator ($500 - 800$ nm); AOM: acousto-optic modulator; L: lens; DM-1, -2, -3: dichroic mirrors; P-1, -2: polarizing beamsplitter cubes; $\lambda/2$: tunable achromatic half-wave plate; Obj.: high numerical objective; M-1: flip mirror; F: filter; Det.1: photodiode detector; Det.2, Det.3: photomultiplier tubes. Inset: Enlarged window of the polarized excitation in the (X, Y) sample plane.

2.1.3 Polarization resolved microscopy

In order to perform the PR measurements, two elements are introduced into the standard experimental set-ups: 1) the polarizing beamsplitter (P; PBS252, Thorlabs Inc.) which induces a *p*-polarization on both lasers, the pump and the Stokes, and 2) an achromatic half-wave plate ($\lambda/2$; AQWP10M-980, Thorlabs Inc.) mounted on a motorized rotational mount (PR50CC, Newport Corp.) which rotates simultaneously both linearly polarized beams (Fig. 2.1, Fig. 2.3, Fig. 2.5). By changing the polarization angle α of the incident electric fields ($\mathbf{E}$) with respect to the X axis (horizontal axis in the sample image) we record the image for each polarization state over the range of 0° to 170° with an α step of 10°. The emitted nonlinear signal is detected either in forward or in epi configuration. We collect the whole modulated intensity signal in so called un-analyzed detection (without any analyzers) which allows us to use multiple detectors at the same time. It has been shown in particular that un-analyzed detection permits to avoid artifact effects from scattering (81).

Although these two elements are standard in the PR schemes their arrangement in the optical path may not have an identical effect on the linear polarization state. For technical reasons, in the picosecond system the polarizing beamsplitter and rotating $\lambda/2$ are placed before the Ag mirror which reflects the linearly polarized incident fields and send them towards the microscope objective (Fig. 2.1). Such a configuration may introduce some distortions in the polarization state of light in such a way that the elliptical or circular polarization is sent to the sample instead of the linear polarization (see Section 2.2.1). Thus, all possible distortions caused by the reflection optics need to be characterized and introduced to the model presented in Chapter 1. The situation is different in the femtosecond system where the rotating $\lambda/2$ is placed after the dichroic mirror (DM-2) just before the focusing objective (Fig. 2.3, Fig. 2.5), resulting in linear excitation polarization free of distortions. Therefore, no corrections of distortions in the model is required in this scheme.

2.2 Artifacts in PR measurements

Investigation of the molecular order by PR microscopy requires the excitation polarization to be well controlled. The distortion of incident fields contributing to generate the polarized nonlinear response needs to be characterized and eventually introduced to the polarimetric model. Different instrumental elements such as the dichroic mirrors or a high numerical aperture objectives as well as the factors induced by the sample itself (mainly birefringence, diattenuation and scattering) can play a role in the polarimetric response and bias the obtained results. A lot of work has been done previously (62, 66, 81, 82) on characterizing and compensating for the polarization distortion effects. In this section we will give a brief description of the effects which are the most relevant to our work.

2.2.1 Polarization distortions induced by reflective optics

Optical mirrors and dichroic beamsplitters reflecting an incident field often induce a phase shift δ (ellipticity) and amplitude factor γ (diattenuation) between two orthogonal polarization state components s and p which in the geometry of experiment also corresponds to the X and Y directions in the sample plane (Fig. 2.1). Such a distorted field can be expressed as (82) in the backfocal plane of the objective before focusing:

$$\mathbf{E}(\alpha,\delta,\gamma) \propto \begin{bmatrix} \cos\alpha \\ (1-\gamma)\sin\alpha\, e^{i\delta} \\ 0 \end{bmatrix} \tag{2.1}$$

where α is the rotating polarization angle of the excitation field with respect to X axis. As it is shown in Fig. 2.6, the effect of the phase shift δ on the electric field strongly affect the incident polarization state. In the free-distortion scheme when the ellipticity $\delta = 0$ the polarization of the incident electric field stays linear whatever the angle α. However, when δ increase and the incident fields rotate the linear polarization become more and more elliptical reaching circular polarization at $\delta = \pi/2$ and $\alpha = \pi/4$. The presence of such distortion effects will affect the symmetry orders read out which strongly relies on the emitted polarized nonlinear signal (71, 82). Therefore, the degree of polarization distortions (e.g. knowing both the δ and γ factors) needs to be carefully characterized before any polarimetric analysis.

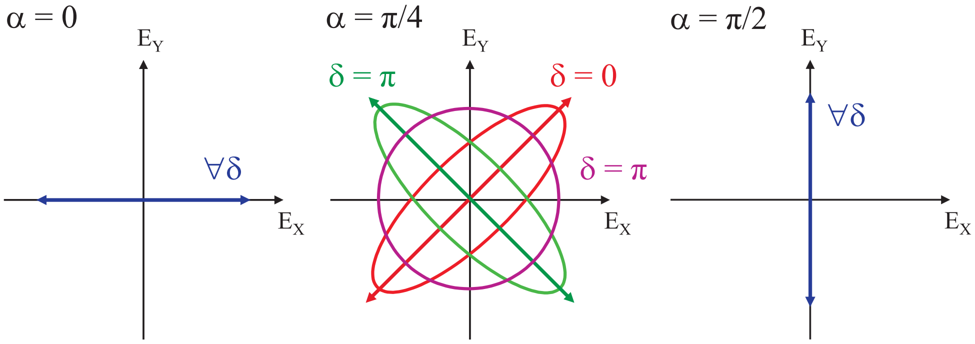

Figure 2.6: Influence of the ellipticity δ and diattenuation γ on the linearly polarized electric field rotating of an angle α. The polarization stays linear when the incident field is horizontal (α=0) or vertical (α=$\pi/2$) with respect to the X axis. The highest elliptical effects appear for the intermediate direction of the incident field (Adapted from ref. (66)).

The measurement of the polarization state has been in particular performed on the pump and the Stokes beams in the picosecond experimental set-up where the incident field is rotated by a $\lambda/2$ placed before the reflective Ag mirror (see Section 2.1.3). We characterized the distortion factors using a polarimeter developed by Xiao Wang as described in (51, 83). The method to retrieve the effect of these distortion factors on the order parameters is based on a rotating quarter-wave plate and can be found elsewhere (71). We have measured that the reflection on the Ag mirror induces a phase shift δ between the E_X and E_Y components equal to 163° for the pump beam set at 735 nm and 176° for the Stokes beam set at 929 nm, which are the wavelengths often used in our experiments to probe the CH stretching vibrations (2845 cm^{-1}). The diattenuation γ factor was found to be 0 for both wavelengths. Such a phase shift can impose a strong bias on values of the order parameters (p_n, q_n) (71). Numerical studies have shown that while p_2 can be biased of 0.05 in the presence of $\delta = 90°$, the p_4 is much more sensitive and can reach a biased value higher than 1 for this phase shift. We included the correction for these distortions into our model when analyzing data from the picosecond experimental set-up, which consists in rewriting the relation between the Fourier coefficients of the PR-CRS signal and the order parameters (See Appendix A and ref (71)).

2.2.2 Polarization distortions induced by high NA objectives

Objectives with a high numerical aperture can be another possible source for polarization distortions. Under a tight focusing of the light the longitudinal component of the electric field can play a role in the generation of the polarized response coupling with the molecular dipoles which possess orientation components along the propagation direction Z (69). It has been shown in particular by Schön et al. (82) that in an isotropic liquid, in which the excitation process is randomized, the fluorescence polarimetric response does not depend on the numerical aperture of the objective. However, in anisotropic samples, the coupling between the off-plane molecular transition dipoles and the longitudinal (Z) component of the excitation field can add some new contributions in the emitted light and lead to deformation of the polarimetric response. Nevertheless, since strongly tilted dipoles also radiate much less efficiently, their contribution is decreased. We will see in Chapter 6 that symmetry orders read by our polarimetric analysis are essentially insensitive to longitudinal contributions when the molecular distribution is lying in the sample plane (e.g. equatorial plane of a spherical membrane) or slightly tilted. We will therefore neglect this factor in the data processing since it does not strongly affect resulting polarization response. The theoretical developments show that in the case of slightly tilted distributions it is recommended to use objectives with NA $<$ 0.8 to avoid possible implications after Z longitudinal field component to the polarization analysis (82).

2.2.3 Influence of sample birefringence on PR analysis

It is common that birefringent materials such as crystalline (84) and biological samples (42, 62) are able to perturb the optical properties of polarized light leading to erroneous or biased results. This is because strongly anisotropic structures can exhibit different refractive indexes and absorption coefficients along their main symmetry axis compared to

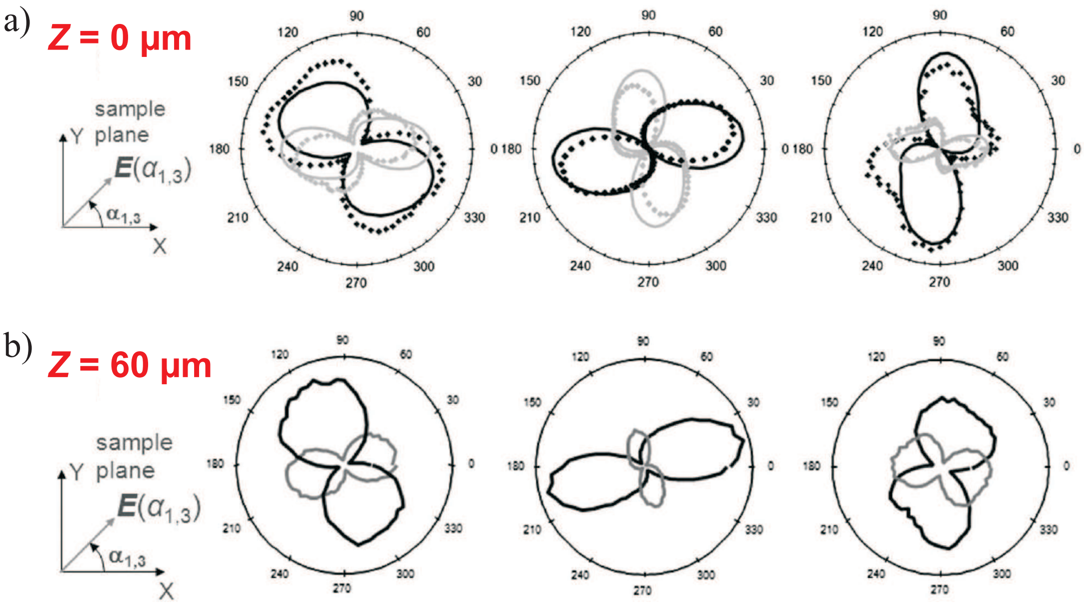

Figure 2.7: FWM intensities along || (black) and ⊥ (gray) analyzed detection to the incident E field as a function of the incident polarization at Z=0 μm (***a***) and Z=60 μm (***b***) in collagen sample (extracted from a rat tail tendon). Solid lines: theoretical intensities given by the best fit; dots: experimental data. From left to right, the polar plots of different position on the rat tail tendon (Adapted from ref. (85)).

the perpendicular optical axis. In microscopy, such a difference in refractive indexes (birefringence) can introduce a phase shift (Φ_b) between the components of the polarized input field. As presented in Fig. 2.7 the degree of distortions induced by birefringence increases with the depth at which the polarized excitation light is focused. In this experiment, performed by Munhoz et al. (85), PR-FWM data were acquired on collagen fibers extracted from rat tail tendon which are known to be highly birefringent (86). The experimental polarization configuration was similar to our approach with this difference that the transmitted FWM intensity was recorded on two channels, polarized parallel or perpendicular to the direction of the excitation field (black and gray curves in Fig. 2.7, respectively). Moreover, it has been also noticed that the detection of polarization distortions can be enhanced in certain orientations of the strongly birefringent structures (62).

Finally, a question arises: how does the birefringence affect the symmetry orders that are read out by PR experiment? Following the method developed previously (62, 67, 71) we characterized the degree of birefringence in our samples and its influence on the deduced order of symmetries. Briefly, we rotate the linear polarization angle α of the excitation field from 0° to 170° and record the transmitted intensity at the laser wavelength after a polarizer of known orientation. Such a measurement provides a direct access to the total phase shift ($\Phi_b(d)$) of the E_X versus E_Y components of the field introduced by a sample of known thickness ($d = L$) when compared with data obtained from an isotropic solution (Appendix C). From the measured birefringence we have numerically calculated how the values of S_2 and S_4 deduced from polarization data are affected by this birefringence. Typically in MLVs, birefringence phase shifts of about 10° are obtained over a 20 μm propagation length (up to 40° has been obtained in MLVs doped with cholesterol). Using models for which the incident fields are affected by birefringence (71), we have estimated the bias on S_4 to be no more than 0.1 in the presence of a 40° birefringence phase shift. The S_2 symmetry order is less sensitive than S_4 and thus much less affected (bias < 0.02). The measurement of birefringence on the myelin in a spinal cord sample leads to very similar values (see Appendix C).

We will thus always perform our PR experiments close to the surface with depth corresponding to a birefringence $< 40°$ to consider the induced bias on S_2 negligible and the S_4 bias less than 0.1. It is however possible to insert a known birefringence into the model used to fit the polarization data (71) in case of higher birefringence.

In addition to refractive index difference, the light passing through an anisotropic structure can also be attenuated on one of the two components of the incident field. Such an effect can lead to deformation of polarimetric responses when penetrating deep in a sample (42). Our PR intensities modulated signals are recorded in the backward direction and close to the surface of poorly absorbing samples and therefore this parameter is negligible in our experiments.

2.2.4 Influence of the scattering on PR analysis

Scattering in the tissues is a main issue when a valuable biological information can be only found deeply under the surface. In highly scattering tissues such as the white matter of the spinal cord when the density of myelin is high, multiple scattering starts occurring and may lead to a strong depolarization of the incident field propagating through a medium due to the randomization of propagation direction. Many works have been dedicated to characterize polarization properties of biological tissues (87, 88). Typically, depolarization starts occurring at depths of a few scattering mean few paths in tissues, which corresponds to a few hundreds of μm in the brain. In a recent fundamental work, de Aguiar et al.

(81) quantified the degree of linear depolarization (DOLP) of either incident or emitted fields in scattering media. He shows that while the polarization state of NIR excitation photons is preserved until a depth when structures can be imaged (few hundreds of μm in brain, 80 μm typically in spinal cords), the polarization of emitted photons (2PEF and CARS) depends on the geometry, the size of scattering centers and on the thickness of the specimen. In thick spinal cord tissue for instance, the emitted epi-CARS photons can be depolarized even though the imaging depths is as low as 20 μm. This is due to the fact that epi-emission is superimposed with back-scattered photons that come from multiple directions. Therefore, when the emission is detected with an analyzer (polarized detection) the results can lead to erroneous conclusions. In what follows, we will discuss how to overcome these problems.

As the spinal cord tissue, which will be investigated in this study, is a highly scattering medium (89, 90) depolarization of emitted CARS should be in principle a very important issue. First of all, we perform a superficial PR imaging with a maximum depth of ≈ 20 μm and therefore the excitation photons involved in the nonlinear coupling are not affected by depolarization. Second, we do not use any analyzer. We record the intensity modulation which is the total nonlinear signal respective of its emission direction thus depending only on the orientation of excitation induced dipoles and therefore providing reliable and robust measurements against scattering effects.

2.3 Data analysis and image processing

2.3.1 Data acquisition

The general method to retrieve the molecular order parameters is shown in Fig. 2.8. When performing PR measurements the sample is scanned pixel by pixel and the resulting image is recorded for each polarization state. For each pixel in the recorded stack of images we retrieve the modulation of the signal depending on the input polarization angle α. The range (typically from 30×30 μm to 100×100 μm depending on the size of the structure) and the step size of the rotating polarized fields should be chosen to retrieve the curve of polarization modulated intensity with the highest signal level (Fig. 2.8b). The average laser power at the focal spot should be chosen to collect at least 10 photons (on a pixel) per polarization angle on average, in order to reliably retrieve S_2 and S_4 values, but in our case the intensities usually greatly overcome this criterion (see Section 2.3.3). Previous studies (71) have shown that the important parameter that governs the precision of the S_2 and S_4 retrieved values is the total number of photons (or signal) summed over all

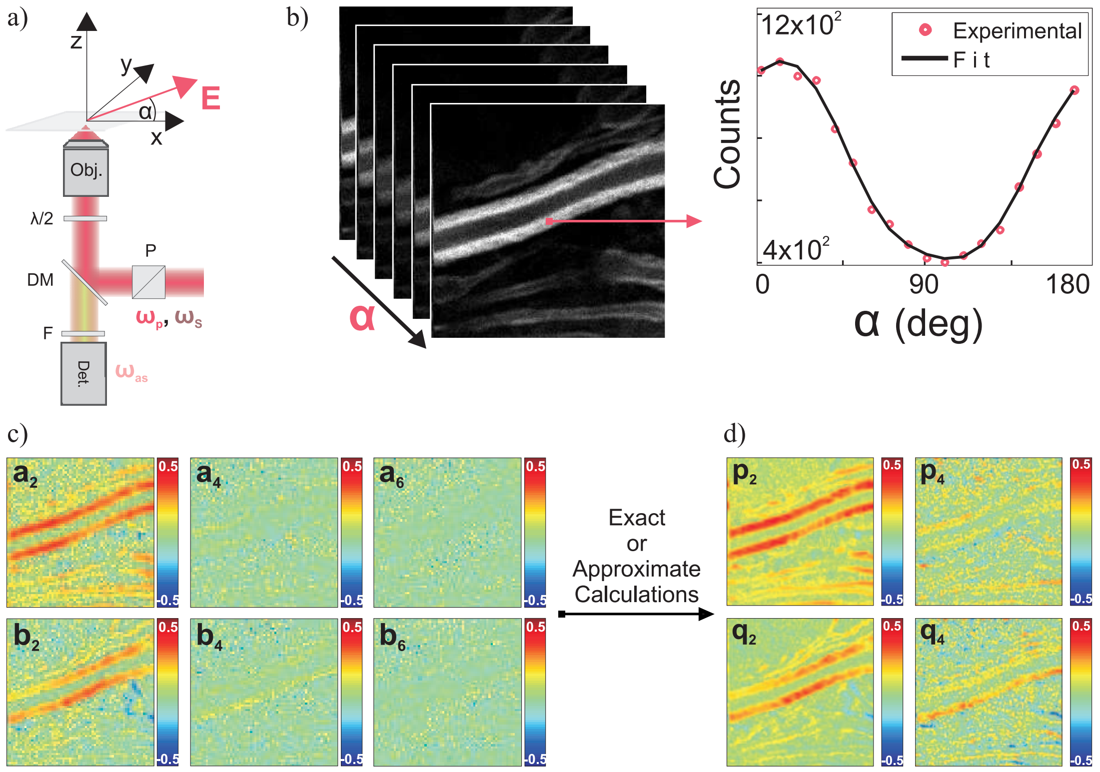

Figure 2.8: (***a***) Schematic of the set-up geometry. (***b***) Stack of PR images recorded by CARS on myelin fiber in the spinal cord tissue and a intensity modulation for one pixel taken from the image (pixel size 100 nm). (***c***) Images deduced from the numerical calculations of the Fourier coefficients (a_n, b_n) of the PR intensity images. (***d***) Images of order parameters (p_n, q_n) deduced from the Fourier coefficients by either exact or approximate calculation. In this case, approximate calculation (see Chapter 1).

incident polarization angles. As long as number of incident α angles is above 5, using many α angles and short integration times is thus equivalent to few α angles with long integration time. We will typically chose 18 incident polarization angles with $\approx 50\ \mu$s integration time (≈ 1 s for the 50 μm $\times 50\ \mu$m) per angle.

2.3.2 Retrieving the order parameters from the PR-measurements

The first step to retrieve the order parameters from the PR measurement uses the Fourier analysis of the recorded polarization dependent intensity. Since the intensity signal $I(\alpha)$ contains powers of cosine and sine functions, it can be decomposed in a Fourier series as follow (74):

$$I(\alpha) \propto 1 + \sum_{k=1}^{+\infty} [A_k \cos(k\alpha) + B_k \sin(k\alpha)] \tag{2.2}$$

where non-zero terms are only for $k = 2$ and $k = 4$ for SRS and 2PEF, in agreement with Eq. 1.14 and Eq. 1.37 k reaches $k = 6$ for CARS (see Eq. A.4, Appendix A). If the measurement is performed at N discrete angles regularly spaced $\alpha_1 = 0$, …, $\alpha_i = \frac{(i-1)\pi}{N}$, …, $\alpha_N = \frac{(N-1)\pi}{N}$ (in radians), the Fourier coefficients of the measured signal are given by

$$A_k = \frac{2}{I_0} \sum_{i=1}^{N} I(\alpha_i) \cos(k\alpha_i) \tag{2.3}$$

$$B_k = \frac{2}{I_0} \sum_{i=1}^{N} I(\alpha_i) \sin(k\alpha_i) \tag{2.4}$$

with $I_0 = \sum_{i=1}^{N} I(\alpha_i)$. If we consider the 2PEF signal the distribution parameters are directly obtained using:

$$S_2 = \frac{3}{2} \sqrt{A_2^2 + B_2^2}, \tag{2.5}$$

$$S_4 = 6 \sqrt{A_4^2 + B_4^2}, \tag{2.6}$$

$$\varphi_2 = \frac{1}{2} \operatorname{arc\,tg}(B_2, A_2), \tag{2.7}$$

$$\varphi_4 = \frac{1}{4} \operatorname{arc\,tg}(B_4, A_4), \tag{2.8}$$

where arctan denotes here the four-quadrant inverse tangent function. One can show mathematically that Eqs. 2.3 and 2.4, which use a discrete sum to compute Fourier coefficients instead of continuous integrals, are valid for $N \geqslant 6$, the case where we only consider $k = 2$ and 4. Note that by definition of a positive measured intensity, the range of values for S_2 and S_4 is confined within [0-2]. This treatment results in maps of the Fourier coefficients (a_n, b_n) deduced from the PR stack of images, similar as shown in Fig. 2.8c.

These values can be biased according to the level of noise as mentioned above. When a special care is taken to acquire data with a good signal-to-noise ratio, which is the case here, an error of only a few percent appears on the coefficients.

The determination of the order parameters (p_n, q_n) from the measured (a_n, b_n) coefficients in the case of the CARS signal relies on the nonlinear expression shown in Eq. A.5 in Appendix A and is therefore not straightforward. In order to resolve this inverse problem two methods of calculation have been developed in our group.

Fitting method

The first procedure, developed by Bioud et al. (71) relies on finding the set of p_2, q_2, p_4, q_4 (with $p_0 = 1$) values according to a minimizing criterion between a model equation and the retrieved (a_n, b_n) parameters:

$$E(p_2, q_2, p_4, q_4) = \|(w^{exp} - w(p_2, q_2, p_4, q_4))\|^2 \tag{2.9}$$

where $w^{exp} = [a_2, a_4, a_6, b_2, b_4, b_6]$ is the set of Fourier coefficients measured and $w(p_2, q_2, p_4, q_4)$ is the expected set of Fourier components for given (p_2, q_2, p_4, q_4) values. To span the expected values we build a database of (a_n, b_n) values expected from all (p_n, q_n) values ranging between $[-1.5, 1.5]$. The choice of the sampling step is made contextually (depending on the precision required) ranging between 0.01 and 0.05. This procedure allows to recover, on each pixel, the best order parameters (p_2, q_2, p_4, q_4) without ambiguities and with a minimal error. It also allows entering possible effects from optical fields distorions (dichroic mirrors, birefringence) in a pre-defined model for the expected polarization response modulation.

In particular due to distortions introduced by the dichroic mirror in the ps set-up (Section 2.1.3) the formulas relating the (a_n, b_n) coefficient and the order parameters (p_n, q_n) becomes more complicated than Eq. A.5 (71). For this reason it was easier to include the measured phase shift δ between E_X and E_Y to the database of $(a_n, b_n) \leftrightarrow (p_n, q_n)$ and use this algorithm to recover the order parameters from the PR measurements performed on the ps set-up.

Approximate calculation

Another method was developed by Duboisset et al. (77) in order to simplify and decrease the time consuming analysis described above (Chapter 1). It is the nature of the CARS signal which makes the analysis not trivial due to the nonlinear dependence between (a_n, b_n) and (p_n, q_n) (Eq. A.5). An approximate calculation of this relation (valid at 1% error) can be obtained if we take the square root of the PR-CARS signal. Then this nonlinear dependence between the Fourier coefficients and the distribution function parameters becomes a linear relation, similarly as for the PR-SRS intensity (see Eq. 1.33). Consequently, $\sqrt{I^{CARS}(\alpha)}$ (eq 1.30) can be easily used to extract (p_n, q_n) and therefore S_2 and S_4 on each pixel from the PR measurement. Fig. 2.8d shows the maps of retrieved (p_n, q_n) values from (a_n, b_n) Fourier coefficients using the approximate calculation.

In a very similar way, SRS polarization modulation can be treated using $I^{SRS}(\alpha)$

(Eq. 1.27) and as shown above, 2PEF. These dependencies lead to linear relations between (a_n, b_n) and (p_n, q_n) that can be directly extractable. Note however that introducing fields distortions in the relations would lead to more complex calculations. These simple equations where nevertheless applicable to our fs configuration where no distortions were expected.

Having the values of the distribution function parameters, the quantification of the symmetry order magnitude and the mean orientation of the distribution function can be easily retrieved as has been shown in Section 1.4.1.

2.3.3 Sensitivity of the polarization resolved measurement on the level of noise

PR measurements can be affected by the level of noise, which is known to induce errors in precision and biases. In order to quantify the accuracy of estimation of S_2 and S_4 symmetry parameters depending on the level of noise, we performed a set of PR-CARS measurements using an isotropic sample where S_2 and S_4 are expected to be 0. This sample is a drop of olive oil placed on the cover slip. This sample was chosen on purpose due to a) the high sensitivity of CARS signal coming from CH stretching vibrations at

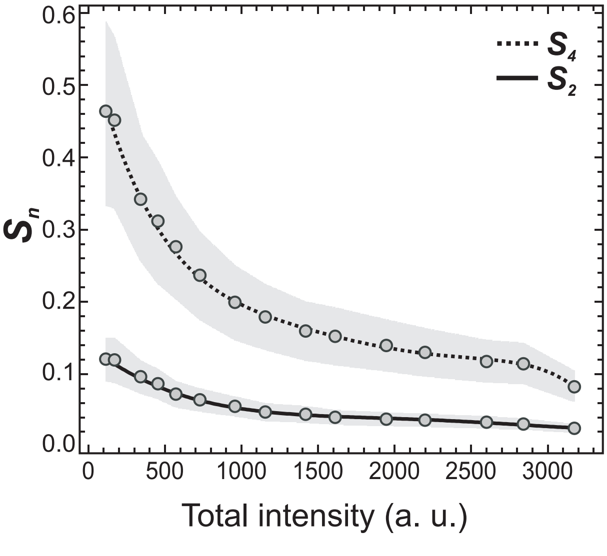

Figure 2.9: (***a***) S_2 and S_4 dependence on the CARS intensity signal (summed over 18 input polarization angles) in an isotropic medium. The shadowed regions denote the standard deviation of the S_2 and S_4 values.

2845 cm^{-1} and b) its isotropy which produces S_2 and S_4 magnitudes dependent only on the intensity level not the directionality (anisotropy) of the sample itself. We recorded PR data (α varying from 0° to 170°with a step of 10°) in epi-direction increasing the input powers for pump and Stokes beams simultaneously from 10 to 80 mW. Each measurement was then analyzed following the same methodology as previously described. To plot the final S_2 and S_4 curves only the small window (of $\approx 30 \times 30$ pixels out of 100×100 pixels of whole image) of the highest intensity values from the center of the Gaussian beam were taken into account.

As can be seen in Fig. 2.9, S_2 and S_4 parameters as well as their standard deviations decrease when the level of the intensity increases. The values are ranging from 0.12 ± 0.06 (lowest intensity) to 0.02 ± 0.01 (highest intensity) for S_2 and 0.47 ± 0.26 to 0.08 ± 0.04 for S_4, respectively. These results illustrate the level of signal needed to estimate the order parameters with a suitable quality. It is clear in particular that the total intensity CARS signal should surpass 1500 counts (note that ”count” means ”analog signal” here and in all further chapters) to reach a good estimation of order parameters with a variance no more than 0.02 for S_2 and 0.07 for S_4. In all our experiments the CARS intensity signal generated from the myelin fiber was easy discriminated from background in surrounding tissue with a good signal to noise ratio (Fig. 2.8b), however, S_2 and S_4 values were corrected for their bias according to the intensity measured for each pixel. This permits to retrieve S_2 and S_4 values not biased by noise.

2.3.4 Image processing

Drift correction of the PR stack of images

The direction of the excitation light beam passing through the rotating $\lambda/2$ waveplate can be progressively shifted when performing the PR measurement if not properly aligned. This shift, which introduces a systematic bias in the analysis can be corrected.

Inherent drift in polar stack images was estimated using fluorescent beads fixed on a coverslip before polarization measurements. The fluorescent beads are insensitive to polarization of excitation light. Therefore a drift in the centroid position of the beads in a polar stack gives us an estimate of the drift caused by the rotation of the $\lambda/2$ plate. The accuracy of this method depends on photon counts from each bead as well as number of beads used. Using more than 20 beads with high photon counts allowed us to estimate a drift of 150 nm in the (X,Y) direction. This drift was later subtracted from measurements.

2.4 Conclusion

In this chapter we have presented the two optical systems used in the studies. We have discussed how to deal with the polarization distortions imposed by the instrumental elements or by the sample itself. For instance, the polarization distortions introduced by the dichroic mirror which reflect the excitation polarized light can be resolved by placing the rotating $\lambda/2$ waveplate just before the objective. We have shown that the polarization distortions such as scattering introduced by the biological tissues can also be minimized by using an un-analyzed detection scheme. With this knowledge, in the following chapters we will apply the developed methods to image the molecular order in model systems as well as in real biological samples without ambiguities of the analyzed results.

Chapter 3

Lipid membranes

3.1 Lipids in biological membranes

In mammalian cells, one of the most important structural components are lipid membranes (Fig. 3.1a). Lipids in cell membranes constitute about 50% of the mass, nearly all of the rest being protein. Although a cell synthesizes over 1000 different lipids, most of them display common chemical properties having hydrophilic (*polar* head) and hydrophobic (*nonpolar* tail) portions. The tendency of the hydrophobic moieties to self associate and the hydrophilic moieties to interact with an aqueous environment and with each other, is the physical basis of the spontaneous formation of membranes. This amphipathic nature of lipids enables cells to segregate the internal constituents from the external environments and also, to produce discrete organelles, such as endoplasmic reticulum (ER), Golgi apparatus or transporting vesicles - lysosomes and endosomes (Fig. 3.1b). Besides the barrier function, lipids as a building material for membranes, are essential for budding, tubulation, fission and fusion, which are characteristic events in cell division, biological reproduction and intracellular membrane trafficking. Some of them, additionally, act as first and second messengers in signal transduction and molecular recognition processes.

3.1.1 The lipid composition of cell membrane

It is difficult to define the exact composition of lipids in the distinct membranes. This is essentially due to the limitation of the quantitative analysis to certain lipid classes, problems with the purity of distinct organelles and the high heterogeneity of cellular membranes (92). Nevertheless, the overall difference in cell membrane composition has been estimated. The major structural lipids in eukaryotic membranes are the glycerophos-

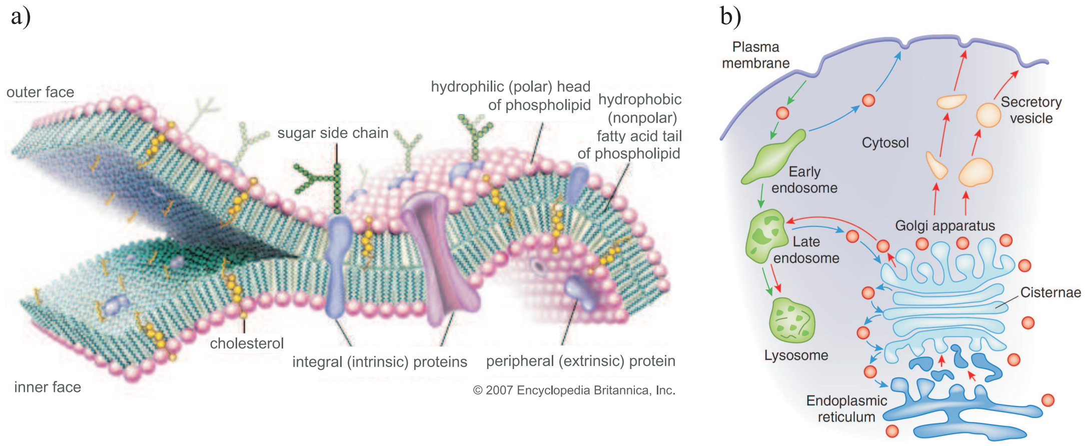

© 2007 Encyclopedia Britannica, Inc.

Figure 3.1: (***a***) A schematic fluid mosaic of the cell membrane (***a***) consisting of proteins which are intercalated with the lipid bilayer. (***b***) The architecture of discrete organelles and a complex trafficking inside a cell (Adapted from (91)).

pholipids, within which the phosphotidylcholine (PC) accounts for more than 50%, phosphatidylethanolamine (PE) about 20%, phosphatidylserine (PS) and phosphatidylinositol (PI) below 20% (Fig. 3.2). Secondary lipids, but of the same importance, are sphingolipids (sphingomyelin (SM)), glycosphingolipids (glucosylceramide (GlcCer)) and non-polar sterols (cholesterol). Alone, they have a role in participating in stabilization and the physical state of the membrane. These different lipid species are not distributed homogeneously within a cell (93). The main determinant of the unique composition of organelles is the local lipid metabolism and the function of specific lipid membranes (see below).

3.1.2 The organization of the cell membrane

According to the fluid mosaic model of Singer and Nicolson in 1972 (94, 95), the biological membranes are considered as a double bilayer of lipids constituting a fluid in which proteins are anchored in between lipids (Fig. 3.1a). Both lipids and proteins interact with each other by non-covalent interactions and are in constant motion rotating and diffusing along or across the membrane. Lipids in most membranes display an asymmetric distribution, which means that the two sides of membrane are not identical. This has an important functional consequence. For example, phosphatidylserine (PS) acts as a signal for apoptosis and blood coagulation, when is placed on the cell surface. Its translocation to the cytosolic leaflet results in the membrane bending, which is required for vesicle

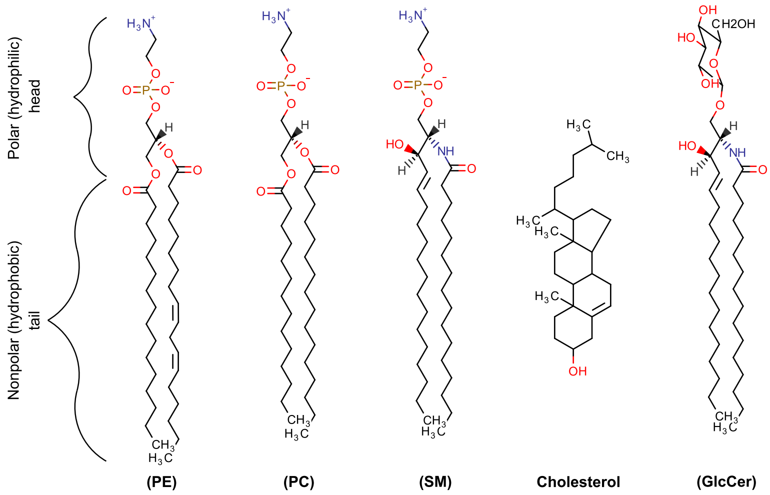

Figure 3.2: The chemical structure of main lipid molecules in biological membranes.

budding (96).

The lateral organization of membranes is closely related to the physical properties of lipids which can occur in different phases depending on their structure and environment. These phases by definition affect the membrane functionality. Lipids in membranes can adopt various fluid and solid phases, which are characterized by several factors such as fluidity, thickness and lipid packing, as shown in Fig. 3.3a. Physiochemical parameters such as temperature, pH, ionic strength, the chemical structure or the presence of cholesterol strongly influence the state of the lamellar phase. Fluidity is promoted by short, unsaturated fatty acids, which reflects the lower packing density of the acyl chains and a rather thin bilayer, as can be seen in the liquid-disordered (L_d) phase. High level of packing and increased thickness present in the solid-ordered or gel (S_o) phase is found in lipids with saturated acyl chains and small head groups. The incorporation of cholesterol to the membrane results in the formation of the so called liquid-ordered (L_o) phase which partly shares some characteristics of S_o and L_d phases (see Fig. 3.3a). This results in the existence of a state where lipids are tightly packed and ordered and at the same time able to diffuse almost as fast as in the L_d phase (98). In membranes, cholesterol has an important role prohibiting the saturated hydrocarbon chains to form crystalline structures making the membrane more fluid (99). Typically, in membranes with no cholesterol, phospholipids pair a saturated with an unsaturated fatty acids leading to the formation

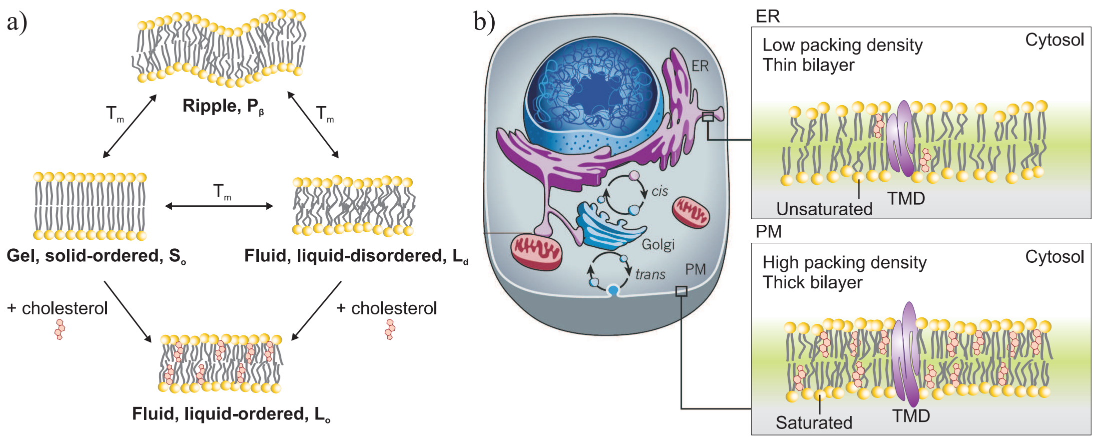

Figure 3.3: (***a***) Lipid phases in membranes. T_m is the main phase transition temperature of a lipid. (***b***) Membranes in different cell organelles have contrasting lipid composition and physical properties (Adapted from ref. (97)).

of ripple phases (P_β), which inhibit transition from L_d to S_o phase (93, 100, 101).

The local function of membranes is the first determinant of the spatial organization of lipids. For example, ER as the main site of structural phospholipids and cholesterol synthesis is responsible for the insertion and a rapid transportation of newly synthesized lipids and proteins to other cell compartments. For this purpose, ER possesses thin and loosely packed membranes (Fig. 3.3b, upper panel). On the other hand, the plasma membrane (PM), as an indispensable barrier protecting and delimiting a cell from the environment, is enriched in phospholipids, cholesterol and sphingolipids, which are tightly packed at high density enabling a cell to resist a mechanical stress. This contrasting behavior is also reflected in the geometry of transmembrane domains (TMDs) of ER and PM, as shown in Fig. 3.3b (93, 97). As a consequence, probing the organization of lipids within the cell and its organelles can deliver an important information about the metabolism of lipids which is closely related to their packing coefficient.

The lateral organization of lipids is highly heterogeneous (104, 105). The equilibrium of cell membrane is constantly disturbed by enzyme activities, membrane recycling and signaling events. Such a dynamical change might create heterogeneity and generate small *domains*. Different protein and lipid features, lipid-protein interactions, protein-protein contact are the main factors of the formation of separated lipid-protein domains. The immiscibility of certain lipids and the preference of a given lipid to a certain protein result in the formation of domains which are highly heterogeneous in size ranging from

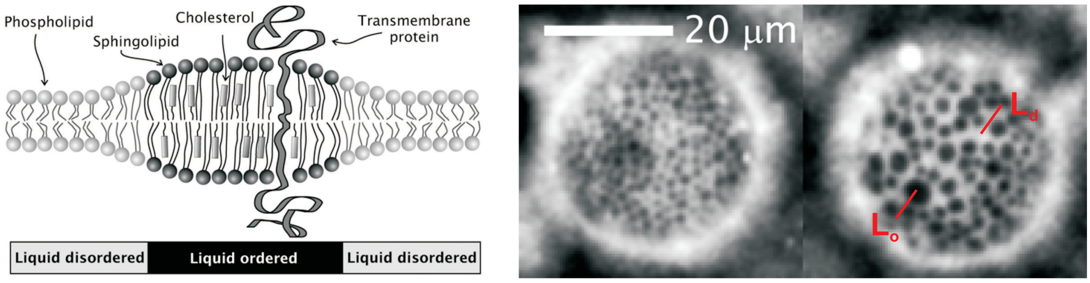

Figure 3.4: Left: Schematic view of the lipid domain separation. Right: Dynamic nature of domains: two sizes on the same phase separated vesicle (two sides) imaged by fluorescence (Adapted from (102, 103)).

less than 100 nm to microns, as shown in Fig. 3.4 (105–107). A special sort of domain called *membrane rafts* were proposed to be small in size (10-200 nm) and *transient* domains, heterogeneous and enriched in sphingolipids and cholesterol (108). These domains are believed to be highly dynamic participating in many cellular functions. Although it is generally accepted that lipid and protein diversity and their local structural dynamics generate a high level of heterogeneity in cell membrane, understanding the molecular organization and its effects on the cell function still remains a challenge (109).

3.2 Model membranes to study the lipid organization and dynamics

As were described above the cellular plasma membrane is a highly complex and dynamic structure that makes fundamental investigations of lipid structural behaviors troublesome. For this reason, a great number of studies from domain formation to membrane fusion were performed using biomimicking model membranes. A main advantage of model membranes is the ability to control the molecular composition, size and geometry and thereby the complexity of the membrane. In principle, it is possible to design any kind of a model membrane suitable to the purpose of the study (110). However, artificial membranes have an important limitation. While the cellular membrane is a dynamic system where the flux of both lipids and proteins occurs constantly, the artificial membranes, as isolated systems, even if very well controlled are unable to fully mimic the natural cellular machines. On the other hand, by using model membrane, bilayers or monolayers, it is possible to probe the physiology and structural transformation of lipids with the detection of a single protein anchored or not within bilayers (111–113).

3.2.1 Different approaches to study the lipid architecture and dynamics

During last two decades, a myriad of techniques have been developed to study the behavior of lipids in membranes, addressing various aspects such as the ordering of lipid molecules assembly as well as their structural and conformational properties (114). In this section we will outline only few of them.
On the atomic scale, techniques such as nuclear magnetic resonance (NMR) (115, 116) and X-ray diffraction (117–119) are able to deliver quantitative information such as the geometric volume of lipid molecules in a stack of bilayers, the spacing between lamellas, head to head separation, their density profile, unit cell constants, elasticity and the interaction between bilayers. Although a detailed amount of information on the bilayer and lipid structure can be obtained, these techniques, however, are highly invasive for the sample itself and cannot be applied to dynamical studies.

Methods based on fluorescence, such as One- and Multiphoton Fluorescence Microscopy (51, 52, 74, 120), fluorescence recovery after photobleaching (FRAP) (121), fluorescence correlation spectroscopy (FCS) (122), fluorescence resonant energy transfer (FRET) (123), spectrally sensitive fluorescence imaging (124), internal reflection fluorescence (TIRF) (125) and PR fluorescent imaging (50, 51, 66) have been particularly used to understand the lipid membrane assembly and their dynamics (126). For example, the use of PR-Two-Photon Fluorescence (2PEF) allowed to quantitatively image the local lipid disorder in model membranes, giant unilamellar vesicles (GUV), determining the molecular distribution orientation of several lipid probes in both L_d and L_o phases (Fig. 3.5a) (52). The approach has been also applied in living cells, using confocal epifluorescence microscopy, where authors were studying the molecular organization of cell membrane and its modification upon the cytoskeleton perturbation (Fig. 3.5b) (51). These techniques, although very powerful, require the use of fluorescence dyes inserted into the plasma membrane, but the effect of these molecules on lipids and *vice versa* is not known. In other fluorescence methods, such as FCS, FRAP or FRET, labelling of lipids may lead to significant changes in their molecular shape and physicochemical properties and therefore influence lipid spatial distribution, lipid dynamics, and functioning of the membrane.

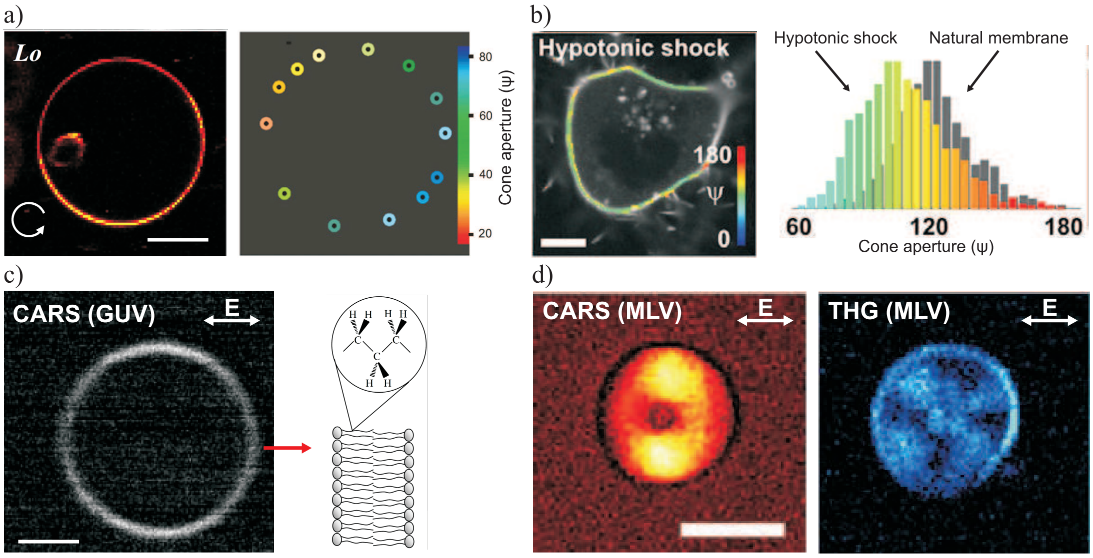

Figure 3.5: (***a***) PR-2PEF image of L_o phase in a C-Laurdan labelled GUV showing the spatial distribution of the angular aperture ψ explored by the lipid probe. The average cone aperture of C-Laurdan in L_o domains is $\approx 33 \pm 6°$. Scale bar: 8 μm. (***b***) PR-1PEF image of COS7 cells (normal membrane and after hypotonic shock provoked by adding water) with a color code indicating the value of the width ψ of the angular distribution. Scale bar: 10 μm. (***c***) Forward CARS image of an erythrocyte ghost at a Raman shift of 2845^{-1} (CH_2 stretching mode) and horizontal polarization. Scale bar: 2 μm. (***d***) PR-CARS (CH_2 stretching mode) and PR-THG on a multilamellar vesicle (MLV) using the horizontal polarization. Scale bar: 15 μm. (Adapted from (23, 49, 51, 52),respectively).

Conventional infrared and Raman spectroscopy and microscopy techniques, providing label-free contrasts based on specific vibrational signatures of chemical bonds, are the standard analytical tool to investigate the structural and conformational changes of lipid molecules and their orientational packing in membranes (73, 127–129). However, main drawbacks such as the poor spectral resolution and low efficiency requiring a long acquisition time, even if partially resolved (130), preclude these techniques for *in vivo* imaging.

The use of coherent nonlinear techniques overcome these issues. By taking advantage of the high density of CH bonds in lipids, the resonant CARS and SRS allow for direct visualization of the lipid assemblies and their organization in model as well as in biological membranes such as the myelin. The PR Coherent Raman Scattering (CRS) microscopy has been applied to investigate the lipid chain order of mono-, bi- (23, 44, 60) and multibilayers (45, 77, 131) (Fig. 3.5c and d). The data show the strong polarization sensitivity of these methods with a more favorable coupling in the direction of the CH_2 oscillators. Imaging of cellular lipid membrane by CRS is not yet leading to high contrast however, due to the low number of CH_2 vibrations in the membrane compared to all other intercellular sources of signal for the similar wavenumber. Detection of a single bilayer has been thus possible after the lipids extraction from the cell membrane and reassembling them again in bilayers (Fig. 3.5c) (23). Therefore, the use of model systems give an access to investigate the lipid packing within a bilayer with a label-free manner. The PR-third harmonic generation (THG), which is sensitive to interfaces, has been also applied to quantify molecular order in multilamellar vesicles (Fig. 3.5d) and skin tissues (49). The fact that the nonlinear THG signal does not involve any specific resonance, but is generated at interfaces, however complicates the data interpretation and limits its applications.

All demonstrations performed so far on lipid order measured by PR microscopy generally rely on rather simplified models of lipids orientational order (Gaussian distribution) and require the knowledge of the lipid or CH_2 stretching mode nonlinear susceptibility tensor. Recent studies have however demonstrated that a more detailed investigation of PR-CARS, PR-SRS or PR-FWM signals shows that information of lipids order can be retrieved without *a priori* knowledge on their angular distribution (65, 71). The approach relies on the decomposition of the molecular PR response into symmetry orders of their angular distributions, as has been detailed in Chapter 1. In particular, the high order of nonlinear interaction in SRS/CARS/FWM makes them sensitive to molecular angular distribution features up to the fourth order of symmetry (53, 59, 85), manifesting clearly the potential of PR third order processes to approach complex molecular organizations coupled with their functional information.

3.2.2 Multilamellar vesicles

Probably the most practiced and applied model lipid membrane are the GUVs (132). Although GUVs are powerful systems mimicking lipid membranes in a very simple way, their thin (≈ 5 nm) bilayers generate a low amount of signal that make them difficult to study by available imaging or spectroscopic techniques. In particular PR measurements necessitate so far stable and efficient sample to address the feasibility of the technique. Therefore, there is a growing interest towards using different models such as the multilamellar vesicles (MLVs), which can amplify the signal by 3 orders of magnitude thanks to higher densities (117). Moreover, it has been shown by Nagle and Tristram-Nagle (117) that interactions between bilayers in fully hydrated MLVs have negligible effect on the intrinsic structure of the bilayer, which might be the first concern when dealing with MLVs.

Multilamellar vesicles consist of multiple bilayers of lipids with the aqueous solution trapped in between, as shown in Fig. 3.6a. The bilayer thickness varies linearly with an acyl chain length and ranges between 4 to 5 nm with the spacing between layers from 1.5 to 3 nm (117). The average area occupied by a single lipid ranges between 0.4 to 0.7 nm of diameter. The order and fluidity of an assembly of lipids originates from their interactions, such as van der Waals and steric constraints. Most of mono-unsaturated lipids in biomembranes has a *cis* configuration which by introducing the "kinks" in their fatty acid chains by a double bond influence the molecular packing decreasing the order and increasing the fluidity (Fig. 3.6b and Fig. 3.3a). In comparison, the *trans* configured lipids resembling the unsaturated ones are supposed to be highly ordered and less fluid (Fig. 3.6b). The degree of saturation also affects the phase in which lipids exist as has been discussed in Section 3.1. The lipid molecule itself is not a fixed entity, but continuously fluctuates in time and space, finding its energy-free position among its neighbors (Fig. 3.6c).

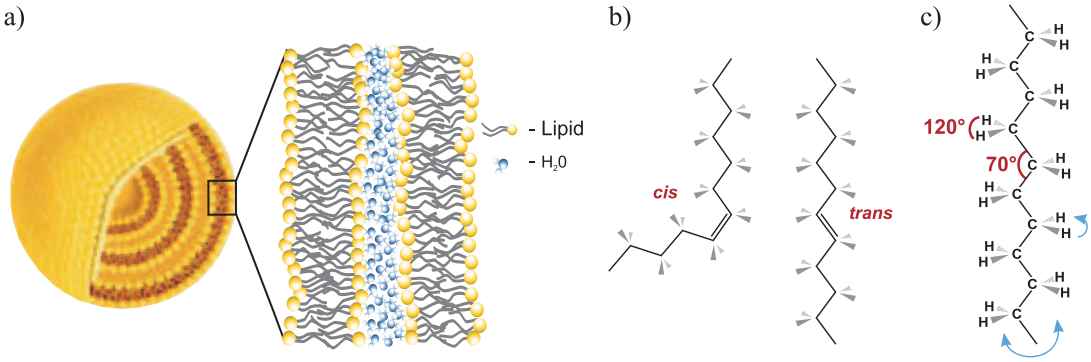

Figure 3.6: (***a***) The structure of a multilamellar vesicle. (***b***) Possible configuration of a hydrocarbon chain of a lipid. (***c***) Atomic structure of a hydrocarbon chain showing important angles between atoms and possible rotations of the molecule (blue arrows).

3.3 Conclusion

In this chapter we have presented the basic knowledge on the cell membrane, its functionality and dynamics in the context of the lipids organization and their thermodynamic properties. We have discussed that it is evidently challenging to investigate the complexity of the lipid membrane in cells and that is why simple model systems found a large interest.

Comparison between different methods have driven us to the conclusion that noninvasive vibrational methods such as CARS and SRS are indeed suitable to probe the behavior of lipids in membranes with a high level of details.

In the following chapter we will show the capacity of the method developed in Chapter 1 to probe the behavior in lipids membranes. We will demonstrate for instance the influence of the saturation of lipid chains on the molecular packing as well as the effect of cholesterol inserted between lipid bilayers.

So far, the fluorescence techniques are widely used to study the organization or thermodynamical state of lipids in membranes. However, lipids itself do not produce any fluorescence and therefore fluorescent dyes need to be inserted into the membrane to address these issues. The influence of these dyes on the lipids organization is not well understood (133). In order to evaluate the effect of molecules on lipids and lipids on molecules, in the next chapter we will compare vibrational label-free (CARS and SRS) and fluorescence (2PEF) contrasts using PR imaging.

Chapter 4

Molecular order of lipids in membranes probed by nonlinear polarized microscopy

In this chapter we will apply the PR nonlinear contrasts to investigate the molecular organization of various lipids and fluorescent dyes in artificial membranes using the method presented in Chapter 1. First, after a description of the studied samples, we will describe the difference in the retrieved molecular order information by the nonlinear contrasts such as CARS and FWM, SRS and 2PEF. We will demonstrate the capacity of the femtosecond laser source to probe the molecular order with high precision, similar to the picosecond system. The second part of the experimental results will be focused on the detailed structural investigations of the lipid assemblies. We will demonstrate for instance the influence of the saturation of the lipid chains as well as the effect of cholesterol inserted between lipid bilayers on the molecular packing. In the next step, by comparison of vibrational label free (CARS and SRS) and fluorescence (2PEF) polarization response from a multilamellar vesicle, we will evaluate the effect of fluorescent dyes on lipids and of lipids on these dyes in the context of the molecular packing. In the perspectives we will present our preliminary PR-SRS result obtained on a COS7 cell.

4.1 Samples and their preparation

4.1.1 Multilamellar vesicles

Lipids characteristics

In order to investigate the molecular order of lipids in membranes we choose structurally similar phospholipids, which as an assembly exhibit different phases at room temperature (T=21 ± 1°C). The characteristics of these phospholipids are summarized in Table 4.1.1. In following studies we used phospholipids: 1,2-dipalmitoyl phosphatidylcholine (DPPC), chain-perdeuterated 1,2-dipalmitoyl-d62-*sn*-glycero-3-phosphocholine (DPPC-d62), dioleoylphosphatidylcholine (DOPC), 1,2-dimyristoyl-*sn*-glycero-3-phosphocholine (DMPC) and the cholesterol molecule. All phospholipids occupy an area ranging between 0.4 to 0.7 nm^2. This area depends on the phase, which the lipids adopt and on the degree of saturation, for instance DOPC exhibits the biggest area because of the "kink" generated by a single double-bound in the acyl chain which additionally increases a fluidity of the membrane (see Chapter 3, Section 3.2.2).

All phospholipids and cholesterol were purchased from Avanti Polar Lipids, stored in -20°C and used without further purification.

Table 4.1: Characteristics of phospholipids used in the study.

Name	Structure	T_m (°C)	Phase^a	A (Å^2)^b
DMPC (14 : 0)	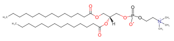	23.6^c	L_d/S_o	59.6 (30°C)
DPPC (16 : 0)	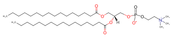	41.3^c	S_o	47.9 (20°C)
DPPC-d62 (16 : 0-d62)	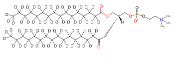	37^d	S_o	-
DOPC (18 : 1c9)	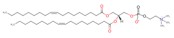	-17^c	L_d	72.5 (30°C)

^{a}The phase at T=21 ± 1°C.

^{b}The average interfacial area per lipid molecule according to ref. (117).

^{c}The temperature according to Avanti Polar Lipids, INC.

^{d}The temperature according to ref. (134).

Fluorophores characteristics

In order to investigate the organization of fluorescent dyes inside the lipid membrane and their effect on the molecular packing of lipid assembly, we choose two following lipophilic organic dyes which have been widely used in the (50, 66):

- di-8-ANEPPQ - 1-(3-sulfonatopropyl)-4-[beta [2-(di-n-octylamino)-6-naphtyl]vinyl] pyridinium betaine
- TMA-DPH - 1-(4-trimethyl ammonium-phenyl)-6-phenyl-1,3,5-hexatriene

Their structural and spectral characteristics are shown in Fig. 4.1. Three main criteria were mandatory for the selection that made us choose di-8-ANEPPQ and TMA-DPH: a) their high quantum yield and large nonlinear absorption cross section making these molecules suitable for two-photon excitation, b) the parallel orientation to the axis of the hydrocarbon chains of lipids inside the membrane, and c) partitioning into both L_d and S_o phases (see Chapter 3). Both fluorescent dyes have proven their ability to probe the organization of saturated and unsaturated lipids regardless the phase (52, 135). TMA-DPH was purchased from Sigma Aldrich and di-8-ANEPPQ from Invitrogen molecular probes.

Preparation of multilamellar vesicles

Multilamellar vesicles (MLVs) were prepared according to the hydration method developed by Bangham et al. (136). First, 100 μl of 10 mM solution of phospholipid, pure or mixed with either 10 mM solution of cholesterol to obtain the final concentration of 5% w/w or with 1 mM solution of the fluorescent probe to obtain the molecular ratio 1 : 1000,

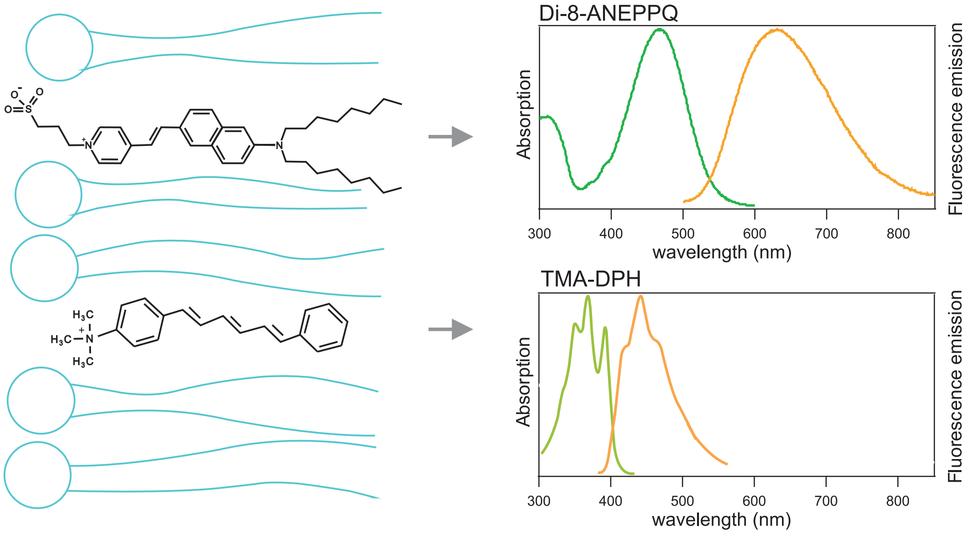

Figure 4.1: Structure of the fluorescent lipid probes and their schematic localization inside the membrane. Absorption and emission fluorescence spectra of di-8-ANEPPQ in MeOH solvent. Absorption and emission spectra of styryl dyes are at shorter wavelength in membrane environments than in reference solvents. The difference is typically 20 nm for absorption and 80 nm for emission, but varies considerably from one dye to another (Adapted from (137)). Absorption and emission spectra of TMA-DPH incorporated into lipid membrane (Adapted from (138)).

was immediately evaporated under a nitrogen stream and then vacuumed for 3 h. The dried phospholipid-cholesterol or phospholipid-fluorophore films were then hydrated (1 h) either in phosphate-buffered saline (PBS, pH 7.4) or in a pure water (miliQ) or in the case of DOPC lipids in 1% agarose in pure water (miliQ) above the main phase transition temperature (Table 4.1.1) gently shaking from time to time. The resulting MLVs were of different size ranging between 1 and 30 μm. For the experiments, a small amount of a suspension was placed between two coverslips separated by 100 μm spacers. In the case of DOPC this suspension was gently heated above the gelling temperature of agarose ($T=25 \pm 5°C$) in order to fix MLVs, preventing their motion.

4.1.2 COS7 cells

COS7 cells characteristics

The COS7 cell line are know as fibroblast-like cells and are mainly utilized in transfection experiments. Their capacity to strongly adhere to the surface makes them an ideal model for our study of membrane organization. Moreover, the COS7 cell line is easy to cultivate due to their low fragility and a high replicative capacity.

Preparation of COS7 cell line

COS-7 cells (American Type Culture Collection No. CRL-1657) were maintained in 37°C with DMEM medium (Lonza, Belgium) completed by 5% FBS, and penicillin-streptomycin (50 units/ml). Before measurement, cells were detached by trypsin and transferred onto glass cover slips, then incubated for 3.5 hour and washed twice with insertion buffer (NaCl 130 mM, KCl 5 mM, CaCl2 10 mM, glucose 5 mM, and HEPES 10 mM (pH 7.4)). COS7 cells were kept in the insertion buffer at room temperature for the whole imaging process.

4.2 Experimental parameters

As can be seen in Table 4.2 a few sets of polarization-resolved experiments were performed on two separate optical systems, the narrow-band picosecond and the broad-band femtosecond pulsed laser set-up (see Chapter 2).

Polarization resolved CARS/FWM/SRS using the ps system

For studies of the orientation of DPPC-d62 lipids in MLVs in the presence or absence of

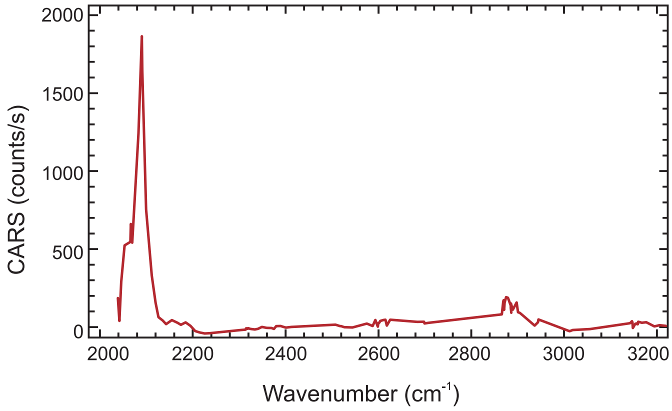

Figure 4.2: CARS spectrum on a MLV made of DPPC-d62 (ps/ps spectral tuning configuration).

cholesterol we choose to use the narrow-band picosecond pulsed laser set-up, which has been discussed in Chapter 2. Based on the CARS spectrum (Fig. 4.2) performed on a MLV made of pure DPPC-d62 different wavelengths configurations were used to address two spectral conditions: FWM centered at 2300 cm^{-1} and CARS centered at 2100 cm^{-1} for CD stretching vibrations (Table 4.2, Appendix B.1). The particularity of this vibration is an intense narrow line that makes the non-resonant contribution quite negligible in comparison. In contrast, pure DPPC exhibits a less intense CARS signal where the effect of the non-resonant background can be non-negligible in the polarization response (see ref.(77)). We therefore applied both CARS and SRS modalities in this case. In order to investigate the nature of polarization CARS and SRS responses we collected CARS and SRS spectral for each wavelength (from 2750 cm^{-1} to 3000 cm^{-1} with a step of 10 cm^{-1}) recording in the same time the polarization stack of images (from 0°to 170° with the polarization step of 10°) in MLV made of pure DPPC.

The image acquisition was done with a pixel dwell time of 50 μs, 100 × 100 pixels, scan range of 15 to 30 μm and typical powers at the focal spot of 5 to 15 mW. In this set of experiments an achromatic half wave plate rotating the excitation light was placed before the last Ag mirror. As has been discussed in Section 2.2 (Chapter 2) the reflection on the mirror can cause distortions in the linearly polarized light. These distortions were taken into account in the data analysis by calculation of the order parameters using the fitting method described in Section 2.3.2, Chapter 2. Moreover, for the CARS analysis, the S_2 and $S_4^{(s)}$ values were corrected for their intrinsic bias introduced for low intensity according to the analysis developed in Section 2.3.3, Chapter 2.

Combined polarization resolved CARS/SRS/2PEF using the fs system

We used the more broad band femtosecond pulsed laser set-up ("Main configuration") (Chapter 2) combining the three nonlinear contrasts, PR-CARS, PR-SRS and PR-2PEF, to investigate the molecular order of both lipids and fluorophores and their mutual orientational effect inside multilayered model membranes. The reason for this choice is governed by the fact that fs illumination provides higher signals, it is thus favored when no spectral resolution information is required. In all cases, optimal wavelengths configurations were chosen to probe lipid vibrations by CARS and SRS centered at 2845 cm^{-1} (this covers CH_2 symmetric and antisymmetric stretching vibrations as well as CH_3 vibrations) as well as fluorophores, di-8-ANEPPQ and TMA-DPH, by 2PEF on the same MLV *in the same time*. The difficulties of such a multimodal experiment come from the fact that all three collected signals need to be set at the optimum such that a) the combination of wavelengths excite both lipids and fluorophores in the same time, b) the peaks of emission wavelengths do not overlap and are well spectrally separated, and c) emitted signals are in the range of the maximal efficiency of collecting detectors.

All three conditions were fulfilled when performing experiments on MLVs made of DOPC or DPPC, pure or labelled with TMA-DPH fluorescent dye (Table 4.2). However, regarding the experiment on MLVs made of DMPC labelled with di-8-ANEPPQ fluorescent dye, we used the "Alternative configuration" due to the photodiode efficiency to collect the SRL signal moreover, emitting signals of CARS and 2PEF were spectrally overlapped and therefore requiring a different methodological step: 1) collection of PR-2PEF stack as first, 2) complete bleaching of the sample and 3) performing PR- CARS and SRS measurements. For the configurations of wavelengths as well as optical elements see Appendix B.2, B.3 and B.4.

In all cases the image acquisition was done with a pixel dwell time from 20 to 50μs, 100 × 100 pixels, scan range of 10 to 50 μm and typical powers at the focal spot of 2 to 10 mW. All PR data recorded on MLVs of 5 to 15μm big were performed at room temperature ($21 \pm 1^\circ$ C) using the polarization angles from 0° to 170° with a step of 10°. All data were treated using the approximate calculations (Chapter 2, Section 2.3.2) and for the CARS analysis, the S_2 and $S_4^{(s)}$ values were corrected for bias accounting for low intensity values according to the analysis developed in Section 2.3.3, Chapter 2.

Table 4.2: Experimental setting and configurations used in these studies.

Param	DPPC-d62	DPPC	DOPC	DMPC	ANEPPQ (ANP)	TMA-DPH (TMA)
Set-up	ps	ps/fs	fs	fs	fs	fs
Contrast	CARS^{R,a}; FWM^{NR,a}	CARS^{a}; FWM^{a}	CARS^{a}; FWM^{a}	CARS^{a,b}; FWM^{a,b}	2PEF^{b}	2PEF^{a}
Lipid composition	pure, cholesterol	pure, ANP, TMA	pure, TMA	pure, ANP	DPPC, DMPC	DPPC, DOPC
λ_p(nm)	735	735(ps); 780(fs); 800(fs)	780; 800	671	900	780
λ_S(nm)	869^{R}; 884^{NR}	931(ps); 1002(fs); 1036(fs)	1002; 1036	830	-	-
ν(cm^{-1})	2100^{R}; 2300^{NR}	2845	2845	2845	-	-
SRG/SRL	-	SRG(ps); SRG(fs)	SRG	SRL	-	-
λ_{TPEF}(nm)	-	-	-	-	≈ 600	≈ 470

[a] Forward un-analyzed detection.
[b] Backward un-analyzed detection.
[R] Resonant.
[NR] Nonresonant.

4.3 Experimental results: Nonlinear contrasts to probe the packing of lipids in MLVs

In this section we will investigate the nature of the molecular order that can be read by the various PR contrasts. We will highlight, in particular, the difference in the information that can be retrieved by PR- CARS and FWM. We will demonstrate that even if the non-resonant background can affect the PR data, its negative effect on the PR analysis can be treated as a systematic error. We will finally discuss the difference in molecular order information that can be retrieved using either the narrow band picosecond or the broad band femtosecond laser source.

4.3.1 PR-CARS response from a MLV using the femtosecond optical set-up

Fig. 4.3a shows the level of signal typically recorded in PR-CARS (centered at 2845 cm^{-1} of the CH$_2$ stretching vibrations) experiment on MLV made of pure DPPC lipid using the femtosecond optical set-up (see Appendix B.2 for specific configuration). The stack of images (summed over all polarization angles α) taken from the equatorial plane of the vesicle shows a high contrast with low intensity values from the surrounding background (approximate signal to noise ratio of 15). As illustrated in polar plots (Fig. 4.3b) obtained at different pixel locations, the polarization dependent intensities are strongly modulated in the vesicle as compared to a surrounding background. Such a modulation is a signature of greatly oriented nonlinear bond dipoles and is consistent with previous studies (23, 43–45) which showed that the CARS polarization response is mainly caused by CH molecular

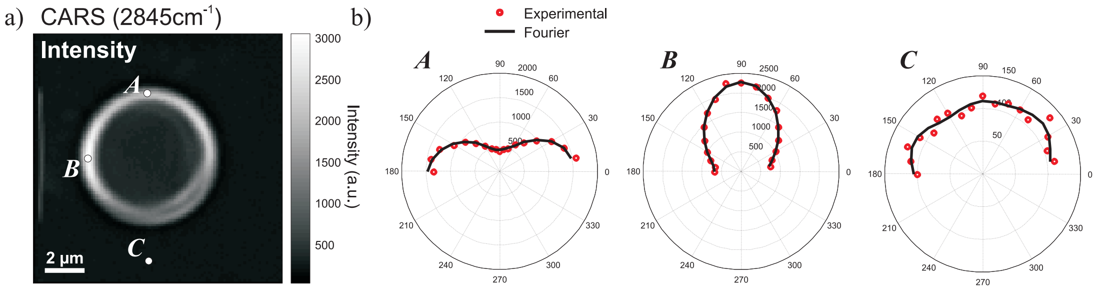

Figure 4.3: (***a***) PR-CARS intensity image of MLV made of pure DPPC lipid summed over all incident polarization angles α. (***b***) Polarization responses at three different pixel locations (**A**), (**B**) and (**C**) corresponding to the intensity CARS image in (***a***).

bonds. The surrounding background shows no polarization dependence, as expected from an isotropic medium.

We further quantify the molecular order based on the model described in Chapter 1.

Symmetry orders deduced from the PR-CARS measurement

The magnitude and the orientation of the symmetry orders (S_2, S_4) have been deduced using the approximate calculations as described in Chapter 2, Section 2.3.2. Fig. 4.4a-c depicts typical maps of (S_2, $S_4^{(s)}$, $S_4^{(a)}$) symmetry magnitudes. The CH molecular bonds display a large level of anisotropy which is manifested by the highly contrasted S_2 image. $S_4^{(s)}$ and $S_4^{(a)}$ magnitudes present low values appearing occasionally on the edge of the vesicular contour (where low intensity values induce a bias) which reveal a distribution function mainly smooth and unidirectional inside the vesicle. In all cases the signal from the surrounding background detected in the intensity image (Fig. 4.3a) is completely suppressed in S_2 and S_4 images, emphasizing the capability of the technique to discriminate organized structures from their isotropic environment. The φ_2 image in Fig. 4.4d shows the molecular distribution orientation of the CH bond dipoles which are found to be, on average, oriented azimuthally with respect to the MLV circular contour as expected from the lipid's geometry in a concentric arrangement. Note that all behaviors described here are reproducible from one MLV to another.

Finally, we relate S_2 and S_4 values to angular distributions of known shapes and increasing disorder σ. To do so, we applied a mask to the PR-CARS image, keeping all intensity contributions well above the background (inset in Fig. 4.4e, f). For each remaining pixel of the image, we plotted a 2D graph of $S_4^{(s)}$ as a function of S_2 and $S_4^{(a)}$ values as shown in Fig. 4.4e, f. The distribution of observed data points exhibits a high level of heterogeneity in the MLV which is not surprising when we consider the complex morphology of multilayers of lipids (see Fig. 3.6). However, a significant degree of order is found as compared to the surrounding background (dark blue data points in the Fig. 4.4e). The distribution of S_2 and $S_4^{(s)}$ values (0.43 ± 0.04 and 0.07 ± 0.07, respectively) fits well with a Gaussian function of width $\sigma \approx 70°$ superimposed with 25%-contribution of an isotropic population on average. This isotropic population could come from the high degree of disorder present inside the multilamellar arrangement. Nevertheless, the 70° of angular width for the ordered population is closed to what has been reported (45) in a different configuration (multiplex CARS), which makes the present measurement in qualitative agreement. Note that the analysis done in previous works (45) was based on the assumption of an *a priori*known distribution of lipids (pure Gaussian). In our work

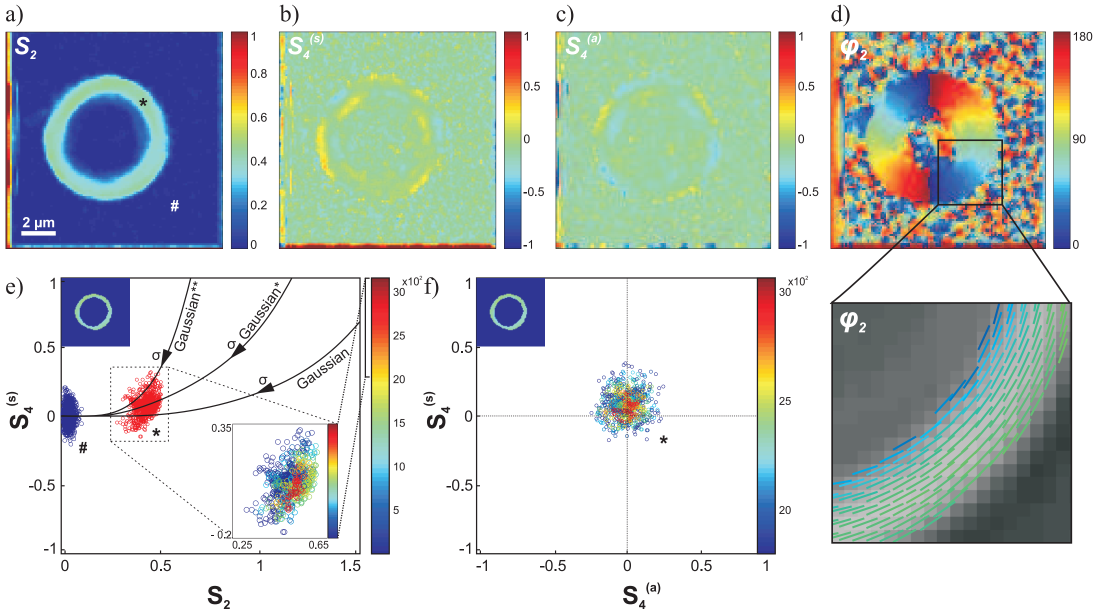

Figure 4.4: (***a***, ***b***, ***c***, ***d***) S_2, $S_4^{(s)}$, $S_4^{(a)}$ and φ_2 deduced images from PR-CARS (pure DPPC MLV) whose values were averaged over 9 pixels. Enlarged image of φ_2 in (***d***) shows the average orientation of CH bonds (illustrated by sticks) whose colors follow the S_2 colorscale. (***e***) Plot of S_2 versus $S_4^{(s)}$ experimental values for pixels taken within a vesicular contour ($*$) and pixels from surrounding background (#). The color indicates the intensity values. Inset (top-left): a mask applied to remove all the pixels in the intensity image from the surrounding background. Inset (bottom-right): Enlarged view of the data points distribution within the vesicle. Solid lines: theoretical (S_2, $S_4^{(s)}$) for a Gaussian function containing a 0%, 25% ($*$) or 50% ($**$) contribution from an isotropic population. (***f***) Plot of $S_4^{(a)}$ versus $S_4^{(s)}$ values for pixels within the vesicle.

the analysis of both S_2 and S_4 allows a more complete view of molecular order without the need to do any hypothesis on the distribution (see Chapter 1). At least, $S_4^{(a)}$ values in Fig. 4.4f are centered on zero, which is a signature of angular distribution of cylindrical symmetry, as expected from the arrangement of the CH molecular bonds in the MLV geometry. At this point, one can wonder if these values are underestimated due to a presence of a non-negligible non-resonant background. We will further discuss how this non-resonant background can affect the read-out of the symmetry orders.

4.3.2 PR-FWM and PR-CARS responses from a MLV using the picosecond optical set-up

In order to investigate how the non-resonant background can bias the polarization analysis in PR-CARS measurements, first we need to understand the nature of this non-resonant contribution. The non-resonant FWM process is highly sensitive to the orientation of the nonlinear electronic induced dipoles in the lipid membrane. If this background is well characterized, it does not necessarily has to be a drawback in PR measurements. To demonstrate this, a PR experiment has been performed on the MLV made of DPPC-d62 lipid using the picosecond optical set-up. As mentioned above, the CD_2 bonds here allows to discriminate better between pure resonant effect (here: CD_2 stretching vibrations) and pure non-resonant. Fig. 4.5 compares the PR response and the level of intensities for both non-resonant FWM (centered at 2300 cm^{-1}) and resonant CARS (centered at 2100 cm^{-1} of the CD_2 stretching vibrations) cases. While only one image per polarization angle α is sufficient to accomplish the high signal to noise ratio in the PR-CARS measurements, the need for averaging over 15 images per polarization angle α is required to obtain reliable

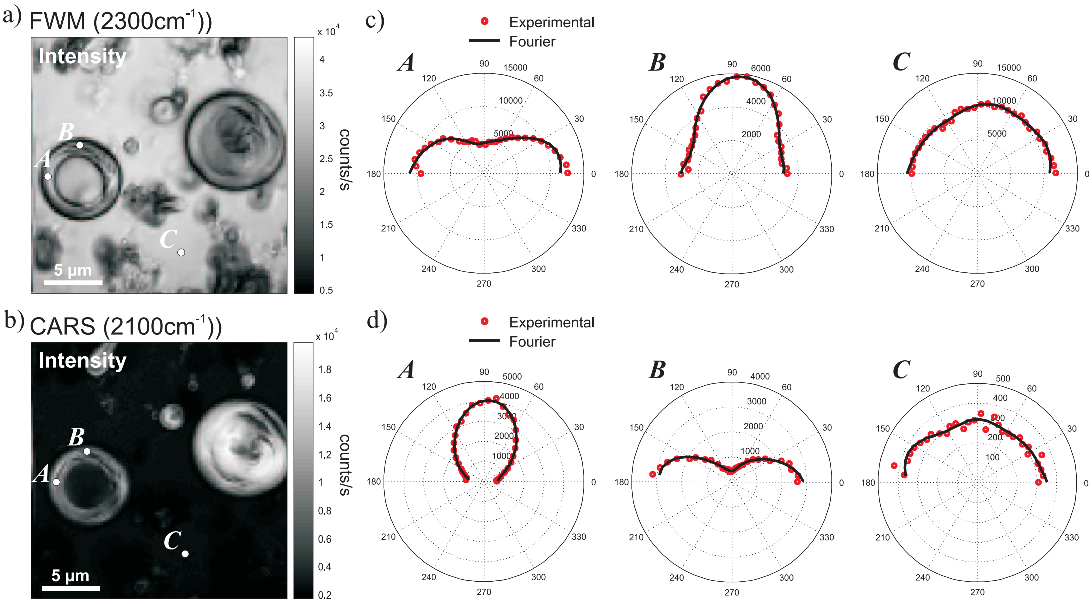

Figure 4.5: Comparison of the PR-FWM (***a***) and CARS (***b***) intensity images of MLVs made of DPPC-d62 lipid summed over all incident polarization angles. (***c***) and (***d***) Intensity modulation over all polarization angles α at three different pixel locations (**A**), (**B**) and (**C**) corresponding to images of FWM in (***a***) and CARS (***b***), respectively.

quality data in FWM. As expected the signal to noise ratio is significantly lower for the FMW ($\approx$ 0.7) than for the resonant case (ratio between 7 and 17). Such a significant difference demonstrates that the two processes CARS and FWM can be largely separated in the PR-analysis, when high intensities of CARS signal are generated.

Fig. 4.5c, d represent the plots of the modulation of the PR-FWM and PR-CARS signals (for comparison) at identical pixel positions of the equatorial plane of the MLV. We can notice the two opposite behaviors of the intensity response depending on the incident polarization α. The resonant PR-CARS contrast mainly originates from the vibrational CH (or in this case CD) molecular bonds as has been already discussed in the previous section. Off resonance rotates the maximum intensity by 90° showing that the polarization response is oriented parallel to the axis of the lipid chain geometry. Similarly as in the resonant CARS, in the non-resonant case the intensity modulation from the surrounding background shows no polarization dependence.

Symmetry orders deduced from the PR-FWM and PR-CARS measurements

Similarly as for the PR-CARS measurement we determined the magnitude and the orientation of the symmetry (S_2, S_4) distributions. The calculation of the order parameters is made using the fitting method (Chapter 2, Section 2.3.2) which encompasses the corrected values for the polarization distortions introduced by the reflective optics. The comparative results from the PR-FWM and PR-CARS are shown in Fig. 4.6. We report few important observations: 1) highly contrasted images of S_2 are visible for both resonant and non-resonant cases indicating the strong anisotropy in the equatorial plane of the MLV; 2) the surrounding background shows zero values for all cases; 3) the values of S_2 as well as the $S_4^{(s)}$ are, on average, lower for the non-resonant case; 4) in both cases the resonant CARS and the non-resonant FWM we observe the distribution function mainly unidirectional with the dominant S_2 values; and 4) in the non-resonant FWM, the φ_2 is changed to a radial orientation, showing that the nonlinear bond dipoles are, on average oriented along the acyl chain of lipid. This result is consistent with the fact that the electronic FWM response is along the longest chain of lipids. It has also indeed shown in the previous studies by Zimmerley et al. (49) that the strongest nonlinear coupling direction involved in the non-resonant third-order susceptibility of lipids is along the CC bonds. Our results fit well with this findings and later on we will demonstrate that the PR-FWM in also highly sensitive to a small changes in the organization of lipidic backbone imposed for instant by the cholesterol (Section 4.5.3).

Finally, the experimental S_2 and $S_4^{(s)}$ values are plotted in the Fig. 4.6c. Also in this

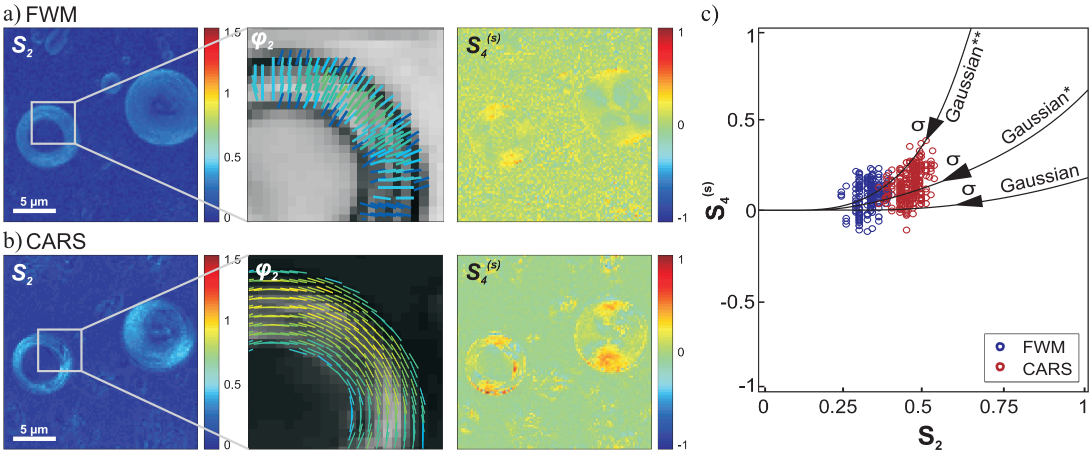

Figure 4.6: Comparison of the FWM (***a***) and CARS (***b***) deduced maps of the order parameters S_2, φ_2 and $S_4^{(s)}$, respectively. (***c***) Plot of S_2 versus $S_4^{(s)}$ values. Solid lines: theoretical (S_2, $S_4^{(s)}$) for a Gaussian function with 0%, 25% ($*$) or 50% ($**$) contribution from an isotropic population.

case the data fits well with a Gaussian distributions which contain 25% contribution from an isotropic population. The average S_2 values for the resonant CARS and the non-resonant FWM (0.46 ± 0.08, 0.33 ± 0.08, respectively) corresponds to Gaussian widths of $\sigma \approx 72°$ and $\sigma \approx 76°$, respectively. The lower order found for FWM can be explained by the larger set of directions taken by the electronic induced nonlinear dipoles in lipid molecules.

4.3.3 PR-SRS and PR-CARS responses from lipids in the MLV using the picosecond optical set-up

Our results show that the non-resonant background, when separated from its resonant case, displays a high level of sensitivity to retrieve molecular orientational information in lipid membranes. On the other hand, this non-resonant background intrinsic to the CARS signal will thus perturb the interpretation of polarized signals if the level of signals for non-resonant and resonant contributions are close (59). Only in the case when the high contrast is obtained on the considered resonance, its non-resonant contribution can be neglected. In order to estimate the bias that can be imposed on the order parameters we performed simultaneously PR-SRS measurements, which is known as 'the background free' contrast, and PR-CARS measurements on a single MLV, using the picosecond optical set-up.

Fig. 4.7 summarizes the result obtained from PR-SRS (centered at 2845 cm^{-1} of the CH$_2$ stretching vibrations) on the MLV made of pure DPPC lipid. The PR response obtained from the SRS signal reveals similar qualitative features as in the PR-CARS (Section 4.3.1). Strong anisotropy is seen in the equatorial plane of the vesicle with a dominant S_2 values. The image φ_2 shows again the same direction of CH molecular bond dipoles which are oriented tangentially with respect to the MLV circular contour. The plot of experimental distribution of (S_2, $S_4^{(s)}$, $S_4^{(a)}$) values is shown in the Fig. 4.7a, b. We compare the data points taken from the high intensity PR-SRS signal of the equatorial plane to the data obtained on the same vesicle by PR-CARS. First, PR-CARS data show values similar as those obtained in the fs regime (see Fig. 4.4), which shows that even though a fs pulse spectrally covers many modes, its average order is possibly dominated by a single stretching bond behavior. This point will be further discussed in Section 4.3.4. The values of S_2 in the plot of S_2 versus $S_4^{(s)}$ (Fig. 4.7b) for PR-CARS and PR-SRS are however different indicating that the non-resonant intrinsic contribution of PR-CARS most probably shifts S_2 towards lower values. We estimate that such a shift of S_2 values from ≈ 0.67 in the SRS analysis to ≈ 0.47 in the CARS analysis corresponds to a decrease of the estimated disorder σ by ≈ 11°. This shows that the interpretation of molecular order values should be considered with great care when non-resonant background is non-negligible. The $S_4^{(s)}$ and $S_4^{(a)}$ values (Fig. 4.7c) appear to be highly heterogeneous in

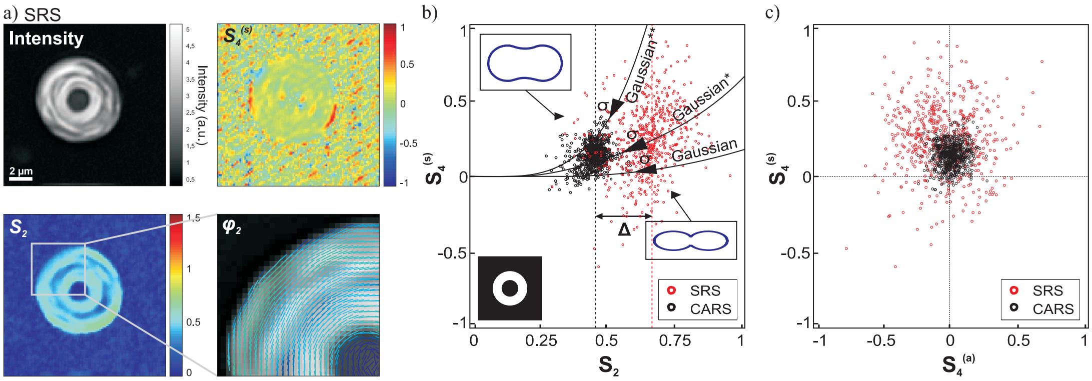

Figure 4.7: (***a***) PR-SRS intensity image summed over all polarization angles α and deduced maps of the order parameters $S_4^{(s)}$, S_2 and φ_2 (pure DPPC MLV). (***b***, ***c***) Plot of S_2 versus $S_4^{(s)}$ values (in black for CARS, in red for SRS) for each pixel of the image within a given mask (inset in the part ***b***) applied to remove all the pixels from the background. Solid lines: theoretical (S_2, $S_4^{(s)}$) for a Gaussian function with 0%, 25% ($*$) or 50% ($**$) contribution from an isotropic population.

the PR-CARS and even more in the PR-SRS case. This dispersion can be due to the heterogeneity of the MLV but also the noise of the measurement, especially in the SRS analysis. In both cases, however, the distribution of the experimental data can be fitted by the Gaussian distribution function containing 25% of contribution from an isotropic population (on average).

The distribution functions retrieved from the PR-SRS and PR-CARS experiments (insets in the Fig. 4.7b) show an obvious anisotropic shape along the CH_2 vibration bond axes with minor fourth order contribution. The difference in magnitudes of these distribution can be explain by a finer analysis of the nature of these two processes, in particular, by the spectral investigation around the lipid resonance, as will be described as follows.

Spectral behavior of PR-CARS and SRS

In order to study more precisely the incidence of spectral lipid bonds an PR data, a PR-CARS and PR-SRS analysis has been performed on the same MLV made of pure DPPC lipid in the whole 2750 cm^{-1} to 3000 cm^{-1} spectral region of the lipid vibrational resonance. The CARS and SRS spectra are shown in Fig. 4.8a. Three strong intensities are distinguishable with CARS and SRS: two bands around 2848 cm^{-1} and 2880 cm^{-1} corresponding to the symmetric and asymmetric CH_2 stretching vibrations and the band at 2935 cm^{-1} corresponding to the symmetric CH_3 stretching (139). A typical CARS spectrum is representative of a coherent superposition of a spectrally-independent non-resonant signal (around 30% of the maximum intensity), and a complex spectral resonance. Contrary to CARS, the SRS spectrum, as a background free process reproduces directly the shape of a lipid Raman spectrum (61).

Fig. 4.8b, c represent the spectral dependence of the order parameters deducted for each addressed wavenumber (ν) in PR- CARS and SRS measurement using the same methodology as previously described. The S_2 values of the PR-CARS signal reach two maxima around the symmetric and asymmetric CH_2 stretching ($\approx$ 0.4). These two values are the same therefore the angular distribution of CH_2 is identical for the two frequencies. The data analysis indeed report average behaviors over angular distributions of the lipids rather than differences between individual symmetries of vibration bonds. The decrease of S_2 in the intermediate spectral region between these two resonances is more difficult to interpret, mainly because the overlapped contribution of the neighboring spectral regions becomes non-negligible. The S_2 value at the CH_3 stretching mode is obviously lower than for the CH_2 stretching modes. The CH_3 group present only in the head and at the end of tail of the lipid is simply less oriented in the MLV. The values of S_2 for SRS show the

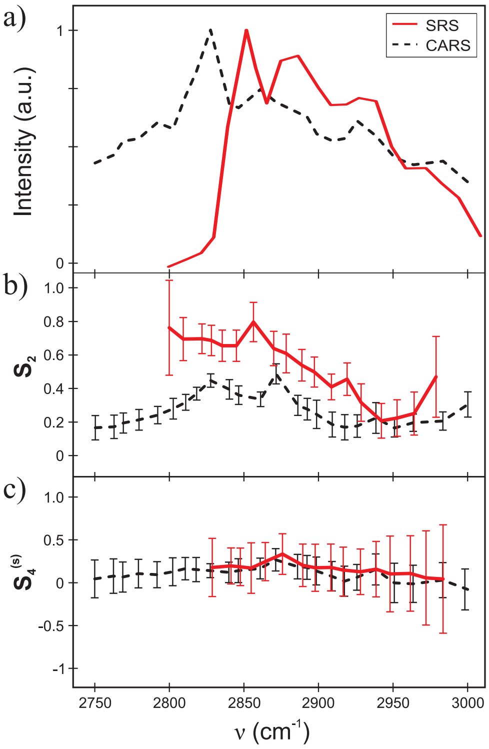

Figure 4.8: Comparison of the spectral behavior of PR -SRS and -CARS response. (***a***) SRS (red line) CARS (black dashed line) spectrum on the MLV made of DPPC lipid. (***b***) Deduced S_2 values as a function of the frequency for SRS (red line) and CARS (black dashed line). (***c***) Deduced $S_4^{(s)}$ values as a function of the frequency for SRS (red line) and CARS (black dashed line).

same behavior with higher S_2 values around ≈ 0.7 at the CH_2 stretching resonances (the analysis has been restricted to a frequency domain where the SRS signal was measurable). Similarly as for CARS, the CH_3 vibrational bond region shows a lower S_2 value. The $S_4^{(s)}$ values on the other hand do not surpass 0.25 for both CARS and SRS showing the absence of high order in the distribution function as discussed in Section 4.3.2.

In practice, over the whole spectrum an obvious difference is seen on S_2 values between CARS and SRS, which are systematically higher in the SRS operating mode. This discrepancy comes from the fact that the CARS analysis assumes no non-resonant background. The non-resonant part which is seen in the CARS intensity spectrum (Fig. 4.8) is indeed significant and can disturb the interpretation of the values obtained by the PR technique.

Impact of the non-resonant background in the PR-CARS measurement

In order to quantify the impact of the non-resonant background on the measured S_2 we developed a simple model which will be briefly discussed here (for details see ref. (77)). The total susceptibility tensor χ read by the CARS process is the sum of the resonant susceptibility (χ_R^3), which is read also by the SRS process, plus an unknown non-resonant contribution (χ^3_{NR}). While a resonant susceptibility χ^3_R is assumed to originate from an anisotropic distribution of dipoles for which $S_2^R = 0.7$ (as deduced by SRS measurement on MLVs, Fig. 4.7c) and $S_4^R = 0$, the non-resonant susceptibility is assumed to originate from various natures of symmetry orders, from totally isotropic ($S_2^{NR} = 0$) to highly organized ($S_2^{NR} = 0.7$), with $S_4^{NR} = 0$. These second orders are moreover assumed to lie perpendicularly to the resonant contributions ($\varphi_2^{NR} = \pi/2$), consistent with the fact that non-resonant signal comes mainly from electronic susceptibilities along the lipid tail, while the resonant CH$_2$ stretching bond orients perpendicularly to this tail (Fig. 4.5 and Fig. 4.6). The whole susceptibility tensor χ is then a sum of the resonant χ^R calculated using the eq 1.13 and a simulated non-resonant χ^3_{NR} part. The "effective" S_2^{eff} values are deduced for various strength of non-resonant with respect to resonant susceptibilities, and various symmetries of the non-resonant background as shown in Fig. 4.9. Clearly, S_2^{eff} decreases with an increasing strength of the non-resonant contribution and can indeed become close to an isotropic distribution ($S_2^{eff} = 0$) in the case where $S_2^R = S_2^{NR}$.

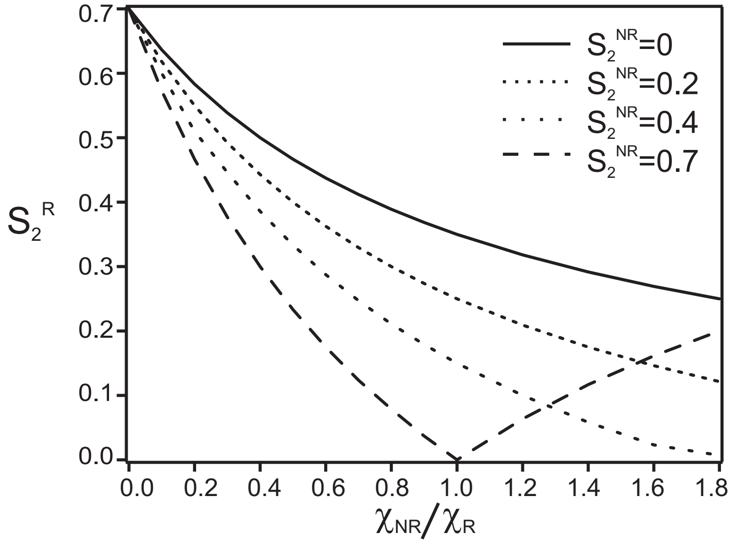

Figure 4.9: S_2^R as a function of the ratio between χ^3_{NR} and χ^3_R for different strength of S_2^{NR}. The χ^3_R is made with $S_2^R = 0.7$, $\varphi_2^R = 0°$ and $S_4^{(s)} = 0$. The χ^3_{NR} is made with different values of S_2^{NR} and with an orientation $\varphi_2^{NR} = 90°$. Calculations provided by P. Berto and J. Duboisset.

In our experimental results, the CARS non-resonant background intensity is seen to be about 30% of the maximum resonant intensity which corresponds roughly to $\chi^{NR}/\chi^R \approx \sqrt{0.3} \approx 0.55$. The S_2^{NR} values obtained on the similar MLVs by the FWM measurement (Fig. 4.6c) are within a range $[0.3 - 0.5]$. Supporting the assumption that φ_2^R and φ_2^{NR}

are perpendicular (the nonlinear susceptibility is dominated by CH and CC bonds, respectively), this would indeed result in the S_2^{eff} to lies within a range $[0.3 - 0.4]$, which corresponds to our experimental values (Fig. 4.7 and Fig. 4.8).

This analysis shows that molecular order values measured in PR-CARS imaging can be easily underestimated due to the existence of an intrinsic non-resonant background. Measuring a reliable orientational information can be nevertheless obtained providing that the resonant strength is large enough with respect to the non-resonant background (see Fig. 4.6). This issue does not occur in the case of SRS providing that other sources of artifact have been removed (140).

4.3.4 Ps vs. fs PR response from lipids in MLVs

In the previous sections we have demonstrated the importance of a high intensities to obtain reliable quality PR data with a minimum bias imposed on the order parameters. Here, we compare the molecular order information obtained from the PR-CRS measurements using the narrow band picosecond laser featuring a high spectral resolution and the broad band femtosecond optical set-up. Fig. 4.10 represent the distribution of the (S_2, $S_4^{(s)}$, $S_4^{(a)}$) symmetry order parameters obtained from the PR-CARS and PR-SRS measurements using the ps or the fs laser sources. Both processes are centered to target the CH stretching vibrations (2845 cm^{-1}) of DPPC lipid in MLVs. The experimental data points are taken from the MLV circular contour which keeps all intensity contributions well above the background (inset in Fig. 4.10a). Visibly, the S_2 values obtained in the PR-CARS measurements (Fig. 4.10a) using both the ps and the fs systems lie in the same range as mentioned above with negligible disparity $\Delta \approx 0.04$ (which corresponds to a difference in the disorder $\sigma \approx 2°$). However, the PR-SRS points out a difference in the deduced S_2 order parameter (Fig. 4.10b) in which values are underestimated with a larger difference $\Delta \approx 0.14$ ($\sigma \approx 9°$) between ps and fs regimes. Similar situation occurs in the $S_4^{(s)}$ values (Fig. 4.10c, d).

Such a discrepancy may come from the fact that the SRS process is not biased by the non-resonant background present in CARS technique and is therefore more sensitive to proximal resonances of lipid species which might have different orientational order. However, the SRS data points obtained with the ps system are much heterogeneous compared to the results deduced from the fs laser due to the higher level of noise. Nevertheless, all experimental values follow invariably the same distribution function (the Gaussian distribution with 25% contribution from an isotropic population) despite a different disorder

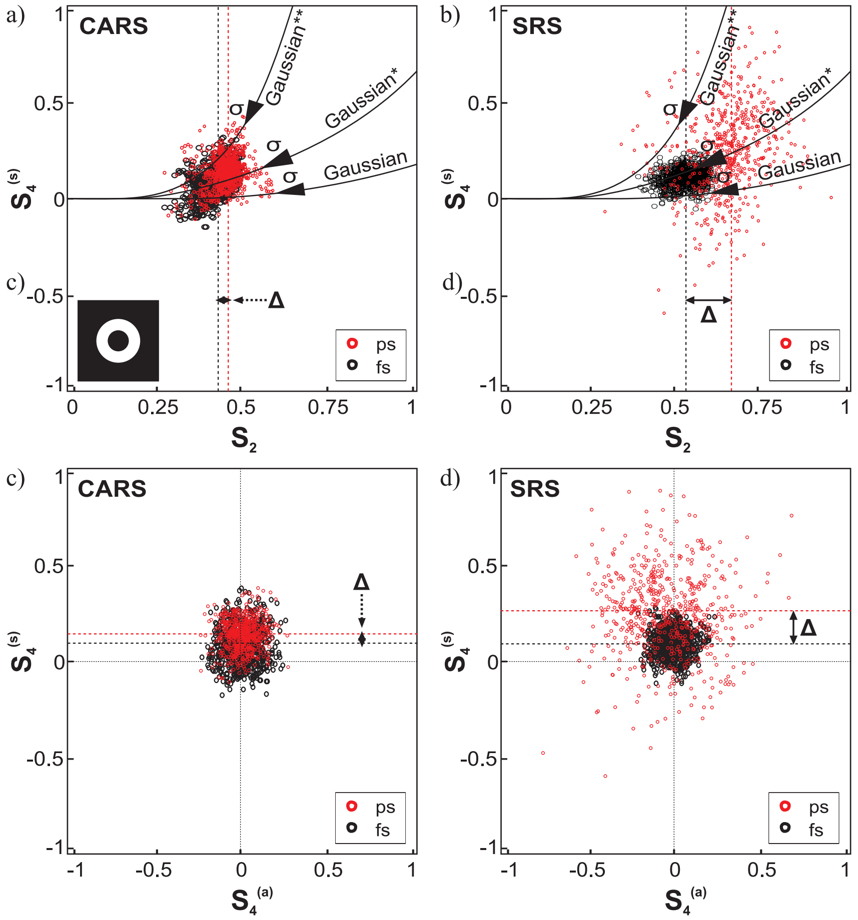

Figure 4.10: (***a***, ***c***) Plots of S_2 versus S_4 values (averaged over 9 pixel) deduced from the PR-CARS for the ps (red) and fs (black) systems. (***c***, ***d***) Identical plots as for PR-CARS. PR-CARS and SRS measurements were performed on the same MLV made of DPPC lipid for ps system. Equivalent measurements were performed using the fs system. Each value corresponds to a pixel of the image within a given mask (inset in the part ***a***) applied to remove all the pixels from the background. The data points are taken from the analysis shown in Fig. 4.7 and Fig. 4.4 for the ps and the fs system, respectively.

width σ. Moreover, we observe the error imposed on the (S_2, $S_4^{(s)}$) order parameters in the PR-CARS with respect to the PR-SRS analysis to be systematic with the approximate values of $[0.2; 0.03]$ using ps and $[0.1; 0.03]$ using fs laser source. This result has important consequences on future measurements: even though absolute values of molecular order cannot be reached using fs PR-SRS or PR-CARS, it can be used for relative measurements.

The ps system, although it features narrower bandwidth than the fs laser (and therefore takes full advantage of the chemical selectivity of the CARS imaging technique) requires high peak power to obtain a well contrasted PR data, which can more easily damage biological samples. In the situation when the high spectral resolution is not necessarily needed, the fs system will thus be employed to perform PR measurements.

4.3.5 PR-2PEF to probe lipid order in MLVs

Another way to probe the molecular organization relies on using fluorophores which are inserted in membranes and acts as orientational markers. Since this nonlinear process is largely used in many studies, in this section we compare it with the label-free techniques, CARS and SRS, in the context of the information that we can retrieve from the PR measurements. To do so, we performed simultaneously PR-CARS/SRS/2PEF experiments on a single MLV made of DPPC lipids and labelled with the TMA-DPH fluorescent dye. Results comparing these three nonlinear contrasts are shown in Fig. 4.11. Visibly, the intensity signal from the equatorial plane of the MLV for all nonlinear processes is well above the background. Note that we ascertain that the two-photon absorption process does not affect the SRS data (141): indeed results are the same before and after bleaching the fluorescence dye.

As expected, the images of deduced S_2 order parameter completely suppress the isotropic background surrounding the MLV. Different magnitudes of S_2 order parameter from the circular contour are observed depending on the contrast used, with the highest values for the 2PEF analysis which is discussed below. As has been already discussed before, deduced φ_2 images from SRS and CARS measurements show the azimuthal orientation of CH bonds with respect to the membrane contour (Fig. 4.11b and c, right panel). This situation is different in the 2PEF response. The maximum emission generated by fluorophores along the emission dipoles (μ^{em}) is oriented parallel to the lipid acyl chain axis and so perpendicular to the CH bond dipoles probed by SRS and CARS microscopy. This is expected from the way TMA-DPH inserts in the membrane (50, 52, 135).

The resulting distribution of order parameters taken from the membrane contour is

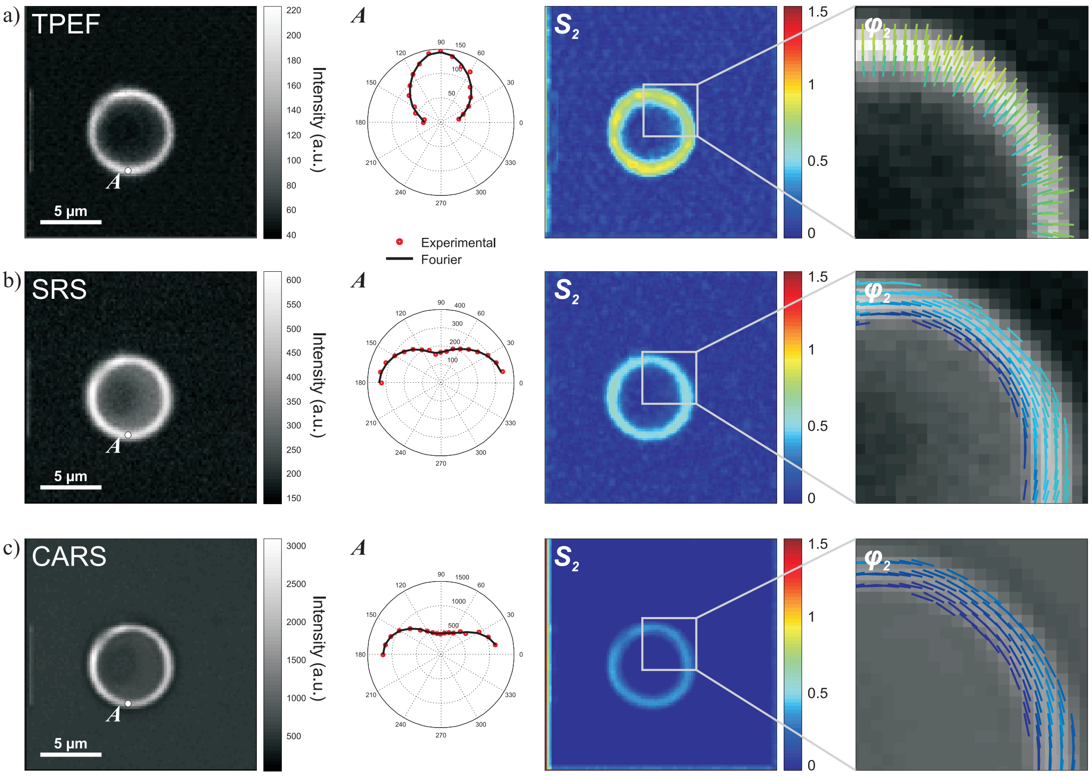

Figure 4.11: PR- 2PEF (***a***), SRS (***b***) and CARS (***c***) results performed on a single MLV made of DPPC lipid and labelled with fluorescent dye TMA-DPH. From the left: The intensity images summed over all polarization angles of electric fields; Intensity modulations taken at point A on the intensity images; deduced S_2 images; φ_2 images representing the orientation of nonlinear induced dipoles (SRS, CARS) or TMA-DPH (2PEF). For the S_2 and $S_4^{(s)}$ values see Fig. 4.12.

shown in Fig. 4.12. Clearly, there is a difference of the retrieved molecular order from CH bonds of lipids and TMA-DPH dyes, which seem to be more organized in comparison to the surrounding lipid assembly. While lipids still fit well with the Gaussian

distribution with a 25% contribution from an isotropic population ($\sigma \approx 73°$ for CARS and $\sigma \approx 67°$ for SRS), TMA-DPH dyes, even if highly heterogeneous, rather fit with a function in between the Gaussian and a cone - a smooth like cone ($\sigma \approx 57°$) with a non-negligible steepness ($a = 3$) (see Section 1.4.2). Indeed, the retrieved $S_4^{(s)}$ can reach non-negligible negative values that cannot be distributed to a smooth Gaussian function. The obtained results demonstrate that the retrieved molecular order information by the 2PEF is clearly distinct from that obtain by the label-free SRS (CARS is not considered as very quantitative here since it is known to provide an underestimated order as discussed above). It is not such a surprising result since these processes address different molecular dipoles. The fluorophore, TMA-DPH, embedded in lipid membranes seem to feature a lower angular freedom imposed by the surrounding lipids. This is not a case of CH molecular bonds of acyl chains probed by the SRS process, which by higher angular freedom reflect possible conformational changes of lipids in multilayers as well as the local lipids interactions. As a result, the significant difference in molecular order ($\sigma \approx 10°$) is seen here in the case of the 2PEF compared to the information probed by SRS. Such a disparity ($\Delta \approx 0.37$), contrary to the SRS and CARS, is an effect of related to lipid-lipid probe interactions which might depend on the nature of the lipid probe, and on the lipid composition, as we will see in Section 4.5.5. Therefore, a special care has to be taken when performing PR measurements by 2PEF microscopy. At last, one can notice that the measured order S_2 for the lipids is roughly the same as measured above *without* the TMA-DPH dye. This seems to indicate that at this lipid probe concentration the lipid order is not perturbed by the presence of the dyes. More refined studies on the lipid/lipid probe interactions are described in Section 4.5.6. Note that the SRS measurement seems to be not strongly affected by the two-photon absorption effect of the fluorescent lipid probes. Indeed when these probes are bleached, the measured lipid order is not modified.

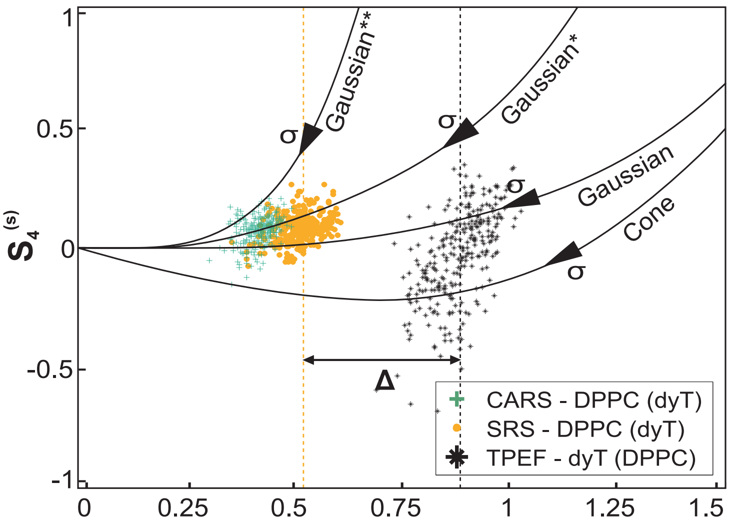

Figure 4.12: S_2 versus $S_4^{(s)}$ for PR-2PEF, CARS and SRS results obtained on a single MLV made of DPPC lipid and labelled with fluorescent dyes TMA-DPH. Solid lines: theoretical (S_2, $S_4^{(s)}$) for a Gaussian function with 0%, 25% ($*$) or 50% ($**$) contribution from an isotropic population and a smooth cone with a steepness $a \approx 3$.

4.4 Conclusion on the methodology

In conclusion, these data demonstrate that PR nonlinear techniques are highly sensitive to the molecular order in complex organizations. However, these techniques are not sensitive to the same degree of organization due to their intrinsic properties. We have shown that the non-resonant FWM process, often seen as ”unwanted guest”, when used properly, can deliver a rich information about the packing of molecules. On the other hand, being a part of the resonant case, can also bias the obtained orientational information when performing PR-CARS experiments. Nevertheless, such an artifact can be removed by using the PR-SRS microscopy. Moreover, it is possible to use either picosecond or femtosecond laser sources depending on the information and sensitivity we want to obtain. The background-free 2PEF contrast requires the use of fluorescent dye to probe lipids in membranes and therefore the information about the molecular order is retrieved indirectly. For this reason, we need to keep in mind that in the case of 2PEF we do not probe the lipids but the fluorescent dye embedded in lipid membrane which not necessarily reflects the behavior of lipids itself.

4.5 Experimental results: PR nonlinear microscopy: an insight into the fine organization of lipids

In this section we present the nonlinear contrasts, PR- 2PEF, SRS, CARS and FWM discussed in the context of their application to retrieve the detailed information about the molecular self-assembly of lipids depending on the morphology of studied model systems and the structural properties of lipids. We address the impact of cholesterol on the organization of lipids. Since the fluorescent molecules are widely use to probe the lipids we discuss their effect on the lipid membranes in this context.

4.5.1 The lipids packing in MLVs depends on their morphology

In order to get insight to the origin of heterogeneity of lipids packing in vesicles, we have investigated vesicles having different morphology. Based on the CARS images, beside MLVs with no intensity in their equatorial plane (denoted ”not-filled (NF)”) (like this shown in Fig. 4.5, left side of the intensity images), we also observed vesicles where high intensity signals from CH vibrations appeared inside (denoted ”filled (F)”) (Fig. 4.5, right side of the intensity images).

The comparison between the two kind of MLVs is shown in Fig. 4.13. The map of S_2 taken from PR-CARS (Fig. 4.13c) clearly shows a presence of two distinct populations in filled DPPC vesicles where lipids are highly organized on the rim and having an isotropic behavior resembling a bulk distribution inside. Moreover, as seen in the image of φ_2, CH molecular bonds have a well defined orientation on the edge following the membrane curvature. However, even in the region inside the MLV where the order is almost isotropic, the orientation φ_2 is not completely random and shows well determined direction that seems to indicate bending of the membrane at the macroscopic scale. In order to compare the organization of lipids of filled- to not filled vesicles we considered only pixels taken from their border in the equatorial planes (red dashed curve in Fig. 4.13a and b). The values of S_2 versus $S_4^{(s)}$ for both CARS and SRS (Fig. 4.13d) show distinct lipid organizations where the S_2 magnitude is visibly lower for the filled ($S_2 \approx 0.25$ for CARS and $S_2 \approx 0.29$ SRS) compare to not-filled vesicle ($S_2 \approx 0.41$ for CARS and $S_2 \approx 0.55$ for SRS). Both vesicle, filled and not filled follow the Gaussian distribution function with aperture σ around 83° and 72° for CARS and 80° and 65° for SRS, respectively. These data suggest that the organizations of lipids in vesicles and their spontaneous self-assembly is highly dependent on the morphology. It is not precluded that the multilayers interact with each other in the inner membranes and that this interaction has a larger scale effects on the lipid disorganization of the outer layers. For this reason, in the following studies we consider only the MLVs having similar morphology appearing as the not-filled (NF)" vesicles.

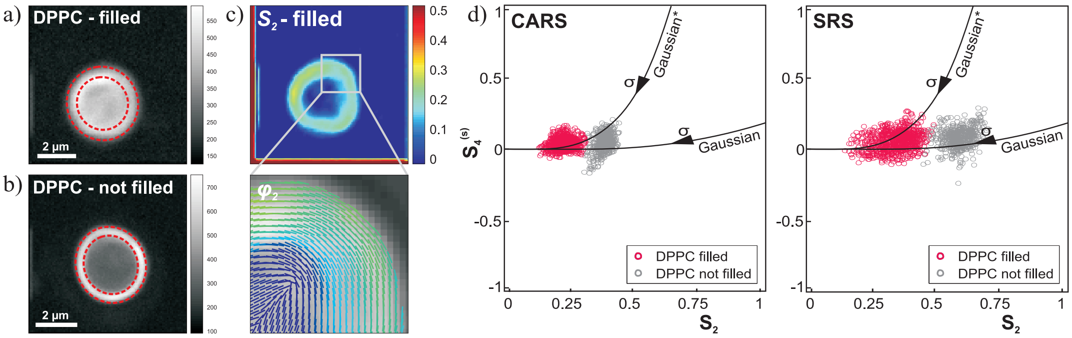

Figure 4.13: Comparison of molecular packing in two different MLVs, "not filled" and "filled" with lipids inside, both made of DPPC and probe by CARS and SRS. (***a***) and (***b***) The intensity images of "filled" and "not filled" MLV, respectively. (***c***) The S_2 map of "filled" vesicle and the φ_2 image of the overall orientation of CH bonds (below). (***d***) Graphs S_2 versus $S_4^{(s)}$ for CARS and SRS, respectively.

4.5.2 The effect of MLVs immobilization in an agarose gel on the polarization resolved analysis.

The PR analysis requires the sample to be stable over all measured excitation polarization angles in order to avoid any bias on the retrieved order parameters. However, sometimes it happens that MLVs made of the unsaturated ("light") lipids are not stable enough in their aqueous solution becoming highly mobile. In such a case MLVs need to be immobilized in some organic material, for instance the agarose gel, in order to prevent these movements. One could ask the question: does the immobilization of the MLV in an agarose gel affect the PR data?

Fig. 4.14 compares the data taken from an individual MLVs made of "light" DOPC lipid suspended in a pure water (Fig. 4.14a) or immobilized in agarose gel (Fig. 4.14b). Visibly, there is a strong heterogeneity on S_2 and $S_4^{(s)}$ values for MLV suspended in water. This highly spread distribution arise due to the movements of the MLV made of DOPC lipid, which is too light to stay in one position when performing a PR experiment (Fig. 4.14a). In comparison, no movements are observed in MLV immobilized in the agarose gel and therefore no distortion introduced on the order parameters as well as no negative general effect on the angular distribution (Fig. 4.14b). Note, that we did not

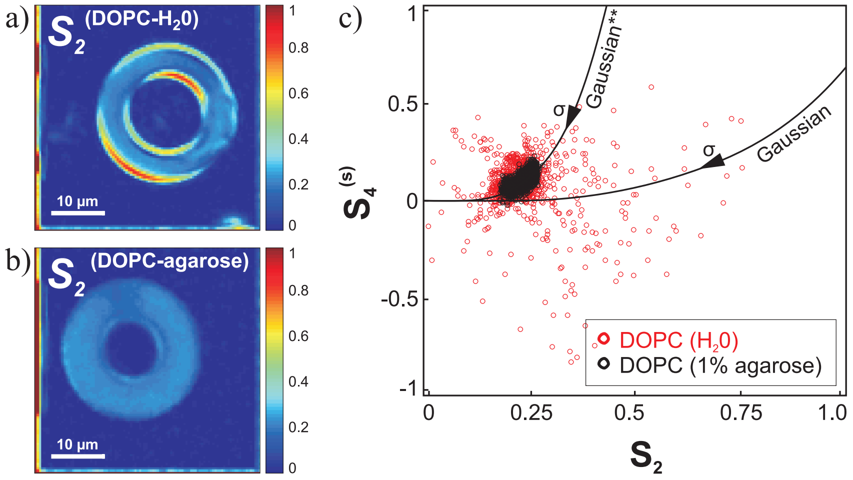

Figure 4.14: The maps of S_2 values deduced for MLVs made of DOPC lipid and suspended in a pure water (***a***) or immobilized in an agarose gel (***b***) imaged with PR-CARS. (***c***) Graph of deduced S_2 versus $S_4^{(s)}$ values for both MLVs showing distortions introduced be the mobility of the MLV suspended in water. Solid lines: theoretical (S_2, $S_4^{(s)}$) for a Gaussian function with 0% and 50% (**) contribution from an isotropic population.

observe such an effect in MLVs made of saturated lipids, which seems to be heavier than the unsaturated once.

4.5.3 The effect of cholesterol on the lipid packing in the MLV

Many studies has been dedicated to the cholesterol effects of the lipid organization (45, 142, 143). Here, we present a direct visualization of the organization of lipid membranes in the presence and the absence of the cholesterol using the PR- CARS and FWM microscopy in the ps experimental set-up.

We compare the organizational behavior of lipids in MLVs made of DPPC-d62, which at room temperature (21°) adopts the gel S_o phase. The results obtained by PR- CARS and FWM for MLV made of pure DPPC-d62 has been already discussed in Section 4.3.2. For MLVs made of DPPC-d62 lipid mixed with 5% (w/w) cholesterol the results of (S_2, $S_4^{(s)}$, $S_4^{(a)}$) are shown in Fig. 4.15. While the values of S_2 is dominant in the PR-CARS response, in the case of PR-FWM $S_4^{(s)}$ is seen to surpass S_2 in magnitude, emphasizing the presence of high frequencies in the angular distribution. These values, especially for S_4 are slightly underestimated due to the presence of birefringence in this sample (we did not observe a strong birefringence for MLVs made of pure DPPC-d62 lipid) (see Section 2.2.3). We, nevertheless, estimated the bias on the S_4 value to be no more than 0.05 in the

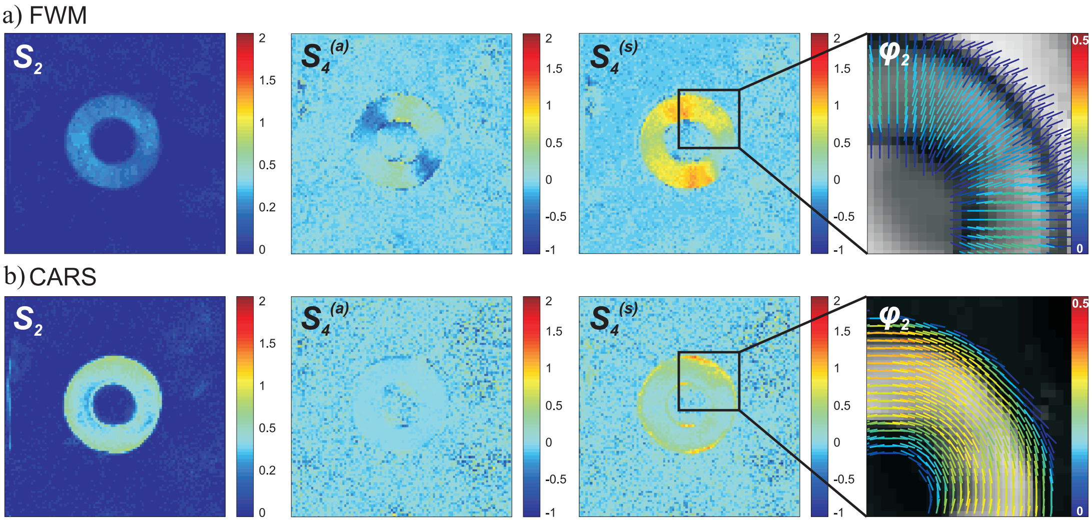

Figure 4.15: S_2, $S_4^{(a)}$, $S_4^{(s)}$ and φ_2 deduced images for FWM (***a***) and for CARS (***b***). The φ_2 images demonstrate the orientation of molecular bond dipoles seen as sticks for each pixel whose colors follow the S_2 scale.

presence of a 20° birefringence phase shift, which is the maximal value experienced here by the incident fields focused at half-height in the MLVs. Both vibrational (CARS) and electronic (FWM) bond dipoles orientation represented as the image of φ_2 seem to follow the same trend as seen in the pure MLVs. However, in both PR- FWM and CARS cases (Fig. 4.6), S_2 and $S_4^{(s)}$ values are found to increase in the presence of cholesterol, which is a signature of a global gain of order.

S_2 and $S_4^{(s)}$ values for all measured samples are summarized in Fig. 4.16, together with expected (S_2,$S_4^{(s)}$) for angular distributions of known shapes and increasing disorder σ. Obviously, in the case of FWM for MLV containing cholesterol none of the measured effective distribution is seen to fit with a pure Gaussian distribution. The PR-FWM data

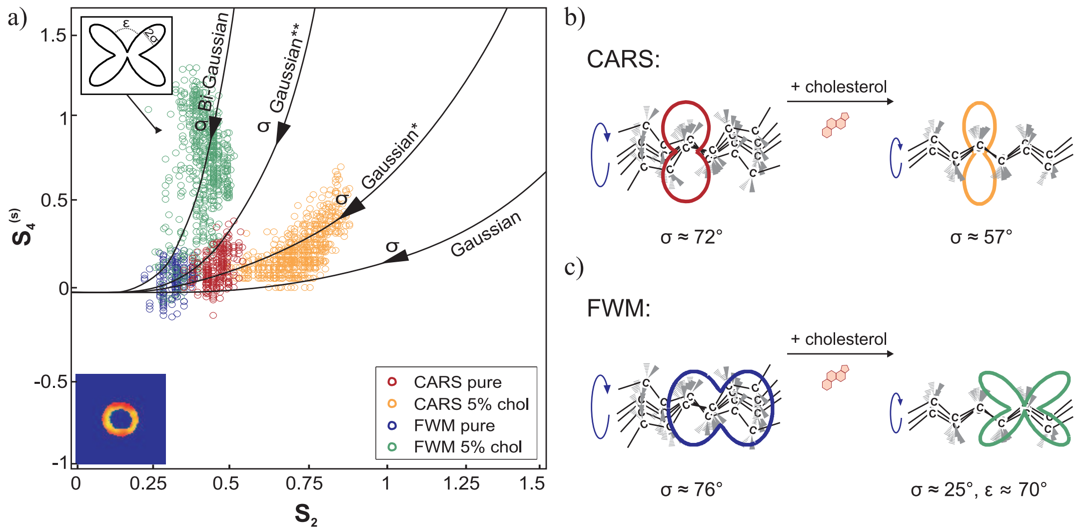

Figure 4.16: (***a***) Experimental (S_2 versus $S_4^{(s)}$) values which are the average over ten pixels and were taken within a give mask (inset in the plot). Solid lines: theoretical (S_2, $S_4^{(s)}$) for a bi-Gaussian function (distant by $\epsilon = 70°$), a Gaussian function with 0%, 25% ($*$) or 50% ($**$) contribution from an isotropic population. (***b***) Scheme of the effective distribution function $p(\varphi)$ of CD dipoles probed by PR-CARS. (***b***) Scheme of the effective distribution function $p(\varphi)$ of nonlinear dipoles (arranged along CC bonds) probed by PR-FWM.

rather fit well with a bi-Gaussian made of two Gaussian functions separated by $\epsilon = 70°$ (Fig. 4.16c), with a visibly high disorder ($\sigma \approx 38°$) in pure DPPC and higher order ($\sigma \approx 25°$) in the presence of cholesterol. The observed symmetry spectrum of the measured angular distribution $\tilde{p}(\varphi)$ is in agreement with nonlinear bond dipoles arranged roughly on the CC bonds frame, similarly as in the simple theoretical model described in Chapter 1. The lower angular freedom imposed by interactions with cholesterol (45) almost reveals the crystalline structure of the individual acyl-chains symmetry as it occurs in the liquid-ordered L_o lipid phase. Note that the observed disorder σ encompasses possible conformational changes of the lipids in the multilayers, local lipid interactions and morphological fluctuations of the membrane at the sub-diffraction scale. The PR-CARS data are representative of lower $S_4^{(s)}$ values which can be interpreted by a Gaussian model superimposed with an isotropic contribution (25% of the total population) rather than by the Gaussian function (45).

The width of this Gaussian population is about $\sigma \approx 72°$. This width decrease in presence of cholesterol (Fig. 4.16) down to $\sigma \approx 57°$, still in presence of an isotropic distribution.

4.5.4 The influence of the acyl chain structure on lipids packing in MLVs

In order to investigate the sensitivity of the polarization-resolved analysis to the lipids thermodynamic behavior we performed the PR-CRS measurements on MLVs made of different lipid species. PR-CARS and SRS measurements were performed using MLVs made of pure DOPC, DMPC or DPPC lipids. All MLVs were measured at room temperature (21 ± 1°C) in which lipids reveal different phase behavior (Table 4.1.1). As has been discussed in Section 3.2.2(Chapter 3), these phase behaviors are characterized by different lateral organizations of lipids depending mainly on the degree of saturation, the acyl chain length and temperature.

The S_2 and $S_4^{(s)}$ values of all measurements, summarized in Fig. 4.17, Fig. 4.18 and Table 4.3 demonstrate the potential of the method to probe lipid phase behaviors by both CARS and SRS microscopy. As expected, S_2 values from CARS polarization response is always slightly lower than from SRS due to the non-resonant background present in the sample, contrary to SRS response which is a background free. Nevertheless, both CARS and SRS signals follow the same trends when lipids change, which makes CARS a valid method for "relative" measurements. We can clearly distinct differences

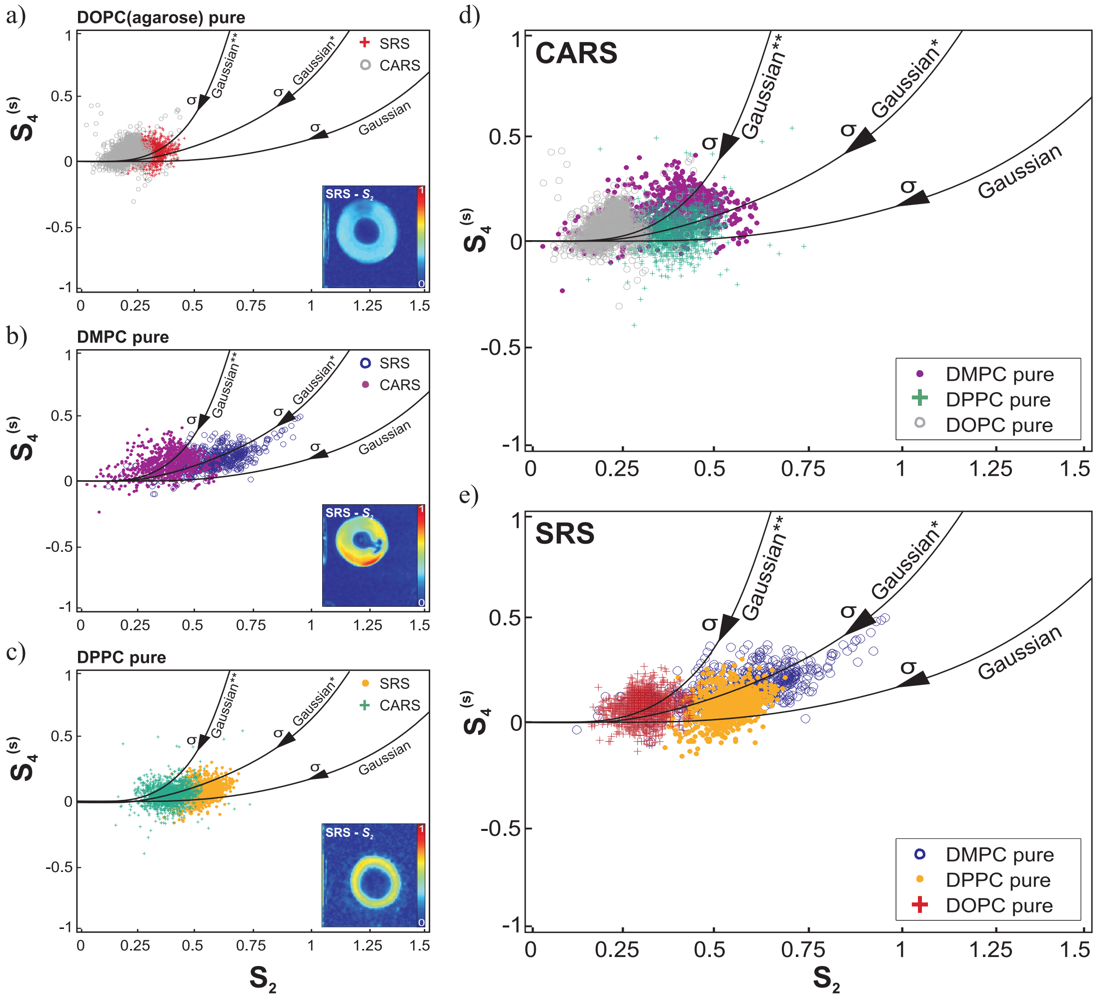

Figure 4.17: Experimental values of S_2 versus $S_4^{(s)}$ for MLVs made of (***a***) DOPC(agarose) (16 samples), (***b***) DMPC (3 samples) and (***c***) DPPC (24 samples) lipids probed by CARS and SRS. Insets in these plots show the examples of S_2 maps for each type of MLV. (***d***) and (***e***) Summarizing graphs of S_2 versus $S_4^{(s)}$ for CARS and SRS for these MLVs, respectively. Solid lines: theoretical (S_2, $S_4^{(s)}$) for a Gaussian function with 0%, 25% ($*$) or 50% ($**$) contribution from an isotropic population.

Table 4.3: Summary of S_2 and $S_4^{(s)}$ values from all PR- CARS, SRS and 2PEF measurements.

Contrast	DOPC, pure	DOPC, labelled[a]	DMPC, pure	DMPC, labelled[b]	DPPC, pure	DPPC, labelled[a]
CARS	$\sigma \approx 86°$ $S_2 \approx 0.22 \pm 0.03$ $S_4^{(s)} \approx 0.06 \pm 0.04$	$\sigma \approx 86°$ $S_2 \approx 0.21 \pm 0.01$ $S_4^{(s)} \approx 0.03 \pm 0.01$	$\sigma \approx 75°$ $S_2 \approx 0.36 \pm 0.06$ $S_4^{(s)} \approx 0.12 \pm 0.05$	$\sigma \approx 82°$ $S_2 \approx 0.27 \pm 0.03$ $S_4^{(s)} \approx 0.07 \pm 0.02$	$\sigma \approx 73°$ $S_2 \approx 0.40 \pm 0.05$ $S_4^{(s)} \approx 0.05 \pm 0.03$	$\sigma \approx 74°$ $S_2 \approx 0.38 \pm 0.05$ $S_4^{(s)} \approx 0.03 \pm 0.02$
SRS	$\sigma \approx 80°$ $S_2 \approx 0.32 \pm 0.03$ $S_4^{(s)} \approx 0.07 \pm 0.02$	$\sigma \approx 80°$ $S_2 \approx 0.32 \pm 0.01$ $S_4^{(s)} \approx 0.06 \pm 0.02$	$\sigma \approx 64°$ $S_2 \approx 0.58 \pm 0.04$ $S_4^{(s)} \approx 0.17 \pm 0.02$	$\sigma \approx 62°$ $S_2 \approx 0.61 \pm 0.06$ $S_4^{(s)} \approx 0.17 \pm 0.04$	$\sigma \approx 66°$ $S_2 \approx 0.53 \pm 0.04$ $S_4^{(s)} \approx 0.08 \pm 0.03$	$\sigma \approx 69°$ $S_2 \approx 0.46 \pm 0.06$ $S_4^{(s)} \approx 0.06 \pm 0.02$
2PEF	- - -	$\sigma \approx 65°$ $S_2 \approx 0.55 \pm 0.01$ $S_4^{(s)} \approx 0.06 \pm 0.03$	- - -	$\sigma \approx 48°$ $S_2 \approx 1.0 \pm 0.14$ $S_4^{(s)} \approx 0.24 \pm 0.13$	- - -	$\sigma \approx 48°$ $S_2 \approx 0.97 \pm 0.1$ $S_4^{(s)} \approx 0.04 \pm 0.06$

[a] TMA-DPH.

[b] di-8-ANEPPQ.

in molecular packing in these lipid species. All measured cases seem to fit with Gaussian distribution function with a 25% contribution from an isotropic population (Fig. 4.17). This contribution is thus most probably due to morphological properties (lipid membrane folds) that are conserved whatever the lipid phase which is related to the multilamellar nature of the sample. MLVs made of DOPC, which are supposed to be the most disorganized due to the single double-bound in the acyl chain, display the highest disorder ($\sigma \approx 86°$ for CARS and $\sigma \approx 80°$ for SRS) as compared to MLVs made of DMPC ($\sigma \approx 75°$ for CARS and $\sigma \approx 64°$ for SRS) or DPPC ($\sigma \approx 73°$ for CARS and $\sigma \approx 66°$ for SRS) lipids (Table 4.3). DPPC made MLVs exhibit a higher order which is attributed to the more rigid structure of this lipids. We can notice, moreover, that the distribution of DMPC data is the most spread encompassing possible heterogeneities made of ordered and disordered areas. This could be explained by the fact that the room temperature in which the experiment has been performed is very close to the temperature of the phase transition of DMPC lipids (23.6°C), resulting in the mixing (within individual MLVs) of two phases - L_d and S_o. The phase transition of DOPC or DPPC lipids is far away from the room temperature indicating that these lipids should display one defined phase (45).

$S_4^{(s)}$ values, on the other hand do not reveal such a clear dependence to the lipids type. It is probably due to the fact that the $S_4^{(s)}$ parameter requires a higher order of angular constraints (lower S_2) to reveal structural changes in the lipid angular distribution, such as seen in the presence of cholesterol (Section 4.5.3), which introduced almost crystalline structure of lipids assembly. The standard deviations of the order parameters, which are signatures of the sample heterogeneity, are plotted in Fig. 4.18. Visibly, the highest diversity within a single MLV is seen for DMPC lipid which confirms the previous observations. $S_4^{(s)}$ parameter displays mostly a higher standard deviation than S_2, which is less sensitive to the noise introduced by the sample (see Section 2.3.3). We can notice that the observed heterogeneity is introduced by the sample itself, which encompasses the conformational changes of lipids, local lipid interactions and morphological time fluctuations of membranes. Nevertheless, even if there is some diversity within a single lipid species, the molecular order still follow a single angular model as shown in Fig. 4.17.

4.5.5 Comparison of molecular packing in *labelled* MLVs made of different lipid species

We investigate now whether the fluorecent dyes embedded in the lipid membranes affect the structure and organization of lipids assembly. To do so, we performed the same exper-

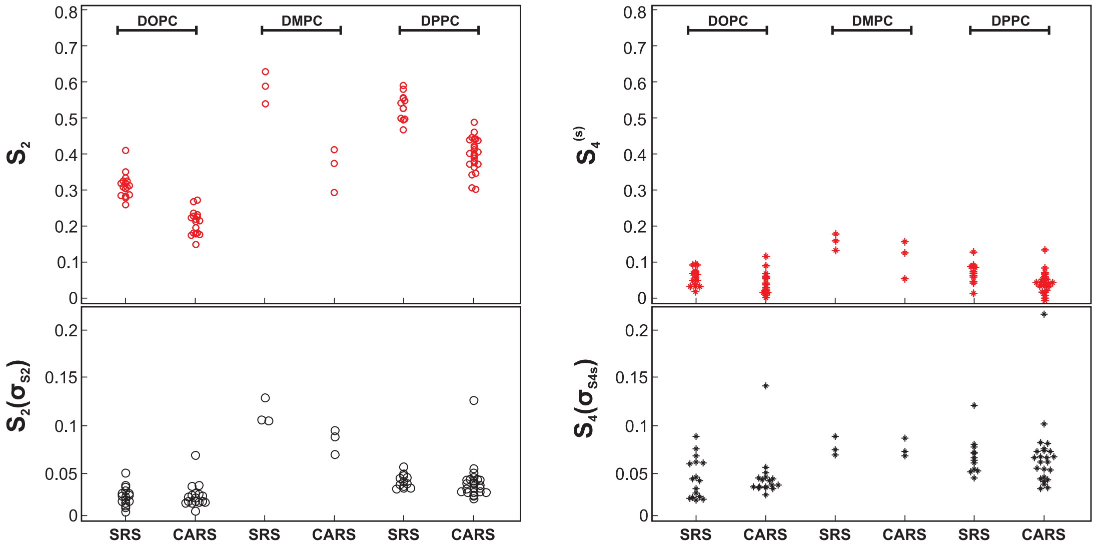

Figure 4.18: Values of S_2 and $S_4^{(s)}$ (red) and their standards deviations of $S_2(\sigma_{S2})$ and $S_4(\sigma_{S4^s})$ (black) for all MLVs made of DOPC (agarose), DMPC and DPPC lipids probed by PR-CARS and SRS. Each point represent a standard deviation measured over pixels of each measured MLV.

iment as demonstrated in the Section 4.5.4 on the MLVs labelled either with TMA-DPH or di-8-ANEPPQ fluorophore using PR-CARS, SRS and 2PEF on a single vesicle. We collected the PR data using MLVs made of DOPC and DMPC lipids. The results from all these measurements are summarized in Fig. 4.19, Fig. 4.20 and Table 4.3. Looking at the Fig. 4.19 we can notice that the polarization responses for both CARS, SRS and 2PEF signals follow the same trend for the three different lipids species, with higher order found systematically for fluorescent dyes. Both fluorescent dyes, TMA-DPH and di-8-ANEPPQ thus change their organizations depending on the lipidic environment in which they are inserted. Among the fluorescent response the lowest molecular order ($\sigma \approx 65°$) is seen for the TMA-DPH dye inserted in DOPC lipid membranes, where the organization follows a Gaussian shape (Fig. 4.19a and d). This is consistent with previous observations (e.g. without the dyes) (Section 4.5.4) where at room temperature DOPC is supposed to be in the liquid L_d phase, which is the most disorganized one. Similarly, the distribution of the di-8-ANEPPQ fluorescent dye in the DMPC lipids also fits with a Gaussian shape function but with much higher order than observed for DOPC membranes ($\sigma \approx 48°$ in DMPC and $\sigma \approx 65°$ in DOPC) (Fig. 4.19b, d). The measured distributions are in contrast with the observations described above (Section 4.3.5) for TMA-DPH inserted in DPPC, where a smooth cone function with a higher steepness and the highest order has been

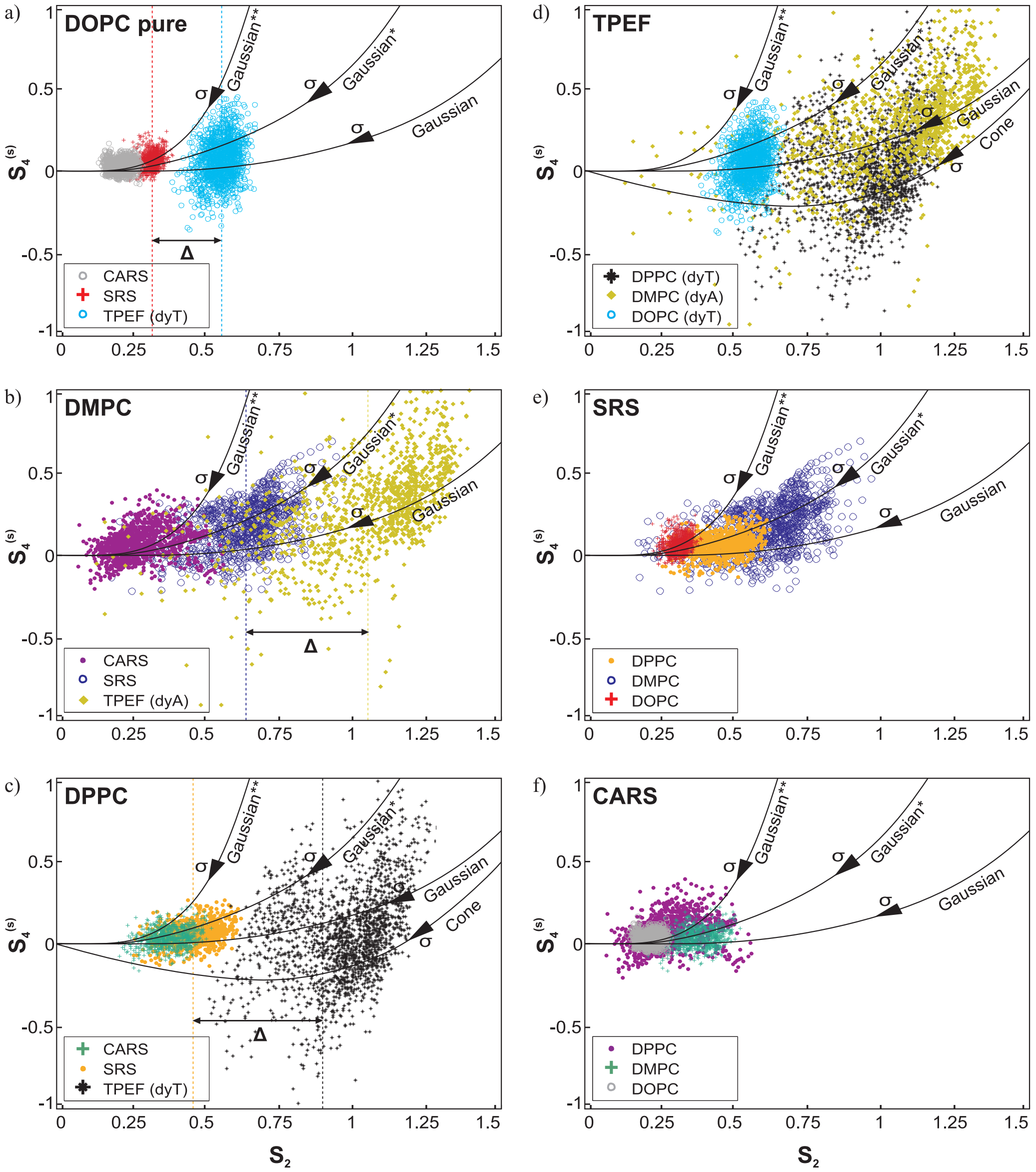

Figure 4.19: Experimental values of S_2 versus $S_4^{(s)}$ for MLVs made of (***a***) DOPC(agarose)-TMA-DPH (2 samples), (***b***) DMPC-di-8-ANEPPQ (3 samples) and (***c***) DPPC-TMA-DPH (12 samples) probed by CARS, SRS and 2PEF microscopy. (***d-f***) Summarizing graphs of S_2 versus $S_4^{(s)}$ for 2PEF (***d***), SRS (***e***) and CARS (***f***) for these MLVs. Solid lines: theoretical (S_2, $S_4^{(s)}$) for a Gaussian function with 0%, 25% ($*$) or 50% ($**$) contribution from an isotropic population and a smooth cone with a steepness $a \approx 3$.

measured. This is probably due to the lower angular freedom imposed by DPPC which at room temperature displays a gel S_o phase (Fig. 4.19c and d). The comparison of S_2 values obtained for lipids (PR-SRS) and dyes (PR-2PEF) permits to draw several conclusions (Fig. 4.19). First, the trend of "order increase" by increasing lipid order phase is followed:

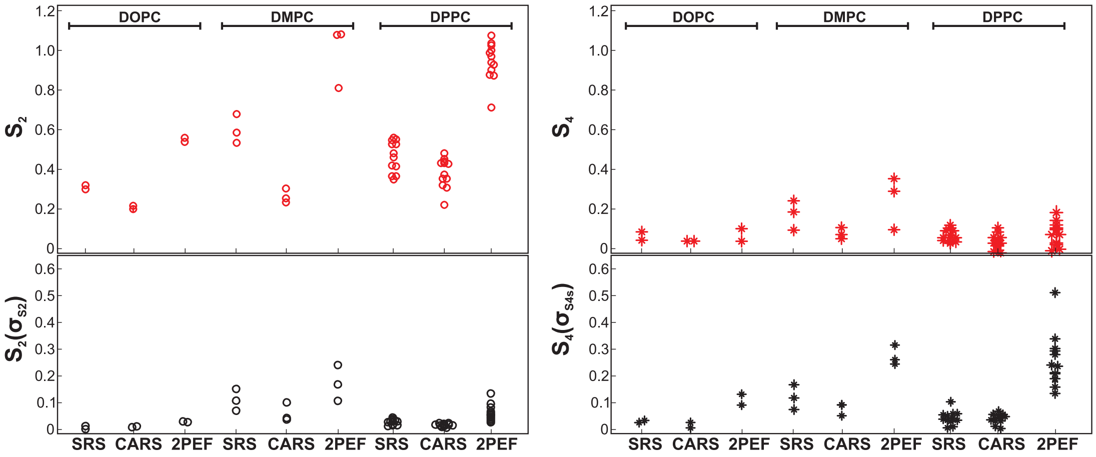

Figure 4.20: Values of S_2 and $S_4^{(s)}$ (red) and their standards deviations of $S_2(\sigma_{S2})$ and $S_4(\sigma_{S4^s})$ (black) for all MLVs made of DOPC(agarose)-TMA-DPH, DMPC-di-8-ANEPPQ and DPPC-TMA-DPH probed by PR- SRS, CARS and 2PEF microscopy. Each point represent an average standard deviation of each measured MLV.

both lipid order and dye order indeed increase when going from DOPC to DMPC or DPPC. However, the shift in S_2 is not necessarily the same for lipids and for the dyes. This shift also depends on the dye (e.g. di-8-ANEPPQ versus TMA-DPH). The standard deviations of deduced S_2 and $S_4^{(s)}$ values measured over the high intensity pixels of MLVs (for several MLVs), are plotted in Fig. 4.20. The orientational response from fluorophores reveal a higher level of heterogeneity from one measurement to another as compared to the molecular order measured for CH bonds probed by CRS microscopy. Moreover, this heterogeneity increases from DOPC to more ordered DPPC environment. A similar effect was already seen from pure lipid order (Section 4.5.4): for both dyes and lipids, an ordered lipid phase tends to create more heterogeneities in the measured samples; maybe due to the presence of more heterogeneous domains.

Finally, this study permits to compare dyes behavior. First, TMA-DPH in DOPC shows very similar order as previously reported (52). Second, we performed also the measurement of di-8-ANEPPQ organization in MLVs made of DPPC lipid. We found similar S_2 and $S_4^{(s)}$ values as for TMA-DPH fluorescent dye. This confirms that both fluorophores give the same information about the molecular order in membranes (52). Even though these dyes are structurally different, they probably exhibit similar lipid interactions.

Based on this data we report few important observations: 1) all fluorophores display a higher molecular order than CH nonlinear bonds, which suggests that their organization is strictly limited by an angular constraint imposed by surrounding lipid molecules, 2) this molecular order of fluorophores can be very different depending on the rigidity of the surrounding lipid assembly, however follows the same trends quantitatively, 3) PR-2PEF does not report the same degree of organization as PR-CARS and SRS and this needs to be taken into account when interpreting PR-2PEF results: in particular the order measured for a dye is not representative of the measured order for the surrounding lipids, and 4) Results obtained from PR-2PEF and PR-SRS are not quantitatively equivalent in terms of shifts of order induced by a change of lipid phase.

PR-2PEF moreover produces results which are highly heterogeneous and therefore the information about the molecular organization depending on the lipid phase can be biased in the case where no careful statistical analysis is made. Therefore, probably the best choice for such an investigation of the lipid assembly behavior is to perform PR-SRS, which directly visualizes the organization of CH bonds in a background-free manner.

4.5.6 The influence of fluorophores on lipids packing in MLVs

Finally, we compare the molecular order of lipids read by PR-CARS and SRS microscopy in the presence or absence of fluorophores. Results from all measurements are summarized in Fig. 4.21. We can see that the general distribution of values of order parameters for MLVs with or without a fluorophore mostly are in the same range. Slight differences are seen for MLV made of DMPC lipids probed by PR-CARS as well as DPPC probed by PR-SRS. In both cases the values of S_2 are lowered for labelled MLV as compared to non labelled. We do not observe such effect in DOPC lipids, which may reflect the preference of fluorophores to accumulate more in a gel phase of DPPC and DMPC lipids thus decreasing general disorder, as it has been shown in a case of higher concentrations of cholesterol (45). Nevertheless, the data suggests that the lipids molecular order is generally preserved. This is a rather positive conclusion with aspect to the use of fluorescence probes, which are often criticized for their negative effects on the lipid membranes' structure. However, we could notice slight differences in the heterogeneity of the parameter, which standard deviations are generally lower in labelled membranes. This can be pictured by more uniform lipid behavior and overall orientational membrane homogeneity imposed by the fluorescent dye (compare also plots in Fig. 4.18 and Fig. 4.20).

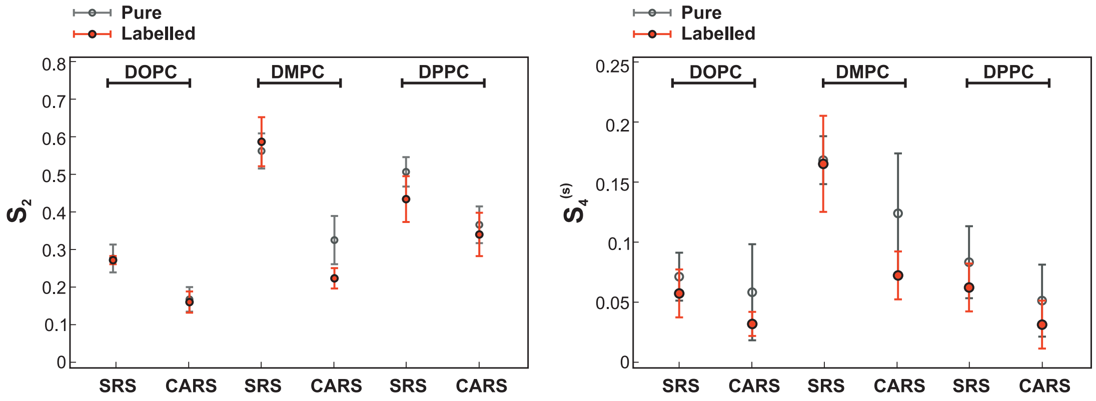

Figure 4.21: The influence of fluorescent dyes on lipid packing probed by PR- CARS and SRS microscopy. Graphs S_2 (left) and $S_4^{(s)}$ (right) compare the values for all MLVs made of DOPC, DMPC and DPPC pure or labelled with TMA-DPH (DOPC, DPPC) or di-8-ANEPPQ (DMPC) fluorescent dyes.

4.6 Conclusion

All of nonlinear contrasts studied, 2PEF, SRS, CARS and FWM provide detailed information and we have shown that are suitable to probe different orientational behaviors of lipid assembly. We have shown that the PR-2PEF is able to read qualitatively the molecular organization of lipids, but the quantitative retrieved information is not the same as the obtained by the label-free techniques as CARS, FWM and SRS. The label-free nonlinear contrast are highly sensitive to the changes of lipids organization imposed by cholesterol or depending on the structure of lipidis acyl chain. Moreover, we have demonstrated that the presence of the fluorophore in the membrane does not modify the molecular order of lipids S_2 at small concentrations, but increases of overall homogeneity of the probed membranes is non-negligible.

4.7 Perspective

The advantage of the SRS technique over the 2PEF is the label-free visualization of the lipids in cell membranes. However, the direct investigation of the cell membrane whose thickness ranges between 0.5 and 0.7 nm remains a challenge, mainly due to the resolution limitation and the high CH bonds content in the interior of the cell. Here, we show preliminary results obtained from PR-SRS measurements of a cell membrane of a COS7 fibroblast-like cell. Fig. 4.22 shows the PR-SRS intensity response (centered to probe the CH stretching vibration of lipids at 2845 cm^{-1}) depending on the input excitation polarization angle α from the COS7 cell. No significant difference is seen for two points taken either from the edge or from a high intensity pixels inside cell, which remains almost isotropic.

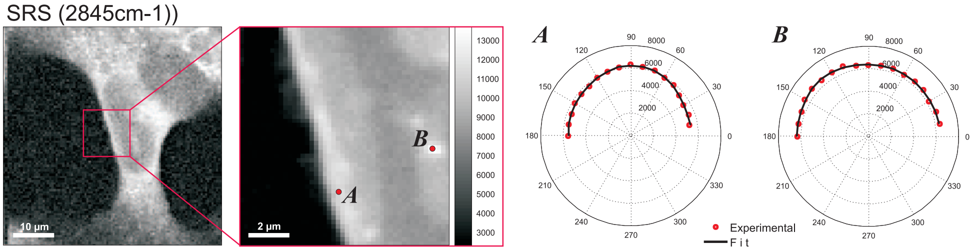

Figure 4.22: PR-SRS intensity signal response from the COS7 cell line.

A closer inspection of the deduced S_2 and $S_4^{(s)}$ values (Fig. 4.23) shows that the interior of the cell is homogeneously isotropic while slightly higher S_2 values are detected at the edge of the cell. The φ_2 image shows that the molecular bonds in average lie along the border of the cell as expected from the geometry of the membrane. Plotting the S_2 versus $S_4^{(s)}$ values in the graph shown in Fig. 4.24 clearly indicates a very low order distribution of the CH molecular bonds (S_2 values $\approx$ 0.1, but still with higher values of S_2 than the considered points inside of the cell. The relatively low S_2 measured is most probably due to the important isotropic population of CH bonds (from lipids and proteins) inside the cell, that is also contributing within the focal spot size.

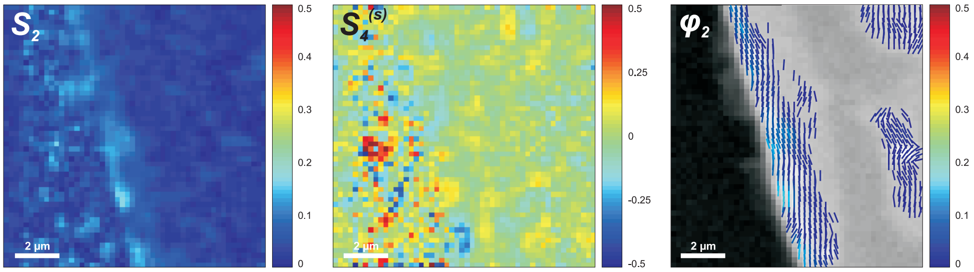

Figure 4.23: The deduced S_2, $S_4^{(s)}$ and φ_2 maps for enlarged view of the border of the COS7 cell.

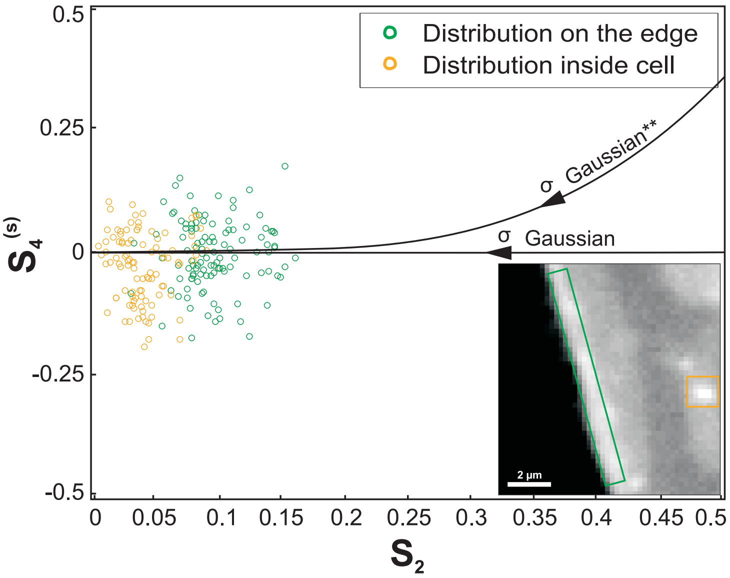

Figure 4.24: Graph of the S_2 versus $S_4^{(s)}$ values taken from the edge (green) and from a high intensity pixels inside the COS7 cell.

The higher S_2 signal at the border of the cell equals to 5 pixels ($\approx$ 1 μ m) which seems, however, too large for the cell membrane of a few nanometers (Fig. 4.23). This can be however explained by the convolution process between nanometric order region and a PSF (focal spot size) of $\approx$ 300 nm. It has been shown indeed, that for such punctual objects, the molecular order map tends to considerably enlarge in scale (Carolina Rendon phD, in preparation). Considering that higher SRS signals could be obtained by more accumulations, there is therefore some hope to be able to better quantify molecular order in cell membranes using PR-SRS.

Chapter 5

Central nervous system, myelin: architecture, disorder and imaging

5.1 Central nervous system (CNS)

5.1.1 Architecture of the CNS

The central nervous system (CNS), which consists of the brain and spinal cord, is composed primarily of two kinds of cells: neurons and glia (Fig. 5.1a) (144, 145). Every aspect of the CNS development and function involves neuron-glial partnership. While neurons are directly involved in the transmission of electrical impulses and information processing, glial cells are responsible for correct neuronal development and for the functionality of mature neurons. There are three types of glial cells; astrocytes, microglias and oligodendrocytes. Each of them display distinct function in the CNS. The first class of cells, astrocytes (of a ramified morphology), the most numerous in the CNS, play a crucial role in the development of the nervous system, including potassium homeostasis, neurotransmitter uptake, synapse formation and regulation of blood-brain barrier (146). Microglias, which constitute about 10% of CNS glia (147), are the immunoeffector cells in the CNS and their role can be either neuroprotective or neurotoxic to the functions of surrounding cells. They continuously migrate through the CNS in order to react to the potential pathogen or to CNS injury. Moreover, they are responsible for removing cellular debris from the brain by phagocytosis, regulating astrogliosis and assisting in the development of CNS (148). The main function of oligodendrocytes is the formation of a plasma membrane, named the myelin sheath (Section 5.1.2) around the elongated body of nerve cells (Fig. 5.1b), which plays an important role for electrical insulation

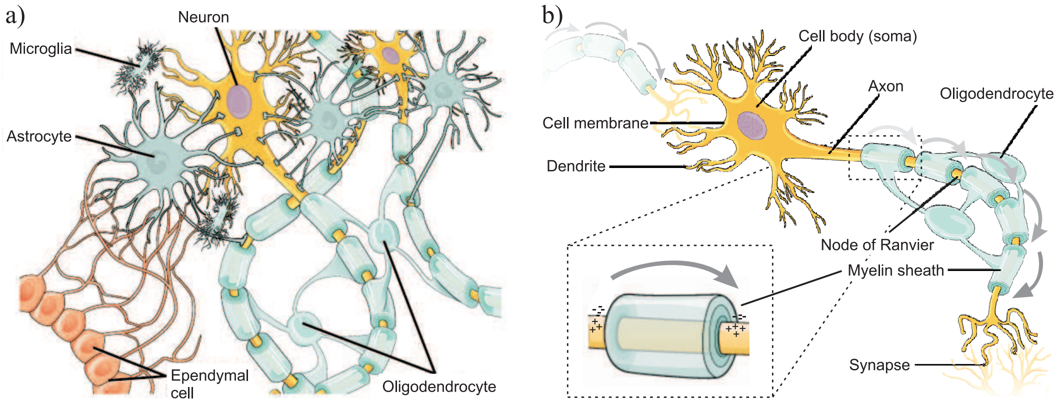

Figure 5.1: Architecture of the central nervous system (***a***) The glial cells and neurons distribution. (***b***) Structure of a neuron. The red arrows show the flow of the action potential on the node of Ranvier (*From: www.cnx.org*).

allowing the fast conduction of electrical impulses (144, 145). It is clear that the correct and balanced cooperation of glial cells is indispensable for the proper function of the CNS.

5.1.2 Myelin

Myelin sheath, for the first time named so by Virchow in 1854 (149), is the most abundant membrane structure in the nervous system of vertebrates. The myelin sheath, as a multilamellar membrane wrapped around the axon (Fig. 5.1b), is responsible for the *saltatory conduction* of nerve impulses. It acts as the electrical insulator enabling the action potential to occur only in the areas on the axon exposed to the extracellular space called the node of Ranvier. The electrical impulse jump from node to node, which might be even 1 mm away. Such a propagation of electrical impulses is much faster (even 100 times) than in unmyelinated nerves (150).

The insulating properties of the myelin sheath are due to its structure, its thickness and its unique composition. Based on the transmission electron microscopy images (TEM), the myelin sheath is a multilayered stack of membranes with a characteristic periodic structure of altering electron-dense and -light layers (Fig. 5.2a). The dense and -light lines represent the closely condensed cytoplasmic and extracellular membranes, respectively (Fig. 5.2a). The compaction of each of these layers is tight and results in periodicity of about 12 nm (Fig. 5.2b) with the myelinated segments of axons around 150 - 200 μm in length (144). The thickness of the myelin sheath varies according to the diameter of the axon: bigger

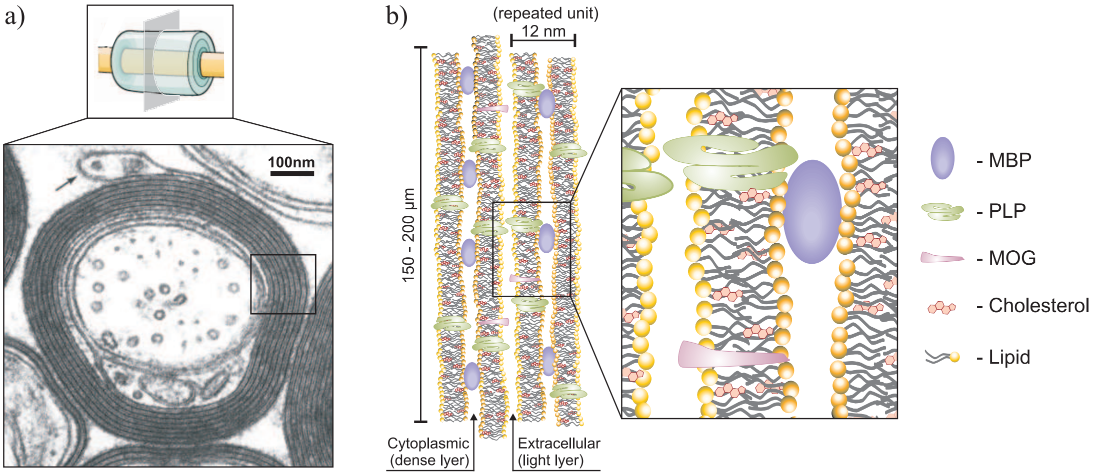

Figure 5.2: (***a***) Representative EM image of the myelin sheath structure (cross section view) (Adapted from (151)). (***b***) Molecular organization of the major myelin components; MBP - myelin basic protein, PLP - proteolipid protein, MOG - myelin-oligodendrocyte glycoprotein.

axons have thicker myelin, and vice versa. Therefore the thickness is better defined by the g-ratio, which is the ratio of the axonal diameter divided by the diameter of the axon and in most vertebrates ranges between 0.6 and 0.7 (152).

One of the most important features defining the functionality of myelin is its unique composition. The myelin sheath is composed of lipids ($\approx$ 70% by dry weight) and proteins ($\approx$ 30% by dry weight) with a low water content (150). According to a last report the myelin sheath contain more than 700 different lipid moieties (153) among which the most abundant are fatty acids, phospholipids and their lyso-derivatives (e.g. phosphatidylcholines (PC) and lysophosphatidylcholines (LysoPC), etc.) which serve as the structural matrix, cholesterol and its derivatives important for myelin functionality, but also lipids involved in several signaling mechanisms, such as ceramides, cerebrosides, sulfatides, di- and triacylglycerolipids and sphingomyelin (SM). Among proteins of the CNS maintaining the correct structure of myelin, the most abundant are myelin basic protein (MBP) and proteolipid protein (PLP), and a secondary by a lower amount the myelin-oligodendrocyte glycoprotein (MOG) (Fig. 5.2b).

The components of the myelin sheath present the extraordinary ability to self-assemble into a highly ordered and stable structure. Due to the balanced intermolecular forces between lipids as well as between lipids and proteins, it results in the formation of organized and tightly packet multibilayers (154). For instance, it has been demonstrated that MBP, by acting as an electrostatic ”glue” between negatively charger bilayers and positively charged amino acids groups, maintain the structure and stability of the cytoplasmic region of the myelin sheath (155). Other studies have shown that the adhesion between bilayers highly depends on the lipid composition (156, 157), in particular, the ratio between the saturated to unsaturated lipid molecules (158).

Any small destabilization of myelin membrane assembly can result in swelling, vesiculation and even desintegration of the myelin structure, which is a common underlying feature of several neurological disorders such as Multiple Sclerosis or Experimental Autoimmune Encephalomyelitis (EAE), spinal cord and brain injuries, leukodistrophies, Alzheimer’s disease and Parkinson’s disease. In this study we will focus on EAE.

5.2 Neurodegenerative disorders: Multiple sclerosis and EAE

Multiple sclerosis (MS) is one of the most common neurodegenerative pathology of the CNS characterized by the formation of multiple lesions, which include a widespread inflammation, focal demyelination, and a variable degree of axonal loss. Although evolution of MS has been shown to be highly heterogeneous (160), many experimental evidences for the pathological sequence of events can be derived from the experimental autoimmune encephalomyelitis (EAE), which is the mice model for MS disease. The most common form of the disease has two distinct clinical phases, the relapsing-remitting episodic phase (RR-EAE) and a chronic, non-relapsing stage (C-EAE), which is a late stage of the RR-EAE often leading to death (Fig. 5.3a) (159). Although the molecular etiology of MS is unknown, a primary event in pathological manifestation of the disease is the breakdown of the blood-brain barrier (BBB) initiated by autoreactive T-cells. Activated T-cells as well as monocytes, B-cells and eventually macrophages migrate through the BBB, which in the normal condition forms a barrier inaccessible for the immune system. The release of cytokines by activated T-cells results in the stimulation of glial cells to transform into their pathological state (gliosis and inflammation) and this process is associated with the demyelination, axonal loss and oligedendrocytes destruction in active MS lesions (Fig. 5.3b and c) (161). Until now, the primary mechanism leading to demyelination process in multiple sclerosis remains unknown, however, morphological transformations of the myelin lamellar structure are well established. Numerous studies of the ultrastructural sequence of the degradation have been reported (163–165). The general pattern of the demyelination

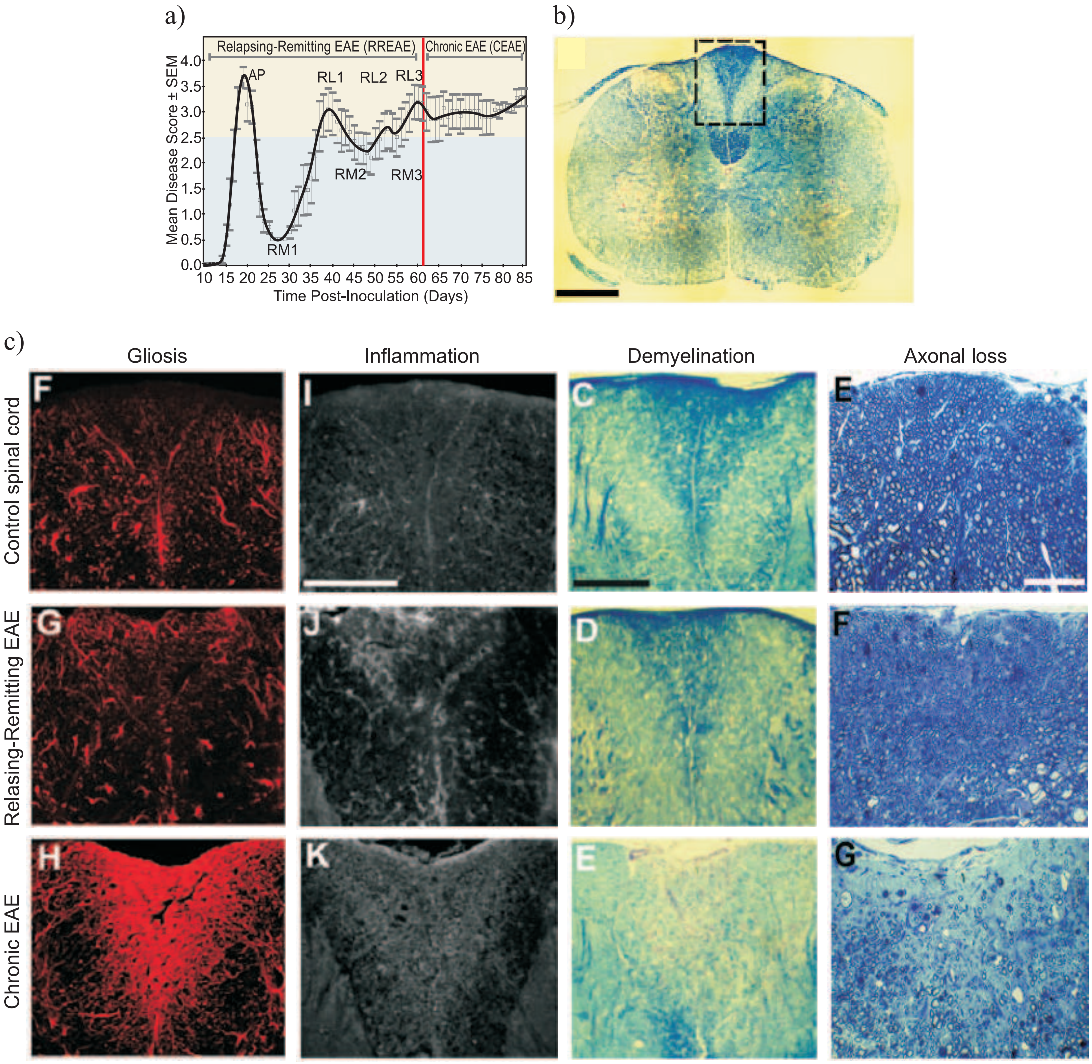

Figure 5.3: (***a***) Schema showing disease progression in RR- and C-EAE with clinical scores of animals post induction (Clinical score: 0, no clinical signs; 1, loss of tail tone; 2, fully flaccid tail; 3, complete hind limb paralysis; 4, complete forelimb paralysis; 5, moribund; 6, dead). Following the acute phase (AP), alternate relapse (RL) and remission (RM) phases, where RL is associated with worsening in clinical score and RM with partial recovering in RR-EAE, lead to the C-EAE. (***b***) and (***c***) Representative large-view images of the architecture of spinal cord in RR-EAE, C-EAE and controls. Histology and immunohistochemistry labelling of astrocytes (gliosis), microglia (inflammation), myelin (demyelination) and axons (axonal loss). Scale bars: B: 500 μm, C-K: 25 μm, E-G: 50 μm (Adapted from (159)).

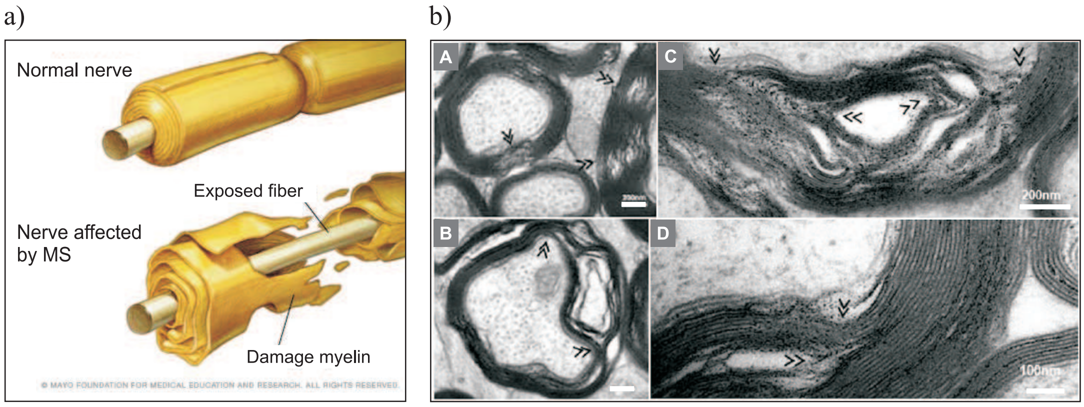

Figure 5.4: (***a***) Scheme of the normal and MS nerve fibers (*From: www.mayoclinic.org*). (***b***) Electron microscopy images of damaged myelin sheaths (cross section view) with ongoing splitting and swelling of myelin membranes. Scale bars: A-C: 200 nm, D: 100 nm (Adapted from (162)).

process encompasses the enlargement of individual myelin sheaths due to a loss of bilayer adhesion, an interlamellar splitting and swelling and, as a consequence, the formation of the vesiculated myelin debris (Fig. 5.4) (162, 164, 166, 167). As multiple sclerosis is a disease specific to humans, the degradation evolution can only be indirectly extrapolated from the mice models, using EAE. However, the structural similarities in the pattern of myelin breakdown between EAE and the acute lesions of human MS indicate a common mechanism for myelin destruction (167).

In the EAE pathology, many factors can contribute to the demyelination process. While evidence that proteins play a structural role in myelin is significant (168), lipids, which constitute 70-85% by dry mass must contribute to the myelin adhesion. For instance, it has been reported that the lipid composition is changing in the heathly and EAE white matter, in particular, the ratio of charged to uncharged lipids (156–158, 169) and such as alteration in the distribution of intermolecular forces can decrease of myelin stability and provoke the swelling process. Moreover, lipid's abnormalities have been also seen in the nonlesional white matter (normal appearing white matter - NAWM) (170). Many findings suggest that lipids play an important role in myelin adhesion and their molecular organization might be affected in EAE tissues, even before any clear morphological sign of damage.

5.3 Structural and functional imaging of the CNS

5.3.1 Different approaches to image myelin sheaths

The architecture of the neuronal networks and their alterations in neurodegenerative diseases has been widely studied by different imaging techniques. Each of them has its own advantages and drawbacks. For instance, the magnetic resonance imaging (MRI) as well as its derivatives (magnetic resonance spectroscopy (MRS), magnetization transfer imaging (MTI), diffusion-weighted imaging (DWI)), although extremely powerful techniques able to map the white matter density in the whole brain and spinal cord with $\approx 200\ \mu$m resolution (171–173), does no provide a sufficient specific information on the myelin architecture. The positron emission tomography (PET), by the use of exogenous radioactive labeling agents, provides ≈ 1 mm resolution images that are more specific since based on direct labeling (174). These techniques, providing three-dimensional (3D) reconstruction, become important tools for the diagnosis of various white matter abnormalities. The produced information, however, is poorly correlated with functional deficits and also insufficiently accurate to evaluate the relative amount of neurodegeneration and demyelination (175), due to the lack of high spatial resolution.

To overcome this problem, fluorescence imaging of myelin, which gives an access to sub-micrometric resolution, has been developed. Immunohistochemistry and immunofluorescence (159, 176), selective binding dyes (167, 177) or lipophilic dyes (178), have been used for myelin staining, allowing for instance observation of myelin vesiculation in the acute lesions of MS and experimental autoimmune encephalomyelitis (EAE) (167). Usually developed for fixed tissue samples imaging, new labels are now accessible for in vivo imaging (179, 180), however the short time of observation accessible (few hours) still hampers the long-term analysis of enzymatic activities and demyelination dynamics. In addition nonspecific binding and inefficient diffusion of dye can also obscure the data analysis.

The transmission electron microscopy (TEM) technique, due to its high spatial resolution capability, is used mostly to provide an ultrastructural information about myelin, even on a single lipid layer. Another technique, X-ray diffraction (181) is also able to provide detailed molecular insights of myelin. However, the complex sample preparation, such as fixation and dehydratation, including a cutting the tissue into sections, exclude these techniques for *in vivo* imaging and disease progression.

Finally, label-free optical methods, such as optical coherence tomography (OCT) (182, 183), third harmonic generation (THG) (36, 184) and confocal reflectance (185) provide high resolution (few 100's of nm) imaging of myelin architecture. The first one, OCT, by measuring the difference in the refractive index between tissues components, can be sensitive to experimental motion artifacts. The two others, THG and confocal reflectance, are specifically sensitive to the inner and outer interface of the myelin sheath and not necessarily to its volume. Complementary studies are therefore still needed to find more reliable optical contrasts.

5.3.2 Coherent anti-Stokes Raman Scattering imaging of myelin

The vibrational based contrast Coherent anti-Stokes Raman Scattering has been applied to visualize the myelin sheath for the first time by Wang et al. in 2005 (46). They have demonstrated that CARS microscopy, sensitive to the CH_2 vibration modes, permits to retrieve the molecular orientation and vibrational spectral profiles of myelin lipids in a live spinal tissue in epi- (E-CARS) and forward (F-CARS) directions. Since this time, CARS microscopy applied to neuronal tissues has been extensively developed. Myelin from the CNS or peripheral nervous system (PNS) was observed using fixed slices (37, 186), fresh tissues (187, 188) or *in vivo* (24, 189, 190). Now, it is possible to perform 3D high resolution, video-rate CARS images (38) in live animals over weeks (25). CARS microscopy in

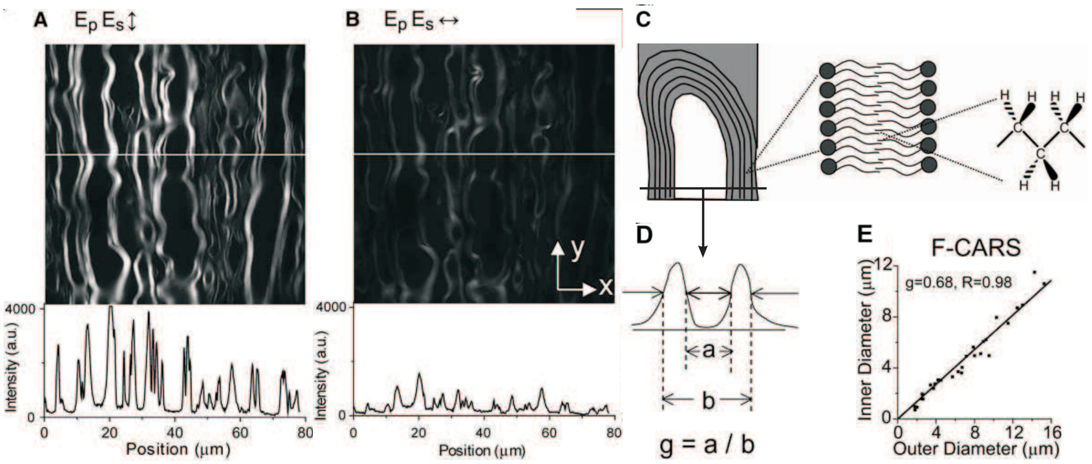

Figure 5.5: F-CARS images of myelin sheath using vertically polarized (***a***) and horizontally polarized (***b***) beams with the intensity profiles below the images for the lines shown in the images. (***c***) The symmetry axis of the CH_2 groups in the equatorial plane of the myelin is perpendicular to the x direction, leading to a larger $I_{\parallel}$ than $I_{\perp}$. (***d***) Diagram depicting the measurement of the g-ratio from CARS images. (***e***) The g-ratio measured with F-CARS images (Adapted from (46)).

combination with other techniques, such as electrophysiology for instance, have allowed to observe the myelin envelope behavior following high-frequency stimulation (188). Small details of the myelin morphology, such as the node of Ranvier or the Schmidt-Lanterman clefts, has been already observed by CARS microscopy (46), but the recently developed method for resolution enhancement in CARS microscopy (191) has given a possibility to obtain even more insights into the structural information of myelin. A serious limitation of the technique is however the depth penetration. CARS signals from myelin reach up to ≈ 250 μm depths for fresh and ≈ 100 μm depths for fixed nervous tissues. This issue has been partially overcome by implementation of laminectomy surgery in the spinal cord (25), or by craniotomy to expose the subcortex white matter (24) or even by microendoscopy to reduce the use of surgery ($\geqslant 2$ mm) (189).

The myelin sheath has been largely characterized in terms of detected level of the signal, spectral profile, polarization dependence and the measurement of g-ratio.

- F-CARS as well as E-CARS images can be obtained from the myelin sheath (Fig. 5.5a). At the equatorial plane of the axon, the CARS radiation from myelin sheath predominantly goes forward and the E-CARS arise from the back-reflected F-CARS. As a result the F-CARS is 18.9 times that of E-CARS, according to Wang et al. (46).

- In the femtosecond regime, the CARS signal of axonal myelin is dominated by symmetric and asymmetric CH_2 stretching vibrations of hydrocarbon chains from lipids (2845 cm^{-1} and 2885 cm^{-1} respectively) which are the major components of myelin. Little signal originates from CH_3 stretching vibration of proteins (2930 cm^{-1}) that constitute $15 - 30\%$ of the weight of the myelin sheath (37, 46). In the picosecond regime, small variations of vibrational bonds intensities can be detected by combination of CARS microscopy and Raman microspectroscopy on the same platform (37) and this can reflect the conformational and/or chemical changes of lipids in myelin multilayers (see below).

- The myelin sheath reveals a strong polarization dependence due to the compact multilamellar structure and highly ordered CH_2 groups inside lipid membranes (Fig. 5.5a and b). In the equatorial plane of myelin fibers CH_2 vibrations are oriented azimuthally with respect to the bilayer normal (Fig. 5.5c). For quantitative analysis of myelin density this polarization effect can by minimized by using a circular polarization scheme (186).

- The *g*-ratio, defined as the ratio of the inner diameter to the outer diameter of a myelinated axon (Fig. 5.5d) (152) was found to be in the range between 0.4 and 0.6 in spinal cord tissue (186, 192) and 0.6 to 0.7 in the sciatic nerve (Fig. 5.5e) (187, 190).

With these advances of CARS microscopy, the mechanistic disruption of myelin in various models has been studied. In CARS imaging, the degeneration is characterized by changes of myelin morphology, such as swelling and vesiculation, reduction of CARS contrast and loss of polarization dependence. Study of the spectral profile of myelin fibers in the different stages of the EAE neurodegenerative model showed interesting results (37). It has been found, for instance, that degraded myelin has higher degree of lipids unsaturation and lower lipid-packing ordering as compare to normal myelin, and that the lipid conformation is not fully recovered in regenerated fibers. Moreover, the morphology and density of myelin has been shown to be strongly affected throughout the progression of EAE pathology *in vitro* with structures showing decreasing straightness with disease progression (37, 38, 193).

The *g*-ratio, as a general myelin health indicator, has been largely quantified using the CARS contrast. It has been found that, in general, the *g*-ratio is increasing i.e. the myelin fiber is thinning in the proximal region of the nerve injury, but also decreasing when measured in the distal area to the lesion (190, 194) or in remyelinated myelin fibers (37). The analysis to calculate a *g*-ratio is, however, a time consuming task because performed on a single myelin fiber level. Further image-based analyses, such as the image segmentation for an automatic *g*-ratio calculation (192) or the 2D Fourier transform method (193), allow to obtain a more accurate and automatic way to assess the myelin health level on a big spatial scale of a few hundreds of μm.

Benefiting from the fact that the myelin sheath displays a strong polarization dependence, the polarization-based method to assess the myelin health was proposed by Fu et al. (187). The progressive degradation of myelin treated by lysophosphatidylcholine (lyso-PtdCho), a well known demyelinating agent has been observed during a time of exposure together with a polarization and g-ratio measurement. Similar study has been performed recently by de Vito et al. (47) applying the developed polarization method to read the loss of polarization dependence of myelin exposed to lyso-PtdCho and comparing the order coefficients to the *g*-ratio measurements. In both cases the g-ratio has been found to increase with the disruption of myelin sheaths together with the loss of the polarization dependence. These measurements were, however, intended to give a degree of demyelination and not to better investigate lipid structural order damages in myelin.

The possibility to image myelin by CARS together with another contrasts such as reflectance (38), two-photon fluorescence (25, 37, 188) or second harmonic generation (coming from fibrous filaments of astroglial cells) (195) opens a door for the future fast live imaging of the architecture of the white matter and its changing in the presence, for instance, a neurological disorders.

5.3.3 Two-photon fluorescence imaging of other components of the CNS

Two-photon fluorescence (2PEF) can be used to visualize the cellular networks of the CNS or PNS in complementary to CARS. It is obvious that imaging of myelin wrapped around the axon cannot provide itself a sufficient information about the structure, dynamics and functionality of the CNS. As has been discussed in Section 5.2, in human pathologies including traumatic injury and multiple sclerosis, numbers of factors, such as axonal and myelin degradation as well as the formation of a glial scar (gliosis), have their own role in the neuronal degeneration leading to dysfunction of the CNS. Apart from myelin imaging by CARS, 2PEF imaging of the concomitant structural dynamics of axonal fibers or glial cells may enable to provide more detailed understanding of disease-related mechanisms in such pathologies.

2PEF has been widely applied to image the functional dynamics of neural tissue either in the brain (12) or in the spinal cord (11). Methods for specific labeling of neuronal subpopulations are numerous (180), but one of the most powerful for *in vivo* studies and surgically non invasive way is transgenic expression of fluorescent proteins (13, 18, 196, 197). Genetically encoded markers provide a good contrast and allow for long-term *in vivo* imaging (Fig. 5.6a and b). 2PEF functional imaging has been applied for monitoring individual regenerating axons and local microvasculature changes (13, 15, 18, 198) or recruitment and dynamics of inflammatory cells (14, 16, 199) after experimental spinal cord or brain injury (Fig. 5.6c). It has been found, for instance, that activated microglia which followed the blood-barrier disruption, can have various behavior, switching their role from patrolling to shielding of the injury site (199), but also are associated with the collapse of certain axon terminals (14) (Fig. 5.6d).

In the context of the animal model for the human multiple sclerosis, the EAE disease, the microglia proliferation and activation (148, 200) or the interaction with the spinal cord blood barrier (201) was directly observed. It has been shown, moreover, that after the invasion of immune cells, axons having intact myelin sheaths start to degenerate but, when detected in the very early stage of degeneration, can be spontaneously reversible

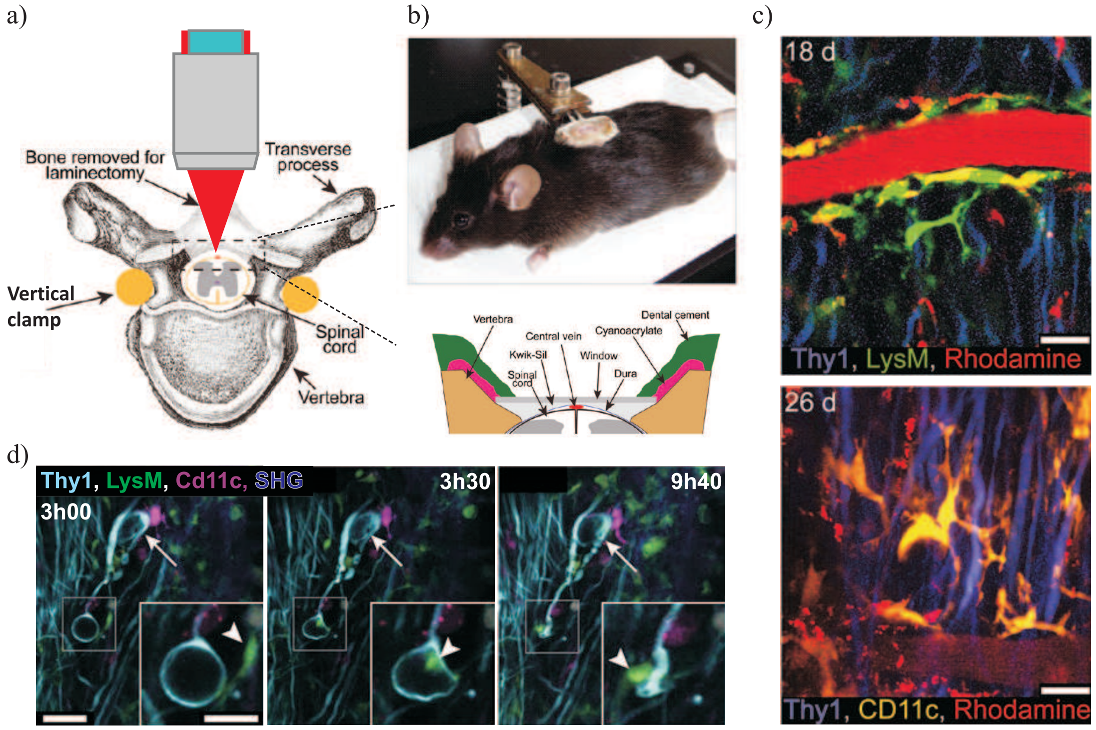

Figure 5.6: (***a***) Schematic diagram showing the vertebral clamp and laminectomy. The tips of the vertebral clamp are inserted under the vertebral transverse processes and glued into place with cyanoacrylate. (***b***) Image of an anaesthetized mouse with an implanted window. The window structure is being supported by a clamp attached to a plastic base. The animal is freely breathing while in the support, but the window remains stationary relative to the clamp. (***c***) 2PEF images showing the morphological characteristics of axons (Thy1-CFP), blood vessels (Rhodamine in blood vessels), myelo-monocytic cells including granulocytes and most macrophages (LysM(+)-GFP), and subpopulations of dendritic cells, microglia and macrophages (CD11c(+)-YFP) after window implantation at day 18 and 26 respectively. Scale bar: 20 μm (Adapted from (13)). (***d***) Time-series images of distended axon terminal (DAT) collapse during close apposition with LysM(+)-GFP cell. Left: the DAT before collapse and a LysM(+)-GFP cell (arrowhead) migrating towards the DAT. Middle: the DAT during collapse. Right: the axon terminal several hours after DAT collapse. The arrow points to a nearby DAT that did not collapse throughout 20h of imaging. Scale bars: 50 μm (Adapted from (14)).

(202).

5.4 The purpose of the study

Recently developed techniques for *in vivo* and *in vitro* imaging helped to better understand the dynamics of the CNS in the presence of neurodegenerative diseases on the cellular level. However, many aspects of molecular mechanisms which leads to degradation of neuronal networks remain still unknown. For instance, what is the role of inflammatory cells on myelin loss in neurodegenerative diseases? Can they be better related to molecular scale mechanisms?

In Chapter 6, we will focus on the fundamental question about the self-assembly of lipids in multilamellar myelin sheaths in process involving the EAE model, which is closer to pathologies than the previously published PR-CARS (47, 187). Using PR-CARS microscopy, we will explore the complexity of the orientational alteration of lipids in myelin sheaths during the active demyelination process. We will demonstrate how the lipid order is changing in the progression of EAE. We will show, in particular, that although the g-ratio is able to reveal small details about the morphology of degenerated myelin, it does not necessary need to be an identifier of the progression of EAE. The label-free PR method developed in this work to read molecular order at the sub diffraction scale can be a very valuable tool, if used properly, giving a unique information not accessible by existing methods.

In Chapter 7, we will demonstrate a potential of CARS and 2PEF microscopy for imaging of the architecture of CNS in the progression of EAE. Both techniques provide a high resolution contrasted images on a large spatial scale and when used on the same microscopy are able to deliver a unique information on the role, behavior and possible cooperation of specific CNR components in the EAE development.

Chapter 6

Local organization of myelin lipids in autoimmune demyelination probed by PR-CARS microscopy

In this Chapter we will study the capabilities of PR-CARS microscopy to explore the molecular scale lipid packing organization in the myelin sheath of axons in spinal cord tissues.

Lipids, as a major components of myelin ($\approx 70\%$ dry weight), undoubtedly play an essential role in the self-organization of myelin. The tight lipid packing within the myelin sheath wrapped around the axon is of vital significance for effective transmission of electrical signals through nerves. The myelin sheath membranes, as multicomponent systems made mostly of lipids and proteins, display however complex phase and structural behavior. Lipids and proteins have a great ability to self-assemble into organized and stable structures (154), relatively insensitive to perturbations (203). In neurological disorders however, the compact, multilamellar structure of myelin is highly perturbed. It undergoes several steps of transformation leading to degradation; loss of bilayer adhesion, swelling, and disintegration from the lamellar structure forming at the end degradation products (myelin debris) (164, 166, 167). Although the large malformations of myelin ultrastructure in the advanced stages of demyelination is known, its subtle structural variations at early stages of demyelination remains poorly characterized.

First, structural changes in neuronal fiber tracts are usually studied by imaging methods that are still limited to access such information specifically and quantitatively. As has been described in Chapter 5, techniques such as Magnetic resonance imaging (MRI) and derivatives, or positron emission tomography (PET), are becoming important tools for the diagnosis of various white matter abnormalities, however the scale of the obtained information is not adequate to evaluate quantitatively demyelination processes at early stage. To access finer scales, the myelin ultrastructure has been studied using higher resolution imaging such as transmission electron microscopy (TEM) (150, 204), neutron scattering (205, 206) and small angle X-ray diffraction (XRD) (181, 207, 208). These techniques are however highly invasive.

In parallel, biochemical and biophysical studies have shown that such fine morphological alterations occur in conjunction with modifications of the lipid composition (charged vs. uncharged (156–158), saturated vs. unsaturated (37)) in the myelin sheath, which are thought to contribute to the loss of lipid membrane inter-layer adhesion. These changes include the formation of liquid-ordered phase (L_o) (46, 169, 209, 210) due to a high content in cholesterol and cerebroside, similarly as in isolated lipid membranes (211). It has been evoked that sub-diffraction scales domains of a liquid-ordered and liquid-disordered phases can lead to budding and vesiculation (212). Note that lipid's abnormalities have also been seen to be already present in the nonlesional white matter (normal appearing white matter) (170). Until now, only the combination of confocal Raman microspectroscopy and CARS microscopy have addressed lipid-packing information by optical means, showing a higher degree of lipid unsaturation in degraded myelin, which tends to increase lipid-packing order. These findings suggest that lipid organization might be affected in EAE tissues, even before any clear morphological sign of damage (37).

Besides glycolipids, phospholipids and cholesterol, myelin contains myelin basic protein (MBP) and proteolipid protein (PLP) making up to 80% of the total proteins. These proteins, in particular MBP, have shown to be also altered to the demyelination process, affecting interaction forces between lipid layers (155, 169, 213). MBPs are thought to contribute to the phase transition of lipid multilayers (214) and reversely, lipid modifications have been seen to provoke a cohesive meshwork of proteins at the membrane interface, which drives structural changes (169, 215).

Being able to read those fine structural alterations in the myelin sheath during the degradation, potentially *in vivo*, is thus of determining importance for a better understanding of the course of the demyelination progression. Optical imaging is able to address such scales, in particular combined with polarization. As was mentioned in Chapter 5, polarization dependence detection has been already applied to CARS imaging in such tissues, emphasizing a loss of polarization contrast dependence upon chemically-induced demyelination.

Benefiting from CARS microscopy, the morphology and density of myelin has been shown to be strongly affected throughout the progression of EAE *in vitro* (37, 38, 193).The g-ratio (ratio between the inner and outer diameter of the myelin fibers (152, 186, 190, 192) has been found to increase with the demyelination process and decrease with the remyelination provoked by injury in mice spinal cord (190) or in EAE (37). The g-ratio measured in mice spinal cords exposed to lysophosphatidylcholine (lyso-PtdCho), a well known demyelinating agent, was also found to be higher than in the normal myelin, due to the swelling process which enlarge the myelin sheath (47, 187). Even though the g-ratio can quantify events of demyelination/remyelination, it does not give any information on the possible molecular alterations within in the course of the disease progression.

To obtain more insight about the myelin structure, e.g. molecular packing information within the myelin sheath, polarization-resolved CARS (PR-CARS) has been developed as a sub-diffraction scale sensitive optical technique. Most of the PR-CARS approaches applied to myelin have been based on the use of tunable incident excitation polarizations to excite CH bonds in lipids. Different strategies have been developed to model molecular order in myelin lipid membranes. These models are based on the calculation of the CH_2 vibrational modes orientations, using either their $mm2$ symmetry tensor (without invoking orientational disorder) (78, 186) or a single diagonal tensor term undergoing a Gaussian orientational disorder (46). These models are over-simplified and in particular do not account for possible variations in lipids conformation, lipids composition and macroscopic disorder present in the complex samples. Other approaches do not interpret molecular organization but rather focus on the correlation between PR-CARS modulation responses and the local g-ratio, with visible correlation found in lyso-PtdCho induced demyelination (47). This suggests that PR-CARS is a good indicator of myelin health, however these studies did not relate the measured polarization dependencies to molecular order properties, nor to the progression of a disease.

In the present work we apply PR-CARS to explore the complexity of the orientational alteration of lipids in myelin sheaths during the active demyelination process that is associated with the progression of EAE. We show, in particular, that the the g-ratio revealing small details about the morphology of degenerated myelin, does not necessary report the myelin damage related to the progression of EAE. PR-CARS analysis of molecular order permits to analyze in more detail the myelin damage progression in EAE, in particular by the read-out by orientational organization of lipids which relates to both lipid composition changes and sub-diffraction scale morphological transformations.

6.1 Sample preparation and Methods

All samples were prepared at Institut de Neurosciences de la Timone (INT Marseille) by Franck Debarbieux and Alexandre Jaouen. All experimental procedures were performed in accordance with the French legislation and in compliance with the European Community Council Directive of November 24, 1986 (86/609/EEC) for the care and use of laboratory animals. The research on animals was authorized by the Direction Départementale des Services Vétérinaires des Bouches-du-Rhône (license $D\text{-}13-055-21$) and approved by the National Committee for Ethic in Animal Experimentation (Section N°14; project $87-04122012$). C57Bl6 mice (chronic MOG($35-55$)/CFA EAE) were housed in cages with food and water ad libitum in a 12 h light/dark cycle at 22 ± 1°C.

For the EAE induction, MOG($35-55$) peptide (75 μg in Freund's adjuvant containing 800 μg of mycobacterium tuberculosis) was injected into 3 different s.q. locations (bilaterally over the femur, and at the base of the tail), and pertussis toxin (400 ng) was injected i.p. Two days later mice were sedated and injected with a second dose of pertussis toxin (400 ng) i.p. Mice had easy access to food and water at all times. Supplement with a 3% agarose jelly containing to maintain animal hydration and weight. Glucose ($1-3\%$) was added to the jelly for additional calories. First clinical signs typically arised $13-14$ days post induction and were translated into clinical score as follows: 0, no detectable signs of EAE; 0.5, tail weakness; 1, complete tail paralysis; 2, partial hind limb paralysis; 2.5, unilateral complete hind limb paralysis; 3, complete bilateral hind limb paralysis; 3.5, complete hind limb paralysis and partial forelimb paralysis; 4, total paralysis of forelimbs and hind limbs (mice with a score above 4.5 to be killed); and 5, death. Control samples were also included from healthy mice.

For the *ex vivo* sample preparation, groups of animals were sacrificed when reaching predetermined clinical scores for subsequent ex vivo imaging of the myelin content in the dorsal spinal cord. Spinal cords were dissected, post-fixed overnight at 4°C and rinsed 3 times in PBS prior to embedding in a 3% agarose matrix to ease handling and 3D positioning under the microscope. Care was taken to align the dorsal surface of the spinal cord with the upper surface of the agarose cube. Note that the fixation method visibly does not affect the results presented in this chapter, indeed we performed a few measurements in fresh tissues that revealed very similar data.

For PR-CARS imaging (see Chapter 2, the OPO femtosecond excitation was chosen

(80MHz 150fs) with excitation wavelengths $\lambda_p = 830$ nm $\lambda_S = 1087$ nm, temporally synchronized and spatially overlapped on the sample plane. The corresponding excited wavenumber corresponds to lipid vibrations around 2845 cm^{-1} (dominated by the CH_2 stretching modes). The total power delivered to the sample lies in the range of 10-12 mW, focused by a water immersion objective (40X/1.15W Nikon Instruments Inc.). Imaging was performed in the epi inverted microscope geometry, using the dichroic mirror T770SPXR (AHF analysentechnik AG). Scanning rate was 20 μs per pixel, over 30 μm size images (100 × 100 pixels). For polarization imaging, the linear polarization angle of incoming beam was then rotated (see Chapter 2) in 10° steps over the range 0°-170°. The nonlinear signal collected by the objective was filtered using a shortpass filter (ET750sp-2p8, Chroma Technology Corp.) before being detected by PMT (R9110, Hamamatsu Photonics K. K.). The PMT detects the signal in the spectral range of 650 nm, previously filtered by a bandpass filter.

For statistical analyses, ANOVA tests where performed over populations with ($* : p \leqslant 0.05$) considered as statistically significant; ($** : p \leqslant 0.01$) as highly statistically significant; ($*** : p \leqslant 0.001$) as extremely statistically significant.

6.2 PR-CARS analysis in the myelin sheath of spinal cord tissues

Fig. 6.1a shows a typical CARS image of myelin sheaths in a mouse spinal cord, imaged at about $20 - 30$ μm below the spinal cord surface with linear polarization excitation along the spinal cord axis, reconstructed from stitched images of 100 μm × 100 μm sizes sub-images (see Chapter 7). The zoomed views show longitudinal sections of lipid multilayers of about $3-5$ μm in total diameter, wrapped around axons, here labeled with CFP, a Cyan Fluorescence Protein mutant (Thy1-CFP) expressed in the mouse and excited with 2PEF at the pump wavelength 830 nm (the modality for CARS/2PEF multimodal imaging will be more detailed in Chapter 7). The myelin morphology is seen to be strongly affected when the EAE score disease increases, from straight myelin tubular structures (Fig. 6.1b, score 0) to swelled features (Fig. 6.1c, score 1) coming from vesiculated myelin, and finally to the formation of debris with spherical shapes of various sizes, coming from disrupted myelin detached from the axon (Fig. 6.1d, score 2.5).

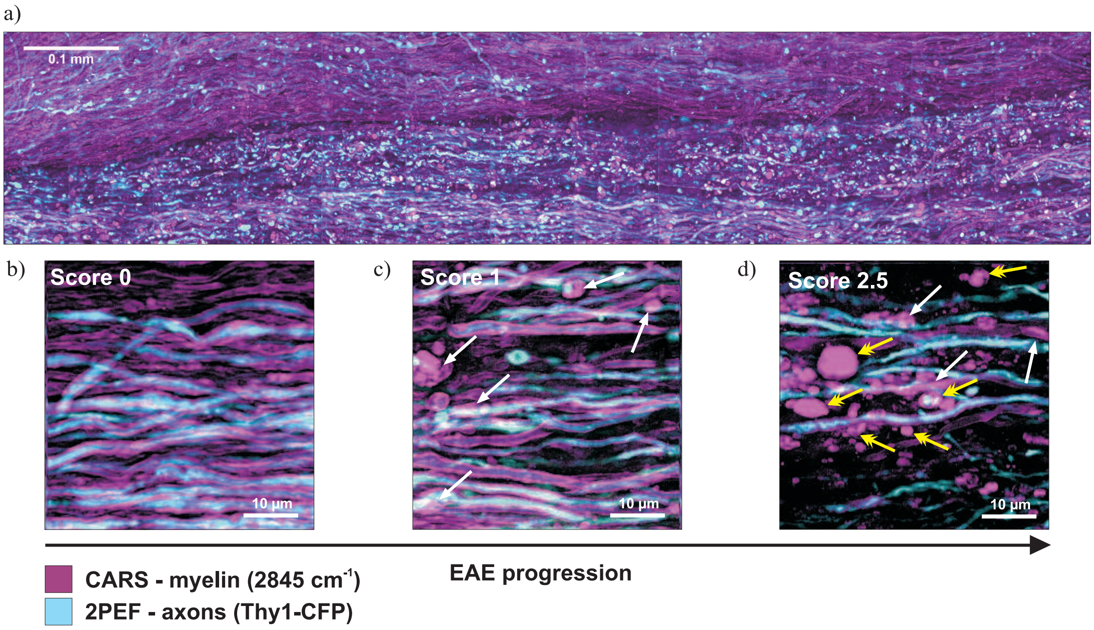

Figure 6.1: (***a***) CARS (violet, myelin lipid region around 2845 cm^{-1}) and 2PEF (magenta, Thy1-CFP labeled axons) image of a fixed spinal cord tissue taken at score 1. Scale bar: 100 μm. (***b-d***) Zoomed view showing the changes of myelin morphology through the progression of the EAE disease. Scale bars: 10 μm. (***b***) score 0, (***c***) score 1, (***d***) score 2.5. White arrows point myelin swelling events, while yellow arrows point myelin debris. All intensity images are formed with polarization lying along the spinal cord axis (horizontal on the image). Measurement depth below the sample surface: 20 μm.

6.2.1 Molecular order of lipids in the myelin sheath

A PR-CARS polarization analysis has then been performed on zoomed views of the myelin sheath structure, benefiting from high image sampling (pixel size is about 20 nm). Fig. 6.2 shows a typical image of a PR-CARS result in from a control spinal cord. The high contrasted intensity image (Fig. 6.2a) displays a strong and homogeneous signal from the longitudinal view of the myelin sheath wrapped around the axon. In our experiment this signal is dominated by symmetric and antisymmetric CH$_2$ stretching vibrations of hydrocarbon chains from lipids (2845 cm^{-1} and 2885 cm^{-1} respectively) which are the major components of myelin ($75 - 80\%$ of the weight of the myelin sheath). Little signal originates from CH$_3$ stretching vibration of proteins (2930 cm^{-1}) that constitute $15 - 30\%$ of the weight of the myelin sheath (37, 46). The analysis of the PR-CARS measurement (Fig. 6.2b-d) shows a strong orientational dependence of lipids, as evidenced by the S_2

image. This is consistent with a tight packing of lipids in the multilamellar structure of myelin. The S_2 image is strongly contrasted, advantageously emphasizing the myelin organized regions on a vanishing background ($S_2 = 0$ in an isotropic environment). A zoom on a φ_2 image shows that the general orientation of CH bond dipoles in the equatorial plane, is along the myelin tubular axis, as expected from lipids chains oriented radially in a concentric axonal structure.

The accessible fourth order symmetry of the CH bonds distribution provides additional information. $S_4^{(s)}$ is non negligible with values higher than the surrounding background (Fig. 6.2b), to an extent that can be informative on the bonds' distribution shape (see below). The $S_4^{(a)}$ values are close to 0 (Fig. 6.2c), confirming the cylindrical symmetry of the orientational distribution of bonds in the lipid organization. In what follows, S_4 will be often used as a shortened notation for $S_4^{(s)}$, and $S_4^{(a)}$ will be discarded.

Finally, $S_2, S_4^{(s)}$ and $S_4^{(a)}$ values plotted in scattered graphs (Figs. 6.2e,f) allow finer interpretation of the CH bonds orientational distribution in the lipid multilamellar structure. Clearly an order is visible (Fig. 6.2e) with $(S_2, S_4^{(s)})$ values above the measured data from the background, which features isotropic behavior. Comparing those values to model orientation distributions such as detailed in Chapter 1 allows moreover deduction of more quantitative signatures. Some comments have to be made however on the degree of relevance of the data interpretation.

First, S_2, S_4 values are only collected for high-enough intensity values, that guaranty sufficiently low bias and low noise. All studies will be performed for total intensities above 1400 counts (counts means here analog signal values), which guaranties standard deviations of 0.02 for S_2 and 0.08 for S_4 (see Chapter 2, figure Fig. 2.9). From the preliminary study performed in Chapter 2 we are also ensured that the S_2 bias is negligible. Concerning S_4, the remaining bias (which does not surpass 0.15 with the chosen intensities) is systematically removed from all measured values, accounting for the local pixel intensities and the reference noise-intensity dependence depicted in Fig. 2.9. The scattered graphs of (Figs. 6.2e,f) finally ascertain that there is no intensity-order correlation of the measured molecular order above 1400 counts, meaning that above this intensity thresholding, the measured parameters can be relevant for statistical analysis and comparison between different myelin regions and scores.

Second, some care has to be taken regarding the existence of non-resonant background in the data (see Chapter 4, Section 4.3.3). Considering our previous studies performed on model multilamellar lipid membrane vesicles, it is obvious that the non-resonant FWM signal can lead to an underestimation of S_2. The difference between measured values and

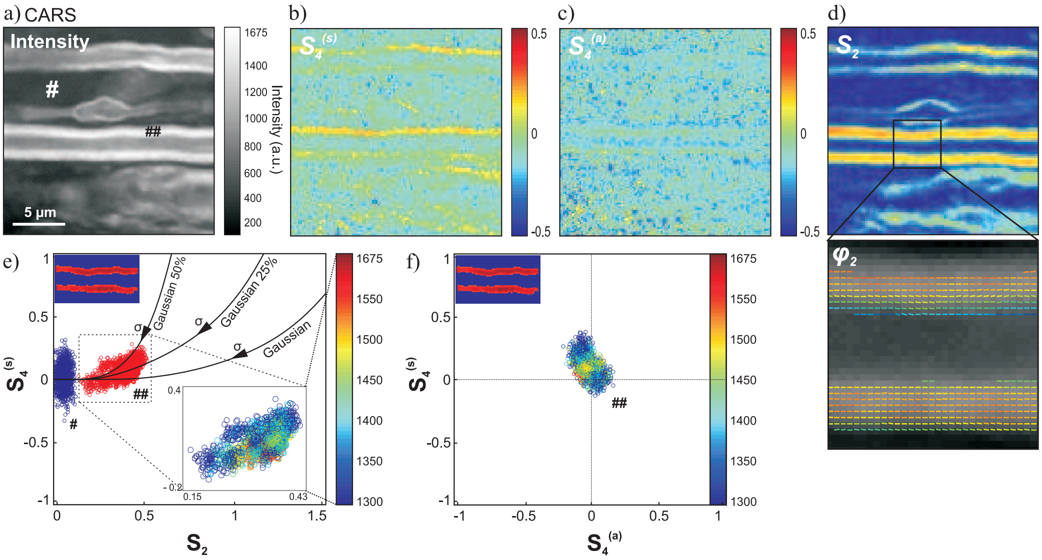

Figure 6.2: (***a***) PR-CARS total intensity image of myelin sheath from a control spinal tissue (summed over 18 input polarization angles α), centered at 2845 cm^{-1} CH-stretching vibrations. Scale bar: 5 μm. (***b***) Corresponding $S_4^{(s)}$ map. (***c***) $S_4^{(a)}$ map. (***d***) S_2 map. For those maps (not for the data analysis below) the PR-CARS dependent intensity is averaged over 3 $\times$ 3 pixels. A region of the S_2 map is zoomed in order to make more visible the complete orientational information, represented by a stick oriented with the φ_2 angle with respect to the horizontal axis, and which color is S_2. (***e***) Experimental values of $S_2, S_4^{(s)}$. These values are taken at high intensity signals from the myelin sheath (## in the intensity image (a)) and the lower intensity signal from a surrounding background (# in the intensity image (a)). For the myelin sheath region, the inset image shows the treated pixels which correspond to intensity above 1300 counts. The inset scattered plot is a zoom of $S_2, S_4^{(s)}$ in the myelin sheath region, emphasizing levels of intensities. To visualize better intensities in this region, a zoomed color bar has been applied between 1300 and 1675 counts. Solid lines: theoretical (S_2, $S_4^{(s)}$) values for a Gaussian distribution which width σ varies from 0° to 170°. Other lines represent a Gaussian superimposed by an isotropic distribution, which proportion in molecular population is 50% and 25% (see Chapter 1). (***d***) $S_4^{(a)}, S_4^{(s)}$ values in the same myelin region.

real ones (measured in absence of non-resonant background by SRS) have been estimated to be about 0.2 in DPPC multilamellar vesicles (MLVs), S_4 being almost un-affected (see Chapter 4). In what follows, we will display raw data, however it is worth noting that the real S_2 values have to be increased by an offset, which is most probably not higher than 0.2, considering that MLVs data are very close to values measured in myelin (see below).

Third, (S_2, S_4) values depend on possible out-of-plane orientations of the observed distributions. All the models in Chapter 1 assume that the molecular angular distributions are lying in the sample plane. In order to properly report structural properties of myelinated axons, one needs to ensure that the PR-CARS measurement is performed at the equatorial plane of the axon/myelin tube. Any out-of-plane orientation of the observed distribution can indeed bias the results interpretation by adding a component which tends towards isotropy. In order to estimate how the (S_2, S_4) order parameters depend on this effect in the myelin sheath, we performed PR-CARS measurements at several focusing

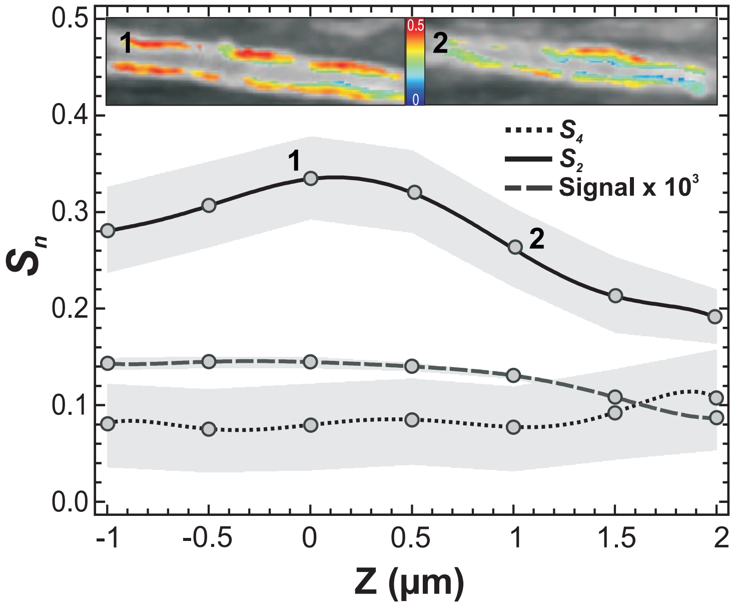

Figure 6.3: S_2 and S_4 mean values measured on a myelin sheath as a function of the sample depth Z. The shadow regions indicate the standard deviation of the order parameters (over all pixels in selected regions along the myelin sheath, according to an intensity thresholding of 75% of the maximum intensity measured in the image). Z= 0 corresponds to the depth of the myelin tube equatorial plane. Insets: S_2 images after intensity thresholding, at Z= 0 (point 1) and 1 μm above (point 2). Both images are superimposed with the CARS intensity images in grayscale.

planes (Z steps every 0.5 μm) crossing the whole 3D tubular structure of the myelin sheath from bottom to top (Fig. 6.3). The mean S_2, S_4 values are measured along a myelin straight feature with an intensity threshold of $\approx 75\%$ of the total intensity. The resulting order parameters exhibit a dependence on the geometrical changes caused by different planes of focusing. First, S_2 decreases when the plane of measurement departs from the equatorial plane of the myelin tube. This is consistent with the fact that when lipid molecular distributions start tilting out of plane, their projection in the sample plane looses order strength, towards more "apparent" isotropic distributions. However S_2 seems to still be robust over a defocus region of ± 5 μm around the equatorial plane. This means that as long as the myelin sheath looks visually in focus (which is the case for this defocus range), the S_2 measurement is reliable. Moreover its standard deviation does not depend on Z. S_4 on the other hand is very robust to a defocus change, which is consistent with the fact that defocus changes the apparent disorder of the distribution, not its shape. The only noticeable changes of S_4 is a slight increase at the largest depth of focus, however in this region the intensity also drops down and bias on S_4 is also most probable.

At last, the measured S_2 values can also be underestimated if the sample exhibits birefringence. Birefringence acts indeed as a distortion for excitation fields polarization state, making them elliptic and tilted relative to their expected directions (85) (see Chapter 2). Birefringence is however known to be non-negligible in the myelin sheath, due to their tight and regular arrangement of lipids (216). We estimated the birefringence phase shift in myelin sample slices of known thicknesses, as described in Appendix C. The found birefringence phase shift extrapolated for a depth of penetration of 30 μm (maximum focus depth used here) is in the range of $10°$ to $20°$. The induced polarization distortions have then been included in a model of the myelin sheath response (using input S_2, S_4 values close to the measured ones). The birefringence values are seen to induce a negligible bias of (< 0.05) for S_2, and of 0.05 for S_4. Even though the myelin birefringence is non negligible, the shallow depth penetration used here therefore allows neglecting this effect in what follows. It means however that care has to be taken in case of future investigations at deeper penetration distances.

Finally, based on proper selection of data points that originate from myelin sheaths equatorial planes, at shallow depths and with intensities above 1400 counts, the analysis of the (S_2, S_4) scatter plots of Fig. 6.2e can reasonably be used to model the observed angular distribution. Overall, a relatively high degree of order can be seen with averages $< S_2 >= 0.33 \pm 0.05$ and $< S_4 >= 0.10 \pm 0.07$ in the investigated region of interest of the myelin sheath (Fig. 6.2e). Interestingly, this molecular order is not far from that observed in DPPC MLVs ($< S_2 >= 0.25$ to 0.41 from PR-CARS data), which is made of pure lipids (see Chapter 4). The presence of several lipid types and proteins visibly does not enlarge much the angular distributions in the myelin sheath, confirming its tight organization along the axons. Looking closer at standard deviations, the orientational behavior of CH bonds exhibits a higher level of heterogeneity than in MLVs, which is coherent with their diversity (these bonds belong to CH_2 and CH_3 in lipids and proteins) and the complexity of the inter-lamellar interactions in myelin. Exploiting the information brought by S_4 brings further information. First, S_4 is non negligible and positive, which means that the orientational distribution of CH bonds in myelin is not a Gaussian nor a cone (see Chapter 1, Section 1.4.2). To explain this feature, a model accounting for the presence of an isotropic distribution (in addition to an existing Gaussian) has been introduced. The measured S_2, S_4 values lie in a region where this isotropic population might raise to an amount of 25% to 50% of the total molecular population, the rest being part of a Gaussian angular dependence. Accounting for the fact that S_2 is probably slightly underestimated due to the presence of non-resonant background, the amount of isotropic population is probably closer to 25%. This population can most probably be attributed to the presence of lipid layer sub-diffraction scale morphological features such as isotropic folds or small vesicles, as already speculated in MLVs (Chapter 4).

6.2.2 Relation between lipid packing orientational order and myelin morphology

The morphology of myelin sheath is changing during demyelination. The mechanism involves a structural transformation of the compact, multilamellar structure of myelin, as seen in the previous section, to swelling and the formation of degradation products named myelin debris. In this section we investigate if there is a correlation between the morphology of the myelin sheath (Fig. 6.1) and PR-CARS observations. When the EAE disease progresses in mice (increasing score), clear morphological features appear that are visible on the images. The number of swelling events increases, and finally the number of debris becomes dominant at high score (a more detailed analysis of these morphological signatures is given in Chapter 7). Here, to focus on the correlation between "visual" morphology and lipid packing orientational order, we show results that distinguish morphological features regardless of the scores. A more quantitative comparison between scores will be given in the next section.

PR-CARS measurements were performed at different stages of the EAE disease pro-

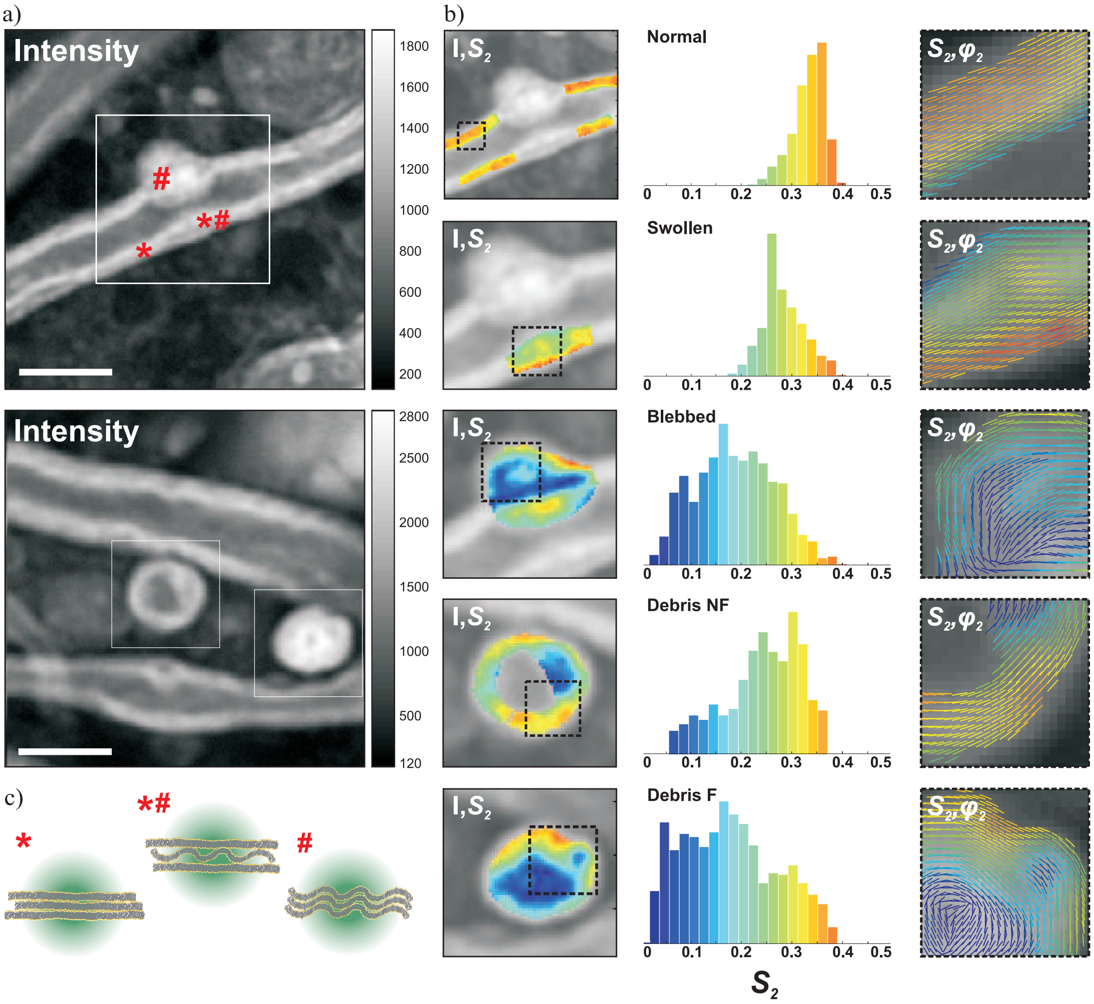

Figure 6.4: PR-CARS analysis of the different characteristic morphological features visible in the demyelination process. (***a***) Example of an intensity images, taken from samples with a clinical score 2 (upper) and 1 (lower). Symbols ($*, \#, *\#$) refer to different membrane location. White square region of interests (ROIs) are represented for (b). Scale bars, 5 μm. (***b***) *left*: S_2 maps (superimposed on the intensity image) of characteristic features of myelin degradation in white ROIs of (a): 'healthy' myelin, 'swollen', 'blebbed' and products of degradation: 'debris not filled (NF)' and 'debris filled (F)'. *middle*: corresponding histograms of S_2 values, taken within the dashed square ROIs in (b). *right*: combined images of S_2 and φ_2, showing S_2 as a colorscale and φ_2 as the orientation of sticks for each measured pixel. (***c***) Schematic morphological interpretation of the myelin multilayer within a pixel position (see (a)) corresponding to ($*$) 'healthy', ($\#$) 'swollen' and ($*\#$) 'blebbed' myelin.

gression in mice. CARS imaging was first performed to localize areas on fixed spinal tissues, chosen randomly over mm distances. Second, PR-CARS was performed in several small ROIs (10×10 to 30×30 μm size) at various places. CARS images permitted to determine 5 categories which are considered as representative of the different characteristic features observed within the demyelination process. These categories are depicted in Fig. 6.4: "normal" myelin has a visibly compact structure, with visible straight borders forming a tubular structure around the axon; "swollen" myelin defines more loose membrane formations within this straight structure, that has been identified to occur from loss of interlamellar adhesion and compacity within the lipid layers assembly; "blebbed" denotes a later stage of swelling, which forms a more pronounced protrusion outside of the straight myelin sheath structure; "debris" denotes a lipid multilamellar structure from vesiculated myelin, that has detached from the myelin sheath. The debris shape is spherical and is not any more physically connected to the membrane. Such debris, reported in the literature (164, 167), are found in two categories: "non filled debris" (debris NF), which show a clear lipid signal on their edge with axon signal inside visible by TPEF (see data in Chapter 7), and filled debris (debris F) that are pure lipids volumetric structures. Note that a few debris were observed in control spinal cords. We assumed, however, that they are not related with a progression of the disease and we did not take them into account. Nevertheless, we detected an increased amount of damaged or vesiculated myelin with the progression of the disease (see Chapter 7), as previously reported (37, 193).

For each category we measured molecular order of CH bonds, deducing (S_2, S_4) from PR-CARS data as previously described. We did not observe significant changes of S_4 in this study, therefore this parameter is omitted in what follows. We depict in Fig. 6.4b (left part) a zoomed image on each type of category found on samples of scores 1 and 2. On these images, S_2 values collected for a characteristic region are represented in an histogram (Fig. 6.4b, middle), illustrating the heterogeneity of molecular order for each mentioned category. At last, mean orientation (φ_2) and order (S_2) are represented in these regions (Fig. 6.4b, right), illustrating the spatial properties of such molecular order in healthy and damaged regions.

A few important observations can be made: 1) the average S_2 values decrease from normal ($S_2 \approx 0.30$) to swollen ($S_2 \approx 0.25$) and blebbed ($S_2 \approx 0.17$); 2) in blebbed and debris structures, S_2 is more heterogeneous than in normal structures, with lower molecular order in their inner membrane part than on their edge ; 3) molecular order in debris is preserved at their edge, with similar S_2 values as in swollen regions, with only inner membranes perturbed with high disorder; 4) the overall orientation of CH bonds, illustrated by (S_2,φ_2) images, seems to follow the membrane macroscopic structure whatever the disorder, even for low S_2 regions where the molecular scale disorder is high.

The transformation of normal, compact myelin structure into the final debris results therefore in important local rearrangements of multilamellar membranes structure. Interestingly, the CH molecular order measured in myelin is very close to that measured in MLVs in PR-CARS (see Chapter 4), which was found from $S_2 \approx 0.22$ (DOPC, not-filled MLVs) to $S_2 \approx 0.40$ (DPPC, not-filled MLVs). This shows that the presence of proteins does not strongly perturb CH order in the normal myelin sheath, confirming its tightly packed structure. Molecular scale order is however visibly decreased from normal to swelled/blebbed myelin, showing that the lipid layers organization is clearly perturbed at a molecular scale, especially in the inner membrane region. This perturbation could be partly due to lipid composition changes, that have been reported but not intensively studied (37, 158). More presumably the membrane morphology is affected, which is well known from the literature with studies essentially done in electron microscopy (150). We can indeed speculate that from one region of the damage to another, the lipid layer adhesion is perturbed from well parallel stacked layers (schematically represented in $*$, Fig. 6.4a) to partly folded inter-layer membrane regions in swollen myelin ($*\#$ in Fig. 6.4a) and finally to completely folded multi-layer membrane regions in blebbed myelin, where layer adhesion is lost ($\#$ in Fig. 6.4a). In particular, it has been shown previously that folds of tens of nanometer in height can lead to important modifications in the measured molecular order (S_2 shifts of up to 0.2), readable by PR microscopy (51).

Interestingly, even though molecular order modifications are strong from normal to blebbed myelin in the inner membrane, the averaged orientation of the CH organization is still following macroscopic membrane directions. It means that the order perturbation occurs at the molecular scale (lipids interactions perturbations) or even at the mesoscopic scale (membrane folds), rather than macroscopically. Sill as a result, the myelin sheath morphology is changed at microscopic scales, creating swelling and blebbing. Therefore even very small disorder events (molecular/mesoscopic scale disorder) are able to create longer scale damage events that extend spatially at up to micrometers distances, ultimately leading to debris.

Debris structure are the products of demyelination that are likely to originate from the loss of lipid organization of the inner membrane, described above in blebbed myelin. However we noticed that lipid order within debris is still high, showing that the overall multilamellar structure is preserved. We observed also that lipid order in the periphery of not-filled debris is rather high as compared to filled debris, similarly as what has been observed in DPPC MLVs in which the filled structures exhibited a lower molecular order (see Chapter 4). In not-filled debris, CH molecular order can even reach values measured in normal myelin sheaths. It is probable that membrane folds are decreased due to higher membrane tensions, as already observed in cell membranes (51). In contrast, the filled debris exhibit high heterogeneities: the lipid population inside the debris shows in particular very high disorder close to isotropy, most probably due to randomized packing.

These observations stay valid over a large population of observed regions; measurements performed on 359 regions (on average 70 regions per category) (note that the number of

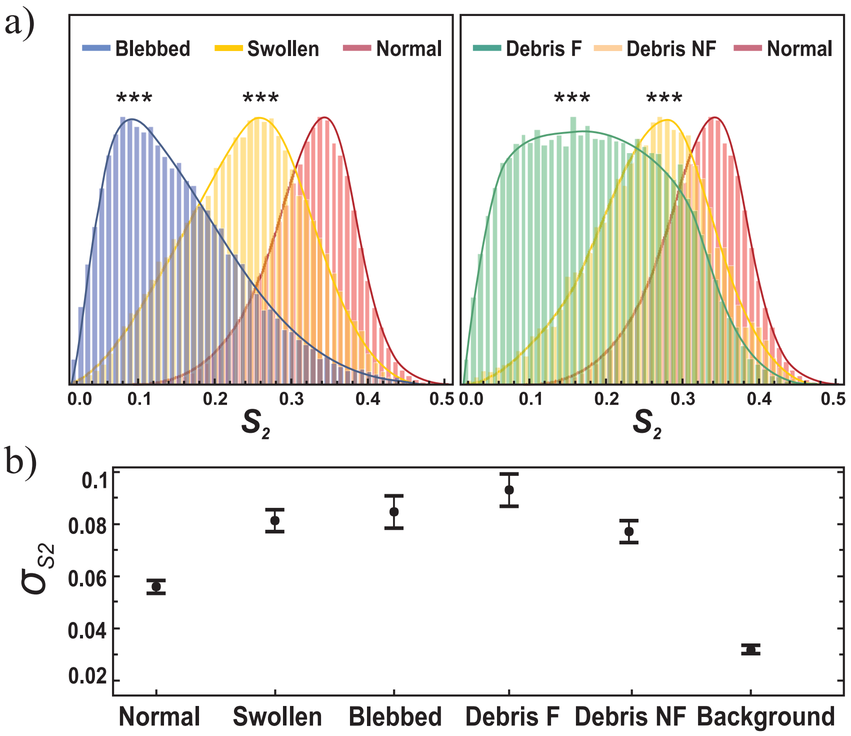

Figure 6.5: (***a***) General histograms (over all measured pixels) of characteristic features of myelin degradation plotted for all measurements, regardless the clinical score of the EAE disease (about 1000 pixels per regions). Number of regions measured: normal myelin (N = 136), swollen (N = 91), blebbed (N = 82), debris filled (F) (N = 30), debris not-filled (NF) (N = 20). $*** : p \leqslant 0.001$. (***b***) Corresponding standard deviations σ_{S_2} within each region, taken per category. The error bars are the standard deviation values over all regions measured.

measurements is quite heterogeneous, from myelin normal (136) to debris (20), since debris are less present at low scores). All measurements are summarized in global histograms in Fig. 6.5a. Independently of the stage of the EAE disease, normal myelin exhibits the highest degree of lipid packing ($< S_2 >= 0.32$), which corresponds to the smallest aperture σ of the effective distribution function $\approx 80°$. The degradation of lipid packing in the myelin lamellar structure of swollen regions is manifested by a decrease down to $< S_2 >= 0.23$, which correspond to an aperture σ of $\approx 100°$. Modeling this increase of angular distribution by membrane folds would correspond to folding amplitudes of about 10 nm over the spatial extent of the optical resolution of the imaging microscope (see reference (51) for the modeling method). In blebbed myelin, the averaged global order goes down to $< S_2 >= 0.14$, which corresponds to an aperture σ of $\approx 120°$. Concerning myelin degeneration products, the outer membrane of not-filled debris exhibit an averaged order of $< S_2 >= 0.25$, which is higher than for filled ones $< S_2 >= 0.17$. All cases show significant differences between each others, except for not-filled debris which resemble normal myelin.

The heterogeneity of molecular order within these regions is seen to increase for degraded myelin, as compared to normal myelin. We depict this trend in Fig. 6.5b, where the standard deviation of S_2 (σ_{S_2}) is plotted per category, over the number of pixels measured in each individual region. Normal myelin exhibits very low standard deviation ($\sigma_{S_2} = 0.06$). This value is not noise-limited (as visible in the low background value where $\sigma_{S_2} = 0.03$), but still characteristics of very homogeneous lipid packing. From normal to debris, this standard deviation increases with $\sigma_{S_2} = 0.08$ in swollen, blebbed myelin and not-filled debris, and $\sigma_{S2} = 0.09$ in filled debris. The filled debris regions indeed exhibit a very large histogram, mostly due to the fact that in these structures the inner membrane shows very disordered characteristics.

From those observations we can conclude that: 1) the lipid structural organization in myelin is affected in regions where myelin is affected morphologically, even in fine modifications such as swelling; 2) these organization changes are occurring at the molecular (lipid composition) and mesoscopic (loss of membrane adhesion, membrane folding) scales, since the macroscopic orientation of lipid distributions is non random even in highly disorder regions; 3) these changes occur principally at the inner part of the myelin sheath, close to the axon; 4) myelin debris are highly organized lipid structures, similarly as in MLVs. These conclusions support the fact that myelin degeneration and the formation of debris occurs most probably in conjunction with a local degradation of the lipid inter-layers contacts, an effect that is strong enough to induce long range deformations of the whole myelin sheath. The lipid organization is able to restore after the formation of debris, which seems to show that the composition has not drastically changed in the myelin debris.

6.3 Evolution of lipid organization in the myelin sheath with the progression of EAE

The different myelin morphological features described above, which characterize demyelination, were visible in all samples independently on the EAE clinical score, even though their occurrences varied from score to score. In this Section, we evaluate how S_2, in these different regions, depends on the clinical scores of EAE. This should allow a better assessment of the finer evolution of myelin microscopic-scale properties during neurodegeneration. For each measured score, two spinal cords have been imaged with equal number of regions per spinal cord, except for score 4 where only one sample was measured. First, normal myelin can be classified depending on its sheath thickness. For this we quantified the *g*-ratio of all measured myelin sheaths, defined by the ratio between the inner to the outer diameter of the myelin sheath (Fig. 6.6a). This parameter has been widely used in the literature to quantify the thinning of myelin sheaths, and more recently related to PR-CARS data in the frame of chemically induced demyelination (37, 47, 192). Values of *g*-ratio are found to be in the range from 0.3 to 0.65, which is consistent with what has been reported in the literature (186, 192). We then plotted *g*-ratio values versus $< S_2 >$ values measured in all studied regions, independently on the EAE score (Fig. 6.6b). We observe only a slight correlation between the two parameters, increasing $< S_2 >$ values corresponding to increasing *g*-ratio.

We then plotted *g*-ratio values for the different clinical scores of EAE (Fig. 6.6c). The variation of *g*-ratio values was seen to be very large even inside a given score population (as visible by the large standard deviations - note that at scores 1.5 and 4, the measured population size is low). There is no drastic trend of dependence between *g*-ratio and score. Notably, this shows that *g*-ratio assessment is probably not an obvious indicator of the disease evolution. Previous works have reported the use of *g*-ratio as a demyelination assessment (37, 47, 190, 192–194). In particular larger correlations were found between CARS polarization contrasts (here quantified with S_2) and the *g*-ratio (37, 47, 192). These works however addressed different situations. Observations of induced lesions have shown in particular that the *g*-ratio was increasing in the proximal region of the nerve injury, but also decreasing when measured in the distal area to the lesion (190, 194). In the present work, random regions are taken in the tissue. Other studies were focussed on remyelinated

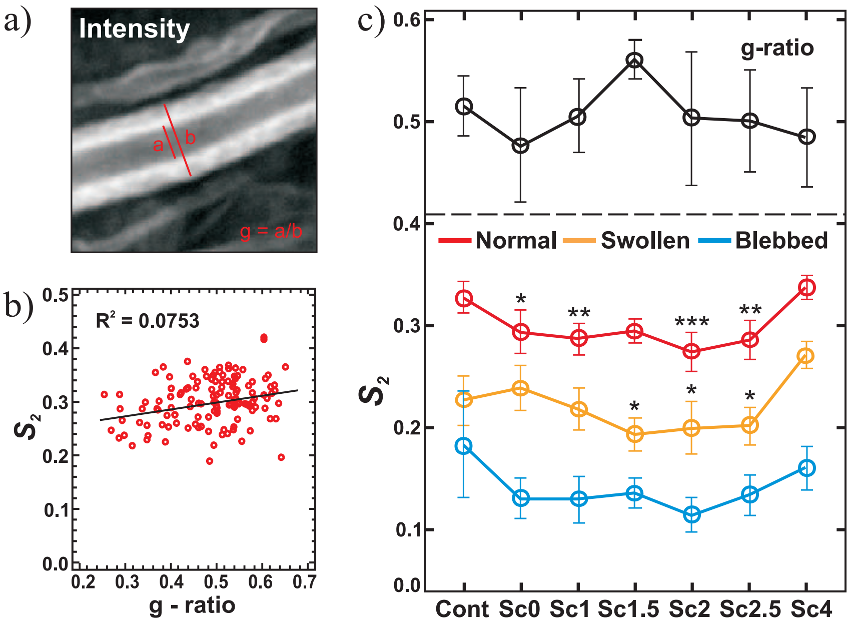

Figure 6.6: (***a***) Calculation of g-ratio in the equatorial plane of myelin fiber on the intensity image (a: inner diameter, b: outer diameter, g-ratio is the ratio between the inner and outer diameters). (***b***) Mean $< S_2 >$ values of all measurements versus g-ratio, with linear interpolation and correlation coefficient of the fit. (***c***) Top: mean g-ratio values versus the EAE score. Bottom: S_2 values versus different scores of EAE, for all different morphological categories of myelin detailed in text. Statistical analyses are shown relative to the control sample: $* : p \leqslant 0.05$, $** : p \leqslant 0.01$, $*** : p \leqslant 0.001$. Samples correspond to number of regions measured: control ($N_{normal} = 26$, $N_{swollen} = 5$, $N_{blebbed} = 3$), score 0 ($N_{normal} = 28$, $N_{swollen} = 26$, $N_{blebbed} = 25$), score 1 ($N_{normal} = 17$, $N_{swollen} = 11$, $N_{blebbed} = 8$), score 1.5 ($N_{normal} = 9$, $N_{swollen} = 5$, $N_{blebbed} = 10$), score 2 ($N_{normal} = 22$, $N_{swollen} = 17$, $N_{blebbed} = 15$), score 2.5 ($N_{normal} = 19$, $N_{swollen} = 16$, $N_{blebbed} = 10$), score 4 ($N_{normal} = 11$, $N_{swollen} = 6$, $N_{blebbed} = 9$).

myelin fibers (37) and explanted sciatic nerved exposed to lysophosphatidylcholine (lyso-PtdCho), a well known demyelinating agent (47). In the sciatic nerve, the myelin sheath is also thicker than in the spinal cord and therefore more easy to address by optical imaging analysis, due to its lower dependence to slight defocussing for instance.

In the present data, more pronounced variations were observed in S_2 values plotted for different EAE clinical scores (red curve in Fig. 6.6c). S_2 decreased from 0.33 ± 0.02 (control sample) to values in the range of 0.29 ± 0.01 (scores 0, 1, 1.5, 2.5) and even down to 0.27 ± 0.02 (score 2), before raising again at score 4 ($S_2 = 0.34 \pm 0.01$). All values show statistically significant changes as compared to the control sample, except scores 1.5 and 4 which are poorer in statistics. These data suggest that the molecular order inside myelin sheath decreases with the clinical signs of the EAE disease.

At last, we studied how molecular order - score relation behaves depending on scores. Fig. 6.6c reports S_2 score dependence in swollen and blebbed myelin. Apart from a small loss of order for scores 1.5 to 2.5, with visible heterogeneities, there is no strong changes of molecular order between scores in swollen/blebbed myelin for these affected regions.

Finally the most striking feature of this study is that in apparently normal myelin sheaths, even though the macroscopic morphology is similar from score to score, lipid order undergoes local molecular/mesoscopic-scale disorder with the EAE disease progression. This result emphasizes the potential of PR-CARS to reveal features that are not visible at a macroscopic scale, which is particularly interesting in the context of the monitoring of the evolution of a pathology. In particular it shows that in the context of EAE, the more traditionally used g-ratio factor, which is based on macroscopic-scale morphological information, seems less robust. Note that normal myelin is the most abundant population regardless the clinical score, and could thus serve ultimately as a convenient and robust assessment of the disease.

The present analysis brings also new elements of information in the understanding of the microscopic scale lipid membrane behaviors in neurodegenerative diseases, which has been a topic of high interest since decades. It has been reported that in the EAE pathology, different factors can contribute to the demyelination process that encompass molecular composition modifications and sub-diffraction scale morphological changes. While PR-CARS microscopy cannot distinguish between those two factors, quantitative elements can be gained from the measured modifications of lipid molecular order. Changes of lipid order phases in model multilamellar membranes (see Chapter 4, Section 4.5.4) have shown for instance that going from a liquid disorder (typically DOPC MLV at room temperature) to liquid order phases (typically DPPC at room temperature) can shift the measured order parameter S_2 from 0.2 to 0.4 (as read by PR-CARS). Our observation in the myelin sheath seems consistent with the changes observed previously in EAE models (37, 158), that have shown that lipids integrity (charge,saturation) is altered to lead to an increase in membrane fluidity, and to a decrease of myelin adhesion that provokes vesiculation. The loss of order and increase of heterogeneity observed with the disease progression is also consistent with the formation of lipid domains (46).

In parallel, it is known from our numerical models that increasing a single lipid membrane curvature can lead to significant changes in the read out of the S_2 parameter. Typically, a 10 nm height change within the diffraction limited spot of 200 nm leads to an increase of S_2 of 0.1 (51). Local folding has been quantified in demyelination processes using X-ray diffraction: it has been reported in particular that the highest efficiency of the myelin sheath to transfer an electrical impulse is reached when the lipid bilayers are highly compact against one to another, with a spacing of $\approx 3 - 4$ nm between lipid layers (155). An increase of spacing between bilayers ($\approx 6 - 7$ nm) has been seen to occur during the swelling process (155). Our data suggest a decrease of S_2 from normal to swollen of about 0.1, that could be consistent with such a small modification. Such fine morphological changes could be due to changes of membrane physical properties mentioned above, that lead to perturbations of electrostatic and hydrophobic forces, especially at the inner interface of the myelin sheath.

6.4 Conclusion

In this Chapter we have shown the possibility to probe lipid molecular orientational organization with a high level of detail, within the myelin sheath of mice spinal cord tissues. Our detailed PR-CARS analysis, performed in *ex vivo* spinal cords, shows that it is possible to follow quantitatively the molecular order of lipids within a single myelin sheath. Modifications of lipid order have been found in myelin structures that seem morphologically unaffected, emphasizing the possibility of the technique to decipher processes that occur at early stages of demyelination. The higher degradation of lipids order have been found in the processes of swelling and blebbing, especially at the inner interface of the myelin sheath, supporting the fact that myelin debris formation is progressing in conjunction with profound modifications of the molecular-scale packing in those regions. This supports early works which addressed local lipid modifications, and provides a way to address those questions in tissues, potentially *in vivo*.

Although these data are at this stage performed in the fs regime and thus un-resolved spectrally, future directions can be envisioned to study more precisely the origin of the observed phenomena by adding more chemical specificity. Indeed addressing lipid types and proteins could bring added values considering previous works performed on the lipid composition changes in the progression of the EAE disease. It would be interesting in particular to report local molecular order measurements on chemically specific units (e.g. saturated versus unsaturated parts of lipids), but also possibly cholesterol and proteins.

Ultimately if applied *in vivo*, this methodology could serve as a early biomarker for demyelinating diseases progression.

Chapter 7

Multimodal imaging of the CNS architecture in the progression of EAE

In this chapter we will present multimodal CARS and two-photon florescence imaging methods that give access into fine details in the architecture of the spinal cord tissue including axons, myelin and immune cell spatial organization. The potential of our method for multimodal imaging relies on the simultaneous imaging of different components of the central nervous system (CNS), which by carrying the information on the structure, dynamics and the morphological alterations reflect the healthiness or a pathological state of the tissue in the progression of a neurodegenerative diseases, Experimental Autoimmune Encephalomyelitis (EAE) and Multiple Sclerosis. Using this methodology, we present qualitatively the features of EAE progression on a sub-micrometric scale.

7.1 Animal model for studying Chronic Experimental Autoimmune Encephalomyelitis

In this study we imaged chronic MOG$(35-55)$/CFA EAE mice model in order to develop a multimodal imaging protocol that allows to monitor the architecture of spinal cord tissues during progression of the EAE disease. We used triple transgenic mice with multiple fluorescent cell populations:

- transgenic Thy1-CFP mice expressing cyan fluorescent protein (CFP) in most dorsal root ganglion (DRG) axons,

- LysM-GFP mice expressing enhanced green fluorescent protein (GFP) in peripheral myelo-monocytic cells, including granulocytes, circulating macrophage precursors and activated infiltrating macrophages,

- CD11c-EYFP mice expressing enhanced yellow fluorescent protein (EYFP) in subpopulations of myelo-monocytic cells resident to the spinal cord, such as dendritic cells and subset of microglia.

These mice were prepared at INT by A. Jouen and F. Debarbieux. They were backcrossed to C57/Bl6 mice (The Jackson Laboratory) and then crossbred to create Thy1-CFP//LysM-GFP//CD11c-EYFP triple transgenic mice (13, 14). A total of 21 adult mice were housed in cages with food and water *ad libitum* in a 12 h light/dark cycle at 22±1°C.

All experimental procedures were performed in accordance with the French legislation and in compliance with the European Community Council Directive of November 24, 1986 (86/609/EEC) for the care and use of laboratory animals. The research on animals was authorized by the Direction Départementale des Services Vétérinaires des Bouches-du-Rhône (license D-13 − 055 − 21) and approved by the National Committee for Ethic in Animal Experimentation (Section N°14; project 87 − 04122012).

All measurements have been made in fixed spinal cords. The description of the C-EAE induction, monitoring of the clinical score of the disease and an extraction of a spinal cord sample is detailed in Chapter 6.

7.1.1 Multimodal imaging and image post-processing

Multimodal imaging of all spinal cord samples from triple transgenic mice has been done using the "Main configuration" of the fs optical set-up described in Chapter 2 (Section 2.1.2 and Appendix B.2). All emitted signals were collected in epi-direction by four identical non-descanned detectors (PMTs).

In our multimodal microscope we excite simultaneously three fluorescent proteins (CFP, GFP and EYFP) by 2-photon excitation processes and the lipids localized predominantly in the myelin sheath by CARS. In order to optimize the excitation wavelengths and to find optimal set of filters for spectral separation of all fluorophores we recorded emission spectra (QE65 Pro, Ocean Optics) in a spinal cord sample from triple transgenic mouse (for this spectrometer replaces the PMT and no emission filter is used). As can be seen in Fig. 7.1a, a cyan fluorescent protein can be efficiently excited at 800 to 900 nm wavelengths while green and yellow fluorescent proteins at 910 to 970 nm wavelengths.

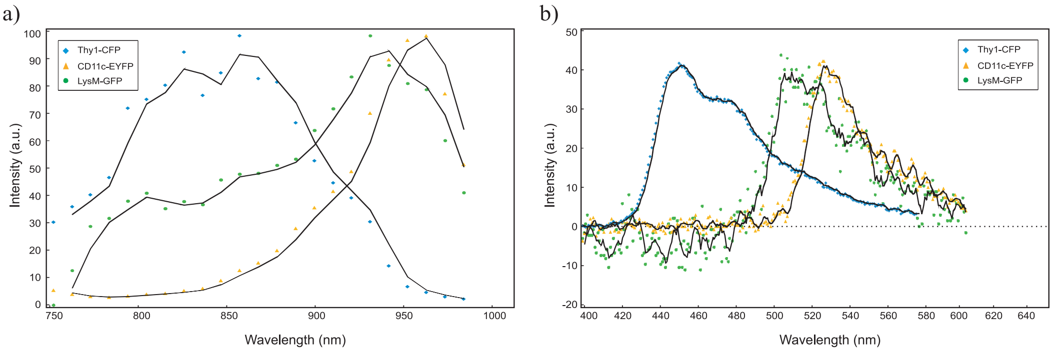

Figure 7.1: (***a***) 2PEF excitation spectra of fluorescent proteins CFP, GFP and EYFP (Adapted from *www.spectra.arizona.edu*). (***b***) 2PEF emission spectra of fluorescent proteins CFP, GFP and EYFP taken from the spinal cord sample.

In our scheme, the cyan fluorescent protein has been excited by the pump ω_p beam (830 nm) coming from a Ti:Sapphire output in a 2PEF process. The Stokes beam, on the other hand, needs to be spatially and temporally overlapped on the focal spot of the objective in order to produce two independent nonlinear processes such as multiphoton excitation of two other fluorophores (GFP and EYFP) and CARS targeting lipids in the myelin sheath. By selecting the frequency difference of the pump ω_p and the Stokes ω_S (1087 nm) beams to resonantly excite the stretching CH vibrations (2845 cm^{-1}) of lipids we detect the myelin sheath in the spinal cord tissue at $\omega_{aS} = 671$ nm. At the same time, the two other fluorescent proteins (GFP and EYFP), which spectrally are close one to another (Fig. 7.1a), can be excited by sum-frequency generation (SFG) process ($\omega_{SFG} = 2/(1/\omega_p + 1/\omega_{aS}) = 941$ nm) similarly as has been done in (10). The resulting fluorescent emission spectra are shown in Fig. 7.1b. Obviously, the emission spectra for GFP and EYFP are partially overlapped. We reduced this crosstalk by spectral filtering of the emission fluorescence signals using a set of narrow bandpass filters and dichroic mirrors as shown in Fig. B.4 (Appendix B.4). We furthermore corrected the residual spectral crosstalk by a post-acquisition image process (see below). The collinearly combined beams ω_p and ω_{aS} were focused into the sample by a 20× air objective lens with a numerical aperture of 0.75.

This method allowed us generate and collect all the signals simultaneously without motion induced mismatch between color channels, which can occur when each contrast is produced separately.

High resolution 3D mapping of a spinal cord tissue

We performed a 3D large-area imaging of spinal cord samples by stitching small scan regions (100×100 μm) together, into a large scan region of mm sizes. The first scan is performed with galvanometric scan mirrors and then the field of view (FOV) is enlarged in (X, Y, Z) with the help of a motorized stage devices (Märzhäuser) for lateral position control (X, Y) while the axial position (Z) was controlled by a piezo-stage device (PiFoc, Physik Instrumente). 10% spatial overlap was maintained between two neighboring FOVs to assist in stitching the individual images into one large area. Scanning and data acquisition were performed using a custom-build LabVIEW (National Instruments Corp.) program (80). In order to obtain high resolution 3D (X, Y, Z) maps, small FOVs of 100 μm $\times$100 μm size with 300×300 pixels each (333 nm/pixel) were recorded across an imaging volume. The typical dwell time for each pixel was 40 μs. 2D maps were recorded plane by plane ($\approx$ 2 mm $\times$1.7 mm size big) over a depth of 50 μm by increasing Z every 2 μm, starting form the spinal cord surface at the bottom of the sample. Complete 3D large-area maps were typically acquired overnight.

Post-acquisition image processing

Prior to analysis, some post-acquisition image processing was required to generate 3D maps of the spinal cord. First, all the raw 2D images were stitched together using "Stitching stack" and "Stitch Grid of Images" plugin on Fiji software (217) or using a home-made Matlab program. Second, due to the partial overlapping of the fluorescence emission spectra (Fig. 7.1b) the correction of the crosstalk between the fluorescence intensity signals was made using the linear spectral unmixing method (218) (see Appendix D). This correction was performed on raw data and all presented images are pseudo-colored and contrast enhanced for clarity. Occasionally, there was a (X, Y) drift between the Z planes in the 3D map. This was realigned using the StackReg plugin on Fiji (219).

7.2 CARS and 2PEF functional imaging of the CNS components

In this section we present the ability of multimodal CARS and 2-photon florescence microscopy to investigate in details the morphology and structural dynamics of CNS components as well as the potential of these techniques to follow the CNS related diseases.

7.2.1 Validation of the method for multimodal imaging of the CNS components

In order to validate our protocol to simultaneously visualize all addressed labeled CNS components, we recorded images on the same FOV of a spinal cord tissue extracted from a mouse manifesting complete tail paralysis (clinical score 1.5 of the C-EAE disease). It has been shown, that at this stage of the disease or spinal cord injury (SCI), in addition to commonly present axons and surrounding myelin sheath, the cells addressed here can be visualized (14, 37, 38). Fig. 7.2a demonstrates obtained 2D images of intensity signals for CARS, 2PEF and SFG processes, addressing myelin (CH stretching vibrations), axons (Thy1-CFP) and two population of cells (CD11c-EYFP and LysM-GFP), respectively. Images representing the intensities from cells expressing CD11c-EYFP and LysM-GFP fluorescent proteins (detector 3 and 4, respectively) were corrected for the crosstalk between the fluorescence signals using the linear spectral unmixing method (see

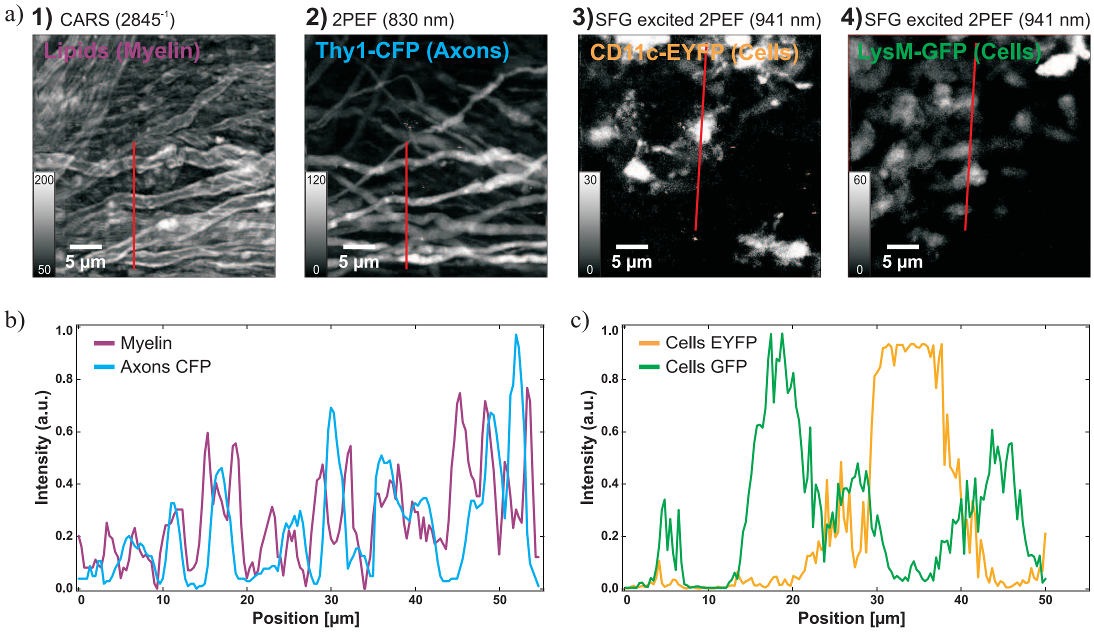

Figure 7.2: 2D images (summed over the entire depth of 50 μm) of the same FOV recorded with CARS and 2-photon processes on in all spectral channels denoted 1 (lipids, CARS), 2 (CFP), 3 (EYFP) and 4 (GFP). Detectors 1 and 2 did not required any image processing while detectors 3 and 4 were corrected for the intensity crosstalk between the fluorescence signals. (***c*** and ***d***) Resulting intensity profiles along the red lines shown in (***a***) for CARS/2PEF and SFG emitted signals, respectively.

Appendix D). High intensity signals are observed, especially for CARS and 2PEF exciting the CFP fluorescent protein. Less contrasted EYFP and GFP are possibly due to the lower efficiency of their fluorescence emissions, however, they are still easily distinguishable from the surrounding background. All addressed components of spinal cord architecture display moreover their distinct, characteristic morphologies. Myelin sheath, imaged by CARS (detector 1), is characteristic for its parallel running multilayered lipid membranes around the Thy1-CFP axons visualized with 2PEF (detector 2). Note, that the highest contribution to the CARS signals recorded in the epi-direction comes form lipids in the equatorial plane of the myelin fiber as has been shown previously (46). The intensity profiles of the myelin and axons fibers, shown in Fig. 7.2b, exhibit a strong 2PEF signal in the inside the myelin lipid layer, as expected. The population of CD11c-EYFP and LysM-GFP cells, imaged by SFG, display distinct morphological features. While CD11c-EYFP cells, as a resident to the spinal cord, have morphologies typical of microglia (220) with ramified processes, the infiltrating LysM-GFP cells localized mostly in the vascular lumen are spheroid or slightly ramified, which is consistent with the expression of this florescent protein in granulocytes and macrophages precursors (221). Fig. 7.2c shows clearly that these two subpopulation of cells do not spatially overlap validating in the same time the ability of the multimodal microscopy to simultaneously image and distinguish between the components of the spinal cord's tissue, even if these structures are spectrally similar.

In the next section we will demonstrate that the multimodal CARS and 2PEF imaging of the components of a spinal cords tissue can deliver rich information about the architecture and morphological alterations caused by the neurodegenerative disease progression.

7.2.2 Architecture of normal appearing white matter studied by CARS and 2PEF

In order to study the architecture of the white matter, we performed the large-view high-resolution 3D maps of spinal cord tissues with CARS and 2PEF multimodal imaging. All spinal segments (lumbar) were imaged on the dorsal side over 50 μm of depth. To facilitate their visualization, we generated 2D images by summing up the whole obtained 3D stacks

Figure 7.3: (Next page) Representative 2D image (summed over the entire depth) of 2PEF and CARS signals demonstrating Thy1-CFP axons (cyan) and myelinated structures (magenta) in spinal cord tissue extracted from the control mouse. Inset: Enlarged view of the longitudinal arrangement of myelin/Thy1-CFP axons structures.

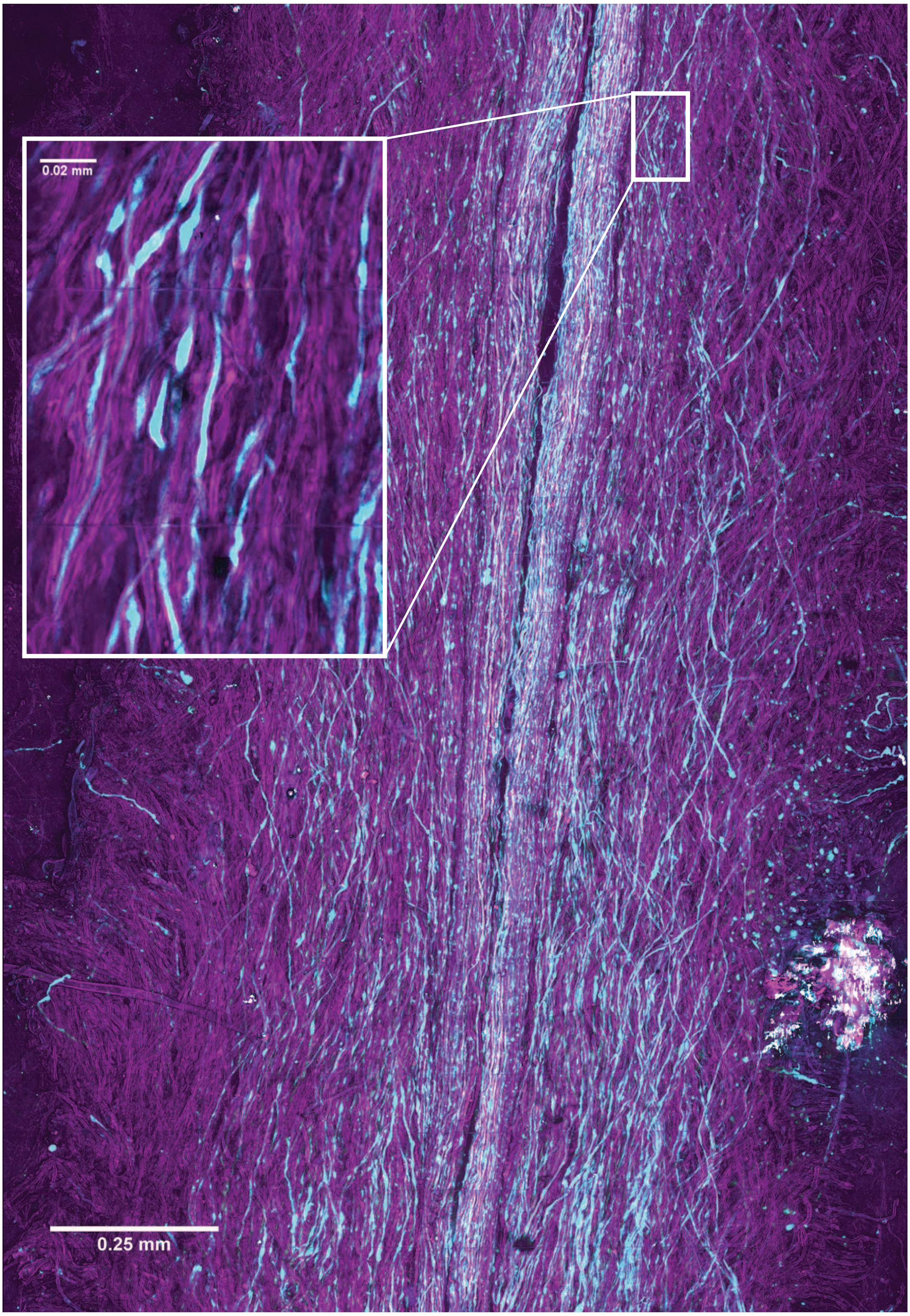
0.02 mm
0.25 mm

of images over its maximum intensity. As a first step we investigate the morphology of normal appearing white matter an a control mouse. Fig. 7.3 illustrates the morphology of normal-appearing white matter in spinal cord tissue extracted from a control mouse. The two recorded intensity signals of CARS addressing the myelin sheath by its lipid membranes and 2PEF exciting Thy1-CFP in axons are merged to obtain 2 color image. Interestingly, we did not observe the population of CD11c-EYFP cells, such as dendritic cells and microglia, which are residential to the spinal cord as has been shown in (13, 37, 38, 222), thus this observation require further investigation. In this high-resolution 2D image we can follow the axons and surrounding myelin sheaths which are distributed in a spatially well organized pattern, running in parallel with the spinal cord geometry. We can delineate, moreover, individual axons surrounded by a myelin sheath as well as their individual profiles (inset in Fig. 7.3). Note that some of the axons are not labelled due to the incomplete level of Thy1-CFP expression.

7.2.3 Multimodal CARS/2PEF imaging for studying the progression of C-EAE

As described in Chapter 5 (Section 5.2), there is a profound alteration of the central nervous system in the progression of EAE and multiple sclerosis pathologies. These alterations encompass a widespread inflammation, degradation of axons and surrounding myelin lipidic membranes as well as oligedendrocytes destruction in active EAE or MS lesions (159). Although the mechanism of progression in EAE and MS is unknown, the recruitment of microglial cells and macrophages has been shown to be associative with the progression of EAE (38, 223–225). In order to investigate the morphological hallmarks of the EAE progression, such as demyelination and axonal loss in relation with spatiotemporal distribution of immune cells, we mapped the extracted spinal cord samples at different stages of the disease by multimodal CARS and 2PEF imaging. The high-resolution 3D large-scale images were performed over a size of 2 mm on spinal tissues. Fig 7.4, Fig. 7.5 and Fig. 7.6 demonstrate the architecture of the spinal cord tissues belonging to mice which show no detectable signs (clinical score 0 for the C-EAE), manifest clinical symptoms as complete tail paralysis (score 1.5 for the C-EAE) and unilateral complete hind limb paralysis (score 2.5 for the C-EAE), respectively.

7.2.4 The morphological features of white matter in clinical score 0 for C-EAE

At score 0 of the EAE disease, where no clinical symptoms were visible, the white matter display, apart from normal-appearing parallel running axons and myelin, slightly enlarged and tortuous myelinated Thy1-CFP axons, suggesting alterations of the axons even at a very early stage of EAE, despite the preservation of myelin (inset 1 in Fig 7.4). On the periphery, a strong degradation of white matter is clearly visible (double arrowheads in Fig 7.4) as well as a spatial displacement of many Thy1-CFP axons. It is possible that this degradation and axonal displacement is caused by extraction of the spinal cord tissue, therefore, we do not consider them as morphological signs of EAE progression. While no presence of LysM-GFP cells is observed the population of CD11c-EYFP cells having a normal ramified morphology with small body and long processes is spread all over the spinal cord tissue (inset 2 in Fig 7.4). Moreover, we observe areas on the spinal cord tissue (inset 3 in Fig 7.4), where the Thy1-CFP axons even if having tortuous-like forms did not degraded while myelin sheath clearly show a signs of degradation such as a swelling, blebbing or has transformed into debris (for details see below). This alterations can, but do not have to occur in a presence of nearby localized CD11c-EYFP cell having a normal morphology. Nevertheless, it has been shown that the close apposition of these cells might participate in modulating the morphology of damaged axons through modification of the spinal cord microenvironment in the case of injured spinal cord (14, 226).

Figure 7.4: (Next page) Representative 2D map (summed over the entire depth) of the spinal cord tissue extracted from a mouse at clinical score 0 for C-EAE. CARS and 2PEF processes illustrate respectively myelin sheaths (magenta), Thy1-CFP axons (cyan) and CD11c-EYFP cells (yellow) which are spread all over the spinal cord tissue. We did not observe signal from LysM-GFP cells. Enlarged views of the morphological features are presented: Inset1: slightly degenerated myelin (arrow) and tortuous-like Thy1-CFP axon (double arrowhead); Inset2: CD11c-EYFP cells of normal, ramified morphology; Inset3: Slightly degenerated Thy1-CFP axons (double arrowhead) and myelin (arrow) fibers with few debris of myelin sheath in the presence of CD11c-EYFP cell. Double arrowheads on the periphery of the spinal cord show degraded myelin and axons possibly caused by extraction of the spinal cord tissue.

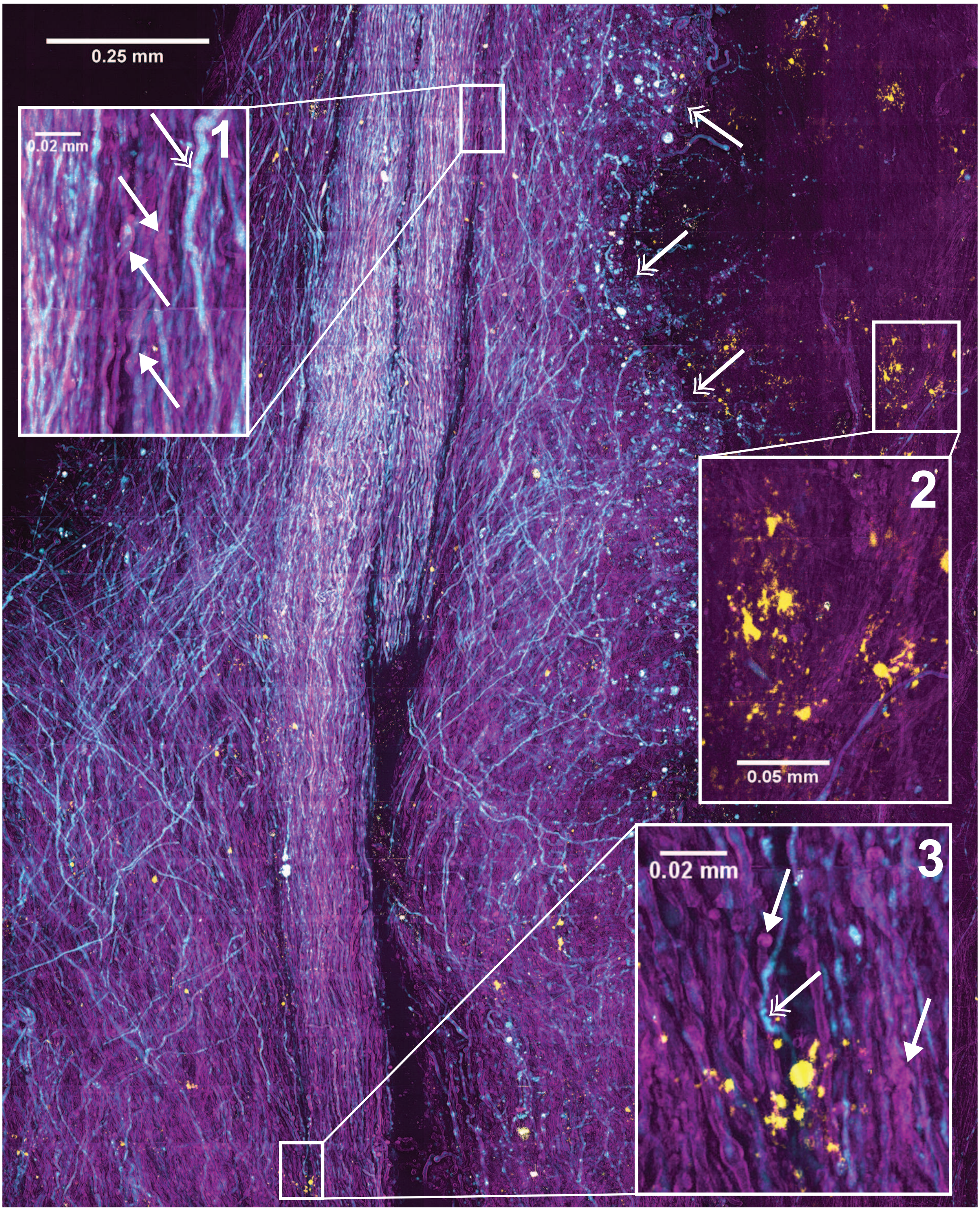
0.25 mm
1
0.02 mm
2
0.05 mm
3
0.02 mm

7.2.5 The immunological response of neuronal tissue to C-EAE progression

Contrary to the spinal cord extracted from mice showing no signs of the EAE disease (score 0), the architecture of CNS components in spinal tissue drastically changes where mice start to manifest a clinical symptoms such as the complete tail paralysis. In the spinal cord tissue extracted from mice determined as score 1.5 of the EAE (Fig. 7.5) we can observe boundary of focal lesions in the interior and on the periphery of the spinal cord tissue. All morphological hallmarks of ongoing neurodegradation are already visible on this stage of the disease. Myelin sheath display active morphological transformation characteristic for demyelination process (inset 1 in Fig. 7.5) such as swelling, blebbing or (less frequently) complete disruption (163–165, 167) at almost every place in the spinal cord tissue (inset 1 in Fig. 7.5). While myelin sheath exhibits clear transformations from its compact form, the Thy1-CFP axons do not degrade in the same way. Axonal degradation, known as Wallerian degeneration is generally seen as an enlargement of individual axons, swelling and forming axonal ovoids in actively demyelinating sides (162, 227, 228). It has been shown that such axonal abnormalities can be related with destabilization and alteration of microtubules that are necessary for axonal transport (159, 229). At this stage of the EAE progression, we observe widespread modifications of axonal fibers, mostly enlargement of individual Thy1-CFP axons and swelling and, less frequently, highly damaged Thy1-CFP axons and axonal ovoids (inset 1 in Fig. 7.5). As has been shown previously (37, 159, 223–225) the demyelination and axonal dysfunction are associated with inflammatory sites in active lesions on spinal cord tissues and brain. Similarly, we observed a high degree of inflammation and gliosis which were manifested by the presence of abundant CD11c-EYFP and LysM-GFP cells representing activated microglia and macrophages. These cells are widely distributed all over the spinal cord tissue and in some areas they formed a large aggregates or clusters (arrowhead in Fig. 7.5). Interestingly, we

Figure 7.5: (Next page) Representative 2D map (summed over the entire depth) of boundaries of lesions in a spinal cord tissue extracted from mouse at clinical score 1.5 for C-EAE. CARS and 2PEF processes illustrate myelin sheaths (magenta), Thy1-CFP axons (cyan), CD11c-EYFP (yellow) and LysM-GFP cells (green) which mostly form aggregates (arrowhead) spread in the spinal tissue. Enlarged views of the morphological features are presented: Inset1: Demyelination process and degeneration of Thy1-CFP axons (arrow); Inset2: Aggregates of spheroid LysM-GFP cells with few amoeboid CD11c-EYFP cells around highly degraded Thy1-CFP axons (arrow).

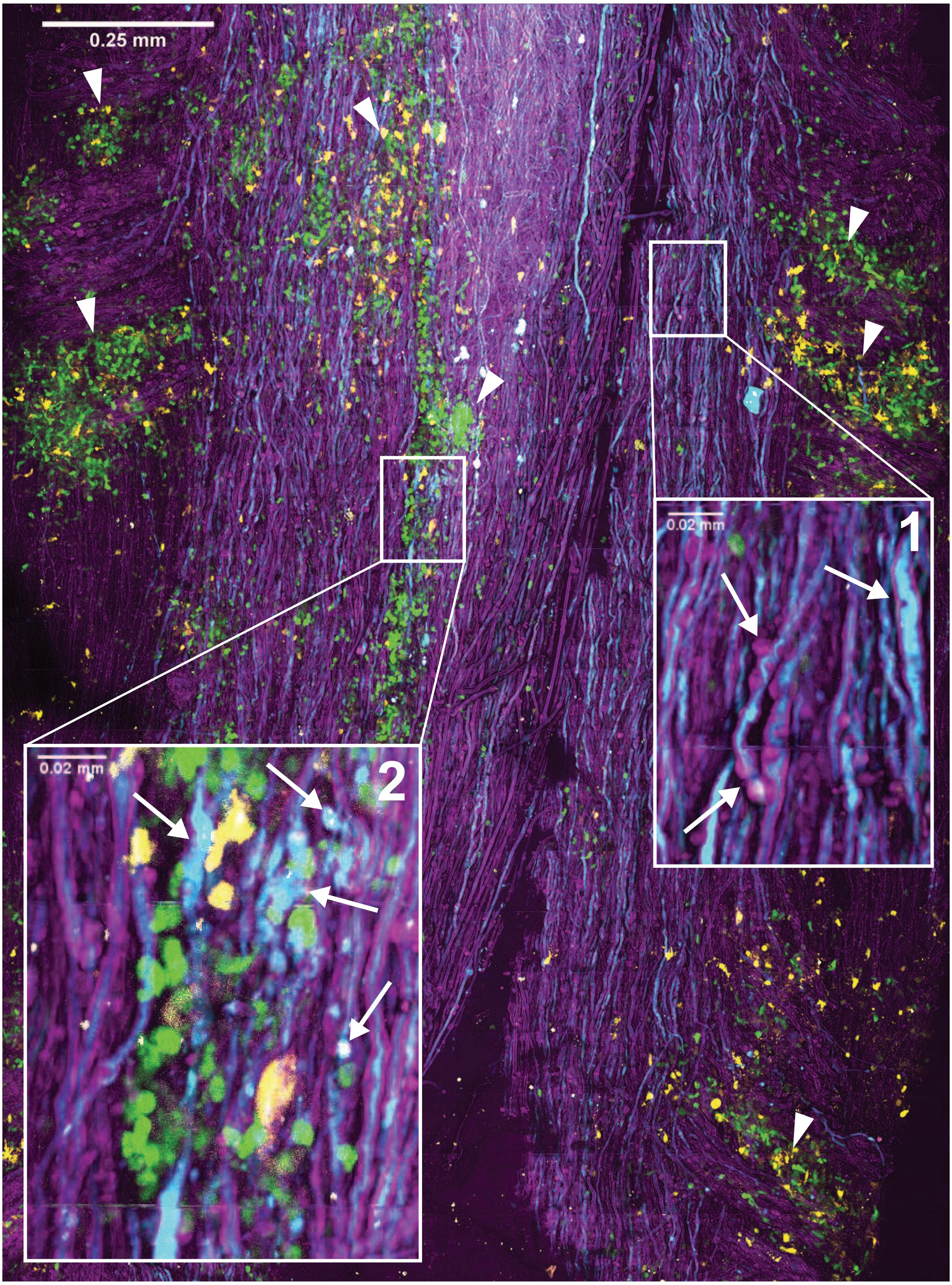
0.25 mm
0.02 mm
1
0.02 mm
2

observed that these clusters of CD11c-EYFP (less frequent) and LysM-GFP cells (more frequent) accumulated more in areas where the Thy1-CFP axons exhibited a high degree of damage (presence of axonal ovoids), although events of active demyelination have been found everywhere. Moreover, the CD11c-EYFP cells undergo morphological and molecular changes in response to EAE. In the mature intact spinal cord CD11c-EYFP cells are ramified with a small body and long processes consistent with typical morphology of microglial cells observed in score 0 of EAE (inset 2 in Fig 7.4, Section 7.2.4). In response to EAE, these cells transformed into amoeboid-like structures with shortened processes and developed large body, consistent with morphology of activated miroglia (inset 2 in Fig. 7.5) (220). The alteration of axons and myelin closely associated with persistent microglial/macrophage activation in the forebrain and the spinal cord has been observed previously in a mouse model of multiple sclerosis (37, 38) as well as a morphological transformation of microglial cells in immunological response after spinal cord injury (14). However, it has been not found yet, to our best knowledge, that the accumulation of the activated microglia/macrophages is associated more to highly damaged axons despite the overall demyalination and neurodegeneration.

7.2.6 Widespread demyelination and axonal degeneration in clinical score 2.5 for C-EAE

At a stage of the EAE disease, where mice show significant symptoms of the EAE disease, such as unilateral complete hind limb paralysis (score 2.5 for the C-EAE) the spinal cord demonstrates a high degree of degeneration (Fig. 7.6). We observe widespread ongoing neurodegeneration of white matter encompassing both demyelination and axonal damage

---

Figure 7.6: (Next page) Representative 2D map (summed over the entire depth) of highly degraded spinal cord tissue extracted from mouse at clinical score 2.5 for C-EAE. CARS and 2PEF illustrate complete or partial degeneration of myelin sheaths (magenta) and Thy1-CFP axons (cyan), as well as amoeboid (interior of the spine) and ramified (periphery of the spine) CD11c-EYFP (yellow) cells spreading all over the spinal cord and spheroid LysM-GFP cells (green) forming mostly an aggregates (arrowhead). Enlarged views of the morphological features are presented: Inset1: Advance stage of demyelination and neurodegeneration in the absence of myelo-monocytic cells. Inset2: myelin and Thy1-CFP axons debris surrounded by aggregates of CD11c-EYFP and LysM-GFP cells. Some of them contain myelin and Thy1-CFP axons debris (arrow).

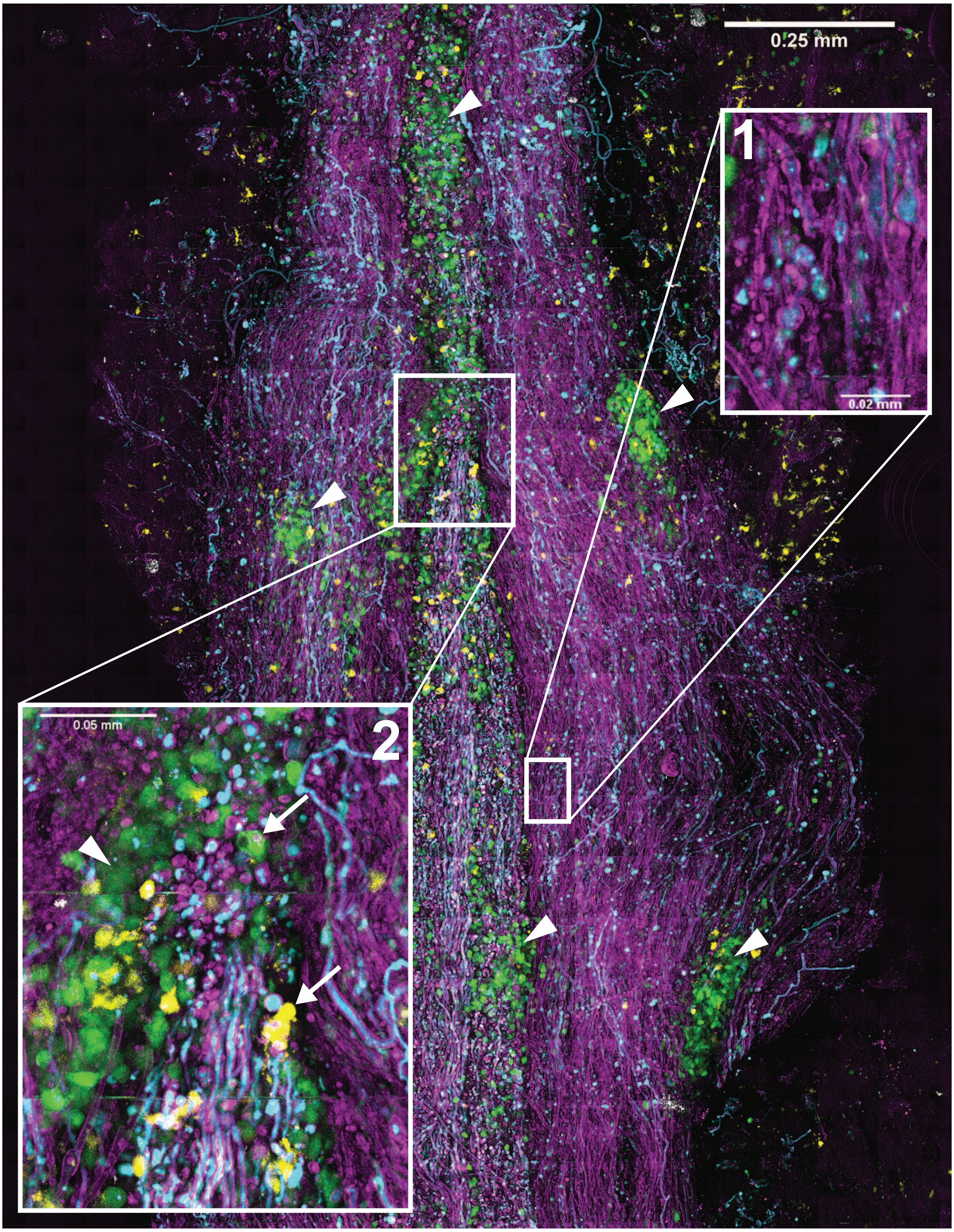
0.25 mm
1
0.02 mm
0.05 mm
2

all over the spinal cord tissue (inset 1 in Fig. 7.6). The degradation of Thy1-CFP axons frequently appears to be in its advance stage (manifested by axonal ovoids) as well as the myelin sheath which is largely swollen or blebbed and surrounded by numerous debris. The middle groove (septum) separating a spinal cord into two sides is dominated by almost completely degraded myelin and Thy1-CFP axons which are accompanied by abundant LysM-GFP cells (activated macrophages) and little CD11c-EYFP cells of amoeboid morphology (activated microglia). We observed that the LysM-GFP and CD11c-EYFP cells often contain remaining products occurring from demyelination and neuronal degradation, in the interior of their body as shown in Fig. 7.6 (arrow in the inset 2). Although the proliferation and activation microglia were observed in active EAE (148, 200, 230) or after spinal cord injury (14), their role is not completely understood. It has been shown, however, that microglia can play a role as a link between myelin degeneration and regeneration (231) by active clearing myelin debris. It has been observed, moreover, that in active EAE lesions inefficient clearance of these debris by microglia can limit demyelination process (232). Here, at this stage of EAE disease, the extreme abundance of myelin and axonal debris, especially in the spinal cord septum, visibly surpass the amount of active CD11c-EYFP cells that contain the degradation products after demyelination and axonal degradation, but the question about their dynamic remains open.

7.3 Final remarks and conclusions

In this chapter we presented the capability of multimodal CARS/2PEF microscopy to map the architecture of spinal cord tissue by addressing its characteristic components, such as myelin sheath, axons and two kinds of cells, resident and infiltrating of CNS. Using this methodology we were able to observe in details the morphology of healthy tissue and its structural alterations during progression of EAE disease on a sub-micrometric scale. Although these studies are yet qualitative, they give an overall and large amount of information about the demyelination, neurodegeneration and importantly, spatiotemporal distribution of resident and infiltrating cells that are associated with many hallmarks of EAE progression. The relationship between all of these CNS components has never been studied in details by using multimodal nonlinear imaging such as presented here. Many questions about the molecular mechanism in progression of EAE remain open and relatively noninvasive methods such as multimodal imaging over a large scale of specimen (still preserving sub-micrometric resolution) can be a first step toward the understanding a pattern of neurodegenerative diseases.

Because of the goal of present discussion is rather to demonstrate a potential of the multimodal CARS/2PEF imaging to investigate such a complex sample and not to give a complete analysis of EAE progression, we presented here only few examples of our data. We performed such measurements on large amount of samples with various pathological stages of EAE disease (from score 0 to score 4, with few samples per score). The examples presented here are consistent with observations found in other samples, however, all of these results require detailed, quantitative and statistical studies. Such studies are currently under work, for example the implementation of recently developed methods such as 2D Fourier transform (193) that can have a great impact on more quantitative conclusions.

Finally, the multimodal CARS/2PEF has been used here to visualize the architecture of fixed spinal cord tissues, but it can be used for any other sample including live tissues for *in vivo* imaging of the disease progression.

Conclusion and perspectives

In this thesis we presented the potential of polarization-resolved nonlinear microscopy to readout the molecular organization of lipid assemblies at sub-micrometric scale. We have seen here, that the methodology to probe the molecular order based on tunable linear polarization depends "only" on the nonlinear process used that drives the nonlinear interaction between light and matter, without invoking any specific constraints on molecular distribution. Such an advantage gave us the possibility to probe the molecular organization using different nonlinear contrasts, label-free methods based on the vibrational oscillations of induced molecular dipoles (SRS, CARS and FWM) but also using fluorescence (2PEF) to specifically excite fluorescent probes that can visualize the bio-molecular assemblies.

Comparison between these methods have driven us to the conclusion that noninvasive vibrational methods are indeed suitable and highly sensitive to probe the orientational behavior of lipids in model as well as biological membranes at sub-micrometric scale. We demonstrated moreover that fluorescent probes, when embedded into the lipid membranes, do not harm spatial organization of lipids, at least on small concentrations, and are able to reflect orientational behaviors with a high precision.

So far, most of approaches developed to probe molecular order have been confined to use a picosecond laser source due to its spectral sensitivity to resolve even a single molecular bond, or mode in complex lipid membranes, often struggling with a small amount of signal. We have shown that using picosecond laser system is not mandatory in such applications and can be replaced by femtosecond laser source in the case when no high spectral resolution is really needed.

With this knowledge, we have applied the femtosecond laser system, to probe the lipid organization and their orientational behavior in highly complex membranes, such as the myelin sheath in mice spinal cords. Using the EAE neurodegenerative disease as a model we have shown that myelin is a highly dynamic structure having fascinating capability to self-assembly into organized structures even during the demyelination process. The PR methodology was able to detect even small changes on molecular organization of lipids in myelin before any signs of damage. Moreover, by multimodal CARS and 2PEF imaging of the spinal cord architecture during the progression of EAE we were able to follow the process of degradation and spatiotemporal organization in which many components of central nervous system have its own role.

All of these results demonstrate a potential of probing the lipids molecular organization in biological samples using both label-free and fluorescence methods. Together with multimodal imaging, such studies could bring a new light not only on the fundamental processes that drive molecules to self-assembly but also to help for understanding certain mechanisms of lipid related diseases progression and the way the evolution of the pathology can be monitor. In this context, it would be of general interest to probe the lipids organization at sub-micrometric and microscopic scales in real time and in the future in living organisms. Such studies necessitate a fast polarization measurement and analysis since dynamical processes are involved with sub-second time scale. Along this direction, the recently developed method in our laboratory which uses direct measurement of order parameters (based on fast polarization modulation per pixel using Pockels cell polarization tuning) could speed-up the time of measurement. Another interesting perspective is also to couple polarization tuning with techniques that allow to image deeper into tissues, such as adaptive optics, providing that birefringence characterizations are accounted for to correct polarization distortions inherent to in-depth tissue penetration.

Overall, this PhD was dedicated mostly to the investigation of lipids organization in model and biological membranes, but it can be also used to probe other molecular assemblies, such as protein aggregates or crystals. Moreover, benefiting from the multimodality of the model it is possible to extend this studies toward probing various structures in biological systems by various nonlinear processes at the same time.

Appendix A

Relation between the order parameters (p_n, q_n) and the Fourier coefficients deduced from the PR-CARS measurement

Deduction of the order parameters from the CARS-FWM intensity is not as straightforward as from the SRS signal since the relation between the nonlinear susceptibility and the electric field is not linear:

$$P_I(\omega_{as}) \quad = \quad \sum_{JKL} \chi_{IJKL} E^*_{s,J} E_{p,K} E_{p,L}. \tag{A.1}$$

with the CARS dipole is oriented along direction I (X or Y). The intensity oriented along X (using electric field polarized in the (X, Y) plane) is thus proportional to the square of the CARS dipole which leads to:

$$I^{CARS}_X \quad \propto \quad \sum_{\substack{JKL \\ MNO}} \chi_{XJKL} \chi^*_{XMNO} E^*_J E_K E_L E_M E^*_N E^*_O. \tag{A.2}$$

and the total intensity is the summation of the intensity along X plus the intensity along Y:

$$I^{CARS} \quad = \quad I^{CARS}_X + I^{CARS}_Y. \tag{A.3}$$

In the same way as for SRS intensity, we can write the I^{CARS} as a truncated Fourier series with the angular frequencies are going up to the sixth order due to the presence of six electric fields in the intensity relationship (71, 78):

$$\begin{aligned} I^{CARS}(\alpha) \propto a_0 & +a_2\cos(2\alpha)+b_2\sin(2\alpha) \\ & +a_4\cos(4\alpha)+b_4\sin(4\alpha) \\ & +a_6\cos(6\alpha)+b_6\sin(6\alpha), \end{aligned} \tag{A.4}$$

where

$$\begin{aligned} a_0 &= \tfrac{1}{64}(36p_0^2+10p_2^2+10q_2^2+p_4^2+q_4^2) \\ a_2 &= \tfrac{1}{32}(24p_0p_2+3p_2p_4+3q_2q_4) \\ a_4 &= \tfrac{3}{32}(p_2^2-q_2^2+2p_0p_4) \\ a_6 &= \tfrac{1}{32}(p_2p_4-q_2q_4) \\ b_2 &= \tfrac{1}{32}(p_0q_2+3p_2q_4-3p_4q_2) \\ b_4 &= \tfrac{3}{16}(2p_0q_4+p_2q_2) \\ b_6 &= \tfrac{1}{32}(p_2q_4+p_4q_2). \end{aligned} \tag{A.5}$$

In the polar-resolved CARS signal, the retrieval of the distribution function from the Fourier coefficients is not straightforward. The nonlinear dependency of the Fourier coefficients with respect to the distribution function parameters is due to the nonlinear dependency of the CARS signal with respect to the susceptibility tensor, which is not the case in SRS. To estimate the distribution function parameters, an iterative algorithm can be employed to find the right set of parameters (71) (see Section 2.3.2, Chapter 2).

The Fourier coefficients (a_n, a_n) of the CARS/FWM intensity written in terms of the angular distribution function parameters (p_n, q_n) can be used in the case when the polarization state of the excitation fields is linear in the excitation volume. In practice, the presence of reflection optics along the path of the excitation light may introduce distortions in the polarization. Therefore, the presence of such distortions which can affect and possibly bias the read out of the symmetry orders, needs to be take into account when calculating the order parameters from the Fourier coefficients found from PR measurement (71). Polarization distortions, especially in the picosecond set up (Fig. 2.1 and Section. 2.1.3), have been introduced to the calculation according to (71).

Appendix B

Configuration of wavelengths and experimental optical elements used in these studies

Common abbreviations used in the description: OPO: optical parametric oscillator; AOM: acousto-optic modulator; $\lambda/2$: tunable achromatic half-wave plate; P, P-1, P-2: polarizing beamsplitter cubes; PMT: photomultiplier tube; PD: photodiode.

Objectives used in the studies:

- Obj. 1: NA = 1.15, 40×, water (Nikon)
- Obj. 2: NA = 0.75, 20×, air (Nikon)
- Obj. 3: NA = 0.45, 20×, air (Olympus)
- Obj. 4: NA = 0.6, 40×, air (Olympus)
- Obj. 5: NA = 1.0, 60×, water (Nikon)

B.1 The configuration in the ps system

Due to it high spectral resolution the picosecond set-up was used in particular:

- to perform CARS and SRS spectra of MLVs made of pure DPPC lipid. For each wavenumber in the range from 2750 cm^{-1} 3000 cm^{-1} with a step of 10 cm^{-1} we recorded SRS and CARS stack of polarization dependence images (from 0° to 170° with a polarization step of 10°) (Chapter 4).

- to perform the spectra (from 2020 cm^{-1} 3220 cm^{-1} with a step of 10 cm^{-1}) and PR-CARS and FWM measurements on MLVs made of deuterated d62-DPPC lipid, pure or mixed with cholesterol (Chapter 4).

Figure B.1 shows the combination of wavelengths and optical elements of the ps set-up used in these studies.

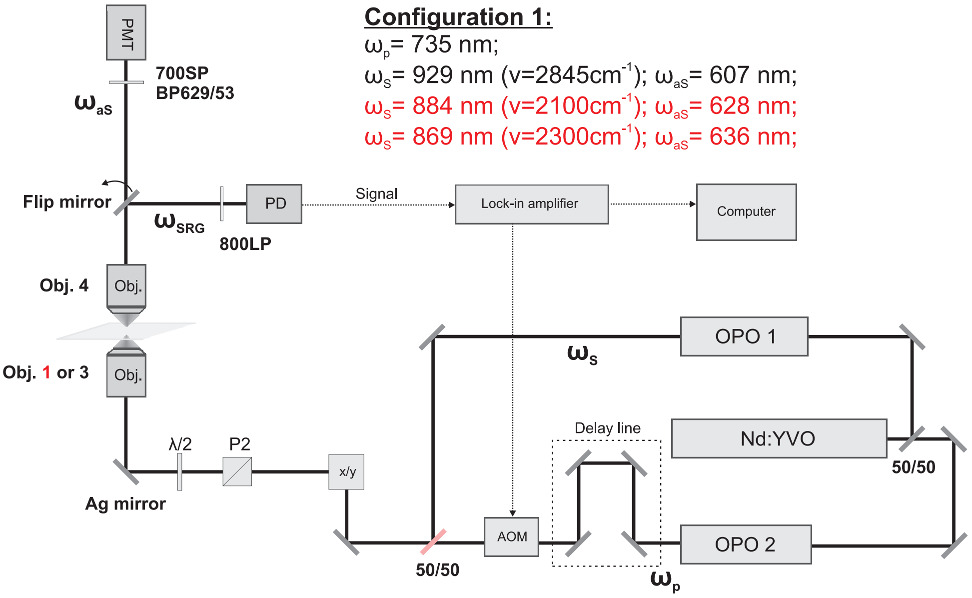

Figure B.1: The experimental configuration used in the picosecond set-up. The sample is illuminated by the different combination of the pump (735 nm) and the Stokes (929, 884 or 869 nm) beams. The spectrally filtered SRS (ω_{SRG}) signal is collected in the forward direction using either PD and lock-in amplifier after reflection on the flip mirror and the CARS (ω_{aS}) signal is directed to the PMT after removing the flip mirror.

B.2 The fs system - configuration 1, 2 and 3

In the case when higher SRS/CARS/FWM intensities were of a superior importance without the need for spectral resolution, we used the femtosecond set-up with a few different configurations (Figure B.2) that differ in their accessible wavenumber and fluorescence excitation/emission spectral ranges:

- Configuration 1 to perform PR- CARS and SRS measurements (centered at 2845 cm^{-1}) on MLVs made of pure DPPC, pure DOPC (immobilized in 1% of agarose gel or suspended in H_2O) lipid (see Chapter 4).

- Configuration 1 to perform all PR-CARS measurements (2845 cm^{-1}) on myelin sheaths in spinal cord tissues (see Chapter 6).

- Configuration 2 to perform the simultaneous PR- CARS, SRS (2845 cm^{-1}) and 2PEF measurements on MLVs made of DPPC, DOPC (immobilized in 1% of agarose gel or suspended in H_2O) lipids labelled with the TMA-DPH fluorescent dye (2PEF excitation: $\approx$ 780 nm, fluorescence emission $\approx$ 450 nm) (see Chapter 4).

- Configuration 3 to perform multimodal measurements on spinal cord samples (see Chapter 7) using the detection scheme shown in the Fig. B.4.

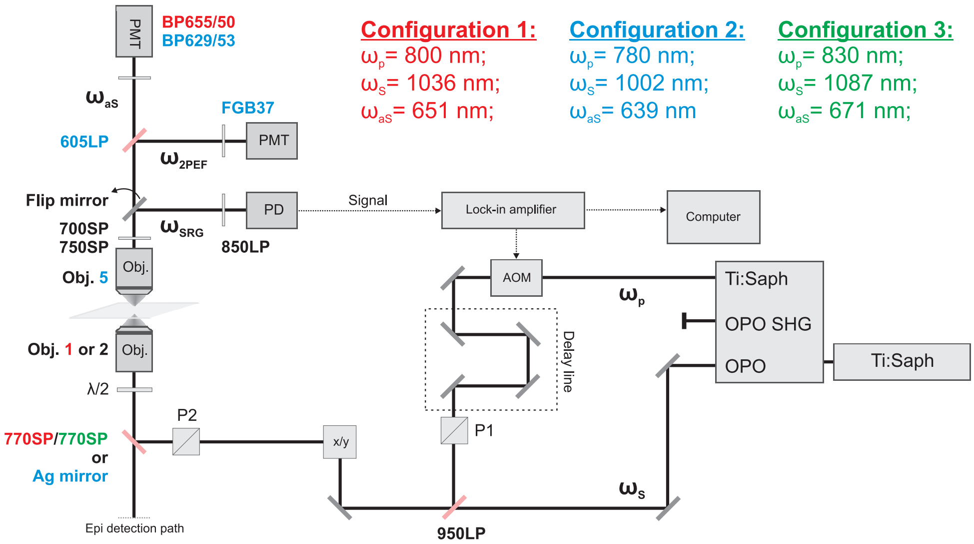

Figure B.2: The experimental configurations 1, 2 and 3 of the femtosecond set-up. The sample is illuminated by the the pump and the Stokes beams in one of the three configurations. The spectrally filtered CARS (ω_{aS}) and 2PEF (ω_{2PEF}) signals are collected either in the forward direction using PMTs or in the backward direction shown in the Fig. B.4. The spectrally filtered SRS (ω_{SRG}) signal is collected in the forward direction using PD detector. Optical elements used specifically in the configuration 1 are color coded in red, in the configuration 2 in blue and in configuration 3 in green. Black color corresponds to elements used in all configurations. The epi-detection path for this configuration is shown in Fig. B.4.

B.3 The fs system - configuration 4

The configuration 4 (Figure B.3) was similar to configuration 1, 2 and 3 but due to its different spectral range we present it separately. It was used to performed PR-CARS, SRS and TPEF measurements on MLVs made of DMPC lipid and labelled with the di-8-ANEPPQ fluorescent dye (see Chapter 4). Since the fluorescence emission in this case ($\approx$ 650 nm) falls in the spectral range of CARS emission of configuration 1, 2 and 3, it was necessary to shift the CARS emission wavelength.

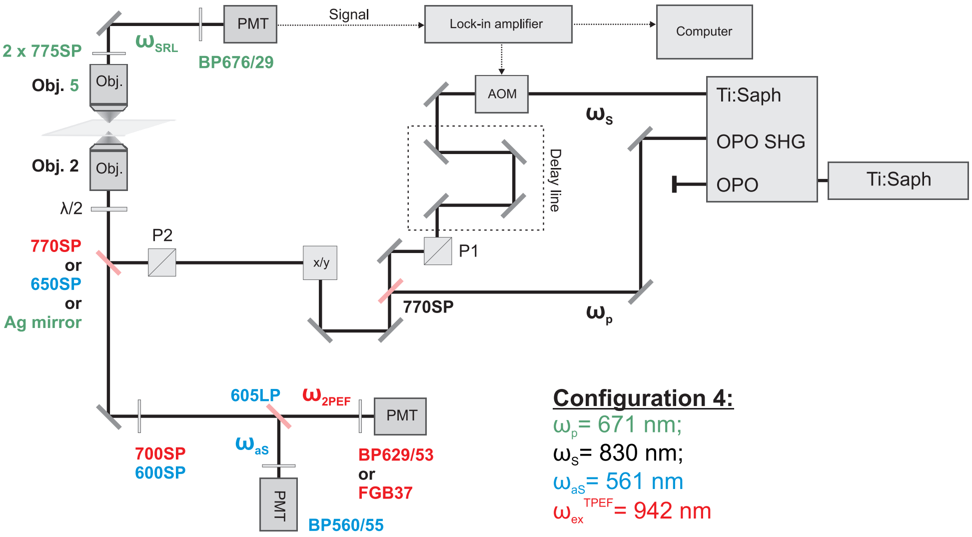

Figure B.3: The experimental configuration 4 in the femtosecond set-up. The sample is illuminated using only the Stokes beam (ω_{ex}^{2PEF}) to target the 2PEF process or by the pump (ω_p) and the Stokes (ω_S) beams to target the CARS and then SRS processes with a minimal 2PEF spectral leakage for the CARS channel. The spectrally filtered signals are collected sequentially. For the sequential measurement, first, we collect the fluorescence signal in the epi-direction using optical elements color coded in red. 2PEF frequency used here (ω_S corresponding to 942 nm) is more favorable for an efficient 2PEF excitation/emission of the lipid probe di-8-ANEPPQ. After shifting the Stokes beam (ω_S corresponding to 830 nm) the CARS signal (ω_{aS} corresponding to 561 nm) is collected in the epi-direction using elements marked in blue and SRS signals (ω_{SRL} corresponding to 830 nm) is collected in the forward detection using elements marked in green. Black color corresponds to elements used in all cases.

B.4 Epi-detection configuration in the fs system

Epi-detection scheme (Fig. B.4) was used to perform all multimodal experiments on mice spinal cord tissues where 4 different nonlinear responses need to be recorded in the same time (Chapter 7). It was also used to obtain all PR-CARS data from myelin in spinal cord samples (Chapter 6).

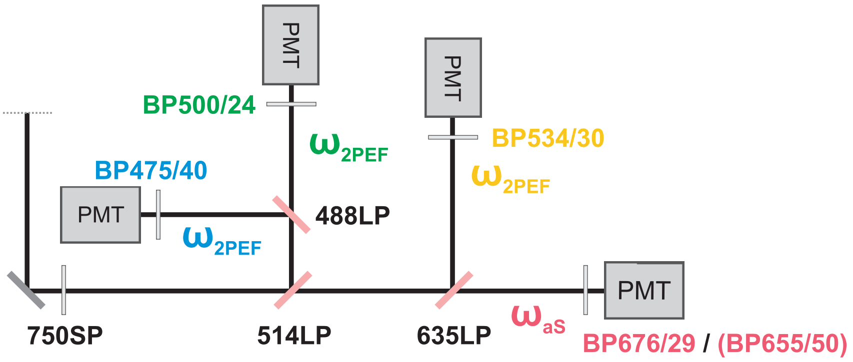

Figure B.4: Epi-detection configuration in the femtosecond system. Emitted light is spectrally divided and collected by 4 × PMTs. The emitted CARS signal is usually detected on the PMT in the straight configuration (Det.1). Colors of filters and dichroic mirrors correspond to the appropriate spectral range.

Appendix C

Birefringence effect measured on myelin in the spinal cord tissue

The measurement of birefringence following the method presented in (62, 67, 71) has been performed on a $d = 30$ μm thick cross section of spinal cord tissue in phosphate-buffered saline (PBS) (Fig. C.1a). Focusing a laser beam ($\lambda = 800$ nm) on the sample surface we rotated the linear polarization α from 0° to 170° with a step of 10°recording the stack of images of transmitted intensity modulation after a polarizer of vertical orientation (e.g. along the Y direction of the sample plane). For comparison, we performed the same experiment on a 170 μm thick glass coverslip next to the spinal cord slice tissue (with PBS) assuming it is isotropic and free of birefringence sample. In brief, the resulting polarization response in this isotropic case should be proportional to $\cos^2(\alpha)$, since there is no perturbation of the incident polarization state. which can be decomposed in a Fourier series ($I(\alpha) = a_0 + a_2 \cos(2\alpha) + b_2 \sin(2\alpha)$). This specific situation corresponds to amplitude and phase of the polarization which can be expressed as:

$$H_2 = \tfrac{1}{a_0}\sqrt{(a_2^2 + b_2^2)} = 1 \tag{C.1}$$

If a birefringence occurs in the sample with local thickness d, along a given direction $\Theta_b(d)$ (typically the local direction of lipid chains in a thick multi-layer membrane), then the fields components along this axis and its perpendicular will be phase-shifted by a value $\Phi_b(d)$. Accounting for this phase shift leads to a new intensity modulation, which contrast is not anymore $H_2 = 1$ since the polarization extinction is lost due to the existence of ellipticity. The new measured modulation characteristics are:

$$\begin{aligned} H_2 &= \tfrac{1}{a_0}\sqrt{(a_2^2 + b_2^2)} < 1 \\ \phi_2 &= 1/2 arctg(b_2/a_2) \end{aligned}$$

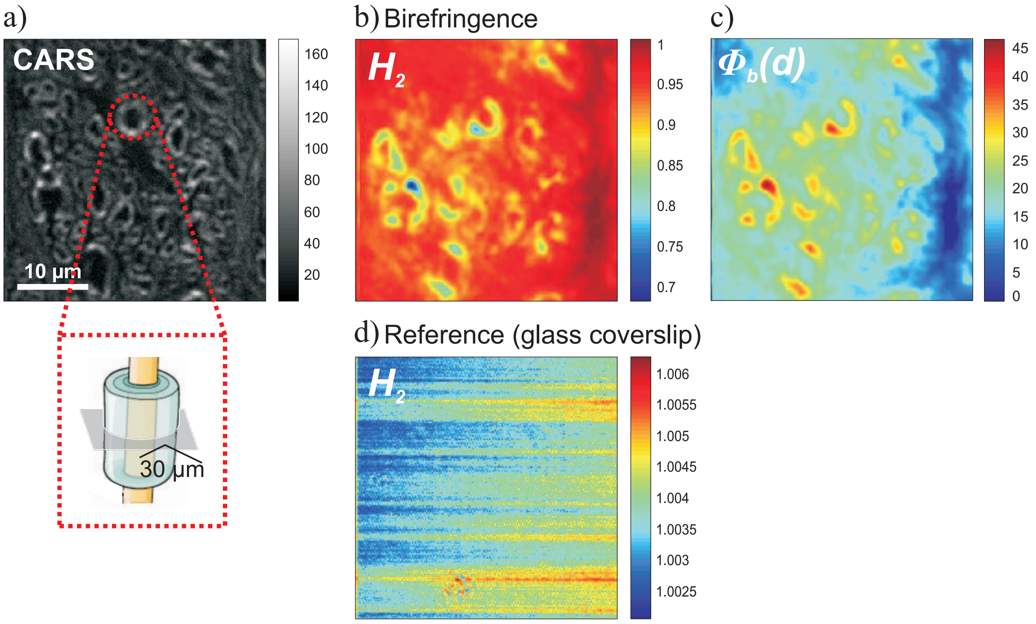

Figure C.1: (***a***) CARS image (2845 cm^{-1}) of spinal cord slice (mean thickness= 30 μm) on the region where the birefringence has been measured. (***b***) H_2 calculated map from the polarized signal measured on the spinal cord slice. (***c***) Deduced birefringence $\Phi_b(d)$ map of the birefringence main axis. (***d***) H_2 calculated map from the signal measured on a glass coverslip.

where H_2 and ϕ_2 are related to the birefringence phase shift $\Phi_b(d)$ and the main birefringence axis direction $\Theta_b(d)$ (see (62, 67, 71) for details).

Values of H_2 calculated from the transmitted signal through the spinal cord sample are depicted in Fig. C.1b. H_2 is clearly lower than 1 in many places of the sample, principally concentrated on the myelin sheath diameters. The deduced phase shift $\Phi_b(d)$ is shown in Fig. C.1c. In comparison, the reference glass coverslip H_2 is very close to 1 as can be seen in Fig. C.1d. The resulting $\Phi_b(d)$ values range from 10° to 20°for the 30 μm (on average) thick slice of the spinal cord sample, which indicates that the sample birefringence is quite large, as also previously reported in the literature. In practice, we do not perform PR measurements deep in the sample (maximum of 40 μm), thus the effect on data interpretation will be minimized, especially for the determination of S_2.

Appendix D

Image post-processing of recorded signals with multimodal microscopy

We used the linear spectral unmixing method (218) in order to spectrally separate the intensity signals recorded with multimodal microscopy. Fig. D.1a presents the 2D raw images (summed over the entire depth of 50 μm) recorded with CARS and 2PEF processes on four separated detectors. Visibly, the CARS signal (detector 1) addressing CH stretching vibrations (2845 cm^{-1}) as well as the 2PEF signal (detector 2) exciting CFP fluorescent protein are characteristic for their pure, high intensity signals and do not require any further image processing (Fig. D.1a, detectors **1** and **2**). On the other hand, the detectors 3 and 4, which display EYFP and EGFP intensities through 2PEF excited by SFG processes, contain an intensity signals from other detectors (Fig. D.1a: detectors **3** and **4**) and therefore required a correction by linear spectral unmixing method.

Finally, Fig. D.1b demonstrates obtained 2D images of intensity signals for CARS, 2PEF and SFG processes, addressing myelin (CH stretching vibrations), axons (Thy1-CFP) and two population of cells (CD11c-EYFP and LysM-GFP), respectively. The graphs in Fig. D.1c and d showing the intensity profile along red lines (Fig. D.1) confirm a spectral separation of signals for myelin and axons (detector 1 and 2) as well as for two population of cells (detectors 3 and 4) after correction with the linear spectral unmixing method. The accuracy of these signals, especially from cells has been further validated by recording emission spectra of resulting fluorescence intensities as shown in Chapter 7.

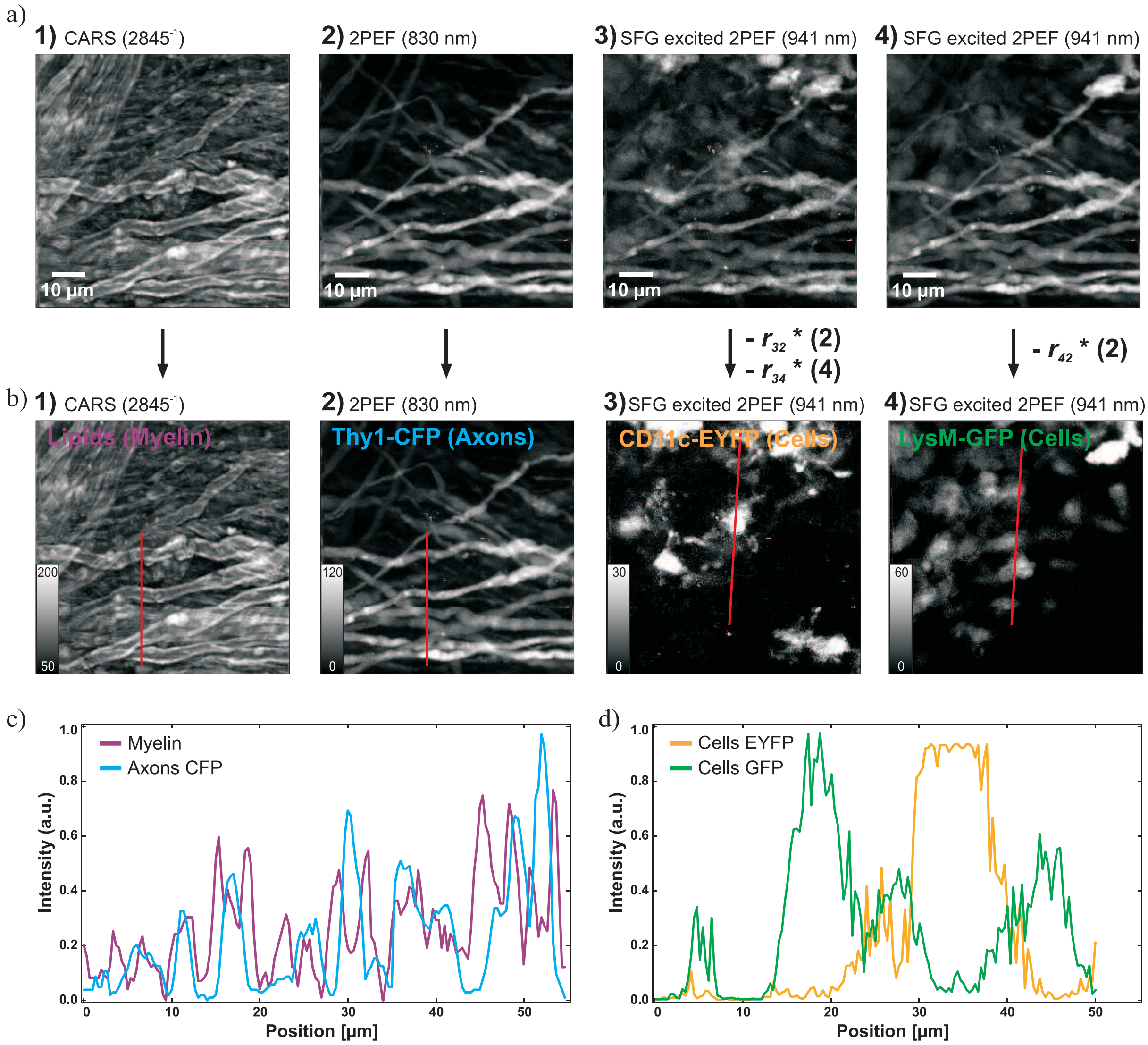

Figure D.1: Scheme showing the post-acquisition image processing used to remove crosstalk between the recorded fluorescence signals. (***a***) Raw images of the same FOV recorded with CARS and 2-photon processes on detector 1, 2, 3 and 4, respectively. (***b***) The same images as in (***a***) after linear spectral unmixing method operation. Detectors 1 and 2 did not require any image processing while detectors 3 and 4 were corrected by subtracting the crosstalk from other detectors with appropriate intensity ratio r_{ij}. (***c*** and ***d***) Resulting intensity profiles along the red lines shown in (***b***) for CARS/2PEF and SFG emitted signals, respectively.

Bibliography

[1] J. R. Lakowicz, *Principles of Fluorescence Spectroscopy.* Springer, 1999.

[2] T. Misgeld and M. Kerschensteiner, “In vivoimaging of the diseased nervous system.,” *Nature Reviews Neuroscience*, 2006.

[3] N. Bloembergen and P. S. Pershan, “Light Waves at the Boundary of Nonlinear Media,” *Physical Review Online Archive (Prola)*, vol. 128, pp. 606–622, Oct 1962.

[4] N. Bloembergen and Y. R. Shen, “Quantum-Theoretical Comparison of Nonlinear Susceptibilities in Parametric Media, Lasers, and Raman Lasers,” *Physical Review Online Archive (Prola)*, vol. 133, pp. A37–A49, Jan 1964.

[5] S. A. Akhmanov and R. V. Khokhlov, “Concerning One Possibility of Amplification of Light Waves,” *Soviet Journal of Experimental and Theoretical Physics*, vol. 16, 1963.

[6] J. Gannaway and C. Sheppard, “Second-harmonic imaging in the scanning optical microscope,” *Optical and Quantum Electronics*, vol. 10, no. 5, pp. 435–439, 1978.

[7] P. Campagnola, A. Millard, M. Terasaki, H. P.E., M. C.J., and M. W.A., “Three-dimensional high-resolution second-harmonic generation imaging of endogenous structural proteins in biological tissues.,” *Biophys Journal*, 2002.

[8] F. Helmchen and W. Denk, “Deep tissue two-photon microscopy.,” *Nature Methods*, 2005.

[9] W. Denk, J. Strickler, and W. Webb, “Two-photon laser scanning fluorescence microscopy,” *Science*, vol. 248, no. 4951, pp. 73–76, 1990.

[10] P. Mahou, M. Zimmerley, K. Loulier, K. Matho, G. Labroille, X. Morin, W. Supatto, J. Livet, D. Débarre, and E. Beaurepaire, “Multicolor two-photon tissue imaging by wavelength mixing.,” *Nature Methods*, vol. 9, pp. 815–818, 2012.

[11] H. C. Johannssen and F. Helmchen, “Two-photon imaging of spinal cord cellular networks,” *Experimental Neurology*, vol. 242, no. 0, pp. 18 – 26, 2013. New imaging techniques.

[12] J. Kerr and W. Denk, “Imaging in vivo: watching the brain in action,” *Nature Reviews Neuroscience*, 2008.

[13] K. K. Fenrich, P. Weber, M. Hocine, M. Zalc, G. Rougon, and F. Debarbieux, “Long-term in vivo imaging of normal and pathological mouse spinal cord with subcellular resolution using implanted glass windows,” *The Journal of Physiology*, vol. 590, no. 16, pp. 3665–3675, 2012.

[14] K. K. Fenrich, P. Weber, G. Rougon, and F. Debarbieux, “Long- and short-term intravital imaging reveals differential spatiotemporal recruitment and function of myelomonocytic cells after spinal cord injury,” *The Journal of Physiology*, vol. 591, no. 19, pp. 4895–4902, 2013.

[15] M. Kerschensteiner, M. Schwab, J. Lichtman, and T. Misgeld, “In vivo imaging of axonal degeneration and regeneration in the injured spinal cord,” *Nature Medicine*, 2005.

[16] D. Davalos, J. Grutzendler, G. Yang, J. Kim, Y. Zuo, S. Jung, D. Littman, M. Dustin, and W. Gan, “ATP mediates rapid microglial response to local brain injury in vivo,” *Nature Neuroscience*, 2005.

[17] Y. Kremer, J.-F. Léger, D. Goodman, R. Brette, and L. Bourdieu, “Late emergence of the vibrissa direction selectivity map in the rat barrel cortex,” *The Journal of Neuroscience*, vol. 31, no. 29, pp. 10689–10700, 2011.

[18] C. Dray, G. Rougon, and F. Debarbieux, “Quantitative analysis by in vivo imaging of the dynamics of vascular and axonal networks in injured mouse spinal cord,” *Proceedings of the National Academy of Sciences*, vol. 106, no. 23, pp. 9459–9464, 2009.

[19] M. D. Duncan, J. Reintjes, and T. J. Manuccia, “Scanning coherent anti-Stokes Raman microscope,” *Opt. Lett.*, vol. 7, pp. 350–352, August 1982.

[20] A. Zumbusch, G. R. Holtom, and X. S. Xie, “Three-Dimensional Vibrational Imaging by Coherent Anti-Stokes Raman Scattering,” *Physical Review Letters*, vol. 82, pp. 4142–4145, May 1999.

[21] C. Evans and X. Xie, "Coherent anti-stokes raman scattering microscopy: Chemical imaging for biology and medicine," *Annual Review of Analytical Chemistry*, 2008.

[22] A. Folick, W. Min, and M. C. Wang, "Label-free imaging of lipid dynamics using coherent anti-stokes raman scattering (CARS) and stimulated raman scattering (SRS) microscopy," *Current Opinion in Genetics & Development*, vol. 21, no. 5, pp. 585 – 590, 2011. Developmental mechanisms, patterning and evolution.

[23] E. O. Potma and X. S. Xie, "Detection of single lipid bilayers with coherent anti-stokes raman scattering (CARS) microscopy," *Journal of Raman Spectroscopy*, vol. 34, no. 9, pp. 642–650, 2003.

[24] Y. Fu, T. B. Huff, H.-W. Wang, J.-X. Cheng, and H. Wang, "Ex vivo and in vivo imaging of myelin fibers in mouse brain by coherent anti-stokes raman scattering microscopy," *Opt. Express*, vol. 16, pp. 19396–19409, Nov 2008.

[25] Y. Shi, D. Zhang, T. B. Huff, X. Wang, R. Shi, X.-M. Xu, and J.-X. Cheng, "Longitudinal in vivo coherent anti-stokes raman scattering imaging of demyelination and remyelination in injured spinal cord," *Journal of Biomedical Optics*, vol. 16, no. 10, pp. 106012–106012–4, 2011.

[26] A. Volkmer, L. D. Book, and X. S. Xie, "Time-resolved coherent anti-stokes raman scattering microscopy: Imaging based on raman free induction decay," *Applied Physics Letters*, vol. 80, no. 9, pp. 1505–1507, 2002.

[27] G. I. Petrov, M. Zhi, D. Wang, and V. V. Yakovlev, "Nonresonant background suppression in coherent anti-stokes raman spectroscopy through cascaded nonlinear optical interactions," *Opt. Lett.*, vol. 38, pp. 1551–1553, May 2013.

[28] W. Min, S. Lu, M. Rueckel, G. R. Holtom, and X. S. Xie, "Near-degenerate four-wave-mixing microscopy," *Nano Letters*, vol. 9, no. 6, pp. 2423–2426, 2009. PMID: 19432483.

[29] P. Mahou, N. Olivier, G. Labroille, L. Duloquin, J.-M. Sintes, N. Peyriéras, R. Legouis, D. Débarre, and E. Beaurepaire, "Combined third-harmonic generation and four-wave mixing microscopy of tissues and embryos," *Biomed. Opt. Express*, vol. 2, pp. 2837–2849, Oct 2011.

[30] B. Pearson and T. Weinacht, "Nonlinear optics: Three-in-one microscopy," *Nature Photonics*, 2012.

[31] B. Saar, C. Freudiger, C. Stanley, G. Holtom, and X. Xie, "Video-rate molecular imaging in vivo with stimulated raman scatter," *Science*, 2010.

[32] L. Kong, M. Ji, G. R. Holtom, D. Fu, C. W. Freudiger, and X. S. Xie, "Multicolor stimulated raman scattering microscopy with a rapidly tunable optical parametric oscillator," *Opt. Lett.*, vol. 38, pp. 145–147, Jan 2013.

[33] C. W. Freudiger, W. Min, B. G. Saar, S. Lu, G. R. Holtom, C. He, J. C. Tsai, J. X. Kang, and X. S. Xie, "Label-free biomedical imaging with high sensitivity by stimulated raman scattering microscopy," *Science*, vol. 322, no. 5909, pp. 1857–1861, 2008.

[34] W. Zipfel, R. Williams, and W. Webb, "Nonlinear magic: multiphoton microscopy in the biosciences.," *Nature Biotechnology*, 2003.

[35] D. Debarre, W. Supatto, A.-M. Pena, A. Fabre, T. Tordjmann, L. Combettes, M.-C. Schanne-Klein, and E. Beaurepaire, "Imaging lipid bodies in cells and tissues using third-harmonic generation microscopy," *Nature Methods*, vol. 3, pp. 47–53, January 2006.

[36] M. Farrar, F. Wise, J. Fetcho, and C. Schaffer, "In vivo imaging of myelin in the vertebrate central nervous system using third harmonic generation microscopy," *Biophysical Journal*, vol. 100, no. 5, pp. 1362 – 1371, 2011.

[37] Y. Fu, T. Frederick, T. Huff, G. Goings, S. Miller, and J. Cheng, "Paranodal myelin retraction in relapsing experimental autoimmune encephalomyelitis visualized by coherent anti-stokes raman scattering microscopy.," *Journal of Biomedical Optics*, vol. 16, no. 5, p. 106006, 2011.

[38] J. Imitola, D. Côté, S. Rasmussen, X. S. Xie, Y. Liu, T. Chitnis, R. L. Sidman, C. P. Lin, and S. J. Khoury, "Multimodal coherent anti-stokes raman scattering microscopy reveals microglia-associated myelin and axonal dysfunction in multiple sclerosis-like lesions in mice," *Journal of Biomedical Optics*, vol. 16, no. 2, pp. 021109–021109–11, 2011.

[39] P. Stoller, K. M. Reiser, P. M. Celliers, and A. M. Rubenchik, "Polarization-Modulated Second Harmonic Generation in Collagen," *Biophys J*, vol. 82, pp. 3330–3342, June 2002.

[40] S. Psilodimitrakopoulos, S. I. C. O. Santos, I. A. Roldan, A. K. N. Thayil, D. Artigas, and P. L. Alvarez, “In vivo, pixel-resolution mapping of thick filaments’ orientation in nonfibrilar muscle using polarization-sensitive second harmonic generation microscopy,” *Journal of Biomedical Optics*, vol. 14, no. 1, pp. 014001+, 2009.

[41] J. Duboisset, D. Aït-Belkacem, M. Roche, H. Rigneault, and S. Brasselet, “Generic model of the molecular orientational distribution probed by polarization-resolved second-harmonic generation,” *Phys. Rev. A*, vol. 85, p. 043829, Apr 2012.

[42] I. Gusachenko, G. Latour, and M.-C. Schanne-Klein, “Polarization-resolved second harmonic microscopy in anisotropic thick tissues,” *Opt. Express*, vol. 18, pp. 19339–19352, Aug 2010.

[43] J. X. Cheng, S. Pautot, D. A. Weitz, and X. S. Xie, “Ordering of water molecules between phospholipid bilayers visualized by coherent anti-stokes raman scattering microscopy,” *Proceedings of the National Academy of Sciences of the United States of America*, vol. 100, no. 17, pp. 9826–9830, 2003. Times Cited: 96.

[44] G. W. H. Wurpel, J. M. Schins, and M. Müller, “Direct measurement of chain order in single phospholipid mono- and bilayers with multiplex CARS,” *The Journal of Physical Chemistry B*, vol. 108, no. 11, pp. 3400–3403, 2004.

[45] G. Wurpel, H. Rinia, and M. Müller, “Imaging orientational order and lipid density in multilamellar vesicles with multiplex CARS microscopy,” *Journal of Microscopy*, vol. 218, no. 1, pp. 37–45, 2005.

[46] H. Wang, Y. Fu, P. Zickmund, R. Shi, and J.-X. Cheng, “Coherent anti-stokes raman scattering imaging of axonal myelin in live spinal tissues,” *Biophysical Journal*, vol. 89, no. 1, pp. 581 – 591, 2005.

[47] G. de Vito, I. Tonazzini, M. Cecchini, and V. Piazza, “RP-CARS: label-free optical readout of the myelin intrinsic healthiness,” *Opt. Express*, vol. 22, pp. 13733–13743, Jun 2014.

[48] M. Zimmerley, R. Younger, T. Valenton, D. C. Oertel, J. L. Ward, and E. O. Potma, “Molecular orientation in dry and hydrated cellulose fibers: A coherent anti-stokes raman scattering microscopy study,” *The Journal of Physical Chemistry B*, vol. 114, no. 31, pp. 10200–10208, 2010. PMID: 20684644.

[49] M. Zimmerley, P. Mahou, D. Débarre, M.-C. Schanne-Klein, and E. Beaurepaire, "Probing ordered lipid assemblies with polarized third-harmonic-generation microscopy," *Phys. Rev. X*, vol. 3, p. 011002, Jan 2013.

[50] A. Kress, *Probing molecular orientational order of lipid reporters and MHC Class I protein in cell membranes using polarization-resolved fluorescence imaging.* PhD thesis, Aix-Marseille University, 2011.

[51] A. Kress, X. Wang, H. Ranchon, J. Savatier, H. Rigneault, P. Ferrand, and S. Brasselet, "Mapping the local organization of cell membranes using excitation-polarization-resolved confocal fluorescence microscopy," *Biophysical Journal*, vol. 105, no. 1, pp. 127 – 136, 2013.

[52] A. Gasecka, T.-J. Han, C. Favard, B. R. Cho, and S. Brasselet, "Quantitative imaging of molecular order in lipid membranes using two-photon fluorescence polarimetry," *Biophysical Journal*, vol. 97, no. 10, pp. 2854 – 2862, 2009.

[53] S. Brasselet, "Polarization-resolved nonlinear microscopy: application to structural molecular and biological imaging," *Adv. Opt. Photon.*, vol. 3, pp. 205–271, Sep 2011.

[54] M. Müller and A. Zumbusch, "Coherent anti-stokes raman scattering microscopy," *ChemPhysChem*, vol. 8, no. 15, pp. 2156–2170, 2007.

[55] C. Krafft, B. Dietzek, M. Schmitt, and J. Popp, "Raman and coherent anti-stokes raman scattering microspectroscopy for biomedical applications," *Journal of Biomedical Optics*, vol. 17, no. 4, pp. 040801–1–040801–15, 2012.

[56] Y. Shen, *The principles of Nonlinear Optics, 1st edition.* Wiley, New York, 2002.

[57] D. Akimov, S. Chatzipapadopoulos, T. Meyer, N. Tarcea, B. Dietzek, M. Schmitt, and J. Popp, "Different contrast information obtained from CARS and nonresonant FWM images," *Journal of Raman Spectroscopy*, vol. 40, no. 8, pp. 941–947, 2009.

[58] Y. Wang, C.-Y. Lin, A. Nikolaenko, V. Raghunathan, and E. O. Potma, "Four-wave mixing microscopy of nanostructures," *Adv. Opt. Photon.*, vol. 3, pp. 1–52, Mar 2011.

[59] F. Munhoz, H. Rigneault, and S. Brasselet, "High order symmetry structural properties of vibrational resonances using multiple-field polarization coherent anti-stokes raman spectroscopy microscopy," *Phys. Rev. Lett.*, vol. 105, p. 123903, Sep 2010.

[60] E. O. Potma and X. S. Xie, "Direct visualization of lipid phase segregation in single lipid bilayers with coherent anti-stokes raman scattering microscopy," *ChemPhysChem*, vol. 6, no. 1, pp. 77–79, 2005.

[61] P. Nandakumar, A. Kovalev, and A. Volkmer, "Vibrational imaging based on stimulated raman scattering microscopy," *New Journal of Physics*, 2009.

[62] D. Aït-Belkacem, A. Gasecka, F. Munhoz, S. Brustlein, and S. Brasselet, "Influence of birefringence on polarization resolved nonlinear microscopy and collagen SHG structural imaging," *Opt. Express*, vol. 18, pp. 14859–14870, Jul 2010.

[63] R. M. Williams, W. R. Zipfel, and W. W. Webb, "Interpreting second-harmonic generation images of collagen i fibrils," *Biophysical Journal*, vol. 88, no. 2, pp. 1377 – 1386, 2005.

[64] R. Davis, J. Andrew Moad, G. Goeken, R. Wampler, and G. Simpson, "Selection rules and symmetry relations for four-wave mixing measurements of uniaxial assemblies," *The Journal of Physical Chemistry B*, vol. 112, no. 18, pp. 5834–5848, 2008. PMID: 18419167.

[65] F.-Z. Bioud, P. Gasecka, P. Ferrand, H. Rigneault, J. Duboisset, and S. Brasselet, "Structure of molecular packing probed by polarization-resolved nonlinear four-wave mixing and coherent anti-stokes raman-scattering microscopy," *Phys. Rev. A*, vol. 89, p. 013836, Jan 2014.

[66] A. Gasecka, *Microscopie non-lineaire polarimetrique dans les milieux moleculaires et biologiques.* Theses, Université Paul Cézanne - Aix-Marseille III, Dec. 2010.

[67] F. Munhoz, *Polarization resolved four-wave mixing microscopy : structural and vibrational read-out in molecular media.* PhD thesis, Aix-Marseille University, 2010.

[68] B. Richards and E. Wolf, "Electromagnetic diffraction in optical systems. ii. structure of the image field in an aplanatic system," *Proceedings of the Royal Society of London A: Mathematical, Physical and Engineering Sciences*, vol. 253, no. 1274, pp. 358–379, 1959.

[69] E. Yew and C. Sheppard, "Effects of axial field components on second harmonic generation microscopy," *Opt. Express*, vol. 14, pp. 1167–1174, Feb 2006.

[70] P. Schön, M. Behrndt, D. Aït-Belkacem, H. Rigneault, and S. Brasselet, "Polarization and phase pulse shaping applied to structural contrast in nonlinear microscopy imaging," *Phys. Rev. A*, vol. 81, p. 013809, Jan 2010.

[71] F.-Z. Bioud, *Polarization resolved four-wave mixing microscopy: a tool to probe molecular order in biological media.* PhD thesis, Université Paul Cézanne - Aix-Marseille III, 2014.

[72] J. Klauda, N. Eldho, K. Gawrisch, B. Brooks, and R. Pastor, "Collective and non-collective models of NMR relaxation in lipid vesicles and multilayers," *The Journal of Physical Chemistry B*, vol. 112, no. 19, pp. 5924–5929, 2008. PMID: 18179193.

[73] F. Picard, T. Buffeteau, B. Desbat, M. Auger, and M. Pézolet, "Quantitative orientation measurements in thin lipid films by attenuated total reflection infrared spectroscopy," *Biophysical Journal*, vol. 76, no. 1, pp. 539 – 551, 1999.

[74] P. Ferrand, P. Gasecka, A. Kress, X. Wang, F.-Z. Bioud, J. Duboisset, and S. Brasselet, "Ultimate use of two-photon fluorescence microscopy to map orientational behavior of fluorophores," *Biophysical Journal*, vol. 106, no. 11, pp. 2330 – 2339, 2014.

[75] N. Bloembergen, "The stimulated raman effect," *American Journal of Physics*, vol. 35, no. 11, pp. 989–1023, 1967.

[76] F. Munhoz, S. Brustlein, R. Hostein, P. Berto, S. Brasselet, and H. Rigneault, "Polarization resolved stimulated raman scattering: probing depolarization ratios of liquids," *Journal of Raman Spectroscopy*, vol. 43, no. 3, pp. 419–424, 2012.

[77] J. Duboisset, P. Berto, P. Gasecka, F.-Z. Bioud, P. Ferrand, H. Rigneault, and S. Brasselet, "Molecular orientational order probed by coherent anti-stokes raman scattering (CARS) and stimulated raman scattering (SRS) microscopy: A spectral comparative study," *The Journal of Physical Chemistry B*, vol. 119, no. 7, pp. 3242–3249, 2015. PMID: 25602288.

[78] G. de Vito, A. Bifone, and V. Piazza, "Rotating-polarization CARS microscopy: combining chemical and molecular orientation sensitivity," *Opt. Express*, vol. 20, pp. 29369–29377, Dec 2012.

[79] S. Brustlein, P. Ferrand, N. Walther, S. Brasselet, C. Billaudeau, D. Marguet, and H. Rigneault, "Optical parametric oscillator-based light source for coherent raman

scattering microscopy: practical overview," *Journal of Biomedical Optics*, vol. 16, no. 2, pp. 021106–021106–10, 2011.

[80] P. Ferrand, "GPScan.VI: A general-purpose labview program for scanning imaging or any application requiring synchronous analog voltage generation and data acquisition," *Computer Physics Communications*, vol. 192, no. 0, pp. 342 – 347, 2015.

[81] H. B. de Aguiar, P. Gasecka, and S. Brasselet, "Quantitative analysis of light scattering in polarization-resolved nonlinear microscopy," *Opt. Express*, vol. 23, pp. 8960–8973, Apr 2015.

[82] P. Schön, F. Munhoz, A. Gasecka, S. Brustlein, and S. Brasselet, "Polarization distortion effects in polarimetric two-photon microscopy," *Opt. Express*, vol. 16, pp. 20891–20901, Dec 2008.

[83] X. Wang, *Confocal angle resolved linear dichroism microscopy for structural fluorescence imaging*. PhD thesis, Université Paul Cézanne - Aix-Marseille III, 2013.

[84] I. Ledoux, C. Lepers, A. Périgaud, J. Badan, and J. Zyss, "Linear and nonlinear optical properties of N-4-nitrophenyl L-prolinol single crystals," *Optics Communications*, vol. 80, no. 2, pp. 149 – 154, 1990.

[85] F. Munhoz, H. Rigneault, and S. Brasselet, "Polarization-resolved four-wave mixing microscopy for structural imaging in thick tissues," *J. Opt. Soc. Am. B*, vol. 29, pp. 1541–1550, Jun 2012.

[86] A. Changoor, N. Tran-Khanh, S. Methot, M. Garon, M. Hurtig, M. Shive, and M. Buschmann, "A polarized light microscopy method for accurate and reliable grading of collagen organization in cartilage repair," *Osteoarthritis and Cartilage*, vol. 19, no. 1, pp. 126 – 135, 2011.

[87] S. P. Morgan, M. P. Khong, and M. G. Somekh, "Effects of polarization state and scatterer concentration on optical imaging through scattering media," *Appl. Opt.*, vol. 36, pp. 1560–1565, Mar 1997.

[88] C. E. Bigelow and T. H. Foster, "Confocal fluorescence polarization microscopy in turbid media: effects of scattering-induced depolarization," *J. Opt. Soc. Am. A*, vol. 23, pp. 2932–2943, Nov 2006.

[89] H. Radhakrishnan, A. Senapati, D. Kashyap, Y. B. Peng, and H. Liu, “Light scattering from rat nervous system measured intraoperatively by near-infrared reflectance spectroscopy,” *Journal of Biomedical Optics*, vol. 10, no. 5, pp. 051405–051405–8, 2005.

[90] S. Schott, J. Bertolotti, J.-F. Léger, L. Bourdieu, and S. Gigan, “Characterization of the angular memory effect of scattered light in biological tissues,” *Opt. Express*, vol. 23, pp. 13505–13516, May 2015.

[91] D. Xu and J. Esko, “A golgi-on-a-chip for glycan synthesis.,” *Nature Chemical Biology*, 2009.

[92] G. van Meer, “Cellular lipidomics,” *The EMBO Journal*, vol. 24, no. 18, pp. 3159–3165, 2005.

[93] G. van Meer, D. Voelker, and G. Feigenson, “Membrane lipids: where they are and how they behave.,” *Nature Reviews Molecular Cell Biology*, 2008.

[94] S. Singer and G. Nicolson, “The fluid mosaic model of the structure of cell membranes.,” *Science*, 1972.

[95] F. Goñi, “The basic structure and dynamics of cell membranes: An update of the singer-nicolson model,” *Biochimica et Biophysica Acta (BBA) - Biomembranes*, vol. 1838, no. 6, pp. 1467 – 1476, 2014. Membrane Structure and Function: Relevance in the Cell’s Physiology, Pathology and Therapy.

[96] T. Pomorski and A. Menon, “Lipid flippases and their biological functions,” *Cellular and Molecular Life Sciences CMLS*, vol. 63, no. 24, pp. 2908–2921, 2006.

[97] J. Holthuis and A. Menon, “Lipid landscapes and pipelines in membrane homeostasis.,” *Nature*, vol. 510, pp. 48–57, 2014.

[98] E. London, “How principles of domain formation in model membranes may explain ambiguities concerning lipid raft formation in cells,” *Biochimica et Biophysica Acta (BBA) - Molecular Cell Research*, vol. 1746, no. 3, pp. 203 – 220, 2005. Lipid Rafts: From Model Membranes to Cells.

[99] N. Kahya, D. Scherfeld, K. Bacia, B. Poolman, and P. Schwille, “Probing lipid mobility of raft-exhibiting model membranes by fluorescence correlation spectroscopy,” *Journal of Biological Chemistry*, vol. 278, no. 30, pp. 28109–28115, 2003.

[100] D. M. Small, “Lateral chain packing in lipids and membranes.,” *Journal of Lipid Research*, vol. 25, no. 13, pp. 1490–500, 1984.

[101] T. Heimburg, *Thermal Biophysics of Membranes. Tutorials in biophysics.* Wiley-VCH, Berlin, 2007.

[102] S. Semrau and T. Schmidt, “Membrane heterogeneity - from lipid domains to curvature effects,” *Soft Matter*, vol. 5, pp. 3174–3186, 2009.

[103] T. Idema, S. Semrau, C. Storm, and T. Schmidt, “Membrane mediated sorting,” *Phys. Rev. Lett.*, vol. 104, p. 198102, May 2010.

[104] K. Gaus, E. Gratton, E. P. W. Kable, A. S. Jones, I. Gelissen, L. Kritharides, and W. Jessup, “Visualizing lipid structure and raft domains in living cells with two-photon microscopy,” *Proceedings of the National Academy of Sciences*, vol. 100, no. 26, pp. 15554–15559, 2003.

[105] K. Jacobson, O. Mouritsen, and R. Anderson, “Lipid rafts: at a crossroad between cell biology and physics.,” *Nature Cell Biology*, 2007.

[106] H. Baumgart and W. Webb, “Imaging coexisting fluid domains in biomembrane models coupling curvature and line tension.,” *Nature*, 2003.

[107] F. Heberle and G. Feigenson, “Phase separation in lipid membranes.,” *Cold Spring Harbor Perspectives in Biology*, 2011.

[108] L. J. Pike, “Rafts defined: a report on the keystone symposium on lipid rafts and cell function,” *Journal of Lipid Research*, vol. 47, no. 7, pp. 1597–1598, 2006.

[109] D. Marguet, P.-F. Lenne, H. Rigneault, and H.-T. He, “Dynamics in the plasma membrane: how to combine fluidity and order,” *The EMBO Journal*, vol. 25, no. 15, pp. 3446–3457, 2006.

[110] Y.-H. M. Chan and S. G. Boxer, “Model membrane systems and their applications,” *Current Opinion in Chemical Biology*, vol. 11, no. 6, pp. 581 – 587, 2007. Model systems/Biopolymers.

[111] I. K. Vockenroth, P. P. Atanasova, J. R. Long, A. T. A. Jenkins, W. Knoll, and I. Köper, “Functional interporation of the pore forming segment of AChR M2 into tethered bilayer lipid membranes,” *Biochimica et Biophysica Acta (BBA) - Biomembranes*, vol. 1768, no. 5, pp. 1114 – 1120, 2007.

[112] J. A. Jackman, W. Knoll, and N.-J. Cho, “Biotechnology applications of tethered lipid bilayer membranes,” *Materials*, vol. 5, no. 12, p. 2637, 2012.

[113] S. Rebaud, O. Maniti, and A. P. Girard-Egrot, “Tethered bilayer lipid membranes (tBLMs): Interest and applications for biological membrane investigations,” *Biochimie*, vol. 107, Part A, pp. 135 – 142, 2014. From Membranes to Pathologies.

[114] A. Mashaghi, S. Mashaghi, I. Reviakine, R. M. A. Heeren, V. Sandoghdar, and M. Bonn, “Label-free characterization of biomembranes: from structure to dynamics,” *Chem. Soc. Rev.*, vol. 43, pp. 887–900, 2014.

[115] D. Warschawski and P. Devaux, “Order parameters of unsaturated phospholipids in membranes and the effect of cholesterol: a 1 H - 13 C solid-state NMR study at natural abundance,” *European Biophysics Journal*, vol. 34, no. 8, pp. 987–996, 2005.

[116] L. Vermeer, B. de Groot, V. Réat, A. Milon, and J. Czaplicki, “Acyl chain order parameter profiles in phospholipid bilayers: computation from molecular dynamics simulations and comparison with 2H NMR experiments,” *European Biophysics Journal*, vol. 36, no. 8, pp. 919–931, 2007.

[117] J. F. Nagle and S. Tristram-Nagle, “Structure of lipid bilayers,” *Biochimica et Biophysica Acta (BBA) - Reviews on Biomembranes*, vol. 1469, no. 3, pp. 159 – 195, 2000.

[118] S. Tristram-Nagle, Y. Liu, J. Legleiter, and J. F. Nagle, “Structure of gel phase DMPC determined by X-ray diffraction,” *Biophysical Journal*, vol. 83, no. 6, pp. 3324–3335, 2002.

[119] D. Marsh, “Lateral order in gel, subgel and crystalline phases of lipid membranes: Wide-angle X-ray scattering,” *Chemistry and Physics of Lipids*, vol. 165, no. 1, pp. 59 – 76, 2012.

[120] A. S. Klymchenko, S. Oncul, P. Didier, E. Schaub, L. Bagatolli, G. Duportail, and Y. Mély, “Visualization of lipid domains in giant unilamellar vesicles using an environment-sensitive membrane probe based on 3-hydroxyflavone,” *Biochimica et Biophysica Acta (BBA) - Biomembranes*, vol. 1788, no. 2, pp. 495 – 499, 2009.

[121] A. Kenworthy, “Fluorescence recovery after photobleaching studies of lipid rafts,” in *Lipid Rafts* (T. McIntosh, ed.), vol. 398 of *Methods in Molecular Biology*, pp. 179–192, Humana Press, 2007.

[122] R. Machan and M. Hof, “Lipid diffusion in planar membranes investigated by fluorescence correlation spectroscopy,” *Biochimica et Biophysica Acta (BBA) - Biomembranes*, vol. 1798, no. 7, pp. 1377 – 1391, 2010. Microscopy Imaging of Membrane Domains.

[123] L. Loura, A. Fedorov, and M. Prieto, “Resonance energy transfer in a model system of membranes: application to gel and liquid crystalline phases,” *Biophysical Journal*, vol. 71, no. 4, pp. 1823 – 1836, 1996.

[124] T. Parasassi, A. Giusti, M. Raimondi, and E. Gratton, “Abrupt modifications of phospholipid bilayer properties at critical cholesterol concentrations,” *Biophysical Journal*, vol. 68, no. 5, pp. 1895 – 1902, 1995.

[125] D. M. Owen, S. Oddos, S. Kumar, D. M. Davis, M. Neil, P. M. W. French, M. L. Dustin, A. I. Magee, and M. Cebecauer, “High plasma membrane lipid order imaged at the immunological synapse periphery in live T cells,” *Molecular Membrane Biology*, vol. 27, no. 4-6, pp. 178–189, 2010. PMID: 20540668.

[126] E. Sezgin and P. Schwille, “Fluorescence techniques to study lipid dynamics,” *Cold Spring Harbor Perspectives in Biology*, vol. 3, no. 11, 2011.

[127] R. N. Lewis and R. N. McElhaney, “Membrane lipid phase transitions and phase organization studied by fourier transform infrared spectroscopy,” *Biochimica et Biophysica Acta (BBA) - Biomembranes*, vol. 1828, no. 10, pp. 2347 – 2358, 2013. {FTIR} in membrane proteins and peptide studies.

[128] C. Lee and C. D. Bain, “Raman spectra of planar supported lipid bilayers,” *Biochimica et Biophysica Acta (BBA) - Biomembranes*, vol. 1711, no. 1, pp. 59 – 71, 2005.

[129] M. J. de Lange, M. Bonn, and M. Müller, “Direct measurement of phase coexistence in DPPC/cholesterol vesicles using Raman spectroscopy,” *Chemistry and Physics of Lipids*, vol. 146, no. 2, pp. 76 – 84, 2007.

[130] K. Suga, T. Yoshida, H. Ishii, Y. Okamoto, D. Nagao, M. Konno, and H. Umakoshi, “Membrane surface-enhanced raman spectroscopy for sensitive detection of molecular behavior of lipid assemblies,” *Analytical Chemistry*, vol. 87, no. 9, pp. 4772–4780, 2015. PMID: 25839320.

[131] M. Müller and J. M. Schins, “Imaging the thermodynamic state of lipid membranes with multiplex CARS microscopy,” *The Journal of Physical Chemistry B*, vol. 106, no. 14, pp. 3715–3723, 2002.

[132] N. Monteiro, A. Martins, R. L. Reis, and N. M. Neves, "Liposomes in tissue engineering and regenerative medicine," *Journal of The Royal Society Interface*, vol. 11, no. 101, 2014.

[133] C. Golding, S. Senior, M. Wilson, and P. O'Shea, "Time resolution of binding and membrane insertion of a mitochondrial signal peptide: correlation with structural changes and evidence for cooperativity," *Biochemistry*, 1996.

[134] J. Davis, "Deuterium magnetic resonance study of the gel and liquid crystalline phases of dipalmitoyl phosphatidylcholine," *Biophysical Journal*, vol. 27, no. 3, pp. 339 – 358, 1979.

[135] C. K. Haluska, A. P. Schröder, P. Didier, D. Heissler, G. Duportail, Y. Mély, and C. M. Marques, "Combining fluorescence lifetime and polarization microscopy to discriminate phase separated domains in giant unilamellar vesicles," *Biophysical Journal*, vol. 95, no. 12, pp. 5737 – 5747, 2008.

[136] A. Bangham, M. Hill, and N. Miller, "Preparation and use of liposomes as models of biological membranes," in *Methods in Membrane Biology* (E. Korn, ed.), pp. 1–68, Springer US, 1974.

[137] *Molecular Probes Handbook, A Guide to Fluorescent Probes and Labeling Technologies (Invitrogen life science).*

[138] D. Illinger, G. Duportail, Y. Mely, N. Poirel-Morales, D. Gerard, and J. G. Kuhry, "A comparison of the fluorescence properties of TMA-DPH as a probe for plasma membrane and for endocytic membrane.," *Biochim Biophys Acta*, vol. 1239, pp. 58–66, Oct 1995.

[139] I. Levin, R. Clark, and R. E. Hester, "Advances in infrared and raman spectroscopy, vol. 11. wiley-heyden, new york. 1984," *Journal of Raman Spectroscopy*, pp. 1–48, 1984.

[140] P. Berto, E. R. Andresen, and H. Rigneault, "Background-free stimulated raman spectroscopy and microscopy," *Phys. Rev. Lett.*, vol. 112, p. 053905, Feb 2014.

[141] J. C. Mansfield, G. R. Littlejohn, M. P. Seymour, R. J. Lind, S. Perfect, and J. Moger, "Label-free chemically specific imaging in planta with stimulated raman scattering microscopy," *Analytical Chemistry*, vol. 85, no. 10, pp. 5055–5063, 2013. PMID: 23581493.

[142] T. P. McMullen and R. N. McElhaney, "Physical studies of cholesterol-phospholipid interactions," *Current Opinion in Colloid & Interface Science*, vol. 1, no. 1, pp. 83 – 90, 1996.

[143] T. McMullen, R. Lewis, and R. McElhaney, "Cholesterol - phospholipid interactions, the liquid-ordered phase and lipid rafts in model and biological membranes," *Current Opinion in Colloid & Interface Science*, vol. 8, no. 6, pp. 459 – 468, 2004.

[144] N. Baumann and D. Pham-Dinh, "Biology of oligodendrocyte and myelin in the mammalian central nervous system," *Physiological Reviews*, vol. 81, no. 2, pp. 871–927, 2001.

[145] K. R. Jessen, "Glial cells," *The International Journal of Biochemistry & Cell Biology*, vol. 36, no. 10, pp. 1861 – 1867, 2004.

[146] M. Sofroniew and H. Vinters, "Astrocytes: biology and pathology," *Acta Neuropathologica*, vol. 119, no. 1, pp. 7–35, 2010.

[147] U. Hanisch and H. Kettenmann, "Microglia: active sensor and versatile effector cells in the normal and pathologic brain.," *Nature Neuroscience*, 2007.

[148] M. Monif, G. Burnstock, and D. A. Williams, "Microglia: Proliferation and activation driven by the P2X7 receptor," *The International Journal of Biochemistry & Cell Biology*, vol. 42, no. 11, pp. 1753 – 1756, 2010.

[149] R. Virchow, "Ueber das ausgebreitete vorkommen einer dem nervenmark analogen substanz in den tierischen geweben.," *Virchows Archiv. Pathological anatomy*, 1854.

[150] R. H. Quarles, W. B. Macklin, and P. Morell, "Myelin formation, structure and biochemistry," in *Basic Neurochemistry: Molecular, Cellular and Medical Aspects. 7th edition.* (G. Siegel, R. Albers, S. Brady, and D. Price, eds.), ch. 04, pp. 51–71, Academic Press Elsevier; New York, 7th ed., 2006.

[151] C. Raine, "Morphological aspects of myelin and myelination," in *Myelin* (P. Morell, ed.), pp. 1–49, Springer US, 1977.

[152] C. Berthold, I. Nilsson, and M. Rydmark, "Axon diameter and myelin sheath thickness in nerve fibres of the ventral spinal root of the seventh lumbar nerve of the adult and developing cat.," *Journal of Anatomy*, 1983.

[153] G. Gopalakrishnan, A. Awasthi, W. Belkaid, O. De Faria, D. Liazoghli, D. R. Colman, and A. S. Dhaunchak, "Lipidome and proteome map of myelin membranes," *Journal of Neuroscience Research*, vol. 91, no. 3, pp. 321–334, 2013.

[154] S. Aggarwal, L. Yurlova, and M. Simons, "Central nervous system myelin: structure, synthesis and assembly," *Trends in Cell Biology*, 2011.

[155] Y. Min, K. Kristiansen, J. M. Boggs, C. Husted, J. A. Zasadzinski, and J. Israelachvili, "Interaction forces and adhesion of supported myelin lipid bilayers modulated by myelin basic protein," *Proceedings of the National Academy of Sciences*, vol. 106, no. 9, pp. 3154–3159, 2009.

[156] C. A. Husted, G. B. Matson, D. A. Adams, D. S. Goodin, and M. W. Weiner, "In vivo detection of myelin phospholipids in multiple sclerosis with phosphorus magnetic resonance spectroscopic imaging," *Annals of Neurology*, vol. 36, no. 2, pp. 239–241, 1994.

[157] X. Banquy, K. Kristiansen, D. W. Lee, and J. N. Israelachvili, "Adhesion and hemifusion of cytoplasmic myelin lipid membranes are highly dependent on the lipid composition," *Biochimica et Biophysica Acta (BBA) - Biomembranes*, vol. 1818, no. 3, pp. 402 – 410, 2012.

[158] B. Ohler, K. Graf, R. Bragg, T. Lemons, R. Coe, C. Genain, J. Israelachvili, and C. Husted, "Role of lipid interactions in autoimmune demyelination," *Biochimica et Biophysica Acta (BBA) - Molecular Basis of Disease*, vol. 1688, no. 1, pp. 10 – 17, 2004.

[159] J. M. Anderson, D. W. Hampton, R. Patani, G. Pryce, R. A. Crowther, R. Reynolds, R. J. M. Franklin, G. Giovannoni, D. A. S. Compston, D. Baker, M. G. Spillantini, and S. Chandran, "Abnormally phosphorylated tau is associated with neuronal and axonal loss in experimental autoimmune encephalomyelitis and multiple sclerosis," *Brain*, vol. 131, no. 7, pp. 1736–1748, 2008.

[160] B. Kornek and H. Lassmann, "Neuropathology of multiple sclerosis - new concepts," *Brain Research Bulletin*, vol. 61, no. 3, pp. 321 – 326, 2003. Laboratory Diagnosis of Brain Damage and Inflammation with New and Old Markers in Human Cerebrospinal Fluid and Blood.

[161] C. Stadelmann, C. Wegner, and W. Brück, "Inflammation, demyelination, and degeneration - recent insights from MS pathology," *Biochimica et Biophysica Acta*

(BBA) - Molecular Basis of Disease, vol. 1812, no. 2, pp. 275 – 282, 2011. Molecular Basis of Multiple Sclerosis.

[162] S. C. Payne, C. A. Bartlett, A. R. Harvey, S. A. Dunlop, and M. Fitzgerald, "Myelin sheath decompaction, axon swelling, and functional loss during chronic secondary degeneration in rat optic nerve," *Investigative Ophthalmology & Visual Science*, vol. 53, no. 10, p. 6093, 2012.

[163] M. C. D. Canto, H. M. Wisniewski, A. B. Johnson, S. W. Brostoff, and C. S. Raine, "Vesicular disruption of myelin in autoimmune demyelination," *Journal of the Neurological Sciences*, vol. 24, no. 3, pp. 313 – 319, 1975.

[164] H. Lassmann, H. Ammerer, W. Jurecka, and W. Kulnig, "Ultrastructural sequence of myelin degradation," *Acta Neuropathologica*, vol. 44, no. 2, pp. 103–109, 1978.

[165] H. Lassmann and H. Wisniewski, "Chronic relapsing experimental allergic encephalomyelitis: Morphological sequence of myelin degradation," *Brain Research*, vol. 169, no. 2, pp. 357 – 368, 1979.

[166] C. M. Deber and S. J. Reynolds, "Central nervous system myelin: structure, function, and pathology," *Clinical Biochemistry*, vol. 24, no. 2, pp. 113 – 134, 1991.

[167] C. P. Genain, B. Cannella, S. L. Hauser, and C. S. Raine, "Identification of autoantibodies associated with myelin damage in multiple sclerosis.," *Nature Medicine*, vol. 5, no. 2, pp. 170 – 175, 1999.

[168] K. A. Williams, C. M. Deber, and O. A. Klrschner, "The structure and function of central nervous system myelin," *Critical Reviews in Clinical Laboratory Sciences*, vol. 30, no. 1, pp. 29–64, 1993. PMID: 7683887.

[169] D. W. Lee, X. Banquy, K. Kristiansen, Y. Kaufman, J. M. Boggs, and J. N. Israelachvili, "Lipid domains control myelin basic protein adsorption and membrane interactions between model myelin lipid bilayers," *Proceedings of the National Academy of Sciences*, vol. 111, no. 8, pp. E768–E775, 2014.

[170] C. Laule, V. Pavlova, E. Leung, G. Zhao, A. L. MacKay, P. Kozlowski, A. L. Traboulsee, D. K. B. Li, and G. R. W. Moore, "Diffusely abnormal white matter in multiple sclerosis: Further histologic studies provide evidence for a primary lipid abnormality with neurodegeneration," *Journal of Neuropathology & Experimental Neurology*, vol. 72, pp. 42–52, Jannuary 2013.

[171] R. Bakshi, A. J. Thompson, M. A. Rocca, D. Pelletier, V. Dousset, F. Barkhof, M. Inglese, C. R. Guttmann, M. A. Horsfield, and M. Filippi, "MRI in multiple sclerosis: current status and future prospects," *The Lancet Neurology*, vol. 7, no. 7, pp. 615 – 625, 2008.

[172] G. W. Moore, "Current concepts in the neuropathology and pathogenesis of multiple sclerosis.," *The Canadian Journal Of Neurological Sciences. Le Journal Canadien Des Sciences Neurologiques*, vol. 37 Suppl 2, no. 37, pp. 5 – 15, 2010.

[173] P. Kozlowski, P. Rosicka, J. Liu, A. C. Yung, and W. Tetzlaff, "In vivo longitudinal myelin water imaging in rat spinal cord following dorsal column transection injury," *Magnetic Resonance Imaging*, vol. 32, no. 3, pp. 250 – 258, 2014.

[174] B. Stankoff, Y. Wang, M. Bottlaender, M.-S. Aigrot, F. Dolle, C. Wu, D. Feinstein, G.-F. Huang, F. Semah, C. A. Mathis, W. Klunk, R. M. Gould, C. Lubetzki, and B. Zalc, "Imaging of CNS myelin by positron-emission tomography," *Proceedings of the National Academy of Sciences*, vol. 103, no. 24, pp. 9304–9309, 2006.

[175] R. M. Vigeveno, O. T. Wiebenga, M. P. Wattjes, J. J. Geurts, and F. Barkhof, "Shifting imaging targets in multiple sclerosis: From inflammation to neurodegeneration," *Journal of Magnetic Resonance Imaging*, vol. 36, no. 1, pp. 1–19, 2012.

[176] B. Erne, S. Sansano, M. Frank, and N. Schaeren-Wiemers, "Rafts in adult peripheral nerve myelin contain major structural myelin proteins and myelin and lymphocyte protein (MAL) and CD59 as specific markers," *Journal of Neurochemistry*, vol. 82, no. 3, pp. 550–562, 2002.

[177] W. T. Regenold, P. Phatak, C. M. Marano, L. Gearhart, C. H. Viens, and K. C. Hisley, "Myelin staining of deep white matter in the dorsolateral prefrontal cortex in schizophrenia, bipolar disorder, and unipolar major depression," *Psychiatry Research*, vol. 151, no. 3, pp. 179 – 188, 2007.

[178] A. G. Condie, S. L. Gerson, R. H. Miller, and Y. Wang, "Two-photon fluorescent imaging of myelination in the spinal cord," *ChemMedChem*, vol. 7, no. 12, pp. 2194–2203, 2012.

[179] P. C. Monsma and A. Brown, "Fluoromyelin red is a bright, photostable and nontoxic fluorescent stain for live imaging of myelin," *Journal of Neuroscience Methods*, vol. 209, no. 2, pp. 344 – 350, 2012.

[180] E. Romanelli, C. Sorbara, I. Nikic, A. Dagkalis, T. Misgeld, and M. Kerschensteiner, "Cellular, subcellular and functional in vivo labeling of the spinal cord using vital dyes," *Nature Protocols*, 2013.

[181] H. Inouye, J. Liu, L. Makowski, M. Palmisano, M. Burghammer, C. Riekel, and D. A. Kirschner, "Myelin organization in the nodal, paranodal, and juxtaparanodal regions revealed by scanning X-ray microdiffraction," *PLoS One*, 2014.

[182] J. Ben Arous, J. Binding, J.-F. Léger, M. Casado, P. Topilko, S. Gigan, A. Claude Boccara, and L. Bourdieu, "Single myelin fiber imaging in living rodents without labeling by deep optical coherence microscopy," *Journal of Biomedical Optics*, vol. 16, no. 11, pp. 116012–116012–9, 2011.

[183] F. P. Henry, Y. Wang, C. L. R. Rodriguez, M. A. Randolph, E. A. Z. Rust, J. M. Winograd, J. F. de Boer, and B. H. Park, "In vivo optical microscopy of peripheral nerve myelination with polarization sensitive-optical coherence tomography," *Journal of Biomedical Optics*, vol. 20, no. 4, p. 046002, 2015.

[184] H. Lim, D. Sharoukhov, I. Kassim, Y. Zhang, J. L. Salzer, and C. V. Melendez-Vasquez, "Label-free imaging of schwann cell myelination by third harmonic generation microscopy," *Proceedings of the National Academy of Sciences*, vol. 111, no. 50, pp. 18025–18030, 2014.

[185] A. Schain, R. Hill, and J. Grutzendler, "Label-free in vivo imaging of myelinated axons in health and disease with spectral confocal reflectance microscopy," *Nature Medicine*, 2014.

[186] E. Bélanger, S. Bégin, S. Laffray, Y. De Koninck, R. Valle, and D. Côté, "Quantitative myelin imaging with coherent anti-stokes raman scattering microscopy: alleviating the excitation polarization dependence with circularly polarized laser beams," *Opt. Express*, vol. 17, pp. 18419–18432, Oct 2009.

[187] Y. Fu, H. Wang, T. Huff, R. Shi, and J. Cheng, "Coherent anti-stokes raman scattering imaging of myelin degradation reveals a calcium-dependent pathway in lyso-ptdcho-induced demyelination.," *Journal of neuroscience research Neurosci Res*, 2007.

[188] T. B. Huff, Y. Shi, W. Sun, W. Wu, R. Shi, and J.-X. Cheng, "Real-time CARS imaging reveals a calpain-dependent pathway for paranodal myelin retraction during high-frequency stimulation," *PLoS ONE*, vol. 6, p. e17176, 03 2011.

[189] H. Wang, T. B. Huff, Y. Fu, K. Y. Jia, and J.-X. Cheng, “Increasing the imaging depth of coherent anti-stokes raman scattering microscopy with a miniature microscope objective,” *Opt. Lett.*, vol. 32, pp. 2212–2214, Aug 2007.

[190] E. Bélanger, F. P. Henry, R. Vallée, M. A. Randolph, I. E. Kochevar, J. M. Winograd, C. P. Lin, and D. Côté, “In vivo evaluation of demyelination and remyelination in a nerve crush injury model,” *Biomed. Opt. Express*, vol. 2, pp. 2698–2708, Sep 2011.

[191] A. Gasecka, A. Daradich, H. Dehez, M. Piché, and D. Côté, “Resolution and contrast enhancement in coherent anti-stokes raman-scattering microscopy,” *Opt. Lett.*, vol. 38, pp. 4510–4513, Nov 2013.

[192] S. Bégin, O. Dupont-Therrien, E. Bélanger, A. Daradich, S. Laffray, Y. D. Koninck, and D. C. Côté, “Automated method for the segmentation and morphometry of nerve fibers in large-scale CARS images of spinal cord tissue,” *Biomed. Opt. Express*, vol. 5, pp. 4145–4161, Dec 2014.

[193] S. Bégin, E. Bélanger, S. Laffray, B. Aubé, E. Chamma, J. Bélisle, S. Lacroix, Y. De Koninck, and D. Côté, “Local assessment of myelin health in a multiple sclerosis mouse model using a 2D fourier transform approach,” *Biomed. Opt. Express*, vol. 4, pp. 2003–2014, Oct 2013.

[194] J. Knöferle, J. Koch, T. Ostendorf, U. Michel, V. Planchamp, P. Vutova, L. Tönges, C. Stadelmann, Brüc., M. Bähr, and P. Lingor, “Mechanisms of acute axonal degeneration in the optic nerve in vivo,” *Proceedings of the National Academy of Sciences*, vol. 107, no. 13, pp. 6064–6069, 2010.

[195] Y. Fu, H. Wang, R. Shi, and J.-X. Cheng, “Second harmonic and sum frequency generation imaging of fibrous astroglial filaments in ex vivo spinal tissues,” *Biophysical Journal*, vol. 92, no. 9, pp. 3251 – 3259, 2007.

[196] F. Kirchhoff, F. Debarbieux, C. Kronland-Martinet, G. R. Cojocaru, and A. Popa-Wagner, “Combined two-photon laser-scanning microscopy and spectral microCT X-ray imaging to characterize the cellular signature and evolution of microstroke foci,” *Romanian journal of morphology and embryology = Revue roumaine de morphologie et embryologie*, vol. 53, no. 3 Suppl, pp. 671–5, 2012.

[197] M. Farrar, I. Bernstein, D. Schlafer, T. Cleland, J. Fetcho, and C. Schaffer, “Chronic in vivo imaging in the mouse spinal cord using an implanted chamber,” *Nature Methods*, 2012.

[198] B. Ylera, A. Ertürk, F. Hellal, F. Nadrigny, A. Hurtado, S. Tahirovic, M. Oudega, F. Kirchhoff, and F. Bradke, “Chronically CNS-injured adult sensory neurons gain regenerative competence upon a lesion of their peripheral axon,” *Current Biology*, vol. 19, no. 11, pp. 930 – 936, 2009.

[199] A. Nimmerjahn, F. Kirchhoff, and F. Helmchen, “Resting microglial cells are highly dynamic surveillants of brain parenchyma in vivo,” *Science*, vol. 308, no. 5726, pp. 1314–1318, 2005.

[200] J. Kim, N. Jiang, C. Tadokoro, L. Liu, R. Ransohoff, J. Lafaille, and M. Dustin, “Two-photon laser scanning microscopy imaging of intact spinal cord and cerebral cortex reveals requirement for CXCR6 and neuroinflammation in immune cell infiltration of cortical injury sites,” *Journal of Immunological Methods*, vol. 352, pp. 89–100, 2010.

[201] P. Vajkoczy, M. Laschinger, and B. Engelhardt, “Alpha 4 - integrin - VCAM - 1 binding mediates G protein - independent capture of encephalitogenic T cell blasts to CNS white matter microvessels,” *The Journal of Clinical Investigation*, vol. 108, pp. 557–565, 8 2001.

[202] I. Nikic, D. Merkler, C. Sorbara, M. Brinkoetter, M. Kreutzfeldt, F. Bareyre, W. Brück, D. Bishop, T. Misgeld, and M. Kerschensteiner, “A reversible form of axon damage in experimental autoimmune encephalomyelitis and multiple sclerosis,” *Nature Medicine*, 2011.

[203] M. Klugmann, M. H. Schwab, A. Pühlhofer, A. Schneider, F. Zimmermann, I. R. Griffiths, and K.-A. Nave, “Assembly of CNS myelin in the absence of proteolipid protein,” *Neuron*, vol. 18, no. 1, pp. 59 – 70, 1997.

[204] A. Hirano, H. Zimmerman, and S. Levine, “Electron microscopic observations of peripheral myelin in a central nervous system lesion,” *Acta Neuropathologica*, vol. 12, pp. 348–356, 1969.

[205] W. Knoll, J. Peters, P. Kursula, Y. Gerelli, J. Ollivier, B. Deme, M. Telling, E. Kemner, and F. Natali, “Structural and dynamical properties of reconstituted myelin

sheaths in the presence of myelin proteins MBP and P2 studied by neutron scattering," *Soft Matter*, vol. 10, pp. 519–529, 2014.

[206] F. Natali, Y. Gerelli, C. Stelletta, and J. Peters, "Anomalous proton dynamics of water molecules in neural tissue as seen by quasi-elastic neutron scattering. impact on medical imaging techniques," *AIP Conference Proceedings*, vol. 1518, pp. 551–557, 2013.

[207] D. Agrawal, R. Hawk, R. L. Avila, H. Inouye, and D. A. Kirschner, "Internodal myelination during development quantitated using X-ray diffraction," *Journal of Structural Biology*, vol. 168, pp. 521–526, 2009.

[208] N. Poccia, G. Campi, A. Ricci, A. S. Caporale, E. Di Cola, T. A. Hawkins, and A. Bianconi, "Changes of statistical structural fluctuations unveils an early compacted degraded stage of PNS myelin," *Scientific Reports*, 2014.

[209] Y. Min, T. Alig, D. Lee, J. Boggs, J. Israelachvili, and J. Zasadzinski, "Critical and off-critical miscibility transitions in model extracellular and cytoplasmic myelin lipid monolayers," *Biophysical Journal*, vol. 100, no. 6, pp. 1490 – 1498, 2011.

[210] D. W. Lee, Y. Min, P. Dhar, A. Ramachandran, J. N. Israelachvili, and J. A. Zasadzinski, "Relating domain size distribution to line tension and molecular dipole density in model cytoplasmic myelin lipid monolayers," *Proceedings of the National Academy of Sciences*, vol. 108, no. 23, pp. 9425–9430, 2011.

[211] J. H. Ipsen, G. Karlström, O. Mourtisen, H. Wennerström, and M. Zuckermann, "Phase equilibria in the phosphatidylcholine-cholesterol system," *Biochimica et Biophysica Acta (BBA) - Biomembranes*, vol. 905, no. 1, pp. 162 – 172, 1987.

[212] T. Baumgart, S. Das, W. Webb, and J. Jenkins, "Membrane elasticity in giant vesicles with fluid phase coexistence," *Biophysical Journal*, vol. 89, no. 2, pp. 1067 – 1080, 2005.

[213] R. Yu, K. Ueno, G. Glaser, and W. Tourtellotte, "Lipid and protein alterations of spinal cord and cord myelin of multiple sclerosis.," *Journal of neurochemistry*, 1982.

[214] P. Riccio, A. Fasano, N. Borenshtein, T. Bleve-Zacheo, and D. Kirschner, "Multilamellar packing of myelin modeled by lipid-bound MBP," *Journal of Neuroscience Research*, vol. 59, pp. 513–529, 2000.

[215] S. Aggarwal, N. Snaidero, G. Pahler, S. Frey, P. Sanchez, M. Zweckstetter, A. Janshoff, A. Schneider, M. Weil, I. Schaap, D. Gorlich, and M. Simons, "Myelin membrane assembly is driven by a phase transition of myelin basic proteins into a cohesive protein meshwork," *PLoS Biol*, vol. 11, p. e1001577, 06 2013.

[216] B. de Campos Vidal, M. L. Mello, A. C. Caseiro-Filho, and C. Godo, "Anisotropic properties of the myelin sheath.," *Acta Histochemica*, vol. 66, no. 1, pp. 32 – 39, 1980.

[217] S. Preibisch, S. Saalfeld, and P. Tomancak, "Globally optimal stitching of tiled 3D microscopic image acquisitions," *Bioinformatics*, vol. 25, no. 11, pp. 1463–1465, 2009.

[218] T. Zimmermann, J. Marrison, K. Hogg, and P. O'Toole, "Clearing up the signal: Spectral imaging and linear unmixing in fluorescence microscopy," in *Confocal Microscopy* (S. W. Paddock, ed.), vol. 1075 of *Methods in Molecular Biology*, pp. 129–148, Springer New York, 2014.

[219] P. Thevenaz, U. E. Ruttimann, and M. Unser, "A pyramid approach to subpixel registration based on intensity," *Image Processing, IEEE Transactions on*, vol. 7, pp. 27–41, Jan 1998.

[220] H. Kettenmann, U.-K. Hanisch, M. Noda, and A. Verkhratsky, "Physiology of microglia," *Physiological Reviews*, vol. 91, no. 2, pp. 461–553, 2011.

[221] N. Faust, F. Varas, L. M. Kelly, S. Heck, and T. Graf, "Insertion of enhanced green fluorescent protein into the lysozyme gene creates mice with green fluorescent granulocytes and macrophages," *Blood*, vol. 96, no. 2, pp. 719–726, 2000.

[222] K. Bulloch, M. M. Miller, J. Gal-Toth, T. A. Milner, A. Gottfried-Blackmore, E. M. Waters, U. W. Kaunzner, K. Liu, R. Lindquist, M. C. Nussenzweig, R. M. Steinman, and B. S. McEwen, "CD11c/EYFP transgene illuminates a discrete network of dendritic cells within the embryonic, neonatal, adult, and injured mouse brain," *The Journal of Comparative Neurology*, vol. 508, no. 5, pp. 687–710, 2008.

[223] C. Jack, F. Ruffini, A. Bar-Or, and J. P. Antel, "Microglia and multiple sclerosis," *Journal of Neuroscience Research*, vol. 81, no. 3, pp. 363–373, 2005.

[224] J. Antel, "Oligodendrocyte/myelin injury and repair as a function of the central nervous system environment," *Clinical Neurology and Neurosurgery*, vol. 108, no. 3,

pp. 245 – 249, 2006. Proceedings of the 3rd Dubrovnik International Conference on Multiple Sclerosis Dubrovnik, Croatia, 19-21 May 2005.

[225] S. Rasmussen, Y. Wang, P. Kivisäkk, R. T. Bronson, M. Meyer, J. Imitola, and S. J. Khoury, "Persistent activation of microglia is associated with neuronal dysfunction of callosal projecting pathways and multiple sclerosis-like lesions in relapsing–remitting experimental autoimmune encephalomyelitis," *Brain*, vol. 130, no. 11, pp. 2816–2829, 2007.

[226] D. A. Hume, "Macrophages as APC and the dendritic cell myth," *The Journal of Immunology*, vol. 181, no. 9, pp. 5829–5835, 2008.

[227] B. Ferguson, M. K. Matyszak, M. M. Esiri, and V. H. Perry, "Axonal damage in acute multiple sclerosis lesions.," *Brain*, vol. 120, no. 3, pp. 393–399, 1997.

[228] B. D. Trapp, J. Peterson, R. M. Ransohoff, R. Rudick, S. Mork, and L. Bo, "Axonal transection in the lesions of multiple sclerosis," *New England Journal of Medicine*, vol. 338, no. 5, pp. 278–285, 1998. PMID: 9445407.

[229] B. Kornek, M. K. Storch, R. Weissert, E. Wallstroem, A. Stefferl, T. Olsson, C. Linington, M. Schmidbauer, and H. Lassmann, "Multiple sclerosis and chronic autoimmune encephalomyelitis: A comparative quantitative study of axonal injury in active, inactive, and remyelinated lesions," *The American Journal of Pathology*, vol. 157, no. 1, pp. 267 – 276, 2000.

[230] J. Bauer, T. Sminia, F. Wouterlood, and C. Dijkstra, "Phagocytic activity of macrophages and microglial cells during the course of acute and chronic relapsing experimental autoimmune encephalomyelitis.," *Journal of Neuroscience Research*, 1994.

[231] H. Neumann, M. R. Kotter, and R. J. M. Franklin, "Debris clearance by microglia: an essential link between degeneration and regeneration," *Brain*, vol. 132, no. 2, pp. 288–295, 2009.

[232] A. Lampron, A. Larochelle, N. Laflamme, P. Préfontaine, M.-M. Plante, M. G. Sánchez, V. W. Yong, P. K. Stys, M.-E. Tremblay, and S. Rivest, "Inefficient clearance of myelin debris by microglia impairs remyelinating processes," *The Journal of Experimental Medicine*, vol. 212, no. 4, pp. 481–495, 2015.